UNIVERSITY OF CALIFORNIA

Santa Barbara

Microstructure Evolution in SiC/BN/SiC Composites During Exposure to Oxidizing Environments

A dissertation submitted in partial satisfaction of the

requirements for the degree Doctor of Philosophy

in Materials

by

Victoria Leah Christensen

Committee in charge:

Professor Frank W. Zok, Chair

Professor Carlos G. Levi

Professor Matthew R. Begley

Professor Michael J. Gordon

September 2024

The dissertation of Victoria Leah Christensen is approved.

_____

Carlos G. Levi

_____

Matthew R. Begley

_____

Michael J. Gordon

_____

Frank W. Zok, Committee Chair

June 2024

Microstructure Evolution in SiC/BN/SiC Composites

During Exposure to Oxidizing Environments

by

Victoria Leah Christensen

ACKNOWLEDGEMENTS

I am extremely grateful for the support I've received throughout my PhD. This dissertation would not have been possible without the help of many people. First and foremost, I'd like to express my sincere gratitude to my advisor, Frank Zok, for pushing me to become the best researcher I can be. I appreciate every lengthy discussion, paper edit, practice talk, word of encouragement, and tough feedback you have given me over the last 6 years. Thank you for giving me the opportunity to build relationships with our industry collaborators and foster new collaborations. Thank you for trusting me to source and manage the ion mill, which has been one of the most important pieces of equipment that made this PhD possible. Thank you for cultivating my strengths and helping me build skills I didn't know I was capable of. I am proud to be an alumnus of Team Zok!

Thank you to my committee members, Matt Begley, Carlos Levi, and Mike Gordon, for your curiosity, guidance, and encouragement. Matt, I appreciate our discussions about research, teaching pedagogy, career paths, and wine. Our trips to Penn State and Japan were filled with fun chats and laughter about both research and life. Carlos, thank you for checking in and supporting me throughout this journey and always encouraging me to ask questions. Mike, Chapter 3 is a long answer to your "simple" question about coating thickness uniformity in my qualifying exam. Thank you for asking the big-picture questions.

Thank you to all our collaborators from IHI, Pratt and Whitney, and ATL Advanced Coating Solutions for providing funding and materials for this work and engaging in insightful discussions. Sharing this research with scientists and engineers at these companies put my work into perspective. I never felt more motivated throughout this entire journey than I did after each meeting and trip. I will never forget our two trips to Japan and feel so grateful to have been given the opportunity to travel and learn about Japanese culture.

Thank you to our incredible research staff in the MPL, Deryck Stave and Dano Pagenkopf, for letting me take over the back corner of the lab and helping me set up my furnace. Thank you to the amazing staff within the Materials Characterization facility for teaching me techniques to obtain the beautiful SEM images within this work: Aidan Taylor, Claire Chisholm, and Ravit Silverstein. A special thank you goes to Pete Maxwell for being our go-to person within the Zok group for all things lab work. I will always remember our early morning lab sessions filled with plenty of conversation and coffee. Thank you for being our "lab dad" and supporting us in any way you could. I'll miss our chats in the office!

Thank you to my extremely supportive friends inside and outside of UCSB. Being roommates with Leah Mills, Emily Foley, and Becca Vincent started this journey on such a positive note. I will never forget family dinners, wine and movie nights, and surviving COVID together. I am so grateful for them and the other amazing women in my cohort (Kira Push, Carolina Frey, Colleen Reynolds, Muna Saber, and Lauren Fey) who always knew when we needed a night

out, camping trip, hike, game night, ski trip, picnic, dinner, workout, venting session, or a good book. It is so unique to be surrounded by such strong, smart, and beautiful women in an engineering field. WE DID IT, LADIES! I also couldn't have made it through this PhD without seeing Amanda Ruschel, Lauren Poole, Maddie McAllister, Collin Holgate, Virginia Collier, Ben Callaway, and Will Summers every day. You all made the hard work so rewarding by helping to celebrate every milestone! Thank you to Riana Catanzaro for your support every Monday evening during our weekly catch-up calls. Thank you to Melissa Hingorani for taking the leap with me into the start-up world! I learned so much from our journey and I'm so glad we got to experience it together. Finally, thank you to my partner, Axel Kleemeier, for your love, support, and encouragement. Thank you for giving me perspective when I was stressed about little things, always making me laugh, and letting me work from the bar at Storm Wines.

Thank you to my family—my mom, dad, and sisters Marisa and Erica—for your endless love and encouragement. Talking to my dad on my way to the office was the best part of my morning routine! I appreciated your pep talks when I needed them most. There wasn't a walk break without a call to one of my family members. Thank you for flying across the country into the little Santa Barbara airport for visits. I love you all so much.

CURRICULUM VITAE

Victoria Leah Christensen
June 2024

EDUCATION

2024 Ph.D. Materials, University of California, Santa Barbara

2022 Graduate Certificate in Technology Management, University of California, Santa Barbara

2018 B.S. Materials Science & Engineering, The Pennsylvania State University

PUBLICATIONS

1. **Victoria L. Christensen**, Frank W. Zok., "Insights into Internal Oxidation of SiC/BN/SiC Composites," *J. Am. Ceram. Soc.*, 106 [2] 1561-1575. EDITOR'S CHOICE

2. **Victoria L. Christensen**, Avery F. Samuel, Nicholas Han, Frank W. Zok, "Microstructure Characterization and Process-Structure Correlations in SiC/BN/SiC Minicomposites," *Acta Materialia*, 264

3. **Victoria L. Christensen**, Andrew R. Ericks, Ravit Silverstein, Isaac Duan, Frank W. Zok, "Oxidation of SiC Fibers in Water Vapor," *J. Am. Ceram. Soc.*, 2024; 1-19 RISING STARS SPECIAL ISSUE

In Preparation

4. **Victoria L. Christensen**, Oriol Gavalda-Diaz, Ryan Skillett, Calvin Prentice, Matthew R. Begley, Frank W. Zok, "Influence of BN Microstructure on the Oxidation of SiC/BN/SiC Composites," To be submitted to Journal of the American Ceramic Society

PRESENTATIONS AND INVITED LECTURES

1. **Victoria L. Christensen**, Frank W. Zok, "Oxidation of Bare and BN-Coated SiC Fibers at Intermediate Temperatures," International Conference on Advanced Ceramics and Composites, oral presentation (2020).

2. **Victoria L. Christensen**, Frank W. Zok, "Oxidation of BN Coatings in SiC/SiC Minicomposites at Intermediate Temperatures," International Conference on Advanced Ceramics and Composites, INVITED oral presentation (2021).

3. **Victoria L. Christensen**, Frank W. Zok, "Oxidation of BN Coatings in SiC/SiC Composites," Materials Science & Technology Conference, oral presentation (2021).

4. **Victoria L. Christensen**, Frank W. Zok, "Oxidation of Si-O-C Fibers in Water Vapor," International Conference on Advanced Ceramics and Composites, oral presentation (2022).

5. **Victoria L. Christensen**, Frank W. Zok, "Oxidation of SiC/BN/SiC Minicomposites in Dry and Wet Air," Gordon Research Conference on Solid State Studies in Ceramics, poster presentation (2022).

PROFESSIONAL AFFILIATIONS

2015 – 2024 **American Ceramic Society (ACerS)**
Diversity & Inclusion Committee, Humanitarian Activities Network Chair, Winter Workshop Committee, Global Young Investigator Forum Chair

2019 – 2020 Chair, ACerS President's Council of Student Advisors (PCSA)

AWARDS

2018 National Science Foundation Graduate Research Fellowship

2018 Holbrook Foundation Fellowship

ABSTRACT

Microstructure Evolution in SiC/BN/SiC Composites During Exposure to Oxidizing Environments

by

Victoria Leah Christensen

Ceramic matrix composites (CMCs) based on SiC/BN/SiC are promising candidates for high-temperature thermostructural applications in aerospace propulsion systems due to their low density and high strength and toughness. However, their long-term durability appears to be limited by oxidation and volatilization of the boron nitride (BN) interphase coatings at intermediate temperatures (700-1100°C), which can lead to significant strength and toughness degradation. Understanding the mechanisms governing microstructure evolution during oxidation is crucial for predicting long-term performance of these composites in service environments.

This dissertation investigates the oxidation behavior of SiC fibers, BN interphase coatings, and SiC matrices in SiC/BN/SiC composites exposed to oxidizing environments containing water vapor. Experiments are conducted on bare fibers, polished minicomposite surfaces, and minicomposites with matrix cracks, all at 1000°C. Advanced characterization techniques, including scanning electron microscopy (SEM), energy-dispersive X-ray spectroscopy (EDS), transmission electron microscopy (TEM) and custom image analysis codes, are employed to characterize and quantify microstructural changes, especially those in the vicinity of the fiber-matrix interface.

The results reveal that small differences in fiber composition can significantly affect the kinetics of scale growth and crystallization as well as the cracking behavior of these scales. The BN coating thickness and uniformity in pristine minicomposites are found to depend on the local fiber volume fraction and distance from the tow exterior, with closed fiber clusters being a major source of coating non-uniformity. Exposure of minicomposites to oxidizing environments lead to formation of oxide plugs and/or open channels, with the extent of BN recession dependent on coating thickness and as well as the transport distances for reaction product removal. Comparisons of oxidation behavior of composites with three types of BN coatings (crystalline, amorphous, and Si-doped) reveal distinct phase evolution and recession mechanisms.

This work yields new insights into the connections between microstructure, composition, and oxidation behavior of SiC/BN/SiC composites. The findings may in turn provide useful guidance in the development of coating designs and processing methods that lead to improved oxidation-resistant composites. Future research directions are proposed, including investigation of the role of oxidation in mechanical behavior, effects of cyclic oxidation, influence of gases representative of real combustion environments, and evolution of properties of borosilicate glasses during their formation and subsequent boria volatilization.

TABLE OF CONTENTS

Chapter 1

Introduction

1.1 Motivation

The aviation industry has revolutionized global connectivity. Nearly 100,000 civilian flights take off worldwide every day, collectively transporting almost 10 million passengers [1].[1] The economic impact is also immense, with aviation contributing over $3 trillion annually to the global GDP [1]. Despite these benefits, air travel exacts an environmental toll: airlines emit nearly 1 billion tons of CO_2 into the atmosphere each year [1]. To mitigate this issue, aerospace companies invest $15 billion annually in developing fuel-efficient technologies. In addition to reducing operating costs, increased efficiency curbs CO_2 emissions, aiding the global effort to cut emissions to half their 2005 levels by 2050.

The most effective approach to improving fuel efficiency focuses on enhancing aircraft engines. Gas turbine engines consist of six primary sections (Figure 1): the air inlet, fan, compressor, combustion chamber, turbine, and exhaust nozzle. The fan draws air into the inlet. The fan's size relative to the engine core (housing the remaining sections) determines the bypass ratio. High bypass ratio engines have large fan diameters, allowing a significant portion of air to bypass the core through a duct, providing thrust. The remaining air enters the core, first passing through the compressor's rotating blades, which compress the air to the pressure required for combustion. In the combustion chamber, fuel mixes with the compressed air and ignites, producing hot, high-pressure gases (primarily CO_2 and water

[1] These numbers, from 2019, reflect a “normal” year for travel pre-Covid19 pandemic.

vapor). These gases flow past the turbine blades, causing them to spin. The turbine shares an axle with the fan and compressor, powering their rotation. Finally, the exhaust gases exit through the nozzle, generating additional thrust [2].

Because high bypass ratio turbofans generate a significant thrust from air bypassing the core (avoiding combustion), they consume less fuel than low bypass ratio engines. Furthermore, their lower pressure requirements necessitate fewer compressor and turbine stages, reducing engine weight. Enhancing the efficiency of high bypass ratio engines therefore focuses on increasing the combustion temperature [3], [4].

Higher combustion temperatures accelerate the exhaust gases flowing through the turbine and nozzle, boosting propulsive efficiency. Additionally, a larger temperature differential between the inlet air and combustion gases increases thermal efficiency per the Carnot principle [5]. However, material limitations for combustor components (liners and fuel injection nozzles) and turbine components (blades and shrouds) constrain combustion temperatures.

Since the 1950s, significant advances in alloy strength, oxidation resistance, and high-temperature creep resistance have enabled higher operating temperatures (Figure 2) [6]. Compositional improvements utilizing solid solution strengthening (1960s-1970s) and precipitation hardening (1970s-1980s) raised operating temperatures from <1000°C to around 1150°C. In the 1980s, directionally solidified and single crystal alloys further enhanced high-temperature strength and creep resistance. Intricate cooling designs employing film cooling then enabled higher allowable gas temperatures with minor efficiency sacrifices (from redirecting compressor air to cooling channels) [7]. Ceramic thermal barrier coatings (TBCs) with low thermal conductivity produced higher temperature

differentials between hot gases and components, allowing for even higher gas temperatures. With these improvements exhausted for nickel superalloys, new higher-temperature material systems are required for further performance gains [4].

1.2 Ceramic Matrix Composites

Ceramics possess higher intrinsic melting temperatures than metal alloys due to their strong, covalent bonds. However, monolithic ceramics exhibit low ductility compared to metal alloys, hindering their safe use as engine components. This deficiency can be mitigated through ceramic matrix composites (CMCs). CMCs of interest consist of continuous ceramic fibers (typically SiC), fiber coatings, and ceramic matrices (also SiC-based). When well-designed, these CMCs exhibit high-temperature strengths about twice that of nickel superalloys with only one-third the mass density, while providing some ductility (Figure 3) [6], [8]. Like nickel superalloy components, ceramic coatings can impart thermal and environmental protection to CMC components, allowing combustion gas temperatures up to 200°C higher than nickel superalloys.

Following 50 years of research and development, the first commercial CMC implementation was in stationary turbine shroud components for CFM International's (a GE Aviation and Safran Aircraft Engines joint venture) LEAP engines, released in 2016 [9]. This engine burns 15% less fuel than previous generations without CMC components [9]. GE's next-generation GE9X engine, designed for Boeing's 777x and slated for 2025 service entry, will have CMCs replace nickel superalloys in inner and outer combustor liners, high-pressure turbine nozzles, and shrouds, totaling over 100 parts [10], [11]. Requiring 60% less cooling air, it will reduce emissions by 50% compared to current engines while being the largest, quietest, and most efficient ever built.

These initial CMC components are stationary parts because they often have simpler form factors and experience lower stresses than rotating blades. The latter parts contain complex joints and thin edges that make part manufacturing particularly challenging.

1.2.1 SiC Fibers

The main constituent providing the CMC its strength is the SiC fiber. With diameters between 10-14 μm and extremely small flaw sizes, these fibers exhibit tensile failure strengths between 2 and 3 GPa.

Fibers are principally produced by two Japanese companies: NGS Advanced Fibers [12], manufacturing the Nicalon family, and UBE Corporation [13], producing the Tyranno family. Each family and generation therein have a unique processing method. Fibers are created by first melt-spinning polycarbosilane (Nicalon family) or polymetallocarbosilane (Tyranno family) polymer precursors, followed by curing in oxidative environments and pyrolyzing at elevated temperatures in inert atmospheres [14]. Engine manufacturers can acquire continuous fiber tows containing 500-800 individual fibers or woven fabrics.

The first-generation Nicalon and Tyranno Lox M fibers are amorphous SiC_xO_y and non-stoichiometric, with C:Si atomic ratios ~1.3 and ~11 wt% oxygen. Tyranno Lox M also contains ~2 wt% titanium from its precursor. Due to excess carbon and oxygen, these fibers only retain strength up to 1100°C and creep resistance up to 1000°C [14].

The second-generation Hi-Nicalon and Tyranno ZMI fibers are also amorphous and non-stoichiometric (C:Si ~1.4) but with lower oxygen content (0.5 wt% for Hi-Nicalon and 9 wt% for Tyranno ZMI). Tyranno ZMI also contains ~1 wt% zirconium. Reduced oxygen levels led to an increase in creep resistance to 1200°C and strength retention to 1500°C for Hi-Nicalon and 1300°C for ZMI [14].

The third-generation Hi-Nicalon Type S (HNS) and Tyranno SA fibers are polycrystalline with ~50 nm and 200 nm grain sizes, respectively. Nearly stoichiometric with C:Si ratios of 1.05 (HNS) and 1.08 (SA), they contain < 1 wt% oxygen, with excess carbon and oxygen in amorphous SiC_xO_y phases and/or graphitic carbon at grain boundaries/triple junctions. Tyranno SA contains < 2 wt% aluminum and free carbon as graphite at grain triple junctions. These fibers maintain creep resistance up to 1400°C and tensile strength of ~2.5 GPa up to 1600°C [14].

Driven by performance and large-scale production capacity, Hi-Nicalon Type S is currently preferred for aeroengine applications, though previous generations like Hi-Nicalon and Tyranno ZMI remain under consideration for some lower-temperature components due to lower costs.

1.2.2 Interphase Coatings

The interphase coating provides CMC toughness. This intentionally weak interphase allows cracks initiating in the matrix to deflect around fibers, keeping them intact. It also enables load transfer between matrix and fibers so both can undergo multiple breaks along their length.

Boron nitride (BN) is the current material of choice for fiber coatings due to its low strength and available processing techniques. BN is typically deposited onto fibers within loose tows or woven fabrics via chemical vapor infiltration (CVI). Precursor gases containing boron (from BCl_3 or $B(CH_3)_3$) and nitrogen (from NH_3 or N_2) [15] infiltrate the spaces between fibers and react on the fiber surfaces to produce BN. Low temperature deposition (700-1000°C) yields amorphous BN coatings containing carbon and oxygen. At higher temperatures (1100-1300°C), BN is essentially stoichiometric and crystalline with a

strongly textured structure of hexagonal crystallites aligned with the fiber surface. Deposition temperature limitations are dictated by the candidate fibers' temperature capabilities.

For effectiveness, BN coatings must be continuous and of uniform thickness around each fiber. Otherwise, local chemical reactions between phases during subsequent processing or service can lead to partial fiber consumption and bonding. Controlling the deposition process, especially within woven fiber preforms, remains challenging. If fibers contact one another, gas transport pathways may close off, resulting in thin coatings in some preform sections. While the effects of coating non-uniformities on composite behavior are currently poorly understood, composite properties usually fall short of model predictions assuming uniform fiber coatings.

1.2.3 SiC Matrices

A dense, continuous SiC matrix surrounding the coated fibers enables load transfer between fibers across the composite. The matrix is typically applied once coated fibers are formed into unidirectional sheets or fabric is shaped using component-specific tooling. SiC matrices are created through various routes including CVI, melt infiltration (MI), and polymer infiltration and pyrolysis (PIP) [16].

CVI matrix deposition faces similar gas transport issues as BN coatings and is sensitive to temperature and deposition rates. Common SiC precursors are methyltrichlorosilane (CH_3SiCl_3 or MTS) and trichlorosilane ($SiHCl_3$ or TCS), used with H_2 and CH_4, respectively, at deposition temperatures in the range of 900-1400°C. Porosity often remains after CVI due to gas pathway closures.

To produce dense parts, additional steps like silicon melt infiltration (MI) and polymer infiltration and pyrolysis (PIP) are used. However, this often results in matrix portions containing silicon and/or amorphous SiC_xO_y pockets, lowering the overall temperature capability (silicon melts at 1414°C and amorphous SiC_xO_y has lower creep resistance than SiC). The role of matrix non-uniformities like variations in local matrix content or porosity is not well understood in the context of composite mechanical response, as analytical models assume a dense, continuous matrix.

1.3 Degradation and failure mechanisms in SiC/SiC composites

When well-designed, these composites' tensile failure strains can reach 1%: a particularly high value for a ceramic material. This ductility is achieved through cracks initiating in the matrix and deflecting around fibers at the BN coating interface. The typical CMC stress-strain curve (Figure 4) exhibits a linear-elastic domain followed by a matrix cracking domain until crack saturation, then a fiber-dominated domain until final failure. The resulting fracture surface features fibers extending above the matrix failure plane, called fiber pullout.

Engine components must endure thousands of hours and numerous takeoff, cruise, and landing cycles before replacement [17]. Therefore, a main challenge facing CMCs is maintaining high strength and toughness over long durations in aggressive engine environments. Depending on their location, CMC components will experience various temperatures, gas velocities, applied stresses, and chemical environments (Figure 1) [18], each potentially degrading the composite by affecting the load-bearing fibers, matrix, or coatings (Figure 5).

Fibers can degrade by subcritical crack growth, the gradual, stable propagation of pre-existing cracks or flaws under sustained loading, even when applied stress is below the critical stress needed for fast fracture (Figure 5a). Subcritical crack growth is driven by a combination of stress and a chemical interaction with the environment. For example, if a pre-existing crack in a fiber intersects a grain boundary containing free carbon, oxidants may react with the carbon to form CO(g), causing incremental crack extension and, over time, fiber fracture.

Creep and creep rupture are additional performance considerations (Figure 5b). The primary creep mechanism in SiC fibers at 1000-1400°C is grain boundary sliding. The resulting stress concentrations occurring at grain boundaries lead to formation of voids/cavities which in turn coalesce into cracks and lead to rupture. At higher temperatures, dislocations are generated and move, causing additional plastic deformation. Cracks may initiate when dislocations pile up at grain boundaries or inclusions [19], [20], [21], [22].

Fiber-fiber fusion (Figure 5c) can occur in fiber bundles when touching fibers either locally sinter at high temperatures (intrinsic fusion) or fuse with oxide in water vapor-containing environments (oxidative fusion). Rather than individual fiber failures, cracks propagate from one fused fiber to another through the fusion point. When many fused fibers break simultaneously, an instability may arise where the remaining fibers cannot bear the applied load, leading to a cascade of fiber breaks.

With prolonged high-temperature exposure, preferential grain growth may occur in fibers in near-surface regions, because of loss of the small amount of graphite that inhibits grain growth (Figure 5d). The larger-grained regions generally contain larger flaws and thus reduce the fiber strength.

Composite degradation can also occur through external oxidation and volatilization of the SiC matrix (Figure 5e). At high temperatures and with high-speed flow of water vapor, SiC oxidizes to form silica, which volatilizes as it reacts with water vapor to form SiO(g) and $Si(OH)_4$(g). In engine-relevant environments, material recession rates can be as high as 1μm/h - 10μm/h; over time durations of interest, the changes in part dimensions may compromise functionality and/or balance within the engine. To combat external oxidation and matrix volatilization, environmental barrier coatings (EBCs) are applied to components, to block the fast-flowing water vapor from interacting with SiC [23], [24].

When cracks inevitably form in the EBC and composite matrix, internal oxidation and volatilization can lead to extreme strength reduction and composite embrittlement (Figure 5f) [25]. The most severe strength degradation occurs not at the highest temperatures (1200-1400°C) but rather at intermediate temperatures (700-1100°C). Oxygen and water vapor gain access to BN coatings and SiC fibers through matrix crack pathways, forming borosilicate and silica glasses that strongly bond fibers to the matrix. Instead of deflecting around fibers, cracks penetrate through them, resulting in brittle fracture. The consumption of BN and SiC, borosilicate glass formation, and eventual silica sealing of fibers to the matrix is a highly coupled problem that depends on oxidant concentrations, gas flow speed, matrix crack opening displacement, fiber location, coating thickness and crystallinity, and fiber composition. This degradation mechanism is currently the least understood and is the subject of this dissertation.

Stress-rupture experiments on 2D and 3D composite specimens have shown significant strength reduction and rupture occurring in short times (< 1h depending on the environment) [26]. Variation in the resulting fracture surface has been observed both between tows and

within tows, revealing differing levels of embrittlement across the composite (Figure 6) [26], [27], [28]. In some cases, glassy oxides are visible in place of the BN coatings. In others, the BN is no longer present, leaving a gap between fibers and matrix [29]. Interpreting these results is difficult in 2D and 3D composite specimens because there are multiple tows in different locations, variations in coating thicknesses around fibers, and residual porosity in the matrix. Developing an understanding of the fundamentals of these failure mechanisms is most readily accomplished using simpler test specimens with controlled, well-characterized microstructures. It also requires an understanding of the thermochemistry and reaction kinetics of the constituent materials, notably SiC and BN, with environmental oxidants.

1.4 Thermochemistry of oxidation

Thermochemistry determines the chemical makeup of reaction products formed when SiC or BN are exposed to oxidative environments. A range of oxidant compositions, pressures, and temperatures within operational domains can be probed relatively quickly using thermodynamic software like FactSage. Such calculations can yield valuable insights into reaction mechanisms, especially in complex multi-material systems.

Some illustrative results from calculations based on the FactSage FactPS database are plotted in Figures 7-8 and Figures 10-11. These are based on the pure components (SiC and BN) at temperatures of 700-1300°C and a range of partial pressures of O_2 or H_2O. Some relevant observations follow.

SiC: When exposed to O_2 (Figure 7), SiC forms CO(g) and SiO(g). At a critical O_2 activity ($a_{O2} \sim 10^{-28}$ for 1000°C), SiO_2(s) forms. At a higher O_2 activity, C forms. C and SiC

are fully consumed at higher O_2 activities. When SiC is exposed to H_2O (Figure 8), a similar reaction sequence occurs, accompanied by formation of H_2(g) and CH_4(g).

While $Si(OH)_4$(g) also forms when SiO_2 is exposed to H_2O [30], thermodynamic data for $Si(OH)_4$(g) are not currently available in the FactSage FactPS database and thus it does not emerge as a potential reaction product. To remedy this deficiency, reported experimental data [31] were used to calculate partial pressures of $Si(OH)_4$ for the temperatures of interest (Figure 9). SiO_2 can also volatilize in H_2O by forming SiO(g) (Figure 8). At 1000°C and a H_2O activity of 0.1, the partial pressure of $Si(OH)_4$(g) is about 5 orders of magnitude greater than that of SiO(g), while at 1300°C and the same H_2O activity, $Si(OH)_4$(g) and SiO(g) are predicted to form in similar amounts and thus both will contribute significantly to SiO_2 volatilization.

BN: Exposed to O_2 (Figure 10), BN initially produces N_2(g), B_2O_3(g), NO(g), and NO_2(g). B_2O_3(l) emerges at higher O_2 activities ($a_{O_2} \approx 10^{-23}$ for 1000°C). At 1000°C, this critical activity is about 5 orders of magnitude greater than that required to produce SiO_2 from oxidation of SiC, indicating that SiC would oxidize in preference to BN. Beyond this point $p_{B_2O_3}$ plateaus and remains the B-containing gas with the highest partial pressure. In H_2O (Figure 11), BN produces HBO(g) and HBO_2(g) in addition to the gases formed in O_2. Once B_2O_3(l) forms, $p_{B_2O_3}$ plateaus while the partial pressures of the borohydroxide gases (including $H_3B_3O_6$(g) and H_3BO_3(g)) rise. B_2O_3(l) is fully consumed at higher H_2O activities. At 1000°C and an H_2O activity of 0.1, the total partial pressure of borohydroxide gases is 5 orders of magnitude greater than the partial pressure of $Si(OH)_4$(g), indicating that volatilization of B_2O_3 is far more severe than SiO_2. Calculation of volatilization rates and their dependence on partial pressure of hydroxide species is discussed next.

1.5 Rates of oxidation and volatilization

Internal oxidation and volatilization within CMCs is a highly coupled problem combining gas transport, consumption of constituents, oxide formation and mixing, and component volatilization within oxides [32], [33], [34]. Here, oxidation and volatilization kinetics are considered individually for SiC and BN, starting with fundamental theory used to calculate reaction rates.

1.5.1 Oxidation

In the domain of passive oxidation, the rate of oxide scale growth is well-described by the Deal-Grove model. The model is based on a 1D analysis of diffusive transport of oxidants or reaction products through the oxide scale, coupled with the reaction rate at the oxidation front [35]. The model leads to a linear/parabolic relation between oxide scale thickness h and time t that, in the absence of an initial oxide scale, has the form:

$$h = \frac{A}{2}\left\{\left[1 + \frac{t}{A^2/4B}\right]^{\frac{1}{2}} - 1\right\} \tag{1}$$

where B [μm^2/h] is the parabolic rate constant, and B/A [μm/h] is the linear growth rate. For short times, when scales are thin, *i.e.* $t << A^2/B$, Equation (1) reduces to the linear form $h = Bt/A$; conversely, for $t \gg A^2/B$, scales are thick, and growth is parabolic and given by $h = \sqrt{Bt}$.

The phenomenological oxidation parameters A and B are manifestations of two fundamental properties. The first is the oxidation rate, k, defined by the ratio of the flux of oxidant molecules to the oxidant concentration at the reaction front. It is related to A and B through:

$$k = \left(\frac{B}{A}\right)\frac{N}{C^*} \tag{2}$$

where N is the number of oxidant molecules per unit volume of oxide and C^* is the equilibrium concentration of oxidant in the scale, defined by Henry's law as $C^* = Hp_{ox}$. Here, p_{ox} is the partial pressure of the oxidant and H is Henry's Law solubility coefficient. The second is the permeability, γ, of the oxidants through the oxide layer, defined as:

$$\gamma = D_{eff}H = \frac{BN}{2p_{ox}} \tag{3}$$

where D_{eff} is the effective diffusivity of oxidants through the oxide scale. The composition of the oxidizing material can influence k, the reaction products formed, and the composition and structure of the oxide scale, which together govern γ.

1.5.2 Volatilization

Volatilization rates depend on the environment's characteristics (gas velocity, temperature, oxidant concentrations) and the equilibrium partial pressures of gas species formed (calculated via equilibrium thermochemistry). A general model used to determine the rate at which an oxide is consumed due to volatilization (the recession rate) is based on mass transfer through a gas boundary layer under laminar flow conditions. The average volatilization rate, $\dot{L_{vol}}$ (cm/s), across the surface of a flat plate is calculated via:

$$\dot{L_{vol}} = \dot{h_{vg}}\left(\frac{M_s\rho_{vg}}{\bar{n}M_{vg}\rho_s}\right) \tag{4}$$

where ρ_{vg} is the density of gas species formed, obtained via the ideal gas law, $\rho_{vg} = \frac{P_{vg}M_{vg}}{RT}$, with P_{vg} being the sum of the equilibrium partial pressures of volatile gases at the prescribed temperature, pressure, and oxidant concentration. $\bar{n}$ is the weighted average number of moles of gas species formed per mole of material consumed (from reaction stoichiometry),

M_{vg} is the weighted average molecular weight of the gas species, and M_s and ρ_s are the molecular weight and density of the material being consumed. $\dot{h_{vg}}$ is the average mass transfer coefficient of gas through a boundary layer which, for laminar flow along a flat plate, is given by [36]:

$$\dot{h_{vg}} = 0.664(Sc)^{\frac{1}{3}}(Re)^{\frac{1}{2}}\frac{D}{L} \tag{5}$$

where L is a characteristic distance on the substrate across which gas is flowing, and Sc and Re are the Schmidt and Reynolds numbers, respectively:

$$Sc = \frac{\mu_{eg}}{\rho_{eg}D} \tag{6}$$

$$Re = \frac{\rho_{eg}\nu_{eg}L}{\mu_{eg}} \tag{7}$$

where μ_{eg} is the environment gas viscosity, ρ_{eg} is the density (calculated via the ideal gas law, $\rho_{eg} = \frac{P_{eg}M_{eg}}{RT}$) and ν_{eg} is the gas speed. D is the Chapman-Enskog diffusivity of the volatile gas species through the environment gas (in cm/s):

$$D = 1.86x10^{-3}\frac{T^{\frac{3}{2}}}{P\sigma_{vg-eg}^2\Omega}\sqrt{\frac{1}{M_{eg}} + \frac{1}{M_{vg}}} \tag{8}$$

where T is temperature (K), *P* is total pressure (atm), σ_{vg-eg} is the average collision diameter of the environment gas and volatile gas (Å), Ω is the temperature-dependent collision integral (unitless), and *M* is molecular weight (g/mol). Estimates for σ_{vg-eg} and Ω can be made using tables in textbooks [36], [37].

1.5.3 SiC

SiC oxidizes to form solid SiO_2 and CO(g) and CO_2(g). At short times (in the linear growth domain), SiO_2 growth is limited by the reaction rate at the SiO_2/SiC interface. The linear rate constant, *B/A*, has an Arrhenius relationship with temperature, according to $\frac{B}{A} = \left(\frac{B}{A}\right)_0 \exp\left(-\frac{Q_{B/A}}{RT}\right)$. If the rate-limiting step is the reaction at the SiO_2/SiC interface, $Q_{B/A}$ is governed by the energy required to break Si-C bonds. While these activation energies have been measured there is considerable scatter and disagreement about these values in the literature. This is partly due to the short times associated with the linear domain and the difficulty in obtaining accurate measurements of thin scales. Additionally, linear oxidation rates are sensitive to material impurities, resulting in a wide range of $Q_{B/A}$ values. Recent molecular dynamics simulations have started to shed more light on the sequence of reactions occurring when oxidants reach the SiO_2/SiC interface and react with SiC [38]

At longer times (in the parabolic domain), SiO_2 growth is limited by either oxidant transport through SiO_2 to the SiO_2/SiC interface or reaction product transport through SiO_2 to the environment. If oxidant transport through SiO_2 is rate-limiting, then $B \propto D_{eff} * C^*$, where D_{eff} is the oxidant's effective diffusivity through SiO_2 and C^* is its saturation concentration in SiO_2. If reaction product transport from the SiO_2/SiC interface to the environment is rate-limiting, B follows the same form, although D_{eff} is now the effective diffusivity of the reaction product through SiO_2, and C^* is its saturation concentration in SiO_2. B also has an Arrhenius relationship with temperature, according to $B = B_0 \exp\left(-\frac{Q_B}{RT}\right)$. If oxidant transport through SiO_2 is rate-limiting, then Q_B is equal to the activation energy for oxidant diffusion (113 kJ/mol for O_2 [39] and 76.6 kJ/mol for H_2O [40]

through amorphous SiO_2). If the amorphous SiO_2 scale structure changes due to defects, impurities or crystallization, D_{eff} and C^* will differ from those of pure, amorphous SiO_2, influencing parabolic oxidation rates.

In general, water vapor accelerates SiC oxidation compared to oxygen because its permeability (product of diffusivity and solubility) through amorphous SiO_2 is greater. While O_2 has a larger diffusivity, H_2O's solubility is 3 orders of magnitude higher than O_2 [35]. This high solubility involves H_2O interacting with the amorphous SiO_2 structure to form -OH groups [41], breaking the glass network and reducing viscosity, allowing structural rearrangement and crystallization. Once the scale crystallizes, the structure becomes more rigid and permeability decreases[42], [43]. Water vapor will also react with the outer SiO_2 scale and form SiO(g) and $Si(OH)_4$(g) [31]. In laboratory furnace environments with 1 atm total pressure and slow gas velocities (~5 cm/s), calculated volatilization rates are typically very small (< 10^{-3} – 10^{-1}μm/h) [44] compared to high-pressure, high-velocity gas flows in engine environments (1-10 μm/h) [45], [46].

1.5.4 BN

BN oxidizes to form boria, B_2O_3, which melts at ~450°C. When B_2O_3 is liquid, gas transport through the scale is likely fast (though data for oxidant diffusion through liquid B_2O_3 are not currently available), making it non-protective. Consequently, the linear oxide growth domain for BN is expected to dominate to much greater scale thickness than that for SiC.

BN's oxidation kinetics depend sensitively on its structure. Crystalline hexagonal BN exhibits anisotropic oxidation kinetics, depending on whether the BN basal planes or crystallite edges are exposed. The crystallite edges are highly reactive sites for oxidants like H_2O because of the high density of dangling bonds. Therefore, oxidation rates for BN

parallel to basal planes, where crystallite edges are more exposed, have been measured to be ~5-20 times faster than rates perpendicular to basal planes [47]. Additionally, crystallite size and basal plane spacing influence oxidation rates, with smaller crystallite sizes and larger basal plane spacings leading to faster oxidation. Typically, amorphous BN has smaller crystallite sizes compared to crystalline CVD BN [48].

Because BN also forms significant partial pressures of $H_xB_yO_z$ gas species (even at ppm levels of H_2O), oxidation of BN is coupled with concurrent B_2O_3 volatilization. Concurrent oxidation and volatilization can be described by a paralinear model [49] [50]. In this model, oxide formation is assumed to be diffusion-controlled (although the non-protective nature of the liquid B_2O_3 scale calls this assumption into question), while the volatilization rate is constant at the external boundary. The growth rate of oxide scale thickness, h_{ox}, with time, t, is given by:

$$\frac{dh_{ox}}{dt} = \frac{k_p}{2h_{ox}} - k_l \tag{9}$$

where k_p is the parabolic rate constant for oxidation (units of length^2/time) and k_l is the linear rate constant for the volatilization reaction (units of length/time).

The paralinear model has been used by Jacobson to interpret experiments in which flat plates of BN produced at various temperatures were exposed to 1 atm oxygen containing ppm levels of H_2O in a thermogravimetric apparatus (TGA) [51]. BN deposited via chemical vapor deposition (CVD) at low temperatures had a lower density and higher oxygen content than high-temperature CVD BN. The low-temperature BN displayed rapid, linear oxidation kinetics. Other researchers have observed faster volatilization rates for BN with larger interplanar spacings and a lower onset oxidation temperature for BN with higher oxygen

content [47], [51]. Oxidation and volatilization rates have been found to be sensitive to BN crystallinity, oxygen impurity level, and water vapor content in the environment.

1.5.5 SiC and BN within a composite

In a composite, BN is constrained between the SiC fiber and SiC matrix. Gas is transported into the composite through matrix cracks with opening displacements typically in the 0.1-5μm range. At low oxidant partial pressures, SiC oxidizes preferentially to BN [32]. When BN oxidizes, liquid B_2O_3 mixes with silica and forms a borosilicate glass. The glass composition evolves depending on the BN oxidation rate, SiC oxidation rate, and B_2O_3 volatilization rate. When boria-rich, the glass has a low viscosity and can flow into the matrix crack channel. Oxidants can diffuse faster through this molten glass than a solid silica scale, so SiC oxidation is expected to follow linear kinetics in regions containing borosilicate. Once boria volatilizes from the glass, the glass becomes silica-rich; in turn its viscosity increases and its permeability to oxidants decreases.

Models have been developed to describe internal oxidation and volatilization within unidirectional CMCs [52], [53]. The models assume the presence of uniformly-coated fibers bridging a matrix crack with prescribed opening displacement and length. Gas in the environment is assumed to diffuse through the crack to the reaction sites. A finite amount of borosilicate with a prescribed B_2O_3 activity is assumed to be always present at the reaction site .

In one common scenario, the consumption rate of BN is assumed to be limited by diffusion of $H_xB_yO_z$ gas species, first out of the coating channel, then out of the matrix crack to the external environment, which is assumed to be a perfect sink. The equilibrium partial pressures of $H_xB_yO_z$ gases are calculated for the prescribed water vapor content and boria

activity. As recession proceeds, the width of the resulting channel decreases as the exposed surfaces of SiC fibers and matrix oxidize at rates unaffected by the borosilicate's presence. Gas diffusivities are updated according to the instantaneous channel width [52]. Under these assumptions, the coating channels are expected to close where the SiC surfaces have been exposed for the longest periods, nearest the matrix crack plane. Once gaps close with silica, the process stops and the terminal recession length i.e. the distance from the matrix crack plane to the intact BN, is attained.

This model was assessed over a range of coating thickness, temperature, and environment [52]. The results showed that:

(i) BN recession lengths are greatest for fibers near the external composite surface because the transport distances for $H_xB_yO_z$ removal are smallest. If the matrix crack quickly saturates with reaction products, little to no recession may be occur in the composite interior.

(ii) Thin coatings seal with oxide in less time than thick coatings, leading to shorter recession lengths.

(iii) Water vapor has two competing effects: it increases the $H_xB_yO_z$ reaction product concentration, driving recession, and accelerates SiC oxidation, which slows recession by closing the channel.

These models have yet to be critically assessed by experimental observations. Depending on the environmental conditions, composite geometry, and BN composition/crystallinity, the process may be limited by other mechanisms involving reaction rates and transport kinetics.

1.6 Objectives and dissertation outline

The overarching goal of this research is to determine the mechanisms governing microstructure evolution in SiC/BN/SiC composites during exposure to oxidizing environments. Visualizing and quantifying microstructural evolution of SiC fibers, BN coatings, and SiC matrices before and after exposure allows for assessment of current models describing internal oxidation and volatilization in ceramic composites. The approach involves direct comparisons between behaviors of various fiber types, coatings, and composite geometries, to uncover sensitivities of thermochemical reactions and reaction kinetics to composition, crystal structure, and geometry.

To determine the underlying mechanisms governing composite response in water vapor-containing environments, experiments are conducted on unidirectional minicomposite specimens, each consisting of an individual tow of SiC fibers, coated with CVI BN and surrounded by a CVI SiC matrix. Additionally, experiments are performed on bare fibers, to provide relevant baselines for interpreting and modeling minicomposite behavior.

A schematic representation of this research and its impact is shown in Figure 12. Based on the classic materials tetrahedron, this research focuses on how processing influences SiC and BN chemistry and composite microstructure and how that microstructure evolves during environmental exposure. The findings can be used to interpret changes in constituent properties and composite performance following oxidation.

To connect local variations in oxidation behavior to composite microstructure, the understanding gap between ideal and real composite microstructures needs to be bridged. Ideal composites have perfectly-aligned, equally-spaced fibers with uniform coatings, all placed in a dense matrix. In contrast, real composites contain various microstructural non-

uniformities resulting from the challenges in controlling the CVI process. These non-uniformities include fiber misalignment, fiber-fiber contacts, and variations in coating thickness. By connecting microstructural features to oxidation and volatilization behavior, future models might be able to incorporate realistic descriptions of composite microstructure and assess their effect on composite response.

All experiments were conducted at 1000°C: an intermediate temperature within the full temperature range of interest (700-1300°C). At this temperature, the gas species formed are representative of the entire temperature window, although the rates of oxidation and volatilization will naturally vary with temperature. Notwithstanding, the experimental methods and models developed here could be employed in future studies across a wider range of temperature and environment.

The remainder of the dissertation is organized as follows: Chapter 2 focuses on the oxidation behavior of 3 commercially-available Si-O-C fibers. Small changes in fiber chemistry are shown to affect oxidation rates and crystallization/cracking of oxide scales. The results represent an important baseline for interpreting minicomposite oxidation, particularly when fibers oxidize at different rates than the SiC matrix.

The remaining chapters focus on unidirectional composites. First, Chapter 3 presents a new methodology to characterize coating uniformity and defects in SiC/BN/SiC minicomposites. The methodology is applied to minicomposites produced by 3 manufacturers and used to demonstrate key correlations of coating thickness uniformity and fiber location with features of the CVI process. Describing the structures of real composites is an important first step in interpreting the experimental results in Chapters 4 and 5.

Chapter 4 provides insights into internal minicomposite oxidation through the first high-fidelity images of oxidation beneath a pristine composite surface and along matrix cracks. This study demonstrates the influence of coating thickness on gap sealing and the effects of limited gas transport through matrix crack pathways. In nominally dry air with ppm-levels of H2O, predictions from the standard model of internal oxidation and volatilization (described in Section 1.5.5) are found to significantly over-predict measured recession lengths. The origins of the discrepancies are identified.

Chapter 5 compares the oxidation behavior of 3 BN coating types: crystalline BN, amorphous BN, and Si-doped BN. Minicomposites produced by the same manufacturer were exposed to a water vapor environment for short and long times. The evolution of condensed phases within the reaction zones were found to differ greatly between the BN coating types and coating thicknesses. New mechanisms are proposed that account for BN crystallinity and composition, and new models are developed to describe recession lengths for crystalline BN coatings. Finally, conclusions and recommendations for future research are presented in Chapter 6.

1.7 References

[1] ATAG, “Aviation Benefits Beyond Boarders: Global Fact Sheet,” 2020. [Online]. Available: www.enviro.aero/SAF

[2] J. G. Leishman, “Turbojet Engines,” in *Introduction to Aerospace Flight Vehicles*, Embry-Riddle Aeronautical University, 2024. doi: https://doi.org/https://doi.org/10.15394/eaglepub.2022.1066.n32.

[3] H. Ohnabe, S. Masaki, M. Onozuka, K. Miyahara, and T. Sasa, “Potential application of ceramic matrix composites to aero-engine components,” *Compos Part A Appl Sci Manuf*, vol. 30, no. 4, pp. 489–496, 1999, doi: 10.1016/S1359-835X(98)00139-0.

[4] and M. National Academies of Sciences, Engineering, “Advanced Technologies for Gas Turbines,” 2020. doi: 10.17226/25630.

[5] J. L. Kerrebrock, *Aircraft Engines and Gas Turbines, second edition*. MIT Press, 1992.

[6] N. P. Padture, “Advanced structural ceramics in aerospace propulsion,” *Nat Mater*, vol. 15, no. 8, pp. 804–809, 2016, doi: 10.1038/nmat4687.

[7] J. C. Han, “Advanced Cooling in Gas Turbines 2016 Max Jakob Memorial Award Paper,” *J Heat Transfer*, vol. 140, no. 11, pp. 1–20, 2018, doi: 10.1115/1.4039644.

[8] J. A. Dicarlo, “Advances in SiC/SiC composites for aero-propulsion,” in *Ceramic Matrix Composites: Materials, Modeling and Technology*, 2015, pp. 217–236. Accessed: Jul. 14, 2019. [Online]. Available: https://onlinelibrary.wiley.com/doi/pdf/10.1002/9781118832998.ch7

[9] G. Gardiner, “A new era for ceramic matrix composites,” Composites World. [Online]. Available: https://www.compositesworld.com/articles/a-new-era-for-ceramic-matrix-composites

[10] “GE Aviation is fired up about CMCs!,” GE Aerospace. [Online]. Available: https://www.geaerospace.com/news/articles/manufacturing-technology/ge-aviation-fired-about-cmcs#:~:text=The GE9X engine for the,provided early insight into manufacturing

[11] “GE9X,” GE Aerospace. [Online]. Available: https://www.geaerospace.com/commercial/aircraft-engines/ge9x

[12] “NGS Advanced Fibers Product Lineup.” [Online]. Available: https://www.ngs-advanced-fibers.com/eng/item/index.html

[13] "UBE Corporation Tyranno Fiber." [Online]. Available: https://www.ube.com/contents/en/chemical/continuous_inorganic_fiber/tyranno_fiber.html

[14] H. Ichikawa, "Polymer-Derived Ceramic Fibers," *Annu Rev Mater Res*, vol. 46, no. 1, pp. 335–356, 2016, doi: 10.1146/annurev-matsci-070115-032127.

[15] G. L. Vignoles, *Chemical vapor deposition/ infiltration processes for ceramic composites*, vol. 1964. Elsevier Ltd., 2015. doi: 10.1016/B978-1-78242-307-2.00008-7.

[16] Krishan K. Chawla, "Chapter 7: Ceramic Matrix Composites," in *Composite Materials: Science and Engineering 4th Edition*, 2019, pp. 251–297.

[17] B. Prade, *Gas turbine operation and combustion performance issues*. Woodhead Publishing Limited, 2013. doi: 10.1533/9780857096067.3.383.

[18] X. T. Centrich, E. Shehab, P. Sydor, T. Mackley, P. John, and A. Harrison, "An aerospace requirements setting model to improve system design," *Procedia CIRP*, vol. 22, no. 1, pp. 287–292, 2014, doi: 10.1016/j.procir.2014.07.127.

[19] M. R. Begley, A. G. Evans, and R. M. McMeeking, "Creep rupture in ceramic matrix composites with creeping fibers," *J Mech Phys Solids*, vol. 43, no. 5, pp. 727–740, May 1995, doi: 10.1016/0022-5096(95)00006-5.

[20] H. M. Yun and J. A. Dicarlo, "Comparison of the Tensile, Creep, and Rupture Strength Properties of Stoichiometric SiC Fibers," 1999. Accessed: Jul. 16, 2019. [Online]. Available: https://ntrs.nasa.gov/search.jsp?R=19990116850

[21] J. A. DiCarlo, "Creep limitations of current polycrystalline ceramic fibers," *Compos Sci Technol*, vol. 51, no. 2, pp. 213–222, Jan. 1994, doi: 10.1016/0266-3538(94)90191-0.

[22] J. J. Sha, J. S. Park, T. Hinoki, and A. Kohyama, "Heat treatment effects on creep behavior of polycrystalline SiC fibers," *Mater Charact*, vol. 57, no. 1, pp. 6–11, Jul. 2006, doi: 10.1016/j.matchar.2005.11.019.

[23] J. A. Dicarlo, "Microstructural factors affecting creep-rupture failure of ceramic fibers and composites," *Ceramic transactions*, vol. 99, pp. 119–134, 1998.

[24] J. A. DiCarlo, H. M. Yun, and J. B. Hurst, "Fracture mechanisms for SiC fibers and SiC/SiC composites under stress-rupture conditions at high temperatures," *Appl Math Comput*, 2004, doi: 10.1016/S0096-3003(03)00570-8.

[25] G. N. Morscher, "Stress-environmental effects on fiber-reinforced SiC-based composites," in *Ceramic Matrix Composites: Materials, Modeling and Technology*, 2015, pp. 334–352.

[26] F. W. Zok, P. T. Maxwell, K. Kawanishi, and E. B. Callaway, “Degradation of a SiC-SiC composite in water vapor environments,” *Journal of the American Ceramic Society*, vol. 103, no. 3, pp. 1927–1941, Mar. 2020, doi: 10.1111/jace.16838.

[27] K. J. Larochelle and G. N. Morscher, “Tensile stress rupture behavior of a woven ceramic matrix composite in humid environments at intermediate temperature - Part i,” *Applied Composite Materials*, vol. 13, no. 3, pp. 147–172, May 2006, doi: 10.1007/s10443-006-9009-8.

[28] G. N. Morscher, J. Hurst, and D. Brewer, “Intermediate-Temperature Stress Rupture of a Woven Hi-Nicalon, BN-Interphase, SiC-Matrix Composite in Air,” *Journal of the American Ceramic Society*, vol. 83, no. 6, pp. 1441–1449, Jun. 2000, doi: 10.1111/j.1151-2916.2000.tb01408.x.

[29] N. S. Jacobson, G. N. Morscher, D. R. Bryant, and R. E. Tressler, “High-Temperature Oxidation of Boron Nitride: II, Boron Nitride Layers in Composites,” *Journal of the American Ceramic Society*, vol. 82, no. 6, pp. 1473–1482, Dec. 2004, doi: 10.1111/j.1151-2916.1999.tb01944.x.

[30] E. J. Opila, J. L. Smialek, R. C. Robinson, D. S. Fox, and N. S. Jacobson, “SiC Recession Caused by SiO2 Scale Volatility under Combustion Conditions: II, Thermodynamics and Gaseous-Diffusion Model,” *Journal of the American Ceramic Society*, vol. 82, no. 7, pp. 1826–1834, Jul. 1999, doi: 10.1111/j.1151-2916.1999.tb02005.x.

[31] N. S. Jacobson, E. J. Opila, D. L. Myers, and E. H. Copland, “Thermodynamics of gas phase species in the Si-O-H system,” *Journal of Chemical Thermodynamics*, vol. 37, no. 10, pp. 1130–1137, 2005, doi: 10.1016/j.jct.2005.02.001.

[32] D. L. Poerschke, M. N. Rossol, and F. W. Zok, “Intermediate Temperature Internal Oxidation of a SiC/SiCN Composite with a Polymer-Derived Matrix,” *Journal of the American Ceramic Society*, vol. 99, no. 9, pp. 3120–3128, Sep. 2016, doi: 10.1111/jace.14275.

[33] F. W. Zok, “Ceramic-matrix composites enable revolutionary gains in turbine engine efficiency,” *American Ceramic Society Bulletin*, vol. 95, no. 5, pp. 22–28, 2016, Accessed: Oct. 03, 2018. [Online]. Available: www.ceramics.org

[34] G. N. Morscher, “Stress-Environmental Effects on Fiber-Refinforced SiC-Based Composites,” in *Ceramic Matrix Composites: Materials, Modeling and Technology*, 2015, pp. 334–352. Accessed: Jul. 14, 2019. [Online]. Available: https://onlinelibrary.wiley.com/doi/pdf/10.1002/9781118832998.ch11

[35] B. E. Deal and A. S. Grove, “General Relationship for the Thermal Oxidation of Silicon,” *J Appl Phys*, vol. 36, no. 12, pp. 3770–3778, Dec. 1965, doi: 10.1063/1.1713945.

[36] D. R. Gaskell, *An Introduction to Transport Phenomena in Materials Engineering*, Second. Momentum press, LLC, 2012. [Online]. Available: https://ocw.mit.edu/courses/materials-science-and-engineering/3-185-transport-phenomena-in-materials-engineering-fall-2003/#

[37] D. R. Poirier and G. H. Geiger, *Transport Phenomena in Materials Processing*. 2016.

[38] D. A. Newsome *et al.*, "Oxidation of Silicon Carbide by O2 and H2O : A ReaxFF Reactive Molecular Dynamics Study, Part I," *Journal of Physical Chemistry C*, vol. 116, no. 30, pp. 16111–16121, 2012.

[39] F. J. Norton, "Permeation of Gaseous Oxygen through Vitreous Silica," *Nature*, no. 4789, p. 701, 1961.

[40] A. J. Moulson and J. P. Roberts, "Water in silica glass," *Transactions of the Faraday Society*, vol. 57, pp. 1208–1216, 1961, doi: 10.1039/TF9615701208.

[41] T. Bakos, S. N. Rashkeev, and S. T. Pantelides, "Reactions and Diffusion of Water and Oxygen Molecules in Amorphous SiO2," *Phys Rev Lett*, vol. 88, no. 5, p. 4, 2002, doi: 10.1103/PhysRevLett.88.055508.

[42] M. A. Lamkin, F. L. Riley, and R. J. Fordham, "Oxygen mobility in silicon dioxide and silicate glasses: a review," *J Eur Ceram Soc*, vol. 10, no. 5, pp. 347–367, 1992, doi: 10.1016/0955-2219(92)90010-B.

[43] V. Presser and K. G. Nickel, "Silica on silicon carbide," *Critical Reviews in Solid State and Materials Sciences*, vol. 33, no. 1, pp. 1–99, 2008, doi: 10.1080/10408430701718914.

[44] E. J. Opila, "Oxidation and Volatilization of Silica Formers in Water Vapor," *Journal of the American Ceramic Society*, vol. 86, no. 8, pp. 1238–1248, Aug. 2003, doi: 10.1111/j.1151-2916.2003.tb03459.x.

[45] R. C. Robinson and J. L. Smialek, "SiC Recession Caused by SiO2 Scale Volatility under Combustion Conditions: I, Experimental Results and Empirical Model," *Journal of the American Ceramic Society*, vol. 82, no. 7, pp. 1817–1825, Jul. 1999, doi: 10.1111/j.1151-2916.1999.tb02004.x.

[46] E. J. Opila, J. L. Smialek, R. C. Robinson, D. S. Fox, and N. S. Jacobson, "SiC Recession Caused by SiO_2 Scale Volatility under Combustion Conditions: II, Thermodynamics and Gaseous-Diffusion Model," *Journal of the American Ceramic Society*, vol. 82, no. 7, pp. 1826–1834, Jul. 1999, doi: 10.1111/j.1151-2916.1999.tb02005.x.

[47] P. Carminati, S. Jacques, and F. Rebillat, "Oxidation/corrosion of BN-based coatings as prospective interphases for SiC/SiC composites," *J Eur Ceram Soc*, vol. 41, no. 5, pp. 3120–3131, 2021, doi: 10.1016/j.jeurceramsoc.2020.07.056.

[48] H. Plaisantin, S. Jacques, J. Danet, G. Camus, and H. Delpouve, “TEM characterization of turbostratic and rhombohedral BN interphases synthesized by chemical vapour infiltration in SiC/SiC-Si composites,” *Mater Charact*, vol. 172, 2021, doi: 10.1016/j.matchar.2020.110857.

[49] E. Opila and R. Hann, “Paralinear Oxidation of CVD SiC in Water Vapor,” *J. Am. Ceram. Soc*, vol. 80, no. 1, pp. 197–205, 1997.

[50] N. Jacobson, S. Farmer, A. Moore, and H. Sayir, “High-Temperature Oxidation of Boron Nitride: I, Monolithic Boron Nitride,” *Journal of the American Ceramic Society*, vol. 82, no. 2, pp. 393–398, Dec. 1999, doi: 10.1111/j.1551-2916.1999.tb20075.x.

[51] N. Jacobson, S. Farmer, A. Moore, and H. Sayir, “High-Temperature Oxidation of Boron Nitride: I, Monolithic Boron Nitride,” *J. Am. Ceram. Soc.*, vol. 82, no. 2, pp. 393–98, 1999.

[52] V. E. Collier, W. Xu, R. M. McMeeking, F. W. Zok, and M. R. Begley, “Recession of BN coatings in SiC/SiC composites through reaction with water vapor,” *Journal of the American Ceramic Society*, no. April, pp. 1–14, 2021, doi: 10.1111/jace.18052.

[53] T. A. Parthasarathy, B. Cox, O. Sudre, C. Przybyla, and M. K. Cinibulk, “Modeling environmentally induced property degradation of SiC/BN/SiC ceramic matrix composites,” *Journal of the American Ceramic Society*, vol. 101, no. 3, pp. 973–997, Mar. 2018, doi: 10.1111/jace.15325.

1.8 Figures

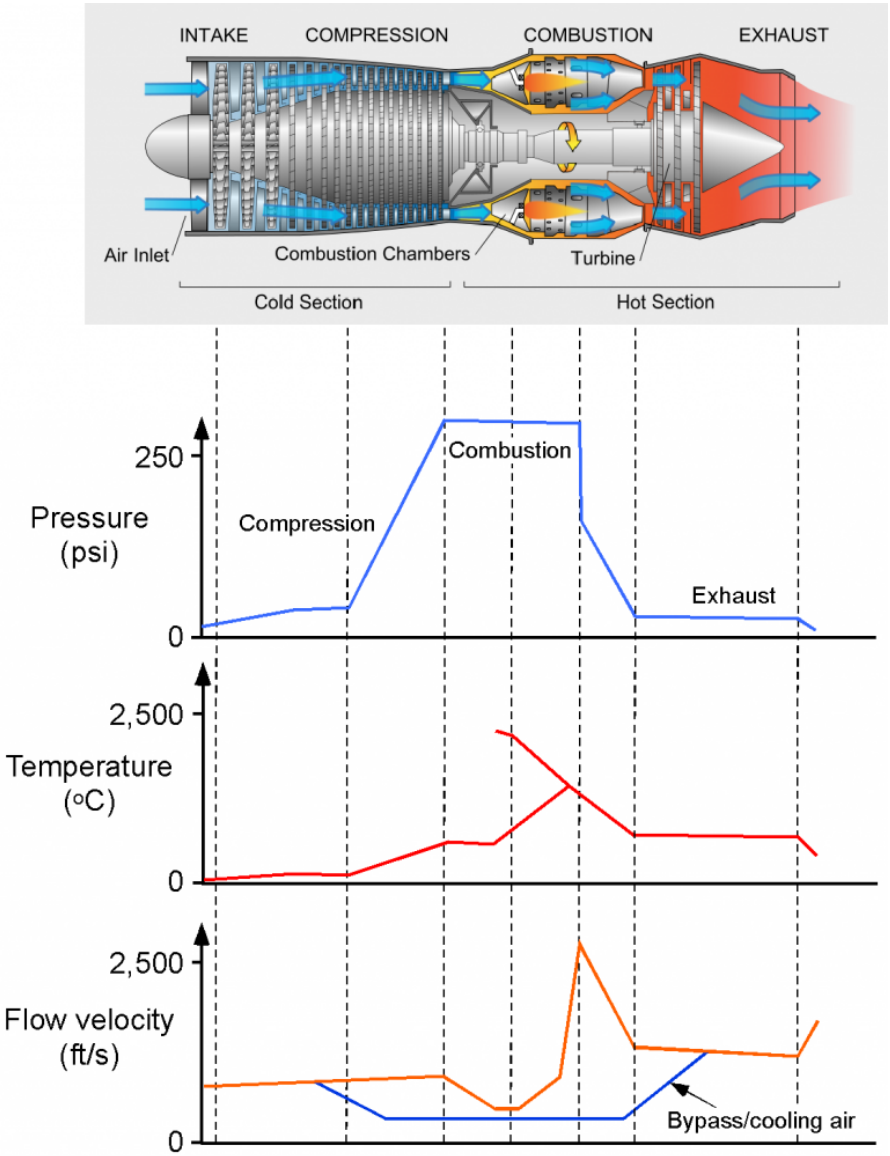

Figure 1: Representative pressure, temperature, and flow velocity variations through the sections a turbojet engine (Introduction to Aerospace Flight Vehicles Copyright © 2022, 2023, 2024 by J. Gordon Leishman is licensed under a Creative Commons Attribution-NonCommercial-NoDerivatives 4.0 International License)

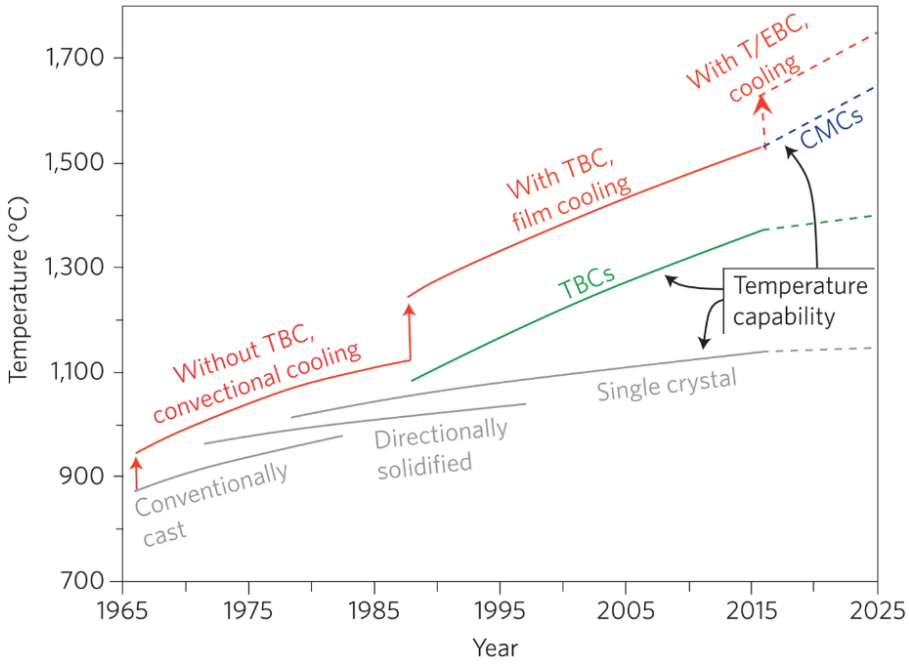

Figure 2: Evolution of combustion gas temperatures with material improvement. Nickel superalloys in grey, thermal barrier coatings in green, film cooling and coatings in red, and ceramic matrix composites in blue. (Re-printed with permission from Springer Nature [6])

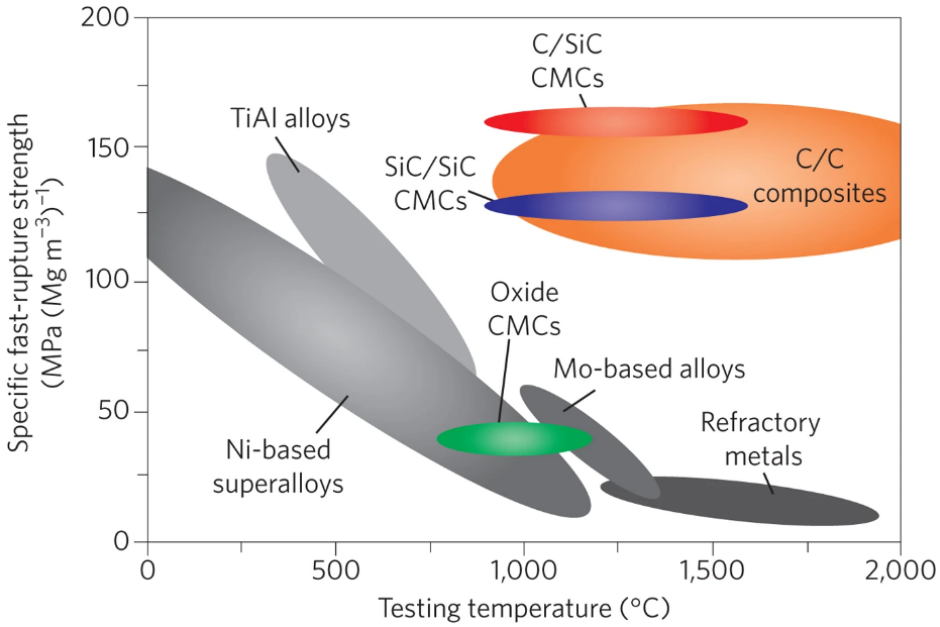

Figure 3: Specific fast-rupture strength as a function of temperature of various metals and composites. (Re-printed with permission from Springer Nature [6])

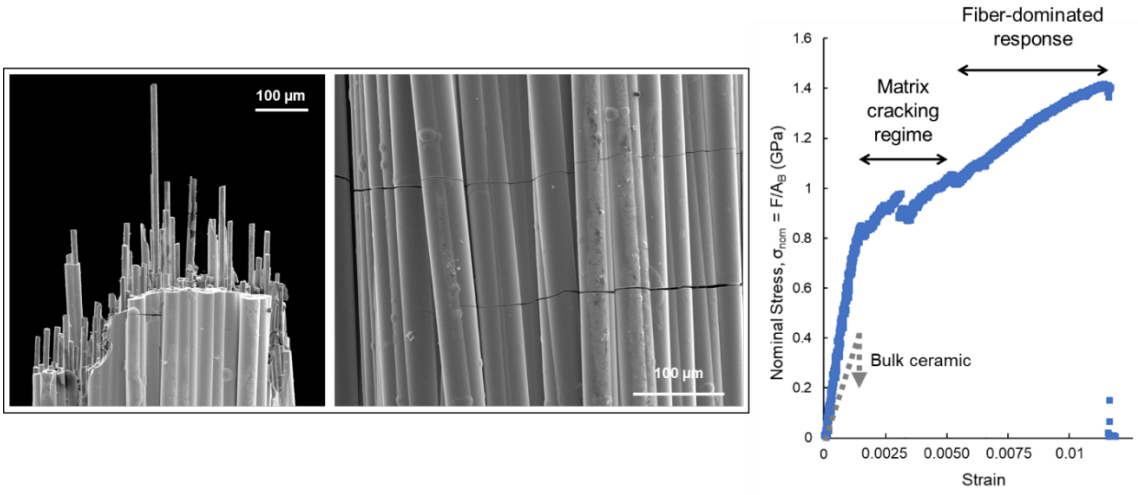

Figure 4: Fiber pull-out and multiple matrix cracking on a fractured ceramic composite. Ceramic composite reach failure strains of 1% or greater depending on the type of fiber used.

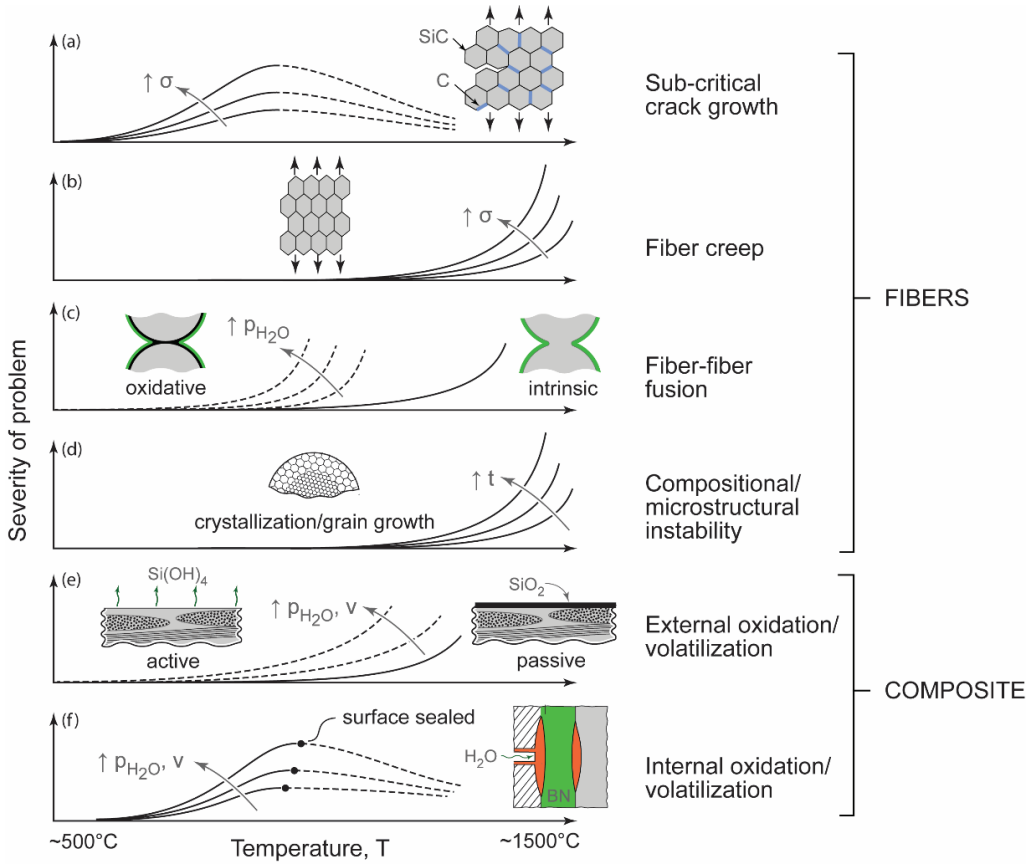

Figure 5: Degradation mechanisms that affect SiC fibers and SiC/BN/SiC composites. The severity of these degradation mechanisms are monotonic with temperature with the exception of composite internal oxidation and volatilization and fiber sub-critical crack growth.

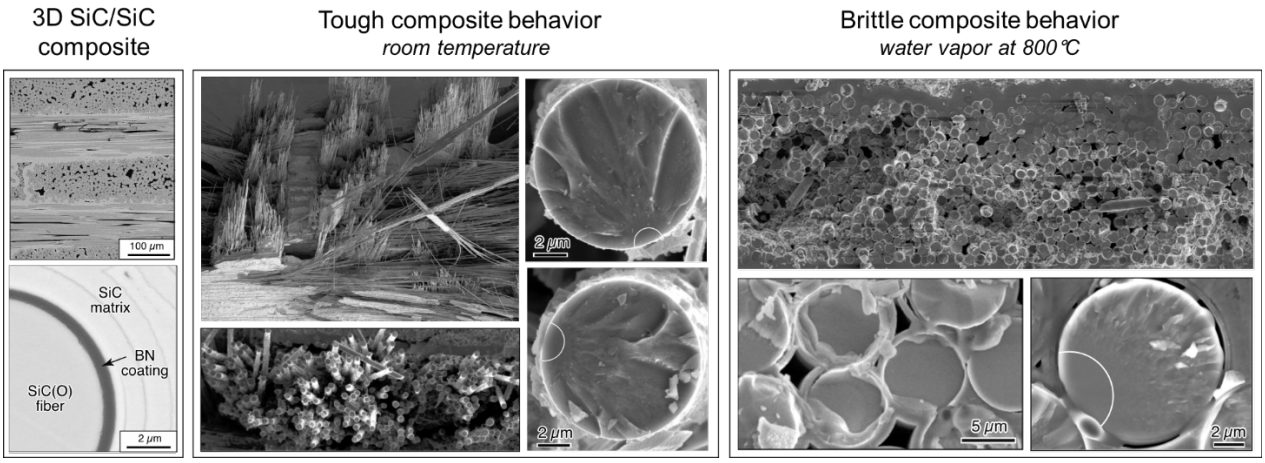

Figure 6: Fracture surface of a 3D composite displaying tough behavior at room temperature with fiber pull-out compared to a composite exposed to water vapor at 800C that failed in a brittle manner. Glassy oxides and gaps are present in place of BN coatings depending on fiber location. (adapted with permission from John Wiley and Sons [26])

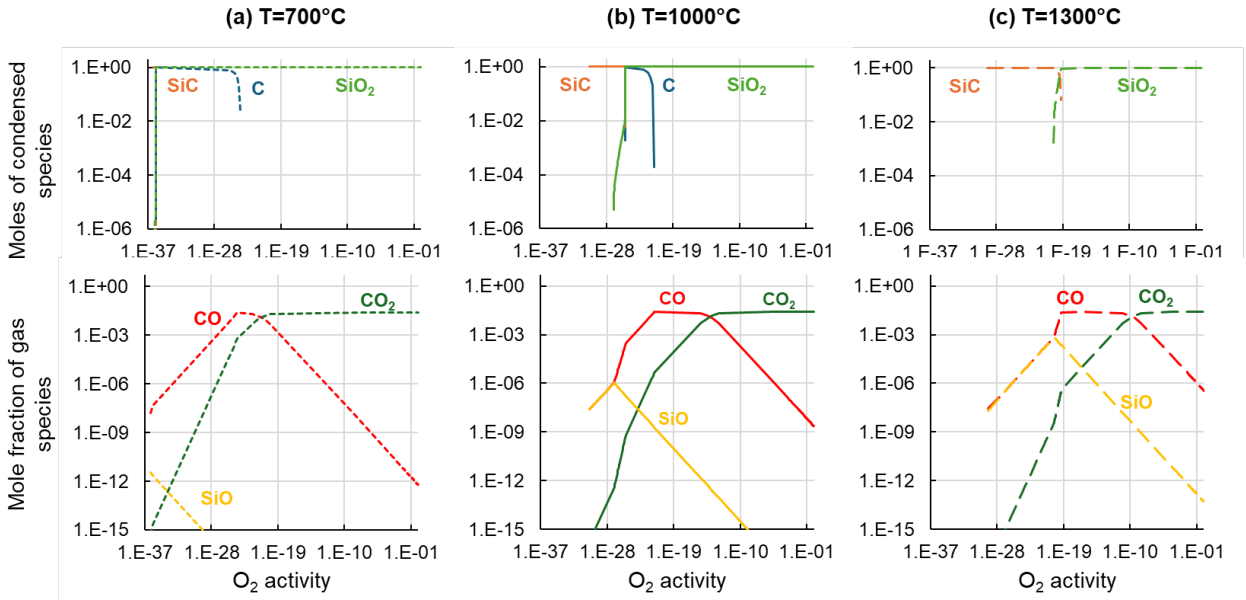

Figure 7: Thermochemistry calculations for 1 mole of SiC in Ar with increasing O_2 activity at 1atm total pressure and (a) 700°C, (b) 1000°C, and (c) 1300°C.

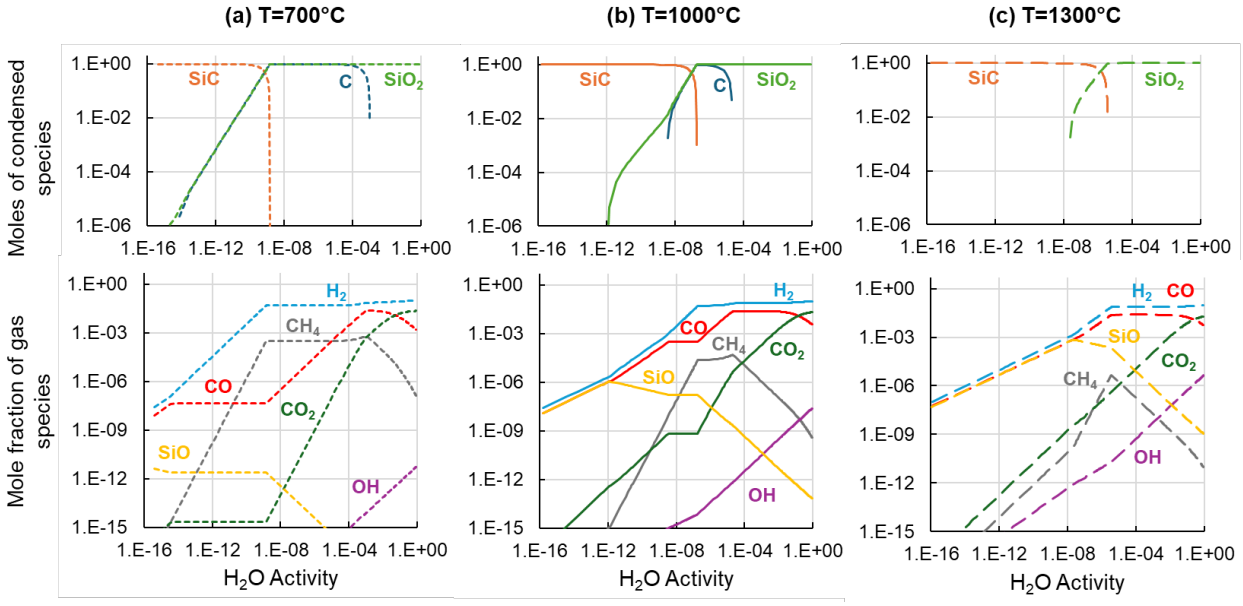

Figure 8: Thermochemistry calculations for 1 mole of SiC in Ar with increasing H_2O activity at 1atm total pressure and (a) 700°C, (b) 1000°C, and (c) 1300°C.

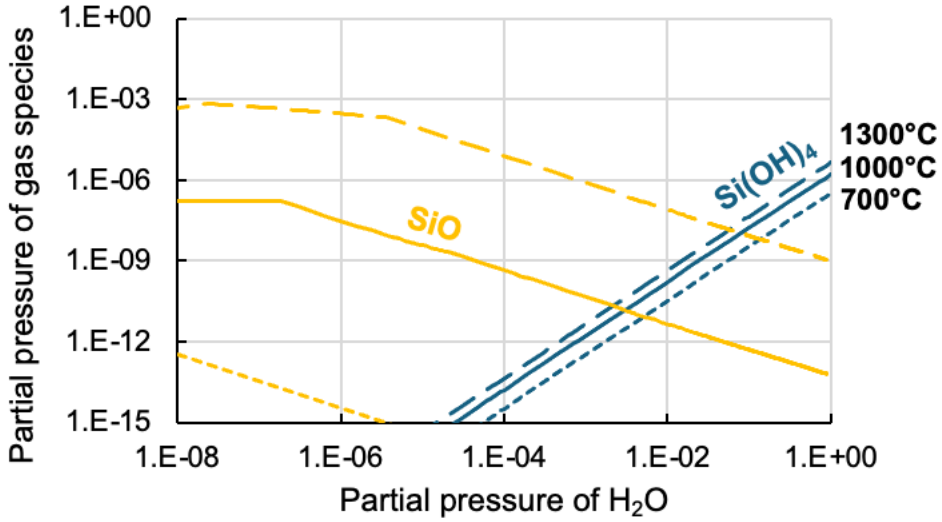

Figure 9: Calculated partial pressures of $Si(OH)_4$ and SiO gas in equilibrium with silica at 1atm total pressure with increasing partial pressure of H_2O for 700°C, 1000°C, and 1300°C [31].

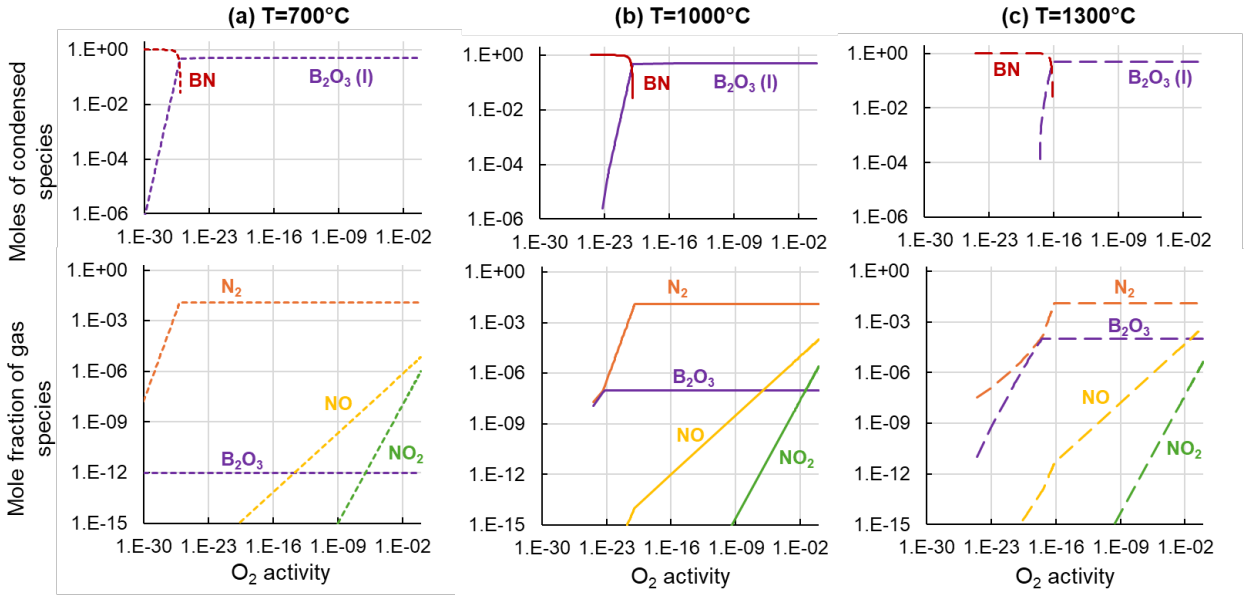

Figure 10: Thermochemistry calculations for 1 mole of BN in Ar with increasing O_2 activity at 1atm and (a) 700°C, (b) 1000°C, and (c) 1300°C.

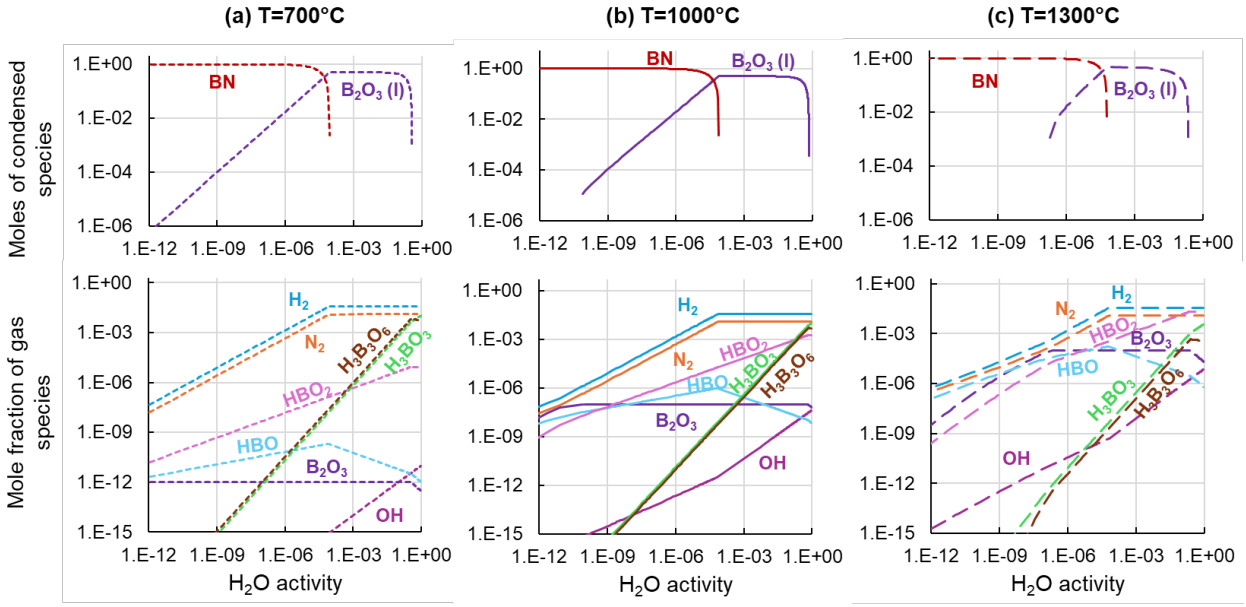

Figure 11: Thermochemistry calculations for 1 mole of BN in Ar with increasing H_2O activity at 1atm and (a) 700°C, (b) 1000°C, and (c) 1300°C.

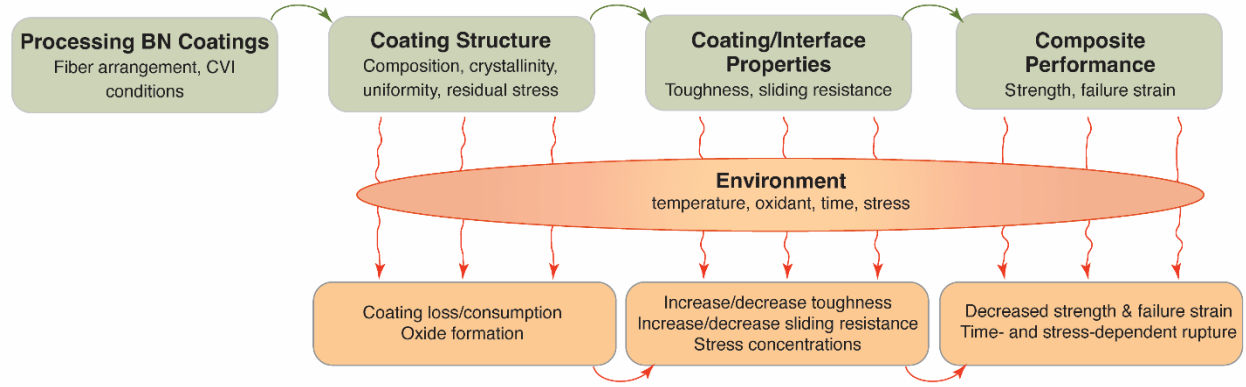

Figure 12: Schematic overview of this research and its impact. Composite processing influences BN coating structure which evolves in an oxidative environment to change its properties. This work uncovers process-structure correlations for the oxidation behavior of constituents within SiC/BN/SiC composites.

Chapter 2[†]

Oxidation of SiC Fibers in Water Vapor

2.1. Introduction

The rapid growth in use of SiC/SiC composites in aeroengine turbine applications has motivated studies on the long-term durability of these composites at high temperatures and in wet oxidizing environments [1], [2], [3], [4], [5], [6]. Internal oxidation in particular has long been recognized as a life-limiting threat and remains the subject of considerable scientific and technological interest. A thorough understanding of internal oxidation is lacking, however, because of the vast complexity of thermochemical and thermomechanical processes involved in the reactions of fibers and BN coatings with environmental gases. The thermochemical processes are highly coupled and highly localized. They include: (i) inward transport of oxidants through microcracks; (ii) consumption of oxidants through reaction with composite constituents; (iii) formation of new internal channels through volatilization of fiber coatings; (iv) outward transport of gaseous reaction products; and (v) formation of condensed reaction products that occupy more space than that created by consumption of the composite constituents. The resulting oxide produces large geometric changes in internal transport pathways, which can have profound effects on the mechanics of load transfer between phases and in turn on composite strength and toughness [7].

[†] The content of this chapter has previously appeared in the Journal of the American Ceramic Society (Christensen, V.L., Ericks, A. R., Silverstein, R., Duan, I., Zok, F.W., "Oxidation of SiC Fibers in Water Vapor," *J. Am. Ceram. Soc.*, 2024; 1-19). It is reproduced here with the permission of John Wiley and Sons.

While progress has been made in developing models and computational tools that capture some of these effects in SiC/SiC composites [8], [9], [10], the impact of such efforts will invariably be limited by the available properties of the composite constituents, both on their own (as a baseline) and in combination with one another. Even when the constituents are isolated, their properties can vary dramatically, depending on their synthesis route, composition and structure. BN is one case in point. It can be deposited on SiC fibers via chemical vapor routes over a wide range of temperatures and with various gas chemistries [11], [12], leading to structures ranging from purely amorphous to fully crystalline and reactivities that similarly span a wide range [13], [14] . SiC fibers, too, are synthesized from various precursors following different thermochemical processes and naturally exhibit a range of compositions, structure and properties [15], [16]. The current study focuses on one specific aspect of high temperature constituent properties, notably the oxidation behavior of the fibers alone.

Oxidation of SiC-based fibers involves several coupled effects of properties and processes. Some of the notable effects and their connections to one another are illustrated in Figure 1 and are summarized as follows.

(i) Commercial SiC fibers are rarely stoichiometric. They contain more C than Si, oxygen at concentrations of 1-10 at%, and in some cases minor amounts (≤1 at%) of metals such as Al or Zr [15], [16]. Some are crystalline while others are amorphous. These differences are expected to manifest in the reaction products formed, the composition of the oxide scale, and the sensitivities of oxidation kinetics to oxidant composition and exposure temperature.

(ii) Scale composition governs scale structure and properties. Properties of interest include permeability of oxidant gases and reaction products through the scales [17], [18]. Changes in permeability naturally affect scale growth kinetics. Scale composition also governs the stress-dependent scale viscosity [19], [20] which in turn controls the rate of stress relaxation via viscous flow.

(iii) While fiber oxidation at moderately high temperatures usually leads to formation of amorphous silica, the amorphous phase can crystallize over time as oxidation proceeds [21], [22]. Crystallization is facilitated by a high mobility of the constituent SiO_4^{4-} tetrahedra which is also manifested in a low viscosity. The consequences of crystallization are two-fold: reduced permeability, which lowers growth kinetics, and increased viscosity, which slows stress relaxation.

(iv) When it occurs, crystallization produces β-cristobalite which, upon cooling, readily transforms to α–cristobalite (at about 250°C) and undergoes a volume contraction of about 5% [23]. This contraction cannot be accommodated by viscous flow of the oxide scale and thus produces high tensile stresses within the scale.

(v) Because of the cylindrical geometry of the fibers, volume expansion accompanying oxidation leads to radial growth of the oxide scale and a tensile hoop strain in the outermost regions of the scale. The resulting hoop stress offsets the initial compressive stress generated upon scale formation and may eventually lead to scale cracking [24]. Poisson effects lead to axial strains within the scale that, because of constraints of the fiber, generate axial stresses.

This chapter presents a comparative study of the oxidation behavior of three commercially-available SiC-based fibers, all targeted for use in SiC-SiC composites for various aeroengine turbine applications. The principal goal is to identify the role of fiber composition in oxidation kinetics, evolution of scale structure and properties, and propensity for scale cracking. Because of the targeted use applications, the study focuses on oxidation in wet (high water vapor) environments. The study reveals a range of behaviors arising from moderate composition differences. The insights gleaned from this work are expected to inform future work on fiber oxidation within SiC/SiC composites.

The chapter is organized in the following way. Section 2.2 provides descriptions of fiber types employed in this study, sample preparation and oxidation procedures, and the nature of chemical analyses. Section 2.3 contains observations of the oxidized fibers, measurements of oxide scale thickness, and chemical compositions of the scales. Section 2.4 includes a discussion of composition effects on scale growth, crystallization, and cracking. Section 2.5 contains a summary of the key outcomes and their potential ramifications.

2.2. Methods

2.2.1 Fiber types

Three fiber types were employed in this study:

(i) Hi-Nicalon Type S^{TM} (HNS), a polycrystalline β-SiC fiber with a grain size of 10-50 nm [25], 1 at% oxygen, and an atomic C:Si ratio of 1.04 [15], [16]. In addition to β-SiC, the fibers contain some amorphous Si-O-C domains at SiC grain triple junctions. Free C, in the form of turbostratic graphite, is also present within the Si-O-C domains [26].

(ii) Tyranno ZMI^{TM}, a nanocrystalline fiber with amorphous Si-O-C/graphitic domains [27]. It contains 10.4 at% oxygen, 0.2 at% Zr, and an atomic C:Si ratio of 1.44 [15].

(iii) Tyranno SA^{TM}, a polycrystalline β-SiC fiber with a grain size of 50-100 nm [28]. Near-surface regions are nearly stoichiometric with a C:Si atomic ratio of 1.08. The core regions, in contrast, contain about 1.2 at% oxygen as well as excess carbon in the form of graphitic C domains located at SiC grain triple junctions [16]; here the overall C:Si ratio is 1.34. A small amount of Al (< 0.7 at%) is also present and is distributed uniformly throughout the fiber [29].

2.2.2 Oxidation experiments

Tows of desized HNS, ZMI, and SA fibers were oxidized concurrently for times ranging from 3h to 96h. Oxidation experiments were performed in a 99.6% alumina tube (Advalue Tech). All other hardware was made from alumina of the same purity. Each tow was placed on a pair of alumina supports at its ends, with the supports resting on the flat surface of an alumina D-tube (shown schematically in Figure 2); in this way the tows are suspended above the D-tube and aligned with the gas flow direction. A humidifier (P-series, Cellkraft) was used to achieve 20 vol% water vapor with the balance of dry air (Airgas). The volumetric flow rate was set to 0.86 L/min which, combined with the tube cross-sectional area (15 cm^2), yields a gas velocity of 4.4 cm/s in the hot zone. Prior to fiber oxidation, the alumina tubes and support hardware were burned out for 5h in flowing wet air at 1200°C. A low heating rate (2°C/min) was used to prevent microcracking of the alumina tube.

To prevent oxidation of the fibers during the temperature ramp, the D-tube with the fiber tows was placed in the cool section of the tube (T < 200°C) during heating. Once the

furnace reached the target temperature of 1000°C, the humidifier was turned on, the water vapor flow was stabilized at the prescribed level, and the D-tube and tows were inserted into the hot zone via alumina rods attached to the D-tube with platinum wire. Upon completion of the exposure, the humidifier was turned off, the D-tube with the tows was extracted from the hot zone, and the furnace cooled at 2°C/min.

2.2.3 Imaging and image analysis

Cross-sections and exteriors of fiber tows were imaged via SEM in both backscatter (BSE) and secondary electron (SE) modes. To create cross-sections, fiber tows were first embedded in a low-viscosity epoxy (Epoxybond 110, Allied) between a glass slide and a glass cover slip and cured on a hot plate at 150°C for 5 min. The glass slide sandwiches were then cut using a slow speed saw and cross-sectioned in an ion mill (Leica TIC3x). Ion milling creates transverse cross-sections of entire fiber tows, each containing 500-800 fibers.

Scale thicknesses were measured on 20-30 fibers in the tow interiors from montages of SEM images using a combination of Adobe Photoshop and FIJI software [30]. First, for each fiber examined, a circle was manually placed at the fiber/scale interface, its area was measured, and the radius of that circle was calculated. Next, the area circumscribed by the outer scale boundary was measured; the radius of a circle with equivalent area was calculated. The difference in the two resulting radii was taken as the average scale thickness for that fiber.

Fibers oxidized for 48h were additionally examined by transmission electron microscopy (TEM, ThermoFisher, Talos G2 200X). TEM lamellae containing fibers and oxide scales were extracted by focused ion beam machining (FEI, Helios Dualbeam Nanolab 600) and characterized using selected-area diffraction (SAD) and TEM EDS.

2.2.4 Scale composition

Comparative composition profiles of oxidized fiber bundles were obtained via x-ray photoelectron spectroscopy (XPS, ThermoFisher ESCALAB QXi X-ray Photoelectron Spectrometer Microprobe). For this purpose, the oxidized fibers in each tow were gently spread laterally and adhered to a holder using copper tape. XPS spectra were acquired using monochromatic Al k-α x-rays (1486eV beam energy) and a flood gun for charge compensation. Scans were collected over a 650 μm x-ray spot size. Depth profiles were obtained by intermittently sputtering the surface for 10 min intervals with a monatomic Ar beam at 3 keV and a 2 mm raster size. Survey spectra were integrated over two scans collected over a binding energy range of 10 eV to 1000eV with a pass energy of 100 eV, dwell time of 50 ms, and energy step of 0.5 eV. High-resolution spectra were integrated over 10 scans collected with a pass energy of 20 eV, dwell time of 50 ms, and energy step of 0.05 eV. The sputtering, survey scans and high-resolution scans were repeated multiple times, until well after the fibers beneath the scale had been exposed. Baseline measurements were also made on pristine (desized, non-oxidized) fibers after a 10 min sputter to reduce surface contaminants.

The XPS data were analyzed following standard protocols. After Shirley background subtraction, the high-resolution peaks were fit by Gaussian/Lorentzian line shapes (GL35) using the CASA XPS software [31], [32]. The relative sensitivity factors (RSF) were based on Scofield values [33], adjusted for the specific instrument employed in this study. RSFs for C, Si and O in particular were 1, 0.817 (Si 2p), and 2.93 (O 1s), respectively. These RSF values were confirmed from spectra obtained on a glass slide control specimen, also sputtered for 10 min immediately before analysis. After subtracting O tied to Mg, Na, Ca

and C (present in small amounts in the glass side), the calculated O:Si atomic ratio of the glass was 2.0, as expected. (Small peaks associated with Ar and Cu were occasionally obtained in survey scans: the former from sputtering and the latter from the mounting tape beneath the fibers. These were not included in the analysis.)

Si 2p was partitioned between Si-C, O-Si-O and Si-O-C [34]. C 1s was partitioned between Si-C and Si-O-C/graphitic C. The C 1s binding energy for graphite (284 eV) overlaps the range of binding energies for Si-O-C (283.7-284.6 eV) [27], [34], [35], so the combined peaks were identified as Si-O-C/graphitic C. Similarly, O 1s cannot be reliably partitioned between O-Si-O, O-Si-C, Si-OH because of overlapping binding energies [31], so the O 1s peak was assumed to be Si-O-C for bare fibers and O-Si-O for oxidized fibers. The low concentrations of Al and/or Zr precluded determination of their binding states with respect to the silica network.

Because of the challenges in quantifying XPS spectra and analyzing XPS data obtained on cylindrical (not flat) surfaces, the resulting compositions are considered largely on a comparative basis, to identify effects of fiber composition on scale composition [36], [37].

2.3. Results

2.3.1 Fiber compositions

Fiber compositions from XPS survey scans are similar to those reported by the fiber manufacturers and by others [15], [16], [29] (Figure 3). Measured oxygen levels are at nominal concentrations of 11.9 at% in ZMI, 4.9 at% in HNS, and 2.6 at% in SA. The C:Si ratios are 0.98, 1.1, and 1.2 for HNS, ZMI and SA respectively. ZMI fibers contain a small

amount of Zr (0.4 at%), comparable to previously reported concentrations [15]. Al was not detected in the SA fibers, a consequence of its low concentration compared to detection limits within a Si-based matrix [38].

High-resolution scans of Si 2p, C 1s, and O 1s (Figure 4) were used to identify SiC, and Si-O-C/graphitic C domains within pristine fibers. The Si 2p and C 1s scans revealed SiC domains for all fibers at binding energies of 100.5 ± 0.1 eV and 283.3 ± 0.1 eV, respectively [35]. All fibers also contained peaks at higher binding energies (101-101.5 eV for Si 2p and 284-284.6 eV for C 1s), indicating the presence of Si-O-C. All O 1s scans were fit to a peak with a binding energy of 532.2 ± 0.2 eV, which is also consistent with Si-O-C [34]. The analyses indicate that both HNS and SA fibers are composed mainly of SiC with ~20-30% Si-O-C/graphitic C phase. In contrast, the ZMI fibers are mainly Si-O-C/graphitic C and only ~20% SiC.

2.3.2 Scale uniformity and morphology

Oxide scales were extremely uniform across all fibers *within* the tow interiors. Scales on fibers near or at the tow exteriors were slightly thinner and often cracked when the scales on interior fibers were intact. Figure 5 shows a representative example of a cross-section of an HNS fiber tow after a 48h exposure; here about 15-20% of fibers near the tow exterior appear to have been affected. Small bright particles visible within the cracked scales at higher magnification in backscatter mode suggest the presence of environmental contaminants [39]. Scale thickness measurements were made only on fibers within the tow interiors.

Scale morphology and its evolution differ among the three fiber types in several respects:

HNS fibers: After all exposure times (3–96h), oxide scales on HNS fibers are intact, amorphous and crack-free (Figure 6). Exterior surfaces are mostly smooth and featureless with only few isolated crystalline spherulites (≤1% area) at longer exposure times (Figure 7). Selected area diffraction patterns obtained from a TEM lamella of an oxidized fiber after the 48h exposure (not shown here) confirm that the scales are amorphous.

ZMI fibers: After exposures up to 12h, oxide scales on the ZMI fibers are uniform and intact; after longer exposures (≥24h), they are invariably cracked. Two types of cracks are evident, distinguished from one another by their orientations and crack opening displacements (COD). These are designated "wide cracks" and "narrow cracks" (Figure 6). The COD of the wide cracks increase with exposure time, from about 0.5 μm to 2.0 μm after 24 and 96h exposures, respectively, while those of the thin cracks remain essentially unchanged.

The lengths of the wide cracks (first seen after the 24h exposure) are about 0.8 μm: somewhat smaller than the scale thickness at that time but close to the scale thickness measured after the shorter exposure (12h). Assuming that cracks do not extend after forming, their length can serve as a proxy for the time at which they formed. For example, cracks seen after the 24h exposure had likely formed after exposure durations of slightly more than 12h. The thin cracks, in contrast, are found to penetrate the entire oxide scale and deflect very near the oxide/fiber interface. (As discussed later, these cracks had formed during a phase transformation upon cooling.) After 48 and 96h exposures, the lengths of the wide cracks remain around 0.8–1 μm, suggesting that these cracks had formed at about the same time. This is consistent with the observation that the number of such cracks (typically 1-2 per fiber) does not appear to change with exposure time.

Following long (≥48h) exposures, regions of local enhanced oxidation are evident at the base of wide cracks, a manifestation of accelerated gas transport through the cracks. Pores or bubbles are also visible in the scale at the base of these cracks. Pore size and number density increase with exposure time and decrease with distance from the crack tip. A TEM lamella taken from a ZMI fiber after the 48h exposure reveals two layers of oxide (Figure 9): an outer layer, identified as twinned α-cristobalite, and an inner layer of amorphous silica. A pore band is present within the amorphous silica between the two layers, with the pores increasing in size from the amorphous layer to the crystalline layer. Small, bright particles are also visible in the crystalline scale and likely contain ZrO_2, which is essentially insoluble in SiO_2. Wide cracks penetrate through the outer crystalline layer with straight edges, then through the porous, amorphous layer in a distinctive V-shape. The clearest example of this behavior is after the 96h exposure (Figure 6). This indicates that the progressive increase in COD with exposure time is accommodated by viscous flow of the oxide formed ahead of the crack front.

The exterior surfaces of the cracked scales on the ZMI fibers after 48h exposure are mostly covered with small crystalline spherulites. From this vantage point, the wide cracks appear remarkably straight and run parallel to the longitudinal axis of the fibers over long distances (Figure 7). A closer examination of the base of these cracks also show secondary cracks in a remarkably periodic sawtooth pattern; these cracks are also evident to some extent in the transverse cross-sections (e.g. Figure 6). The narrow cracks on the other hand form a random mud-crack pattern.

SA fibers: After 3h exposure, oxide scales on the SA fibers are very thin (≤ 0.1μm): and somewhat irregular and facetted. The lengths of the facets appear comparable to the

grain size of the SiC grains in the SA fibers (~100nm). These features differ appreciably from the other fibers; compare, for example, images in the left column of Figure 6.

Small angular voids are present in the fiber core; SE images in particular highlight the void edges (Figure 8). These voids correspond to the former graphitic domains seen in pristine fibers. The void size and density do not appear to change noticeably over the range of exposure times probed here.

As the oxide grows, the fiber/oxide interface develops a scalloped shape, with a wavelength that also appears comparable to the SiC grain size. Additionally, SiC grains are frequently dislodged from the fiber and become embedded in the oxide scale, suggesting that grain boundaries serve as preferred oxidation paths.

The oxide scales remain intact for exposures up to 24h; thereafter the scales become heavily cracked (Figure 6). The crack characteristics differ from those in the ZMI fibers in a number of aspects. First, the cracks are shorter, by a factor of about 3 after 48h. Second, enhanced fiber oxidation at the base of the cracks is not visible or not as pronounced as it is in the ZMI fibers; pores in the oxide are also absent. Third, on the external surfaces the scales exhibit a fine sub-micron nodular texture; well-defined spherulites are not present (Figure 7). Finally, the crack patterns on the external surfaces are more irregular. While a large fraction of the cracks are roughly aligned with the fiber direction, the cracks are not straight or continuous over great lengths. Instead they are jagged with a wavelength comparable to the nodule spacing and are interspersed with cracks that are more random in orientation; the COD of the latter is somewhat smaller than that of the former. Together these features suggest that the scale is crystalline.

A TEM lamella taken from an SA fiber after 48h exposure shows a fully crystalline silica scale (Figure 9). Moreover, the SiC grains near the fiber exterior (to a depth of ~2 μm) are nearly twice as large as those in the fiber interior. EDS maps show low O in the region in which grain size is larger. Such grain growth has been reported previously and has been attributed to a local loss of intergranular C that inhibits grain growth [40]. On the fiber interior, Si and O are present at void locations, presumably a result of internal oxidation of the SiC pore surfaces after removal of the graphite domains (Figure 10).

2.3.3 Scale composition

Compositions of the oxide scales based on XPS on the three fiber types (to the left of the dashed lines in Figure 11) are similar to one another. The average atomic ratio of O to Si in the oxide is 1.33 for HNS and 1.15 for both ZMI and SA: all significantly lower than the expected value of 2 for SiO_2. The measured O:Si for the scale on the SA fiber after 48h exposure via TEM EDS is 2.2 (67.5 at% O, 30.5 at% Si, 1.4 at% C, and 0.6 at% Al). This discrepancy reiterates the challenge in accurate quantification of XPS depth profile data on fiber surfaces. On a comparative basis, C (graphite/Si-O-C) is present throughout all scales at concentrations ≤ 3 at%. Once sputtering has removed sufficient oxide scale to reveal the underlying fibers, Si-C and Si-O-C peaks emerge, similar to those for the pristine fibers.

2.3.4 Scale growth kinetics

In all cases the scale thickness increases with time in a roughly parabolic fashion (Figure 12), broadly consistent with the predictions of the linear/parabolic (Deal-Grove) oxidation model [41]. Closer examination of the data, however, reveals some nuanced differences, a consequence of the evolving microstructure, revealed by the SEM and TEM observations

presented in Section 3.2. To interpret these measurements, we begin with a brief summary of the Deal Grove model; then, an analysis of oxidation kinetics of each of the three fiber types is considered in turn.

The Deal-Grove model is based on a 1D analysis of oxidation controlled by diffusive transport of oxidants or reaction products through the oxide scale coupled with the reaction rate at the oxidation front [41]. The model leads to a linear/parabolic relation between oxide scale thickness *h* and time *t* that, in the absence of an initial oxide scale, has the form:

$$t = \frac{h^2}{B} + \frac{Ah}{B} \tag{1}$$

where *B* is the parabolic rate constant and *B/A* is the linear growth rate. For short times, *i.e.* $t << A^2/B$, Eqn (1) reduces to the linear form $h = Bt/A$; conversely, for $t \gg A^2/B$, growth is parabolic and given by $h = \sqrt{Bt}$.

The phenomenological oxidation parameters *A* and *B* are manifestations of two fundamental properties. The first is the oxidation rate, *k*, defined by the ratio of the flux of oxidant molecules to the oxidant concentration at the reaction front. It is related to *A* and *B* through:

$$k = \left(\frac{B}{A}\right)\frac{N}{C^*} \tag{2}$$

where *N* is the number of oxidant molecules per unit volume of oxide and *C** is the equilibrium concentration of oxidant in the scale. The second is the permeability, γ, of the oxidants through the oxide layer, defined as:

$$\gamma = D_{eff}H = \frac{BN}{2p_{ox}} \tag{3}$$

where $C^* = Hp_{ox}$, p_{ox} is the partial pressure of the oxidant, and *H* is Henry's Law solubility coefficient. *C** has been measured experimentally at 1000°C for 1 atm H_2O in amorphous

SiO_2 via infrared-absorption ($C^*_{H2O} = 3.4 \times 10^{19}\ cm^{-3}$) [42]. Since C^* is proportional to the partial pressure of oxidant in the gas stream, the pertinent concentration for the current study (0.2 atm H_2O) is $C^*_{H2O} = 6.8 \times 10^{18}\ cm^{-3}$.‡ N depends on reaction stoichiometry. Assuming water vapor is the dominant oxidant, the pertinent reaction, accounting for differences in fiber composition, is

$$SiC_xO_y + [2 + x - y]H_2O \rightarrow SiO_2 + xCO(g) + [2 + x - y]H_2 \quad (4)$$

where x and y are C:Si and O:Si atomic ratios, respectively. N is then calculated via

$$N = \frac{[2 + x - y]\ moles\ H_2O}{1\ mole\ SiO_2} \frac{N_A\ \rho_{SiO_2}}{M_{SiO_2}} \quad (5)$$

where N_A is Avogadro's number (6.022 x 10^{23} molecules/mole), ρ_{SiO_2} is the density of amorphous SiO_2 (2.2 g/cm^3) and M_{SiO_2} is the molecular weight of SiO_2 (60.08 g/mol).

In water-containing environments the silica scale may volatilize through a reaction that produces $Si(OH)_4$ gas [43]. The volatilization rate depends on the partial pressure and velocity of H_2O in the environment and is estimated using a boundary layer flux model [44], [45]. The equilibrium partial pressure of $Si(OH)_4$ in this environment (1000°C, 1atm total pressure, 0.2 atm H_2O) is about 7 x 10^{-8} atm. With a gas velocity of 4.4 cm/s and a specimen length of 10 cm, the calculated SiO_2 volatilization rate is about 10^{-3} μm/h. Thus, a 100h exposure would lead to a loss of about 0.1 μm of silica on the tow exterior; the loss would be considerably lower in the tow interior because of the lower gas velocity. In the context of the current scale thickness measurements (made on fibers within the tow interiors), the losses are deemed to be negligible.

‡ At 1000°C, the solubility of water in amorphous SiO_2 is 3 orders of magnitude greater than the solubility of oxygen (for 1 atm O_2, $C^*_{O2} = 5.5 \times 10^{16}\ cm^{-3}$) [55]. Although there is also 0.16 atm O_2 in the gas stream in this study (from the balance of dry air), water vapor is assumed to be the dominant oxidant controlling oxidation behavior.

HNS fibers exhibit straightforward oxidation behavior in that scale evolution $h(t)$ is well-described by the linear-parabolic model (Eqn. 1) over the entire time range. The parabolic and linear rate constants *B* and *B/A,* obtained by fitting Eqn. 1 to the data in Figure 12, are summarized in Table I.

ZMI fibers exhibit two oxidation regimes: one in which the scales are amorphous and intact (roughly $t \leq 12$h) and another in which the scales have crystallized and cracked ($t > 12$h). The values of *B* and *B/A*, obtained by fitting Eqn. 1 to the data in the first regime, are listed in Table I. Extrapolating the curve to longer times, the predictions overestimate the measured values; this is attributed to the crystallized layer at the outer surface and its lower permeability relative to the amorphous phase. To account for the presence of two distinct layers, we assume that the thickness of the crystalline scale, once formed and cracked, remains constant and that all new oxide formed subsequently is amorphous; these assumptions are broadly supported by the observation that the crystalline layer thickness inferred from the crack lengths remains constant and that amorphous silica is present beneath the crystalline layer with an intervening region containing a high density of pores. With these assumptions, the Deal Grove model is modified to yield[§]

$$t = \frac{1}{B}\left[(h-\delta) + \frac{1}{2}\left(A + 2\frac{\gamma_A}{\gamma_C}\delta\right)\right]^2 - \left[\frac{\left(A + 2\,\frac{\gamma_A}{\gamma_C}\,\delta\right)^2}{4B} - \tau_c\right] \qquad (6)$$

where *h* is *total* scale thickness, *B* and *B/A* are the parabolic and linear oxidation parameters for *amorphous* SiO_2 (obtained from a fit in the domain $t \leq 12$h), δ is the thickness of the crystalline layer (0.8μm), γ_A/γ_C is the ratio of permeability of amorphous SiO_2 to that of

[§] This adaptation was first presented by Sullivan [56] in the context of Si bondcoat oxidation beneath an oxide environmental barrier coating.

crystalline SiO_2, and τ_c is the time at which the amorphous scale crystallizes (taken to be 12h). Eqn. 6 was fit to the scale growth data over the time period 24 to 96 h using the nonlinear least-squares curve fitting tool within MATLAB and the value of *B* from the fit in the first domain. The resulting fit yields a permeability ratio $\gamma_A/\gamma_C = 2.1$.

SA fibers also exhibit two oxidation regimes, although the nature of the transition differs from that in the ZMI fibers. A fit of Eqn 1 to the data at short times ($t \leq 24h$) yields a parabolic rate constant that is about half that obtained for the HNS fibers. This difference is consistent with the two-fold difference in permeabilities of amorphous and crystalline oxide inferred from data on the ZMI fibers. Furthermore, the linear rate constant *B/A* is also half that for HNS. Extrapolating the resulting linear/parabolic curve to longer times yields predictions that *under*estimate the measured values.

We hypothesize that the seemingly low linear rate constant at short times and the transition in behavior are associated with changes in the internal oxidation process. Before the surface is sealed by a continuous oxide scale, oxidants in the environment can access the internal graphite via grain triple junctions (an assumption supported by the TEM observations of internal oxide beneath the fiber surface). Graphite oxidation produces CO(g) and CO_2(g). Egress of these gases to the fiber surface alters the chemical environment at the SiC/oxide interface, diminishing the driving force for the oxidation reaction in Eqn. 4. The process ceases once either the internal channels become blocked by silica formed on the internal SiC surfaces or the oxide on the external surface becomes sufficiently hermetic to block gas transport in or out of the fiber. This cessation point is believed to be responsible for the increase in linear scale growth rate at longer times (relative to the extrapolated curve from the short time domain).

To account for these effects, the linear-parabolic model in the longer time domain is modified to read [41]

$$h = \frac{A_{late}}{2}\left\{\left[1 + \frac{t^* + \tau_{tr}}{A_{late}^2/4B}\right]^{\frac{1}{2}} - 1\right\} \quad (7)$$

where $t^* = t - t_{tr}$ and $\tau_{tr} = (h_{tr}^2 + Ah_{tr})/B$, with t_{tr} and h_{tr} being the time and the scale thickness at the transition. τ_{tr} is a time shift correcting for oxide growth prior to the transition. It follows the same form as τ used to correct for the presence of an initial oxide scale in the original Deal-Grove model. Because the proposed mechanism involves only a change in the chemical environment at the SiC/oxide interface, the parabolic oxidation rate, *B*, is assumed to be equal to that obtained for the early time domain ($B = 0.018\mu m^2/h$). Fitting Eqn 7 to the data for $t \geq 12h$ (Figure 12), and using t_{tr} between 6h and 24h, a linear growth rate $B/A = 0.024\mu m/h$ was obtained: about 40% larger than that at short times.

2.4. Discussion

The following discussion focuses on the effects of fiber composition and scale structure on the interface reaction rate, scale permeability and scale cracking.

2.4.1 Interface reaction rate

The results indicate that the linear oxidation rate *B/A* and the corresponding interface reaction rates *k* increase with amorphous Si-O-C content (Table 1). As a baseline, *k* of pure bulk SiC (prepared via the Lely method, with no Si-O-C) for 0.2 atm H_2O is $280\ \mu m/h$ for the C-face and $90\ \mu m/h$ for the Si-face [46]. By comparison, the value for HNS is $400\ \mu m/h$, about 40% greater than that for C-face SiC; here the Si-O-C content is about 20%. For ZMI, *k* is about 7 times that for HNS; its Si-O-C content is 70–80%.

While *k* could not be reliably estimated for the SA fiber (because the solubility of H_2O in crystalline silica is unknown), the inferred increase in *B/A* from short to long exposures is plausibly related to internal oxidation of graphite. To assess this hypothesis, thermodynamic calculations of the oxidation process were performed using FactSage and the FactPS database [47]. The calculations begin with 1 mole of either C or SiC and 10 moles of inert gas (Ar); then, either O_2 or H_2O are added incrementally in place of Ar and the equilibrium fractions of various gas phases are computed. The most relevant gases in the current context are CO and CO_2. The results (Figure 13) show that, in the early stages of oxidation, the mole fractions of CO and CO_2 in equilibrium with C are greater than those in equilibrium with SiC; this result holds for both oxidant types. The implication is that the free energy change for SiC oxidation would increase (i.e. become more positive) in the presence of CO/CO_2 generated by concomitant oxidation of C. This, in turn, would decrease the reaction rate of SiC. But these effects would persist only while the oxidants and the reaction product gases can be readily transported in and out of the fibers; formation of a continuous silica scale would essentially arrest this process.

2.4.2 Scale permeability

Permeability of the oxide scale governs the oxidation rate at long times through the parabolic rate constant *B*. Molecular diffusion of gases (oxidants H_2O and O_2, and products CO, CO_2, CH_4 and H_2) occurs through channels created by rings of SiO_4^{4-} tetrahedra [48]. While the structure of cristobalite comprises only 6-member rings, the channels available for molecular diffusion in amorphous silica include ones that are smaller (with 5 or fewer member rings) and others that are larger (more than 6 member rings). On average, the channels in the latter are likely larger and therefore diffusivity is higher [18]. Although diffusivity data for crystalline silica are sparse, the observed buildup of pores at the amorphous/crystalline boundary on the ZMI fiber essentially confirms that gas transport through the scale is indeed hindered significantly by the crystallized layer.

Differences in parabolic rate constants for crystalline and amorphous scales can be assessed in terms of activation energies Q of the corresponding diffusive processes, assuming that the temperature-dependence of scale growth is the same as that for diffusion. The two are related by [21]:

$$\frac{\ln(B_{cr})}{\ln(B_{am})} \approx \frac{Q_{cr}}{Q_{am}} \tag{8}$$

where subscripts *cr* and *am* refer to crystalline and amorphous silica, respectively. Taking $B_{cr} = B_{SA}$ and $B_{am} = B_{HNS}$ yields $\ln(B_{cr})/\ln(B_{am}) \approx 1.25$. By comparison the activation energies for crystalline and amorphous silica reported by Hay and Corns [21] are $Q_{cr} = 95 \pm 5\, kJ/mol$ and $Q_{am} = 80 \pm 5\, kJ/mol$ and thus $Q_{cr}/Q_{am} \approx 1.2$. The correspondence between these ratios supports the hypotheses regarding differences in oxidation behavior of SA and HNS fibers and the change in oxidation behavior in ZMI fibers following crystallization.

Difference in crystallization kinetics may be partly due to the presence of small amounts of Zr and Al in the ZMI and SA fibers. Zr in particular is expected to modify the silica network and reduce its viscosity, thereby facilitating the structural re-arrangements needed for crystallization [18], [49]. In the SA fibers, the nodular fiber surface and resulting scalloped fiber/oxide interface may provide a more favorable nucleation environment for crystalline silica and therefore lead to formation of crystalline scale from the outset.

The inferred permeability of amorphous scale on the HNS fiber is larger than that reported for amorphous scales on bulk SiC (1.1×10^9 $\mu m^{-1}h^{-1}$ [46]) by a factor of 4. We speculate that the difference is caused by the presence of defects. Based on a recent DFT study, CO(g) produced by SiC oxidation may react with O in the SiO_2 network to form CO_2(g), leaving behind oxygen vacancies [50]. Such vacancies would facilitate gas transport

via both molecular and network diffusion [51]. Vacancies may also create sites at which H_2O molecules can react with the network to form Si-OH groups and therefore increase its solubility. Higher concentrations of defects may be present on scales formed on fibers because of additional CO(g) formed from oxidation of C and Si-O-C domains. Scales formed on curved surfaces may also contain higher defect concentrations to accommodate stress compared to scales formed on flat substrates.

2.4.3 Scale cracking

The main sources of stress in the oxide scale are the volume expansion during conversion of SiC (or the fiber material in general) to silica and the subsequent radial fiber growth; the effect of crystallization, when it occurs, is relatively small because the mass densities of amorphous and crystalline silica (as β -cristobalite) are very similar to one another [52]. At sufficiently high temperatures, these stresses can be mediated by viscous flow of the scale. Additional stresses arise during cooling because of fiber/oxide thermal expansion mismatch and, if crystallization has occurred, a transformation of the high-temperature β-cristobalite to the low-temperature α–cristobalite, at about 250°C [23], [53], [54]. The transformation stress, being generated at low temperatures, cannot be mediated by viscous flow.

An analysis of stress evolution in a growing oxide scale is presented in the Appendix. The numerical results (plotted on Figure 14) are based on reported elastic and flow properties of amorphous silica and the growth parameters for each of the fiber types. These results are expected to apply to the scale on HNS and the scale on ZMI in the short-time domain (while scales are amorphous). Because of the absence of suitable data, the viscosity of cristobalite was assumed (notionally) to be higher than that of amorphous silica by a

factor of either 10 or 100; calculated stresses for the latter cases should therefore be considered illustrative and not predictive.

In all cases the calculated hoop stress at the outer surface of the scale is initially compressive (~10 GPa) but relaxes quickly over a period of minutes. Eventually, it is overtaken by the tensile hoop stress associated with radial fiber growth. The fiber-specific behaviors are as follows: (i) On the HNS fibers, the hoop stress reaches a peak of about 0.6 GPa after 20h and then gradually decays. Evidently this stress is insufficient to crack the amorphous (very uniform) scale. A further implication is that continued oxidation should not exacerbate the problem provided the scale remains amorphous. (ii) On the ZMI fibers, the hoop stress initially evolves in a similar (though not identical) fashion, while the scale is amorphous. Then, upon crystallization (assumed to occur after 12h), the rate of relaxation decreases because of the increase in scale viscosity, while the rate of further scale growth also decreases, because of the accompanying reduction in permeability. In this case the hoop stress reaches about 1.5 GPa over the duration of the test, evidently large enough to crack the scale. (iii) The hoop stress in the SA fibers reaches similar values, though with a different loading history. Because the scale is crystalline throughout, stress relaxation requires longer times but, once those stresses become tensile, the stress can attain higher values, albeit more gradually. In sum, longitudinal cracks in ZMI and SA fibers are attributable to the development of hoop stresses developed *at* the exposure temperature after the scale has crystallized.

In cases where the scales have crystallized, additional axial and hoop stresses are generated during cooling because of the $\beta-\alpha$ cristobalite transformation. Based on the transformation strain and the elastic properties of the scale, the additional stress is about 1

GPa. This stress, combined with the growth stress, is almost certainly large enough to cause additional cracking; indeed this is consistent with the mud crack patterns observed on both ZMI and SA fibers. These cracks naturally have small CODs.

Interestingly, after longitudinal cracks have formed on the ZMI fibers and oxidation continues (forming an amorphous underlayer), the growing hoop stress in the crystallized layer evidently facilitates formation of bubbles in the vicinity of the crack tip. The phenomenon appears to be a chemo-mechanical process in which outward transport of gases generated at the oxide/fiber interface is impeded by the crystallized layer and the elevated stress near the crack tip promotes formation of gas bubbles near the amorphous/crystalline boundary.

2.5. Conclusions and outlook

The current study has examined the oxidation behavior of three commercial SiC fibers in a steam-containing environment at 1000°C. Variations on the standard linear/parabolic oxidation model have proven useful both in gleaning insights into subtle changes in oxidation behavior over time and, with various microstructural examinations, in identifying the origins of differences among the three fiber types. The key findings follow.

(i) Oxidation of HNS fibers follows the established linear/parabolic oxidation model. The interface reaction rate is greater than that for pure CVD SiC by a factor of about 2; the difference is attributed to the presence of amorphous Si-O-C domains in HNS fibers.

(ii) Oxidation of ZMI fibers in the early stages also follows linear/parabolic behavior. However, the interface reaction rate is about an order of magnitude greater than that for HNS, likely due to the high content of amorphous Si-O-C, and the parabolic rate constant is about 50% greater, possibly because of defects that facilitate molecular

diffusion. Later in the process the scale crystallizes and further oxidation leads to new amorphous scale; thereafter the oxide growth rate is reduced because of the twofold reduction in permeability of the crystallized layer.

(iii) The oxide that forms on the SA fibers appears to be crystalline from the outset. Here the initial parabolic rate constant is about half that for HNS, consistent with the lower permeability. The linear rate constant is also about half that for HNS. The latter effect is attributed to CO/CO_2 gas formed by oxidation of graphite in the interior of SA fibers in the early stages and the corresponding reduction in the chemical driving force for oxidation at the fiber/oxide interface. Once the external fiber surfaces are sealed by a continuous silica scale and the oxidants can no longer access the internal graphite, the linear rate constant increases.

(iv) Scale crystallization proves to be crucial in the oxidation process. In addition to its role in retarding oxide growth, crystallization renders the scale susceptible to cracking because of its increased viscosity. Equally importantly, the crystallized oxide readily transforms upon cooling to ambient temperatures, producing additional GPa-level tensile stresses that exacerbate cracking. The implications for fiber durability upon thermal cycling are likely to be significant.

Finally, while oxidation of bare fibers involves numerous chemical, physical and mechanical phenomena that have only recently come to light and are not yet fully understood, the complexity of the problem is likely to be far greater for fibers embedded within SiC/SiC composites. Interactions with other constituents, most notably BN, are known to alter the chemical processes that lead to fiber consumption, oxide formation, and scale cracking. The ramifications for long-term durability of SiC-based composites in high-temperature, steam-containing environments have yet to be fully exposed. Addressing these

problems should be a high priority in future research activities in the ceramic composite community.

2.6. Appendix: Analysis of stresses in oxide scale

Stresses within oxide scales are influenced by fiber geometry, fiber composition, and oxide scale structure. Initially, the scale experiences high compression due to the volume expansion associated with conversion of SiC to SiO_2. The volume ratio in general is:

$$\frac{V_{SiO_2}}{V_{SiC_xO_y}} = \frac{M_{SiO_2}\ \rho_{SiC_xO_y}}{M_{SiC_xO_y}\ \rho_{SiO_2}} \qquad (A.1)$$

where M is molecular weight, ρ is density and the subscripts refer to properties of SiO_2 and fiber material (SiC_xO_y). The volume ratio for stoichiometric SiC is 2.2; for HNS, ZMI and SA fibers it is 2.0, 1.4, and 2.0, respectively. From an elastic analysis, the initial hoop stress $\sigma_{\theta\theta}^0$ and axial stress σ_{zz}^0 are

$$\sigma_{\theta\theta}^0 = \sigma_{zz}^0 = -\frac{E}{1-\nu}\left[\left(\frac{V_{SiO_2}}{V_{SiC_xO_y}}\right)^{\frac{1}{3}} - 1\right] \qquad (A.2)$$

where E is Young's modulus (70 GPa) and v is Poisson's ratio (0.17). These stresses are relaxed at a rate that depends on scale viscosity, η.

While determination of the multiaxial stress states throughout the oxide scale requires involved numerical calculations [24], [49], the radial stress component remains on the order of 1 MPa, much smaller than the hoop and axial components. Applying the simplification $\sigma_{rr} = 0$ to the constitutive law of the oxide scale results in an accurate description of the evolution of hoop and axial stresses. Assuming that viscosity follows the Eyring model [9], [24], [50], [51], [52], the hoop and axial strain rates, $\dot{\varepsilon}_{\theta\theta}$ and $\dot{\varepsilon}_{zz}$, can be expressed in terms of the hoop and axial stresses, $\sigma_{\theta\theta}$ and σ_{zz}, via

$$\dot{\varepsilon}_{\theta\theta} = \frac{\dot{\sigma}_{\theta\theta}}{E} - \nu\frac{\dot{\sigma}_{zz}}{E} + \frac{\tau_o\,(2\sigma_{\theta\theta} - \sigma_{zz})}{6\,\tau_{max}\,\eta_0}\sinh\left(\frac{\tau_{max}}{\tau_o}\right) \qquad (A.3)$$

$$\dot{\varepsilon}_{zz} = \frac{\dot{\sigma}_{zz}}{E} - \nu\frac{\dot{\sigma}_{\theta\theta}}{E} + \frac{\tau_o\,(2\sigma_{zz} - \sigma_{\theta\theta})}{6\,\tau_{max}\,\eta_0}\sinh\left(\frac{\tau_{max}}{\tau_o}\right) = 0 \qquad (A.4)$$

where the over-dot indicates a derivative with respect to time, τ_{max} is the maximum shear stress, τ_o is the Eyring shear stress, and η_0 is a reference stress-free viscosity; for amorphous SiO_2 at 1000°C , $\tau_0 \approx 100$ MPa and $\eta_0 \approx 6 \times 10^{15}$ Pa s [19]. The hoop strain rate can be further expressed in terms of the radial growth rate via:

$$\dot{\varepsilon}_{\theta\theta} = \left[\frac{1-\Omega}{R_0 - \Omega\,h}\right]\frac{dh}{dt} \qquad (A.5)$$

where R_0 is the initial fiber radius (6.2μm for HNS, 5.7μm for ZMI, and 4.6μm for SA from experimental measurements) and Ω is the ratio of thickness of SiC consumed to thickness of oxide formed (including radial elastic strains due to hoop and axial stresses):

$$\Omega = \frac{1}{1 + \left[\left(\frac{V_{SiO_2}}{V_{SiC_xO_y}}\right)^{\frac{1}{3}} - 1\right]\left(1 + \frac{2\nu}{1-\nu}\right)} \qquad (A.6)$$

Variations in hoop stress with time were evaluated by numerically solving the coupled ordinary differential equations in (A3) and (A4) subject to the initial condition in (A2) and the hoop strain rate in (A5), using growth parameter values unique to each fiber type.

2.7. References

[1] F. W. Zok, P. T. Maxwell, K. Kawanishi, and E. B. Callaway, "Degradation of a SiC-SiC composite in water vapor environments," *Journal of the American Ceramic Society*, vol. 103, no. 3, pp. 1927–1941, Mar. 2020, doi: 10.1111/jace.16838.

[2] K. J. Larochelle and G. N. Morscher, "Tensile stress rupture behavior of a woven ceramic matrix composite in humid environments at intermediate temperature - Part i," *Applied Composite Materials*, vol. 13, no. 3, pp. 147–172, May 2006, doi: 10.1007/s10443-006-9009-8.

[3] G. N. Morscher and J. D. Cawley, "Intermediate temperature strength degradation in SiC/SiC composites," *J. Euro. Ceram. Soc*, vol. 22, pp. 2777–2787, 2002, [Online]. Available: www.elsevier.com/locate/jeurceramsoc

[4] L. U. J. T. Ogbuji, "A Pervasive Mode of Oxidative Degradation in a SiC-SiC Composite," *Journal of the American Ceramic Society*, vol. 81, no. 11, pp. 2777–2784, Jan. 2005, doi: 10.1111/j.1151-2916.1998.tb02696.x.

[5] N. S. Jacobson, G. N. Morscher, D. R. Bryant, and R. E. Tressler, "High-Temperature Oxidation of Boron Nitride: II, Boron Nitride Layers in Composites," *Journal of the American Ceramic Society*, vol. 82, no. 6, pp. 1473–1482, Dec. 2004, doi: 10.1111/j.1151-2916.1999.tb01944.x.

[6] W. Wu, G. Yu, X. Gao, F. Wang, and Y. Song, "Degradation of SiC/BN/SiC minicomposites in heat-stress-moisture-oxygen coupling environments: I. static fatigue test study," *J Eur Ceram Soc*, 2024, doi: 10.1016/j.jeurceramsoc.2024.02.036.

[7] V. L. Christensen and F. W. Zok, "Insights into internal oxidation of SiC/BN/SiC composites," *Journal of the American Ceramic Society*, vol. 106, no. 2, pp. 1561–1575, 2022, doi: 10.1111/jace.18834.

[8] F. W. Zok, V. E. Collier, and M. R. Begley, "Coating recession effects in ceramic composite strength," *J Mech Phys Solids*, vol. 156, no. June, p. 104608, 2021, doi: 10.1016/j.jmps.2021.104608.

[9] W. Xu, F. W. Zok, and R. M. McMeeking, "Model of Oxidation-Induced Fiber Fracture in SiC/SiC Composites," *Journal of the American Ceramic Society*, vol. 97, no. 11, pp. 3676–3683, 2014, doi: 10.1111/jace.13180.

[10] V. E. Collier, W. Xu, R. M. McMeeking, F. W. Zok, and M. R. Begley, "Recession of BN coatings in SiC/SiC composites through reaction with water vapor," *Journal of the American Ceramic Society*, no. April, pp. 1–14, 2021, doi: 10.1111/jace.18052.

[11] V. Cholet and L. Vandenbulcke, “Chemical Vapor Infiltration of Boron Nitride Interphase in Ceramic Fiber Preforms: Discussion of Some Aspects of the Fundamentals of the Isothermal Chemical Vapor Infiltration Process,” *Journal of the American Ceramic Society*, vol. 76, no. 11, pp. 2846–2858, 1993, doi: 10.1111/j.1151-2916.1993.tb04026.x.

[12] P. Fenetaud and S. Jacques, “SiC/SiC ceramic matrix composites with BN interphase produced by gas phase routes: An overview,” *Open Ceramics*, vol. 15, no. December 2022, p. 100396, 2023, doi: 10.1016/j.oceram.2023.100396.

[13] S. C. Farmer, G. N. Morscher, and N. Lewis, “Improved interface coatings for SiC fibers in Ceramic Composites,” *Ceramic Engineering and Science Proceedings*, vol. 16, no. 4, pp. 409–416, 1995.

[14] M. Leparoux, L. Vandenbulcke, and C. Clinard, “Influence of isothermal chemical vapor deposition and chemical vapor infiltration conditions on the deposition kinetics and structure of boron nitride,” *Journal of the American Ceramic Society*, vol. 82, no. 5, pp. 1187–1195, 1999, doi: 10.1111/j.1151-2916.1999.tb01894.x.

[15] H. Ichikawa, “Polymer-Derived Ceramic Fibers,” *Annu Rev Mater Res*, vol. 46, no. 1, pp. 335–356, 2016, doi: 10.1146/annurev-matsci-070115-032127.

[16] A. R. Bunsell and M. H. Berger, “Fine diameter ceramic fibres,” *Journal of the European Ceramic Society*, vol. 20, no. 13. Elsevier Science Ltd, pp. 2249–2260, 2000. doi: 10.1016/S0955-2219(00)00090-X.

[17] J. E. Shelby, “A Limited Review of Water Diffusivity and Solubility in Glasses and Melts”, doi: 10.1111/j.1551-2916.2007.01946.x.

[18] M. A. Lamkin, F. L. Riley, and R. J. Fordham, “Oxygen mobility in silicon dioxide and silicate glasses: a review,” *J Eur Ceram Soc*, vol. 10, no. 5, pp. 347–367, 1992, doi: 10.1016/0955-2219(92)90010-B.

[19] G. Hetherington, K. H. Jack, and J. C. Kennedy, “The viscosity of vitereous silica,” *Physics and Chemistry of Glasses*, vol. 5, no. 5, pp. 130–136, 1964.

[20] R. H. Doremus, “Viscosity of silica,” *J Appl Phys*, vol. 92, no. 12, pp. 7619–7629, 2002, doi: 10.1063/1.1515132.

[21] R. S. Hay and R. Corns, “Passive oxidation kinetics for glass and cristobalite formation on Hi-Nicalon^{TM}-S SiC fibers in steam,” *Journal of the American Ceramic Society*, vol. 101, no. 11, pp. 5241–5256, Nov. 2018, doi: 10.1111/jace.15763.

[22] R. S. Hay *et al.*, “Hi-Nicalon-S SiC Fiber Oxidation and Scale Crystallization Kinetics,” *J. Am. Ceram. Soc.*, vol. 94, no. 11, pp. 3983–3991, 2011, doi: 10.1111/j.1551-2916.2011.04647.x.

[23] R. C. Breneman and J. W. Halloran, “Stress Development and Fracture of Surface Nucleated Cristobalite on Silica Glass,” *Journal of the American Ceramic Society*, vol. 97, no. 11, pp. 3483–3488, 2014, doi: 10.1111/jace.13181.

[24] R. S. Hay, “Growth stress in SiO2 during oxidation of SiC fibers,” *J Appl Phys*, vol. 111, no. 6, p. 063527, Mar. 2012, doi: 10.1063/1.3698305.

[25] R. S. Hay and R. J. Chater, “Oxidation kinetics strength of Hi-Nicalon-S SiC fiber after oxidation in dry and wet air,” *Journal of the American Ceramic Society*, vol. 100, no. 9, pp. 4110–4130, Sep. 2017, doi: 10.1111/jace.14833.

[26] R. S. Hay, “SiC fiber strength after low pO2 oxidation,” *Journal of the American Ceramic Society*, vol. 101, no. 2, pp. 831–844, Feb. 2018, doi: 10.1111/jace.15198.

[27] R. Mo, X. Yin, F. Ye, X. Liu, L. Cheng, and L. Zhang, “Mechanical and microwave absorbing properties of Tyranno® ZMI fiber annealed at elevated temperatures,” *Ceram Int*, vol. 43, no. 12, pp. 8922–8931, 2017, doi: 10.1016/j.ceramint.2017.04.030.

[28] H. Oda and T. Ishikawa, “Microstructure and mechanical properties of SiC-polycrystalline fiber and new defect-controlling process,” *Int J Appl Ceram Technol*, vol. 14, no. 6, pp. 1031–1040, 2017, doi: 10.1111/ijac.12719.

[29] S. M. Dong *et al.*, “Characterization of nearly stoichiometric SiC ceramic fibres,” *J Mater Sci*, vol. 36, no. 10, pp. 2371–2381, 2001, doi: 10.1023/A:1017988827616.

[30] J. Schindelin *et al.*, “Fiji: An open-source platform for biological-image analysis,” *Nat Methods*, vol. 9, no. 7, pp. 676–682, 2012, doi: 10.1038/nmeth.2019.

[31] G. Pintori and E. Cattaruzza, “XPS/ESCA on glass surfaces: A useful tool for ancient and modern materials,” *Optical Materials: X*, vol. 13, p. 100108, 2022, doi: 10.1016/j.omx.2021.100108.

[32] D. Sprenger, H. Bach, W. Meisel, and P. Gütlich, “XPS study of leached glass surfaces,” *J Non Cryst Solids*, vol. 126, no. 1–2, pp. 111–129, 1990, doi: 10.1016/0022-3093(90)91029-Q.

[33] J. H. Scofield, “Hartree-Slater subshell photoionization cross-sections at 1254 and 1487 eV,” *J Electron Spectros Relat Phenomena*, vol. 8, no. 2, pp. 129–137, 1976, doi: 10.1016/0368-2048(76)80015-1.

[34] C. Önneby and C. G. Pantano, “Silicon oxycarbide formation on SiC surfaces and at the SiC/SiO2 interface,” *Journal of Vacuum Science & Technology A: Vacuum, Surfaces, and Films*, vol. 15, no. 3, pp. 1597–1602, 1997, doi: 10.1116/1.580951.

[35] L. Porte and A. Sartre, “Evidence for a silicon oxycarbide phase in the Nicalon silicon carbide fibre,” *J Mater Sci*, vol. 24, no. 1, pp. 271–275, 1989, doi: 10.1007/BF00660966.

[36] C. R. Brundle and B. V. Crist, “X-ray photoelectron spectroscopy: A perspective on quantitation accuracy for composition analysis of homogeneous materials,” *Journal of Vacuum Science & Technology A: Vacuum, Surfaces, and Films*, vol. 38, no. 4, 2020, doi: 10.1116/1.5143897.

[37] D. R. Baer, G. E. McGuire, K. Artyushkova, C. D. Easton, M. H. Engelhard, and A. G. Shard, “Introduction to topical collection: Reproducibility challenges and solutions with a focus on guides to XPS analysis,” *Journal of Vacuum Science & Technology A: Vacuum, Surfaces, and Films*, vol. 39, no. 2, 2021, doi: 10.1116/6.0000873.

[38] A. G. Shard, “Detection limits in XPS for more than 6000 binary systems using Al and Mg Kα X-rays,” *Surface and Interface Analysis*, vol. 46, no. 3, pp. 175–185, 2014, doi: 10.1002/sia.5406.

[39] E. Opila, “Influence of Alumina Reaction Tube Impurities on the Oxidation of Chemically-Vapor-Deposited Silicon Carbide,” *J. Am. Ceram. Soc.*, vol. 78, no. 4, pp. 1107–10, 1995.

[40] L. Silvestroni, D. D. Fabbriche, and D. Sciti, “Tyranno SA3 fiber-ZrB2 composites. Part I: Microstructure and densification,” *Mater Des*, vol. 65, pp. 1253–1263, 2015, doi: 10.1016/j.matdes.2014.08.068.

[41] B. E. Deal and A. S. Grove, “General Relationship for the Thermal Oxidation of Silicon,” *J Appl Phys*, vol. 36, no. 12, pp. 3770–3778, Dec. 1965, doi: 10.1063/1.1713945.

[42] A. J. Moulson and J. P. Roberts, “Water in silica glass,” *Transactions of the Faraday Society*, vol. 57, pp. 1208–1216, 1961, doi: 10.1039/TF9615701208.

[43] N. S. Jacobson, E. J. Opila, D. L. Myers, and E. H. Copland, “Thermodynamics of gas phase species in the Si-O-H system,” *Journal of Chemical Thermodynamics*, vol. 37, no. 10, pp. 1130–1137, 2005, doi: 10.1016/j.jct.2005.02.001.

[44] E. J. Opila, “Oxidation and Volatilization of Silica Formers in Water Vapor,” *Journal of the American Ceramic Society*, vol. 86, no. 8, pp. 1238–1248, Aug. 2003, doi: 10.1111/j.1151-2916.2003.tb03459.x.

[45] E. Opila and R. Hann, “Paralinear Oxidation of CVD SiC in Water Vapor,” *J. Am. Ceram. Soc*, vol. 80, no. 1, pp. 197–205, 1997.

[46] A. Suzuki, H. Ashida, N. Furui, K. Mameno, and H. Matsunami, “Thermal oxidation of SiC and electrical properties of Al-SiO2-SiC MOS structure,” *Jpn J Appl Phys*, vol. 21, no. 4, pp. 579–585, 1982, doi: 10.1143/JJAP.21.579.

[47] C. W. Bale *et al.*, “FactSage thermochemical software and databases, 2010-2016,” *CALPHAD*, vol. 54, pp. 35–53, 2016, doi: 10.1016/j.calphad.2016.05.002.

[48] T. Bakos, S. N. Rashkeev, and S. T. Pantelides, “Reactions and Diffusion of Water and Oxygen Molecules in Amorphous SiO2,” *Phys Rev Lett*, vol. 88, no. 5, p. 4, 2002, doi: 10.1103/PhysRevLett.88.055508.

[49] C. Cheng, H. Li, Q. Fu, L. Guo, J. Sun, and X. Yin, “Effect of Zr doping on the high-temperature stability of SiO2 glass,” *Comput Mater Sci*, vol. 147, pp. 81–86, 2018, doi: 10.1016/j.commatsci.2018.01.051.

[50] K. Chokawa, M. Araidai, and K. Shiraishi, “Effects of annealing with CO and CO2 molecules on oxygen vacancy defect density in amorphous SiO2 formed by thermal oxidation of SiC,” *J Appl Phys*, vol. 124, no. 13, 2018, doi: 10.1063/1.5041794.

[51] V. Presser and K. G. Nickel, “Silica on silicon carbide,” *Critical Reviews in Solid State and Materials Sciences*, vol. 33, no. 1, pp. 1–99, 2008, doi: 10.1080/10408430701718914.

[52] W. Pabst and E. Gregorová, “Elastic properties of silica polymorphs-a review,” *Ceramics - Silikaty*, vol. 57, no. 3, pp. 167–184, 2013.

[53] R. C. Breneman and J. W. Halloran, “Effect of cristobalite on the strength of sintered fused silica above and below the cristobalite transformation,” *Journal of the American Ceramic Society*, vol. 98, no. 5, pp. 1611–1617, 2015, doi: 10.1111/jace.13505.

[54] M. J. F. Guinel and M. G. Norton, “Oxidation of silicon carbide and the formation of silica polymorphs,” *J Mater Res*, vol. 21, no. 10, pp. 2550–2563, 2006, doi: 10.1557/jmr.2006.0317.

[55] F. J. Norton, “Permeation of Gaseous Oxygen through Vitreous Silica,” *Nature*, no. 4789, p. 701, 1961.

[56] R. M. Sullivan, “Reformulation of oxide growth equations for oxidation of silicon bond coat in environmental barrier coating systems,” *J Eur Ceram Soc*, vol. 39, no. 16, pp. 5403–5409, 2019, doi: 10.1016/j.jeurceramsoc.2019.06.057.

2.8. Tables and Figures

Table 1: Oxidation rate constants for the three fiber types

Fiber	Time (h)	Model	Scale	B ($\mu m^2/h$)	B/A ($\mu m/h$)	N (μm^{-3})	k ($\mu m/h$)	γ ($\mu m^{-1}h^{-1}atm^{-1}$)
HNS	0-96	Linear/ parabolic	Intact/ amorphous	0.040	0.043	$6.4x10^{10}$	400	$6.4\ x10^{9}$
ZMI	0-12	Linear/ parabolic	Intact/ amorphous	0.068	0.313	$6.3\ x10^{10}$	2900	$1.1\ x10^{10}$
	24-96	Linear/ parabolic with barrier	Cracked/ crystalline	0.068	0.019			$5.1\ x\ 10^{9}$
SA	0-24	Linear/ parabolic	Intact/ crystalline	0.018	0.017	$6.9\ x10^{10}$		$3.1\ x10^{9}$
	12-96	Linear/ parabolic with shift	Crystalline	0.018	0.024			

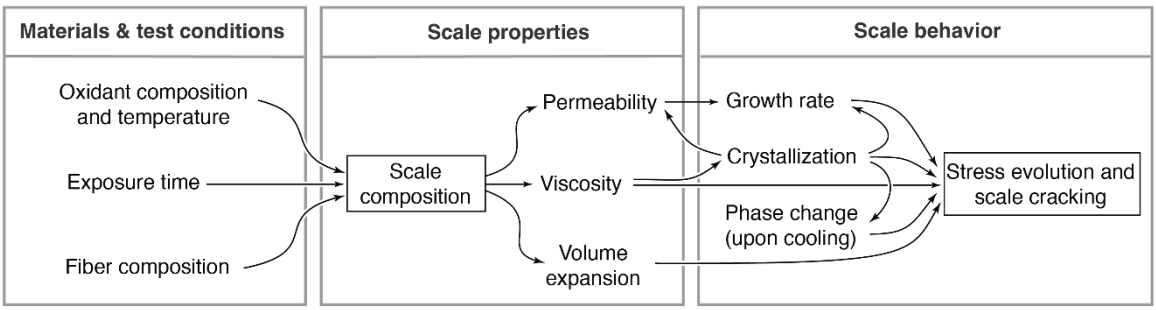

Figure 1: Flow chart illustrating the influence of materials and test conditions on scale composition and, in turn, the influence of scale composition on thermophysical scale properties and behavior.

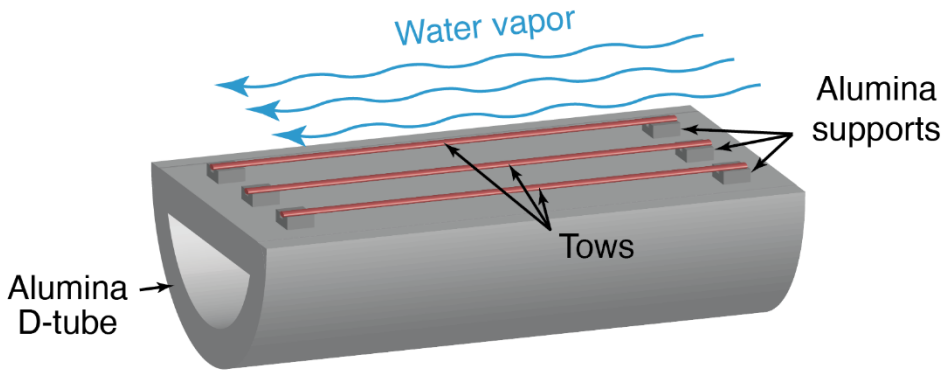

Figure 2: Tow configurations in furnace during oxidation experiments.

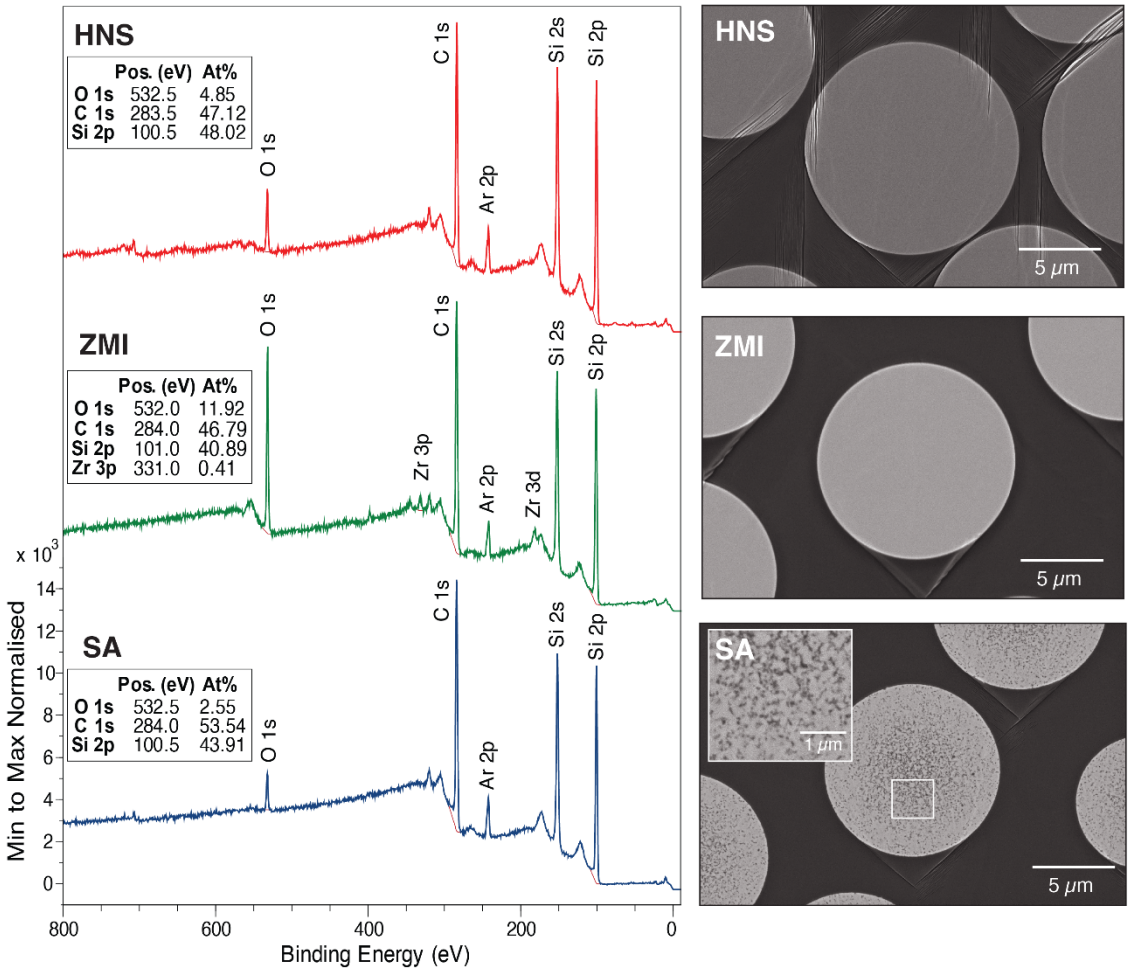

Figure 3: XPS survey scans and SEM images of cross-sections of bare fibers. Inset shows graphitic domains in the core of the SA fibers.

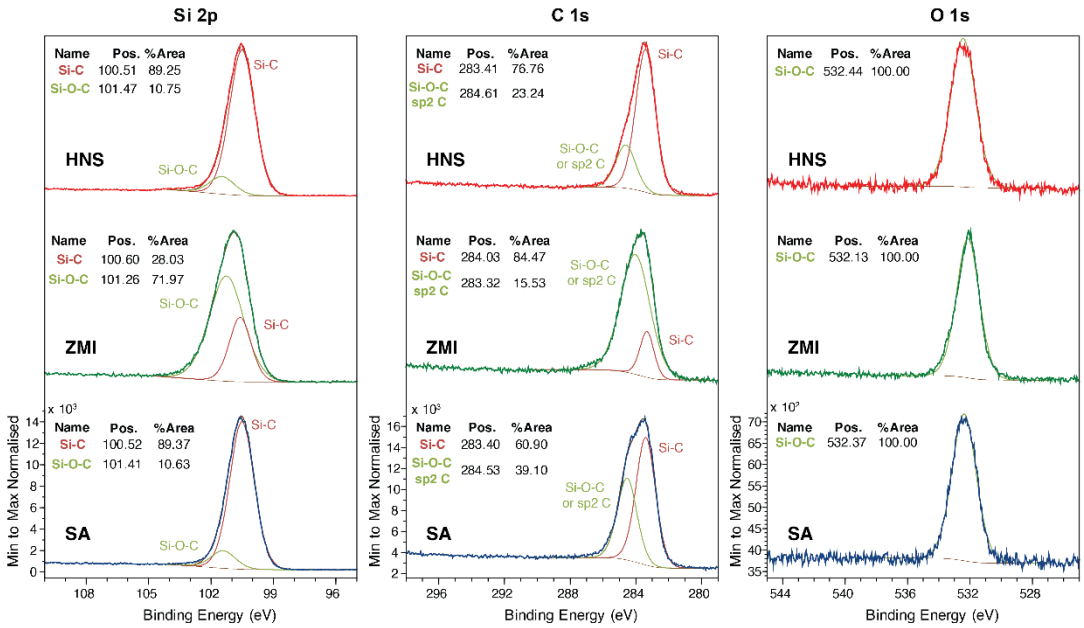

Figure 4: High-resolution scans of Si 2p, C 1s, and O 1s peaks for HNS, ZMI and SA fibers and corresponding fits. Si-C and Si-O-C phases were identified in all fibers. Overlap in binding energies for graphitic carbon (sp2 C) and Si-O-C precludes unambiguous identification of the two phases. (Note that the summed fitted curves are almost indistinguishable from the experimental data.)

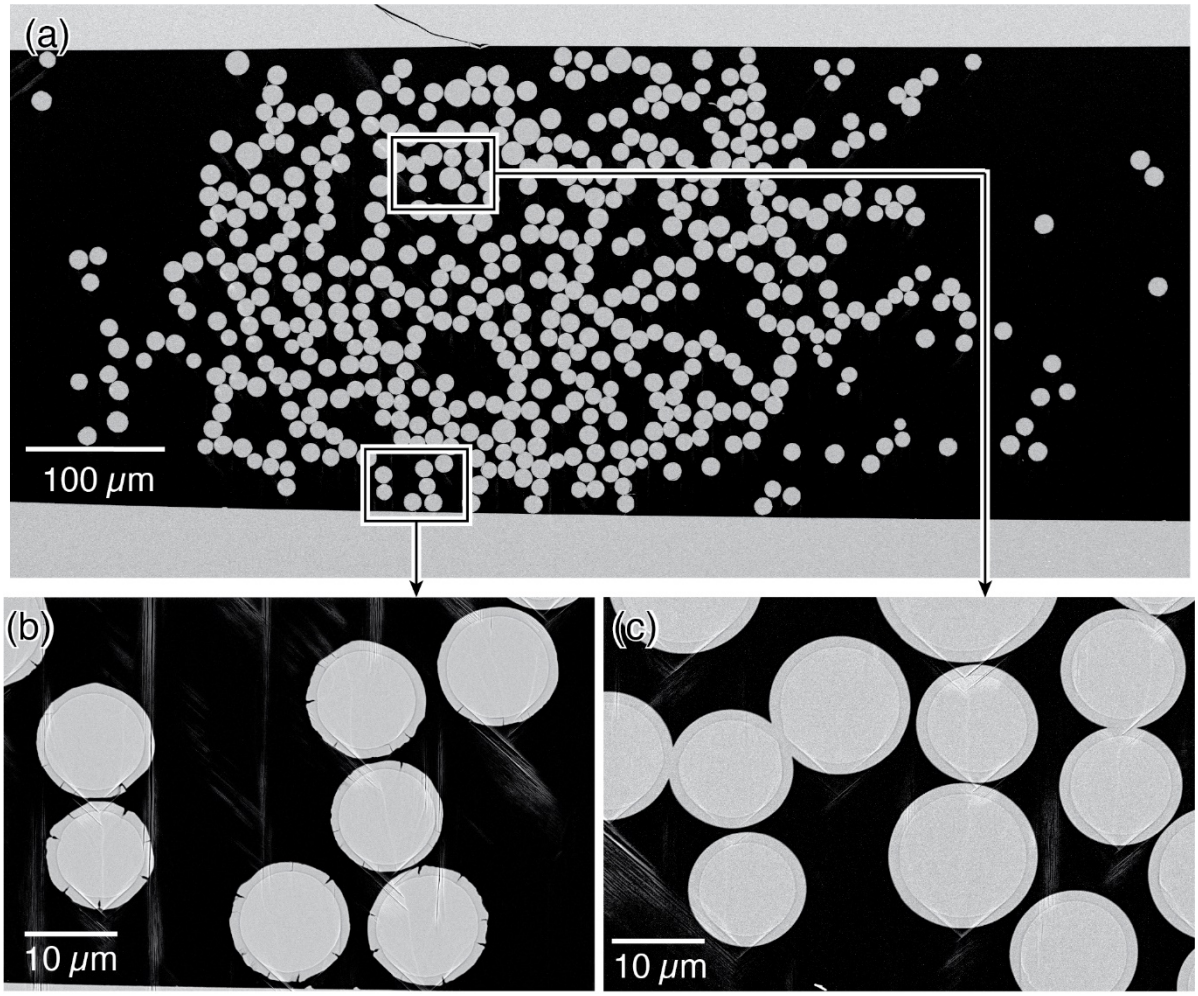

Figure 5: (a) Cross section of HNS fiber tow after 48h exposure. (b, c) Scales on interior fibers are uniform, smooth and intact while those on the near-edge fibers are somewhat non-uniform, faceted and cracked. Coating thicknesses were measured only on interior fibers.

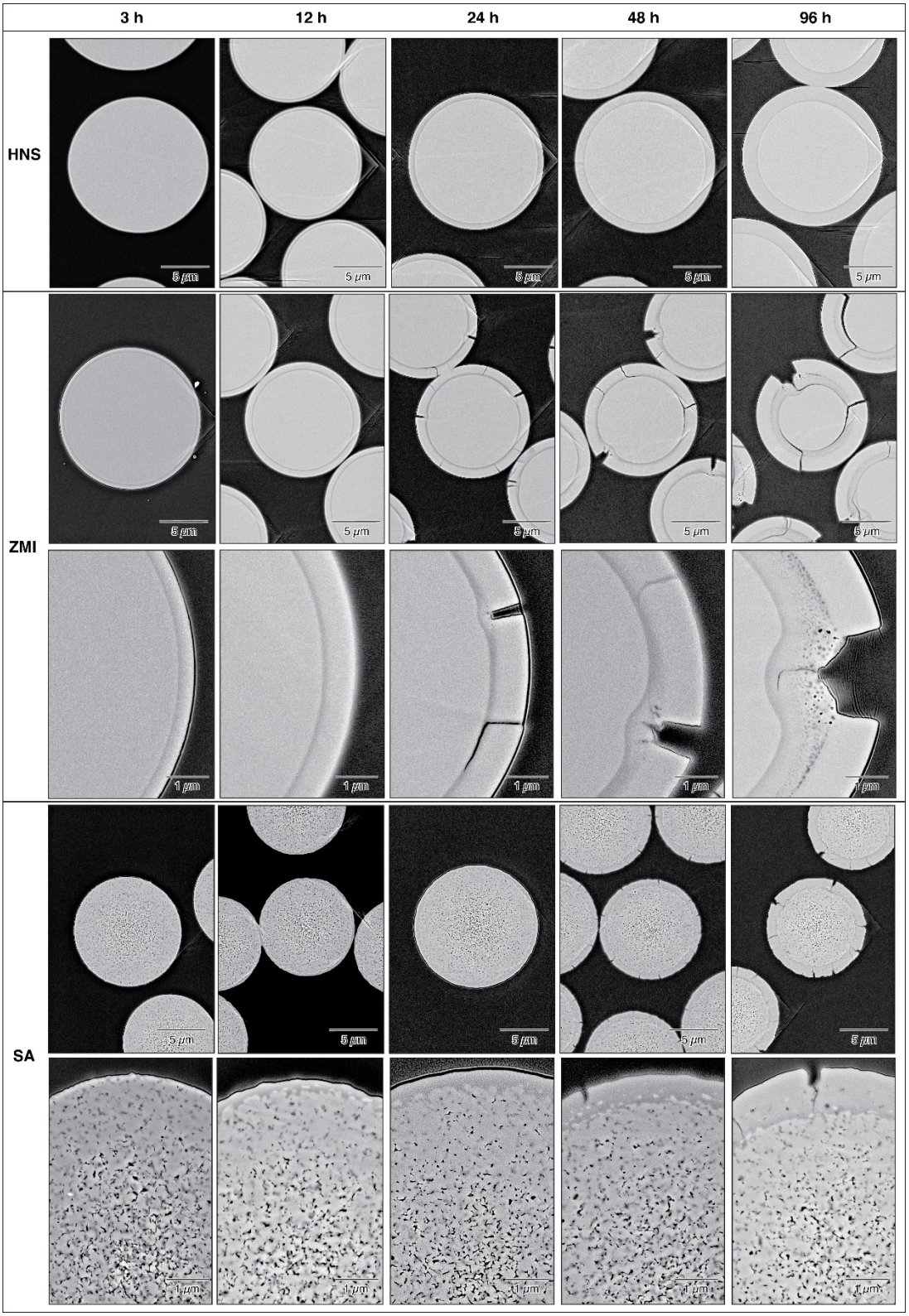

Figure 6: SEM images show that oxide scales on HNS fibers (top row) remain crack free while those on ZMI and SA fibers are cracked after 24h and 48h exposures, respectively.

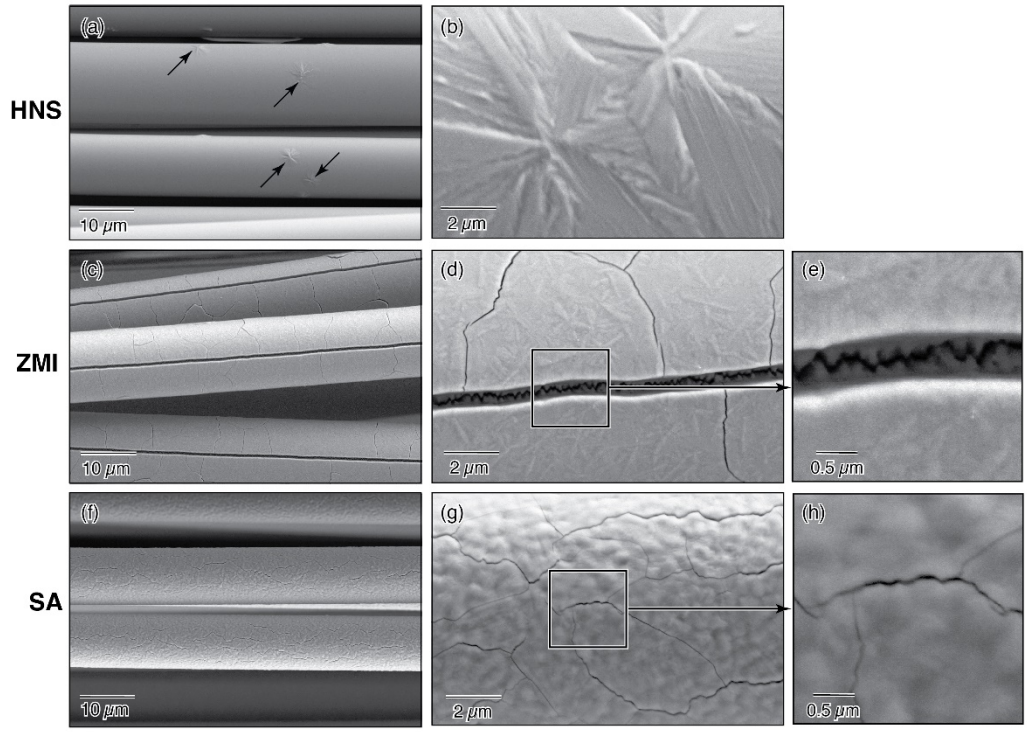

Figure 7: External fiber surfaces after 48h exposure show varying levels of texture and cracking. Corresponding TEM images in Figure 9 show that scales on ZMI and SA fibers are crystalline while those on HNS remain amorphous (the latter not shown).

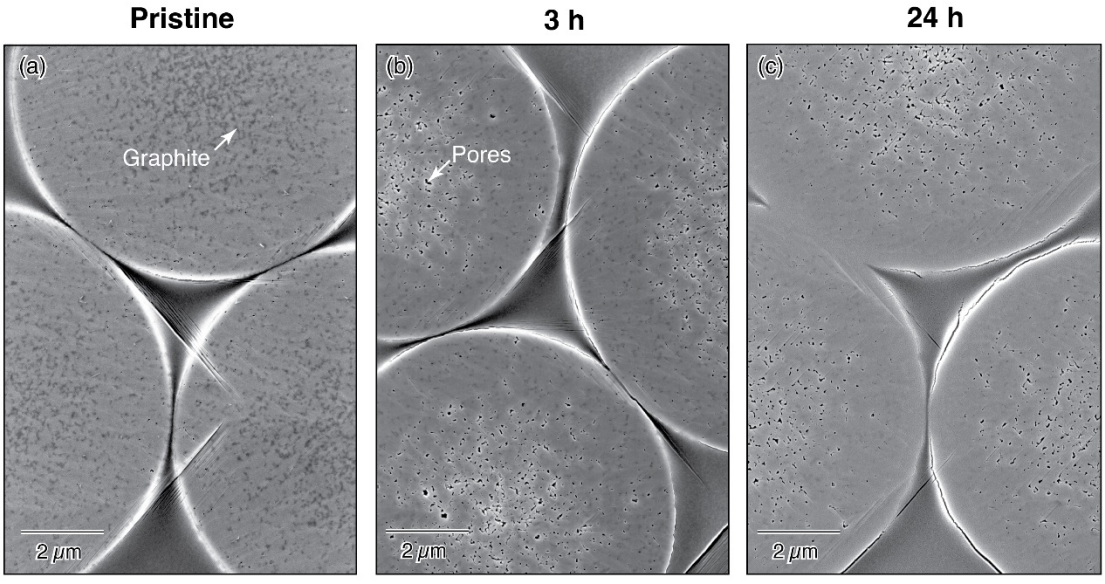

Figure 8: Secondary electron SEM images of SA fibers (a) before oxidation and (b,c) after 3h and 24h exposures, respectively. Voids in the fiber interior are evidenced by bright edges.

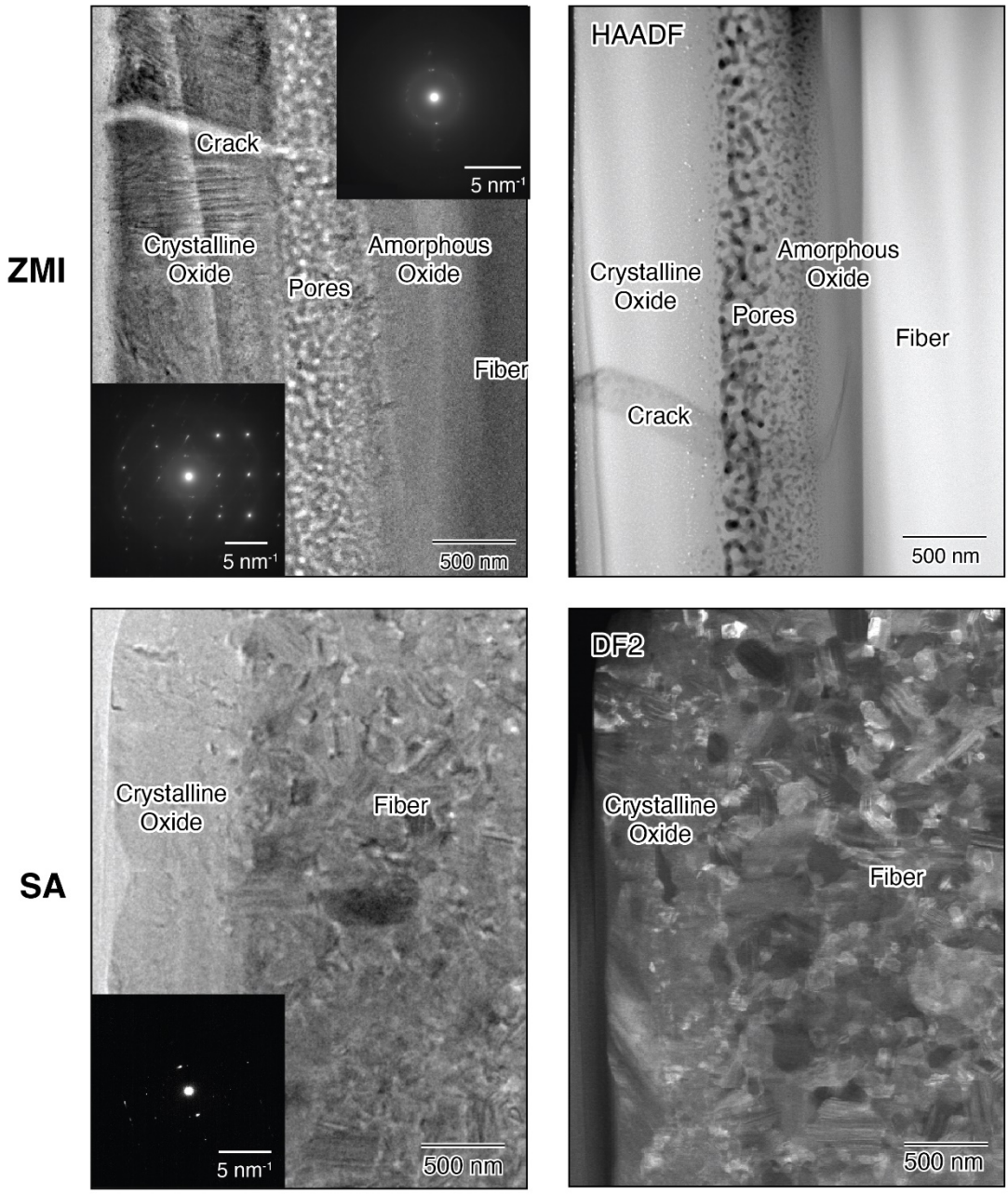

Figure 9: TEM (left) and STEM (right) images of lamella extracted from ZMI (top) and SA (bottom) fibers after 48h exposure. Selected area diffraction patterns confirm an outer crystalline oxide and inner amorphous oxide for the ZMI fiber and a fully crystalline oxide for the SA fiber.

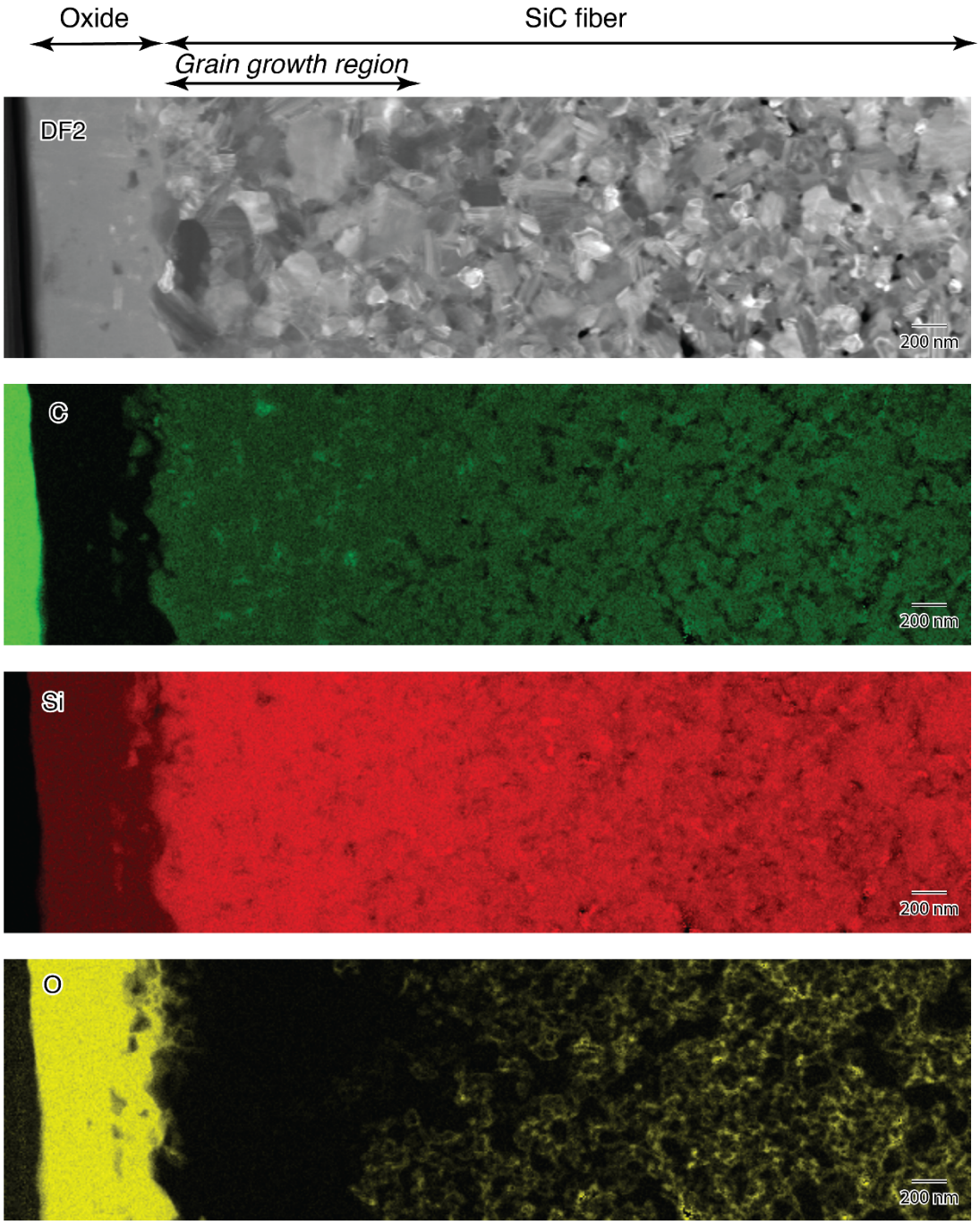

Figure 10: Dark field STEM image of SA fiber with corresponding TEM EDS maps of C, Si and O. SiC grains near the external surface are about twice as large as those in the interior. The region of grain growth is devoid of oxygen and contains pockets of carbon. Oxygen is present in the fiber interior in regions where carbon had oxidized and volatilized and the exposed SiC surfaces had subsequently oxidized.

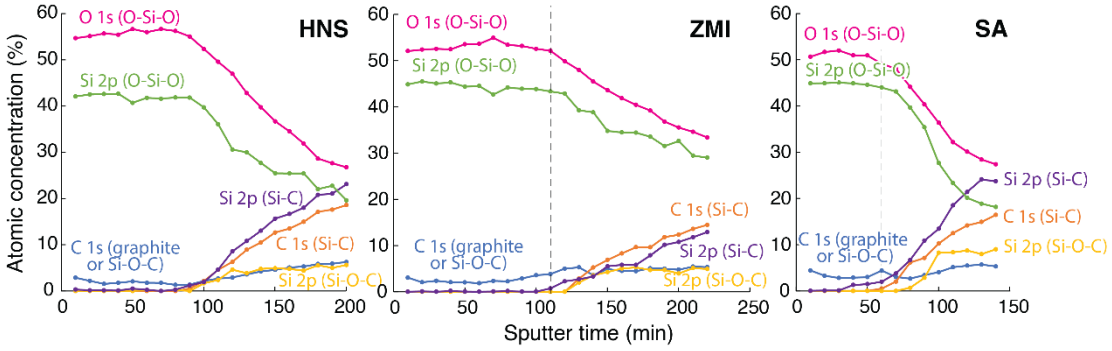

Figure 11: Atomic concentration of elements within O-Si-O, Si-C, Si-O-C and graphite from fitting high resolution scans of C 1s, Si 2p, and O 1s for (a) HNS, (b) ZMI, and (c) SA fibers. Each data point represents an individual scan after a 10 minute sputter. Vertical dashed lines indicate times at which fibers were exposed.

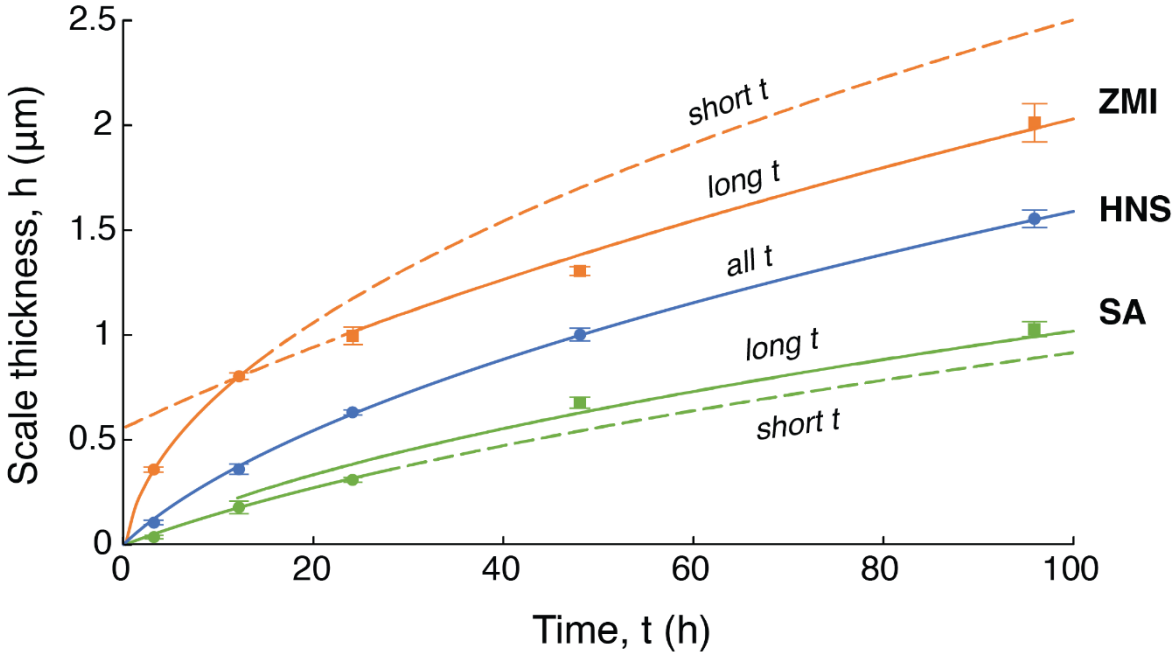

Figure 12: Measurements and analyses of oxidation kinetics of the three fiber types. Circular symbols indicate uncracked scales while square symbols indicate cracked scales. Linear-parabolic (L-P) and the adjusted L-P fits are denoted for each, with a transition from solid to dashed to show where curves were extrapolated away from points used in the fits.

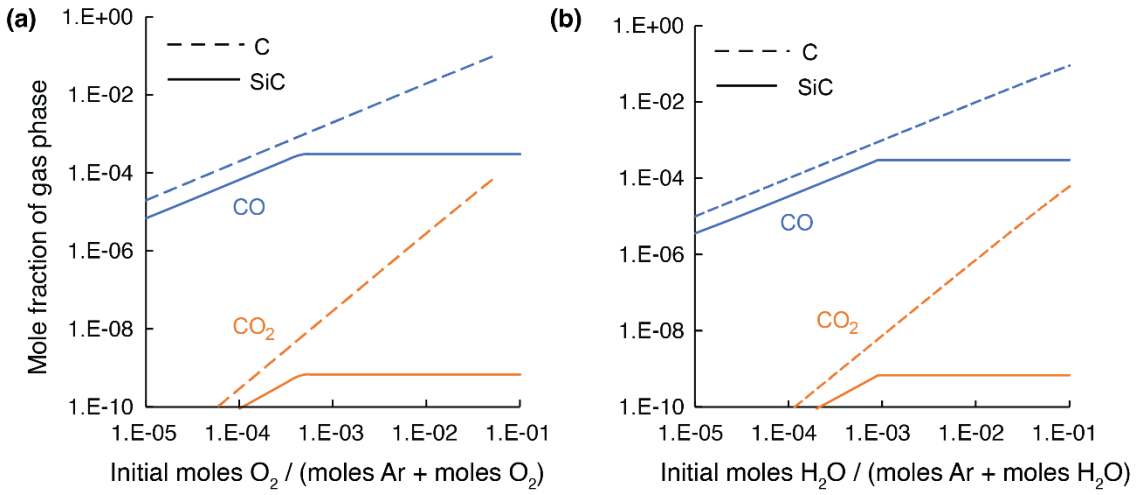

Figure 13: Thermodynamic calculations show that, in the early stages of oxidation, the mole fractions of CO and CO_2 in the gas phase are greater for C oxidation than those for SiC oxidation.

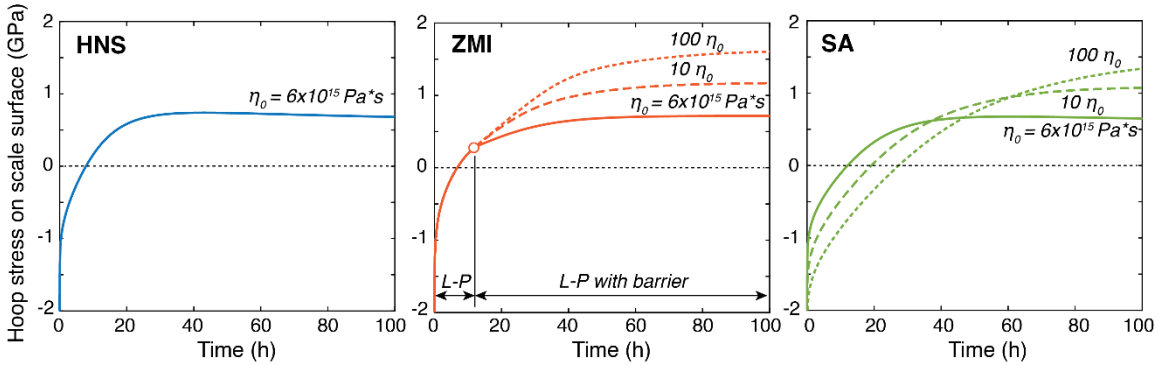

Figure 14: Calculated hoop stress on the outer surface of oxide scale on the three fiber types. Higher viscosities lead to higher tensile hoop stresses. The linear-parabolic (L-P) model was used for HNS and SA fibers. The adjusted L-P model with the crystalline barrier was used for ZMI fibers for t > 12h.

Chapter 3[**]

Microstructure Characterization and Process-Structure Correlations in SiC/BN/SiC Minicomposites

3.1. Introduction

Boron nitride (BN) fiber coatings enable crack deflection and provide a protective barrier between fibers and matrix in SiC-based ceramic matrix composites (CMCs) [1], [2]. To be effective, the coatings must be continuous and uniform in thickness around each fiber. Otherwise, local chemical reactions between phases can lead to partial fiber consumption and bonding of the phases during subsequent processing or in service. Since SiC fibers have been engineered to eliminate all but the smallest (sub-μm) flaws, even highly localized reactions can lead to significant strength reduction [3]–[5]. Additionally, coating non-uniformity can lead to non-uniform coating oxidation and volatilization at high temperatures and accelerate composite degradation [6]–[8]. While the need for uniform coatings is well-recognized, it has not been met universally (Table I).

Non-uniform and incomplete coatings result from the inherent limitations of the chemical vapor infiltration (CVI) process used for BN deposition [9]–[12]. Sources of non-uniformity include gradients in reactant gas concentration and deposition rate from the exterior to the interior of fiber preforms [13]–[16]. In principle the conditions can be tuned to reduce the consumption rate relative to the transport rate, leading to more uniform

[**] The content of this chapter has previously appeared in Acta Materialia (Christensen, V.L., Samuel, A.F., Han, N., Zok, F.W., "Microstructure Characterization and Process-Structure Correlations in SiC/BN/SiC Minicomposites," *Acta Materialia*, 264). It is reproduced here with the permission of Elsevier.

deposition. Incomplete coatings manifest in part as fiber-fiber contacts, fiber-matrix contacts, and fiber-coating debonds.

Since coating uniformity is unlikely to be achieved in practice, an improved understanding of coating quality and its role in composite performance will be crucial for developing composite lifing strategies. But quantitative characterization of coating uniformity and defects has been lacking. Methods like X-ray computed tomography cannot resolve coating thickness variations [17], [18] while transmission electron microscopy is impractical for large surveys [19], [20]. Here, a methodology is presented using scanning electron microscopy (SEM) of polished cross-sections. Broad ion beam milling is used to prepare high quality surfaces spanning entire minicomposite cross-sections. Segmentation and image analysis are performed to identify fibers, measure coating thicknesses, and determine microstructural metrics. These include intra- and inter-fiber coating variations, local fiber volume fraction non-uniformity, and defect densities. The methodology is demonstrated on minicomposites fabricated under differing conditions.

In notable previous studies, Hay and co-workers [21], [22] had made coating thickness measurements using SEM images of mechanically-polished cross-sections of oxide fiber cloths with (relatively hard) monazite coatings. They reported average thicknesses and standard deviations over many fibers and fractions of both uncoated areas and areas where the coatings bridged across multiple fibers, among other metrics. Conceptually the current study builds on that work, using improved surface preparation and imaging methods, somewhat different coating metrics, and alternative analysis methods. It also expands the scope of analysis to include correlations between various coating and fiber characteristics. Comparable studies on SiC/BN/SiC composites have not been reported previously, perhaps

in part because of the challenges in preparing samples with high surface quality over large areas.

The chapter is organized in the following way. The nature of exemplar minicomposite test specimens and the methods employed for sample preparation, imaging, image segmentation and measurement of various microstructural characteristics are described in Section 3.2. In Section 3.3, correlations between coating characteristics and fiber locations and local volume fractions are examined to elucidate dependencies. A meso-scale diffusion/reaction model, presented in Section 3.4, provides insight into effects of distance from the tow boundary on coating uniformity. The model shows uniformity is governed by a Thiele modulus dependent on deposition temperature and tow porosity. Comparisons to experiments suggest the methodology can be used to glean insights into process-structure linkages. Finally, Section 3.5 provides a summary of findings, conclusions and outlook. The image-based measurements, microstructure metrics, and process-based models enable quantitative characterization of coating quality which in turn can help guide improvements in CVI processing of BN coatings in SiC/BN/SiC composites.

3.2. Materials and methods

3.2.1 Synopsis of workflow

The characterization workflow follows four main steps: (i) Cross-sections of unidirectional minicomposites are prepared by ion milling and imaged via scanning electron microscopy. Images are segmented to identify and isolate phases. (ii) Measurements are made of each fiber centroid location and fiber radius as well as coating thickness at multiple points around each fiber. (iii) Key microstructure characteristics are extracted from the measurements.

These include: numbers of fiber-fiber and fiber-matrix contacts, fiber-coating debonds, and clusters of touching fibers; *intra*- and *inter*-fiber coating thickness variations; variation in local fiber volume fraction; and shortest distance to a tow boundary. These features are illustrated in Figure 1. (iv) Correlations are established between pertinent coating and fiber characteristics.

3.2.2 Minicomposites

Four types of unidirectional minicomposites (denoted **A**, **B**, **C**, and **D**) were used in this study (Figure 2). Composites **A**, **B**, and **C** each consist of a single tow of Hi-Nicalon Type S fibers while **D** consists of a single tow of Tyranno ZMI fibers. BN coatings and SiC matrices had been deposited via CVI using BCl_3 as a precursor gas at three industrial facilities (**B** and **C** at the same one).

The tow in composite **A** had been twisted prior to BN deposition. Twisting brings the fibers closer to one another and increases the propensity for fiber-fiber contact. From examination of exterior fibers of the minicomposite the twist rate is estimated to be 14 turns per meter. Based on available information on processing conditions used in making similar minicomposites [11], [23], the deposition temperature is estimated to be in the range 800-950°C.

Tows in **B** and **C** had not been twisted prior to coating and exhibit the greatest degree of fiber splaying. The coatings differ in their deposition temperature and in the degree of BN crystallinity; coatings in **B** had been deposited at a high temperature (1275-1400°C) in order to produce crystalline BN while coatings in **C** had been deposited at a lower temperature (775-875°C) in order to produce amorphous BN. The targeted structures (crystalline BN in

B and amorphous BN in **C**) have been confirmed by independent evaluations [O. Gavalda Diaz, *private communication*].

The tow in **D** had been coated at a relatively low temperature while still straight and then twisted prior to SiC matrix deposition. Twisting of coated tows causes clusters of fibers with shared coatings to break-up and the coatings to spall off the fibers to some extent.

3.2.3 Sample preparation and image segmentation

Transverse cross-sections of the composites were produced using a broad beam ion mill (Leica TIC3X) *without* embedding the composites in resin. Previous experience has shown that this method yields a remarkably fine polish with excellent edge retention between dissimilar phases [6]. The sections were imaged in backscatter mode in a scanning electron microscope (Thermofischer Apreo C). Collections of images with a resolution of 0.08 μm/pixel were obtained over entire composite cross-sections and assembled into montages using tools in Adobe Photoshop. The images were then thresholded to isolate coatings, fibers, matrix[††], and debonds between fibers and coatings (when present). The accuracy of each segmented image was assessed by overlaying the original SEM montage and checking for consistency of all features. In cases where thick coatings were shared by two adjacent fibers, a thin line (2 pixels wide) denoted as matrix was manually inserted through the center of the neck region to separate the coatings between the two fibers.

[††] In the current iteration of the code, the CVI SiC matrix is not distinguished from voids in the space surrounding fibers. The only segmented voids are debond cracks between fibers and coatings. The code could be readily extended to segment matrix and voids.

3.2.4 Image analysis and microstructure metrics

Segmented images were analyzed using a combination of built-in and custom MATLAB codes. First, an algorithm based on the two-stage circular Hough transform is used to identify all fiber centroid locations (in x-y coordinates) and to determine fiber radii R_f. The fiber volume fraction f and porosity, $\phi = 1 - f$, are obtained from the total fiber area and the total tow area. (Table II contains a complete list of symbol definitions.) The external tow boundary for computing the tow area is obtained using the boundary command in MATLAB.

Using the fiber centroids as seed points, a Voronoi tessellation is constructed of the minicomposite section. The tessellation is used to compute two characteristics at each fiber location: (i) the shortest distance r between the fiber centroid and the tow boundary and (ii) the local fiber volume fraction, defined as $v = \pi R_f^2/A$ where A is the area of the Voronoi cell. The uniformity of the spatial arrangement of fibers is characterized by a coefficient of variation, $\mu_v \equiv s_v/\bar{v}$, where $\bar{v}$ is the mean value and s_v the standard deviation[‡‡].

Next, a series of radial line scans is constructed for each fiber at regular angular intervals ($\Delta\theta = \pi/50$, for a total of 100 scans per fiber), starting at the fiber centroid and extending to a length of 1.5x the maximum fiber radius. The line scans are used to determine coating thickness profiles $h(\theta)$ and to identify coating defects in the following way.

(i) In the most common scenario, the line passes from fiber to coating and then to matrix. The coating thickness is then taken as the line length within the coating segment.

[‡‡] Because the external tow boundary cannot be clearly delineated, v_i and r_i in the Voronoi cells bordering the tow boundary are set to 0 in subsequent analysis.

(ii) When instead the line passes from fiber to coating and then to another fiber, the thickness is taken as half of the length of the coating segment; the other half is eventually assigned to the neighboring fiber at the same location.

(iii) When the line passes directly from fiber to matrix, the coating thickness is taken as zero and the point on the fiber surface is designated as a fiber-matrix contact. If the same condition is met at the next scan in the sequence, the new contact is lumped together with the preceding one.

(iv) Similarly, when the entire line passes through only fiber material, the coating thickness is taken to be zero and the location is designated a fiber-fiber contact. Here again contacts identified from sequential line scans are lumped into one.

(v) When the line passes from fiber to void space and then through coating and matrix, the coating thickness is determined from the line length within the coating segment and the location is designated as a point of debonding.

The thickness profile $h(\theta)$ for each fiber is used to compute the mean $\bar{h}$ and standard deviation s_h of coating thickness for that fiber and to identify its maximum value h^{max}. The average *intra*-fiber thickness variation is characterized by $\mu_{h,intra} \equiv \langle s_h \rangle / \langle \bar{h} \rangle$ where $\langle \bar{h} \rangle$ and $\langle s_h \rangle$ are the mean values of $\bar{h}$ and s_h, respectively. Analogously, the average *inter*-fiber thickness variation is characterized by $\mu_{h,inter} \equiv s_{\bar{h}} / \langle \bar{h} \rangle$ where $s_{\bar{h}}$ is the standard deviation of the mean thickness $\bar{h}$ of all fibers. The numbers of fiber-matrix contacts N_{fm}, fiber-fiber

contacts N_{ff}, and fiber-coating debonds N_d are counted and reported on a per fiber basis; their average values are denoted $\overline{N}_{fm}$, $\overline{N}_{ff}$, and $\overline{N}_d$.[§§]

The four minicomposites are compared on the basis of 6 characteristics: the average defect densities, $\overline{N}_{fm}$, $\overline{N}_{ff}$, and $\overline{N}_d$, and the metrics characterizing microstructural uniformity, $\mu_{h,intra}$, $\mu_{h,inter}$ and μ_v. In select cases the effects of tow porosity ϕ and mean coating thickness $\bar{h}$ on these characteristics are also examined.

Further analysis at the meso-scale addresses effects of closed clusters of contacting fibers on coating thickness. Clusters are identified using a Delaunay triangulation with the fiber centroids as seed points. The edge-to-edge distance between each neighboring fiber pair is calculated by subtracting the sum of the two fiber radii from the length of the corresponding Delaunay edge. Touching fibers or coated fibers with an edge-to-edge distance less than 0.2 μm are identified as contacting. Closed clusters are defined by a minimum of three contacting fibers that form a closed loop. In cases where the degree of clustering appears significant its influence is examined by further parsing the coating thickness measurements. Here the data are binned according to whether measurements were made within a cluster interior, on the external surface of a fiber on a cluster border, or on a lone (non-contacting) fiber.

3.2.5 Statistical analysis

To identify the origins of coating non-uniformity, correlations are sought between the coating characteristics – notably thicknesses $\bar{h}$ and h^{max} and intra-fiber thickness variation

[§§] Other defect metrics can be envisaged. Examples include fractional area of debonded interfaces (complementary to number of debonds) and fractional area of fiber-matrix contacts (complementary to number of fiber-matrix contacts). Studies on correlations between defects and composite performance would help identify the most relevant and useful metrics.

$\mu_{h,intra}$ – and the fiber characteristics r and v. Selection of the latter two parameters is based on the understanding that the BN deposition rate decreases with distance into a tow and the expectation that the space available for gas transport near a fiber (a local permeability, of sorts) may limit the local deposition rate. Finally, the *sensitivity* of $\bar{h}$ to r and v, the potential *influence* of r and v on $\bar{h}$, and the degree of *uniformity* of $\bar{h}$ with respect to variations in r and v are examined. These parameters are defined and described later.

3.3. Results and analyses

3.3.1 Synopsis of measurements

Qualitative features of the fiber spatial distributions and the resulting Voronoi tessellations and Delaunay triangulations are displayed in Figure 2. More detailed images showing the nature of coating defects and coating variations as well as the frequencies of these features are presented in Figures 3 and 4. As described earlier and shown schematically in Figure 1, the composites exhibit three types of apparent defects: fiber-fiber contacts, fiber-matrix contacts and fiber-coating debonds.

Among these, fiber-fiber contacts are most common. Their frequency is particularly high in composite **A**. Here less than 10% of all fibers are *not* in contact with a neighboring fiber; the average number of contacts is $\overline{N}_{ff} \approx 2$. In contrast, in the other three composites at least 70% of fibers are contact-free. The high number of contacts in **A** results from the high degree of tow twisting prior to coating.

Composite **D** exhibits an unusually high number of coating-fiber debonds ($\overline{N}_d \approx 1.7$); only 23% of fibers do not have a single debond. The debonds are likely due to a combination of stresses from thermal expansion mismatch during cooling and poor

coating/fiber adhesion. This composite also exhibits a high number of fiber-matrix contacts; more than ¼ of fibers have at least one fiber-matrix contact. These are due to coating loss after deposition, probably exacerbated by tow twisting.

Composites **B** and **C** contain the fewest defects, with $\overline{N}_{fm} \ll 0.1$ and $\overline{N}_{ff} \approx 0.1 - 0.3$. Since the tows were somewhat splayed (not twisted) during coating, the resulting average fiber volume fractions are low (f = 8% and 14% in **B** and **C,** respectively), resulting in large fiber-to-fiber spacings. For comparison, f = 44% and 31% in **A** and **D**, respectively. While the average number of fiber-coating debonds in **B** is not insignificant ($\overline{N}_d \approx 0.5$), it is less than 1/3 that in **D**.

3.3.2 Comparison of average properties across composites

Comparisons of average values of microstructural metrics, including coating defect densities and non-uniformities in coating thickness and local fiber volume fraction, are summarized in Figure 5 in the form of a spider plot. Here the properties of each composite are represented by discrete points along each of 6 axes and the points joined to form a distorted hexagon. Three of the axes (across the top) represent average defect densities ($\overline{N}_{fm}$, $\overline{N}_{ff}$, and $\overline{N}_d$) while the other three (along the bottom) represent microstructural non-uniformities ($\mu_{h,intra}$, $\mu_{h,inter}$ and μ_v). Properties are "best" at the center hexagon (where all metrics are 0).

The figure shows that *inter*-fiber thickness variations on average are essentially the same in all composites ($\mu_{h,inter} \approx 0.4 - 0.5$). *Intra*-fiber variations in **B**, **C** and **D** are similar as well ($\mu_{h,intra} \approx 0.3 - 0.4$), while that for **A** is considerably higher ($\mu_{h,intra} \approx 0.65$). The spatial non-uniformity in fiber volume fraction μ_v spans the widest range of

values, from $\mu_v \approx 0.6$ for **A** and **D** to $\mu_v \approx 0.9$ and 1 for **C** and **B**, respectively. The distributions are more explicitly depicted by the histograms of $\bar{h}$, s_h, and v in Figure 4(c-e).

Differences in $\mu_{h,intra}$ and μ_v in composites **A**, **B** and **C** appear to be associated with differing levels of tow porosity ϕ. The results, plotted on Figure 6, show that $\mu_{h,intra}$ decreases while μ_v increases with ϕ. These trends are consistent with the expectation that, when more space is available to a collection of fibers, the fibers experience less influence of neighboring fibers and may take on a wider range of spatial configurations (analogous to configurational entropy).

3.3.3 Correlations within composites

The following analysis focuses on correlations between coating characteristics ($h^{max}, \bar{h}$ and $\mu_{h,intra}$) and fiber characteristics (v and r) within each composite. A preliminary analysis confirmed that, in all cases, v and r are not correlated with one another and can therefore be treated as independent variables. Fiber-matrix contacts are excluded from the analysis since they were confined to only one of the four composites and do not appear to be common defects in SiC/BN/SiC composites in general. Correlations between N_{ff} and r (not shown) were found to be insignificant ($R^2 < 0.1$). On the other hand, N_{ff} and v were positively correlated with R^2 values in the range 0.2 to 0.3. But these correlations are unsurprising: regions containing fiber-fiber contacts naturally have high local fiber volume fraction and thus N_{ff} and r are not entirely independent. (These, too, are not shown.) The main results, presented in Figures 7 and 8, are scatter plots of variations in h^{max}, $\bar{h}$, and $\mu_{h,intra}$ with v and r along with the computed coefficients of determination, R^2. In the ensuing discussion

the R^2 values are interpreted as fractions of the variance in the dependent variable that are attributable to the respective independent variable [24].

Inter-fiber variance in $\bar{h}$: For composite **A**, the local fiber volume fraction v accounts for almost 50% of the variance in $\bar{h}$ while the distance to the tow boundary r accounts for <10%. The opposite trend is obtained in **B**: v accounts for only slightly over 15% of the variance in $\bar{h}$ while r accounts for 55%. In **C**, r and v contribute almost equally (about 40% each). Together, r and v account for 2/3–3/4 of the variance in $\bar{h}$ in **A, B** and **C**. For **D**, $\bar{h}$ exhibits only weak correlations with r and v (R^2 = 0.16 and 0.09 respectively). The weak correlations are due to fiber movement during tow twisting, which obscures information about the fiber locations during coating. Composite **D** is therefore excluded from some of the further analysis.

Intra-fiber variance in $\bar{h}$: The intra-fiber variance $\mu_{h,intra}$ is not significantly correlated with v for any of the four composites (R^2 < 0.1). It does, however, appear to be correlated with r for **B** and **C.** But these trends closely parallel those for $\bar{h}$: that is, both $\mu_{h,intra}$ and $\bar{h}$ decrease with increasing r. The interpretation, based on the physical processes involved, is that the intra-fiber variance is probably not controlled by the fiber location per se but rather by the coating thickness, which is indeed affected by fiber location. Effects of $\bar{h}$ on $\mu_{h,intra}$ are plotted in Figure 9. For both **B** and **C** the correlations are significant (R^2 ≈0.25–0.30), indicating that coatings tend to grow progressively more non-uniformly as deposition proceeds.

Coating debonds*:* Excluding **D**, composite **B** exhibits the greatest number of debonds. The prevalence of debonding in **B** is positively correlated with $\bar{h}$, as shown by the overlaid histogram in Figure 4(c). The histogram shows that debonding occurs only when the coating

thickness exceeds a critical value of 0.6 μm; thereafter the likelihood of debonding increases with $\bar{h}$. This trend is consistent with the linear scaling of energy release rate of putative interface cracks with coating thickness [25].

The higher propensity for debonding in **B (**compared to **C**, for example) is attributable to two factors. First, the higher deposition temperature naturally leads to higher thermal stresses upon cooling. Second, the high deposition temperature for **B** causes formation of crystalline hexagonal BN with the basal planes of the crystallites preferentially aligned with the fiber surface. Because of the highly disparate bonding characteristics inherent to h-BN in and out of the basal plane, alignment results in high thermal expansion anisotropy: the CTE within the basal plane being near zero and that perpendicular to the basal plane over 20×10^{-6} K^{-1} [26], [27]. By comparison the fiber CTE is 5×10^{-6} K^{-1} [28]. Together these CTE values indicate high radial tensile stresses at the fiber-coating interface upon cooling from the deposition temperature. (Assuming perfect alignment of BN crystallites, the radial misfit strain is estimated to be 0.006.)

Closed fiber clusters: Among the four composites, **A** is the only one that exhibits a significant number of closed clusters of contacting fibers. Indeed more than 1/3 of all fibers are part of a cluster. The role of these clusters in coating thickness is shown in Figure 10. Here the data are distinguished by measurement location: within cluster interiors, on external surfaces of fibers that define the borders of clusters, or on lone (non-contacting) fibers. As a group, coatings on lone fibers are thickest; their average thickness (1.5 ± 0.46 μm) is more than 60% greater than the average of the entire population (0.9 ± 0.67 μm). Coatings within cluster interiors are thinnest by a large margin. The entire range of their thickness falls within the first two quartiles of the thickness distribution on the exterior

cluster surfaces. Furthermore, the median value within clusters is only about 10% of that on exterior surfaces (0.08 vs. 0.8 μm). Clearly, closed clusters of contacting fibers severely impede ingress of CVI gas into the cluster interiors during the coating process.

3.3.4 Sensitivity, influence, and uniformity

The sensitivities of coating thickness $\bar{h}$ to r and v were examined through bivariate linear regression analyses of $\bar{h}(r, v)$ using the IBM SPSS software [29]. Because the variables have different scales, they are first centered and normalized by standard deviations in accordance with:

$$\alpha_h \equiv \frac{\bar{h} - \langle\bar{h}\rangle}{s_{\bar{h}}}, \qquad \alpha_r \equiv \frac{r - \bar{r}}{s_r}, \qquad \alpha_v \equiv \frac{v - \bar{v}}{s_v} \tag{1}$$

Regression analysis yields the coefficients in the relationship

$$\alpha_h = \frac{\partial \alpha_h}{\partial \alpha_r}\,\alpha_r + \frac{\partial \alpha_h}{\partial \alpha_v}\alpha_v \tag{2}$$

where the partial derivatives are assumed constant. The sensitivities of $\bar{h}$ to r and v are represented by the rate of change of $\bar{h}$ relative to its mean $\langle\bar{h}\rangle$ with respect to the independent variables r and v relative to their respective means $\bar{r}$ and $\bar{v}$, defined by:

$$S_{h,r} \equiv \frac{\partial(\bar{h}/\langle\bar{h}\rangle)}{\partial(r/\bar{r})} = \frac{\mu_h}{\mu_r}\frac{\partial \alpha_h}{\partial \alpha_r} \; and \; S_{h,v} \equiv \frac{\partial(\bar{h}/\langle\bar{h}\rangle)}{\partial(v/\bar{v})} = \frac{\mu_h}{\mu_v}\frac{\partial \alpha_h}{\partial \alpha_v} \tag{3}$$

where, to re-iterate, μ_h, μ_r and μ_v are the coefficients of variation of $\bar{h}$, r and v.

The resulting sensitivities are summarized in Table III and plotted against ϕ in Figure 11. Both $S_{h,r}$ and $S_{h,v}$ are negative; that is, $\bar{h}$ decreases as r or v increase. But they show differing trends with ϕ: the magnitude of $S_{h,r}$ increases while that of $S_{h,v}$ decreases with increasing ϕ.

Sensitivities on their own do not completely capture the effects of r and v on $\bar{h}$. For example, if $S_{h,r}$ is large but the full range of r is small, the impact of r on $\bar{h}$ may be small, and vice-versa. The combined effects of sensitivity to the independent variables and the range of those variables are described by *influence parameters*, defined by $I_{h,r} \equiv S_{h,r}\,\mu_r$ and $I_{h,v} \equiv S_{h,v}\,\mu_v$. The influence parameters represent the variations in coating thickness that could arise from variations in the corresponding independent variables. For example, if $\bar{h}$ were normally distributed, most of the range of $\bar{h}$ associated with variations in r would be essentially $1 \pm I_{h,r}$ (in normalized form). Alternatively, the influence can be couched in terms of a spatial *uniformity index*, η_r, defined as the ratio of $\bar{h}$ at one standard deviation below and one standard deviation above the mean:

$$\eta_r \equiv \frac{1 + I_{h,r}}{1 - I_{h,r}} \tag{4}$$

Analogously, a uniformity index associated with v is defined as

$$\eta_v \equiv \frac{1 + I_{h,v}}{1 - I_{h,v}} \tag{5}$$

The values of influence parameters and uniformity indexes are summarized in Table 3 and plotted against ϕ in Figures 11(b) and 12.

As with the sensitivities, both influence parameters, $I_{h,r}$ and $I_{h,v}$, are negative. Across composites **A**, **B** and **C**, the magnitude of $I_{h,r}$ increases with ϕ while that of $I_{h,v}$ decreases with ϕ. Their magnitudes can be substantial: $I_{h,v} \approx$ -0.3 at low porosities ($\phi \leq 0.5$) and $I_{h,r} \approx$ -0.3 at high porosities ($\phi \geq 0.9$). The uniformity indexes follow the opposite trends: η_r decreasing and η_v increasing with ϕ. The differences in these trends reflect the competing effects of local and meso-scale microstructure characteristics on coating thickness.

3.4. Meso-scale analysis of coupled diffusion and reaction

Here we address the effects of r on variance in $\bar{h}$ in the CVI process. Since the process relies on inward diffusion of reacting gases through the fiber preform while the gases are concomitantly consumed in the formation of BN, gradients in deposition rate naturally ensue. An analysis of the coupled diffusion/reaction process under steady-state conditions is presented in the Appendix.

The competition between diffusion and reaction is characterized by the Thiele modulus, Γ, defined by [14]–[16], [30]

$$\Gamma^2 = \left[\frac{2(1-\phi)\,\dot{h}\,\rho\,L^2}{\bar{R}_f\,\phi\,D_{eff}}\right]^{1/2} \tag{6}$$

where $\dot{h}$ is the coating deposition rate (in m/s), ρ is the molar density of BN (kg/mol), L is a characteristic preform dimension that defines diffusion distance, $\bar{R}_f$ is the mean fiber radius, and D_{eff} is the effective gas diffusivity. When Γ >>1, reaction outpaces diffusion and the coatings at the preform exterior grow much faster than in the interior; this is the *diffusion-limited* domain. Conversely, when Γ<<1, diffusion outpaces reaction and the reaction rates are more uniform across the preform; this is the *reaction-limited* domain. Schematics of the diffusion and reaction processes in the two domains are shown in Figure 13. Analyses based on the Thiele modulus have been used previously for the CVI process to achieve rapid yet uniform deposition, subject to limits on deposition temperature, to avoid, for example, residual chloride contamination in coatings at low temperatures [31] and homogeneous (rather than surface) nucleation of BN at high temperatures [12], [32].

The analysis in the Appendix considers two geometries: (i) an infinite slab with 1D inward diffusion of reacting gas from both external surfaces, and (ii) an infinite circular

cylinder with radial inward diffusion of gas. The reaction is assumed to be of first order such that the deposition rate is proportional to local concentration of reactant gas. The analyses lead to second-order ordinary differential equations governing the relation between gas concentration (and, by extension, deposition rate) and position. The resulting analytical solution for the slab model yields a spatial uniformity index $\eta_r = 1/\cosh\Gamma$. The differential equation governing the cylinder model does not have a convenient closed-form analytical solution. Nevertheless, as demonstrated in the Appendix, the spatial uniformity index for the cylinder is given to a good approximation by $\eta_r = 1/\cosh\left(\Gamma/\sqrt{2}\right)$.

To compare the analytical predictions with the uniformity indexes obtained from the experimental measurements, the parameters that enter into Γ are estimated in the following way. When gas concentration is low (as it is in CVI of BN [16], [33]), the effective gas diffusivity is $D_{eff} = D_K/\tau$ where τ is a measure of tortuosity, which, for cylindrical fibers, scales inversely with porosity ($\tau \approx 1/\phi$) [34], and D_K is the Knudsen diffusivity, given by [35]

$$D_K = \frac{2R_p}{3}\sqrt{\frac{8RT}{\pi M}} \tag{7}$$

R_p is the mean pore radius, R is the ideal gas constant, T is temperature, and M is the molar mass of the principal reacting species, BCl_3 (in kg/mol). In a cylindrical array of aligned fibers with average fiber radius, $\bar{R}_f$, the average pore radius is $R_p = \bar{R}_f\left\{\sqrt{1/(1-\phi)} - 1\right\}$. Combining the preceding results yields:

$$D_{eff} = \frac{2\phi\bar{R}_f}{3}\left(\frac{1}{\sqrt{1-\phi}} - 1\right)\sqrt{\frac{8RT}{\pi M}} \tag{8}$$

The diffusivity is sensitive to porosity ϕ but only weakly dependent on temperature. Additionally, for a cylindrical array of N fibers, L is given approximately by $L = \bar{R}_f\sqrt{N/(1-\phi)}$. Finally, the deposition rate $\dot{h}$ is described by an Arrhenius rate equation for a first-order reaction:

$$\frac{\dot{h}}{\dot{h}^o} = \frac{C}{C^o}\ exp\left\{-\frac{Q}{R}\left(\frac{1}{T}-\frac{1}{T^o}\right)\right\} \tag{9}$$

where Q is the activation energy, and $\dot{h}^0$ is the growth rate (in m/s) measured at a reference gas concentration C^o (in mol/m^3) and reference temperature T^0. Combining, the Thiele modulus becomes

$$\Gamma = \frac{1}{\phi}\left[\left(\frac{3N\,\rho\,\dot{h}^o}{C^o\sqrt{(1-\varphi)}-1}\right)\exp\left(-\frac{Q}{R}\left(\frac{1}{T}-\frac{1}{T^o}\right)\right)\right]^{1/2}\left(\frac{\pi M}{8RT}\right)^{1/4} \tag{10}$$

Using data for CVI of mixtures of BCl_3 and NH_3 gases from Patibandla and Luthra [36], we find Q = 146 x 10^3 J/mol and $\dot{h}^0$= 3.4 x 10^{-9} m/s at C^0=6.2 x 10^{-3} mol/m^3 and T^0=1223K. (Others have reported comparable values [37].) The other parameter values are $N = 500$, ρ = 9.2 x 10^4 mol/m^3, and $M = 0.12$ kg/mol. Using these values, variations in Γ with ϕ for representative deposition temperatures (700–1400°C) are computed and plotted on Figure 14. At high temperatures and low porosities the CVI process is diffusion-limited while at low temperatures and high porosities it is reaction-limited. The boundary between the two domains is demarcated by $\Gamma = 1$; it occurs at a critical temperature that is sensitive to ϕ.

The results are re-interpreted in terms of the coating uniformity index for a cylinder ($\eta_r = 1/\cosh(\Gamma/\sqrt{2})$) and compared with the values obtained from the experimental measurements in Figure 12(a). While the experimental measurements suggest that η_r decreases with increasing porosity, the model predictions (at constant temperature) follow

the opposite trend. The seeming discrepancy is attributable to different deposition temperatures employed in the various composites (lowest for **A** and highest for **B**). Notably, η_r for **A** is close to unity (0.94) and lies in the expected range predicted for deposition temperatures of 800-900°C, consistent with the actual deposition temperature; thickness variations in **A** are attributable almost entirely to local volume fraction effects, as manifested in a low value of η_v (0.57). The value of η_r for **B** is relatively small (0.59) and lies in the domain predicted for deposition temperatures of 1300-1400°, again broadly consistent with the actual deposition temperature. The result for **C** falls in between, albeit with an inferred deposition temperature (about 1200°C) somewhat above the actual range (775-875°C).

While these results are encouraging, additional study is needed to validate the methodology for characterizing coatings and to critically assess the correlations between microstructure metrics and process history.[***] Indeed we expect that the value of the methodology would be more fully realized if integrated within a process modeling framework.

3.5. Summary, conclusions, and outlook

A methodology has been developed to quantify coating uniformity, defects, and correlations with fiber characteristics in SiC/BN/SiC minicomposites. The main components include: broad ion beam milling to prepare high quality polished cross-sections for SEM imaging; image segmentation and analysis to identify fibers, measure coating thickness, and compute

[***] Detailed information about process parameters are not usually made available by composite manufacturers. To this point, Kerans [44], in a review article on SiC-SiC composites, aptly notes that the vast majority of research that has enabled implementation of ceramic composites in turbine engine applications (including that on CVI of BN) has been performed within the private sector (notably by the engine OEMs). Thus the current state-of-the-art in CVI is, understandably, unknown outside these organizations and is largely absent from the open literature.

microstructure metrics; measurement of fiber locations, radii, and local volume fractions; quantification of intra- and inter-fiber coating variations and defect densities; and correlation analysis between coating and fiber characteristics.

The methodology provides quantitative insights into coating quality that can help to interpret experimental measurements and to guide CVI process improvements:

(i) Closed fiber clusters produced by tow twisting severely limit coating deposition and cause large variations. Avoiding clustering is critical.

(ii) In the absence of closed clusters, coating uniformity correlates with local fiber volume fraction and distance to tow edge. The influence of local fiber volume fraction and distance from tow edge on coating variance trend in opposite directions: the former decreasing and the latter increasing with tow porosity. Thus, ameliorating coating non-uniformity due to one source may exacerbate non-uniformity due to another.

(iii) Coating uniformity decreases while the propensity for debonding increases as deposition proceeds, especially at the highest deposition temperatures. Together these results imply a practical thickness limit below which coatings remain adherent and maintain uniform thickness.

(iv) The meso-scale model shows coating uniformity is governed by a Thiele modulus dependent on deposition temperature and tow porosity. Comparisons to experiments suggest the methodology can elucidate process-structure linkages.

Future work could apply the methodology to more complex woven preforms and extend the analysis to multi-tow length scales. Since large numbers of fiber-fiber contacts are inevitable in woven preforms, coating variance in these preforms is expected to be

heavily influenced by local effects and may differ substantially from that in minicomposites, even under equivalent process conditions. The implication is that optimal process conditions may depend strongly on preform topology and geometry [38]–[40]. Studies on correlations between microstructural characteristics and composite performance would also help identify the most relevant metrics which in turn could guide process modifications to improve coating quality.

3.6. Appendix: Analysis of steady-state diffusion and reaction during CVI

Here we present analyses for reactant gas concentration profiles in porous media and, by extension, relative rates of BN deposition under steady-state CVI conditions. While the analysis is largely generic, it is ultimately applied to the chemical reaction:

$$BCl_3(g) + NH_3(g) \rightarrow BN(s) + 3HCl(g) \qquad (A.1)$$

Two geometries are considered: an infinite porous slab of thickness $2L$ and an infinite porous cylinder of diameter $2L$. While only the former yields a simple analytical solution, the latter is more representative of a fiber bundle. The two geometries and pertinent variables are shown in Figure A1.

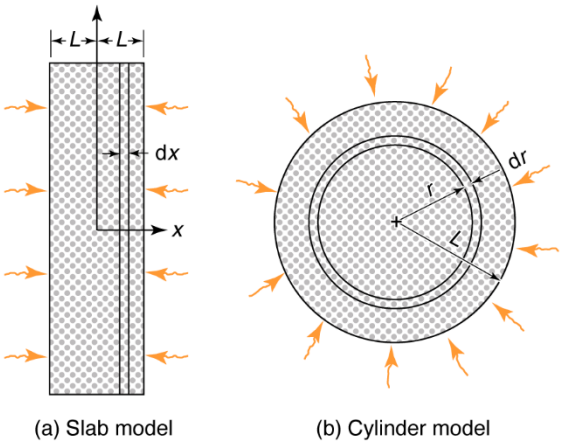

Figure A1: Schematics of the two geometries analyzed.

A.1 Infinite Slab

Performing a mole balance for concurrent diffusion and reaction under 1D conditions through a control volume of width d*x* yields

$$-\frac{dJ}{dx} - \dot{h}\,\rho\,A_{int} = 0 \qquad (A.2)$$

where J is the flux of reactant gas (BCl_3, in moles/m^{2}s); $\dot{h}$ is the rate of BN deposition [in m^3/m^{2}s or equivalently m/s]; ρ is the molar density of BN (in moles/m^3); A_{int} is the internal surface area per unit volume available for BN deposition, which, for an array of cylindrical fibers, is $A_{int} = 2(1-\phi)/\bar{R}_f$; and ϕ is the porosity. The flux, from Fick's law, is

$$J = -\phi\,D_{eff}\frac{dC}{dx} \qquad (A.3)$$

where C is the concentration of BCl_3 (in moles/m^3). Combining Eqs. A2 and A3:

$$\frac{d^2C}{dx^2} - \frac{2(1-\phi)\,\dot{h}\,\rho}{\bar{R}_f\,\phi\,D_{eff}} = 0 \qquad (A.4)$$

Introducing two non-dimensional parameters, $\psi \equiv C/C_s$ and $\lambda \equiv x/L$ where C_s is the surface concentration of BCl_3, and combining with the preceding equations yields

$$\frac{d^2\psi}{d\lambda^2} - \Gamma^2\psi = 0 \qquad (A.5)$$

where

$$\Gamma^2 = \frac{2(1-\phi)\,\dot{h}\,\rho\,L^2}{\bar{R}_f\,\phi\,D_{eff}} \qquad (A.6)$$

The exact solution to Eq. (A5) is

$$\psi = \frac{\cosh\Gamma\lambda}{\cosh\Gamma} \qquad (A.7)$$

It satisfies the condition that ψ is a minimum at the slab center ($d\psi/d\lambda = 0$ at $\lambda = 0$, from symmetry) and the condition that the concentration of BCl_3 is the same in the gas as it is in the slab at the slab surface ($\psi = 1$ at $\lambda = 1$).

The limits on Eq. (A7) are $\psi = 1/\cosh\Gamma$ (the minimum value) at $\lambda = 0$, and $\psi = 1$ (the maximum value) at $\lambda = 1$; the ratio of the two defines a uniformity index, $\eta = 1/\cosh\Gamma$. When $\Gamma \ll 1, \eta = 1$ (the most desirable scenario, since BN deposition occurs uniformly throughout) while when $\Gamma \gg 1, \eta = 0$ (the least desirable, since the reactants are consumed before reaching the slab center).

A.2 Infinite circular cylinder

Performing an analogous mole balance for inward radial diffusion of BCl_3 gas and concurrent BN deposition in a circular annular control volume of radius *r* and of thickness d*r* yields

$$-\frac{d}{dr}\left[-\phi D_{eff}\frac{dC}{dr}r\right] - \frac{2(1-\phi)\,\dot{h}\,\rho}{\bar{R}_f}r = 0 \qquad (A.8)$$

Assuming ϕ and D_{eff} are independent of *r* and applying the product rule to the first term in this equation:

$$\phi D_{eff}\left[\frac{dC}{dr} + \frac{d^2C}{dr^2}r\right] - \frac{2(1-\phi)\,\dot{h}\,\rho}{\bar{R}_f}r = 0 \qquad (A.9)$$

Re-expressing in terms of $\psi \equiv C/C_s$ and $\lambda \equiv r/L$ yields

$$\frac{d^2\psi}{d\lambda^2} + \frac{1}{\lambda}\frac{d\psi}{d\lambda} - \Gamma^2\psi = 0 \qquad (A.10)$$

where again Γ^2 is given by Eq. A6. The solution to this differential equation is $\psi(\lambda, \Gamma) = I_o(\lambda\,\Gamma)/I_o(\Gamma)$ where I_o is the modified Bessel function of the first kind. The results are plotted on Figure A2.

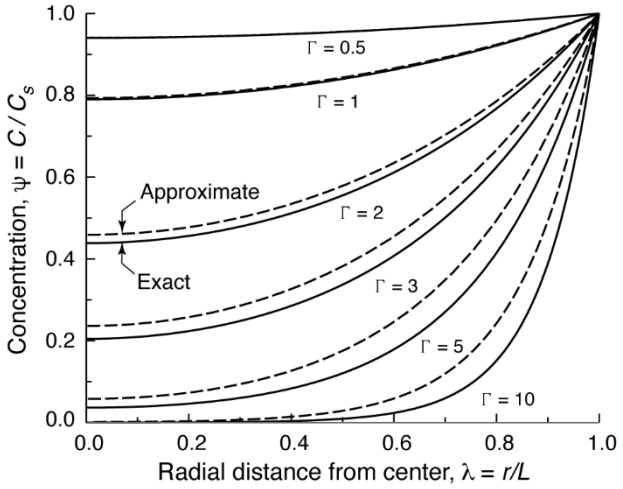

Figure A2: Exact and approximate concentration profiles in an infinite cylinder during CVI at steady state, showing effects of the Thiele modulus Γ on the degree of uniformity.

A useful approximate solution to (A.10) is derived from a modification of the exact solution for the infinite slab (A.8). Here we assume that $\psi = \cosh(\alpha\Gamma\lambda)/\cosh(\alpha\Gamma)$ where α is a constant. Combining this solution with (A.10) and taking the limit of $\Gamma\lambda \to 0$ we find that $\alpha = 1/\sqrt{2}$ (independent of Γ). The resulting concentration profile, given by $\psi = \cosh\left(\lambda\Gamma/\sqrt{2}\right)/\cosh\left(\Gamma/\sqrt{2}\right)$, is remarkably accurate in the domain $\Gamma \leq 1$ and is a reasonable approximation to the exact result for $\Gamma > 1$ (Figure A2). The uniformity index from the analytical prediction, given by $\eta = 1/\cosh\left(\Gamma/\sqrt{2}\right)$, is also a good approximation.

3.7. References

[1] W. A. Curtin, “Theory of Mechanical Properties of Ceramic-Matrix Composites,” *J. Am. Ceram. Soc.*, vol. 74, no. 11, pp. 2837–2845, Nov. 1991.

[2] R. J. Kerans, “The Role of Coating Compliance and Fiber/Matrix Interfacial Topography on Debonding in Ceramic Composites,” *Scr. Metall. Mater.*, vol. 32, no. 4, pp. 505–509, 1994.

[3] G. Morscher, “Tensile Stress Rupture of SiCf/SiCm minicomposites with carbon and boron nitride Interphases at Elevated Temperatures in Air,” *J. Am. Ceram. Soc*, vol. 80, no. 8, pp. 2029–42, 1997.

[4] H. . Yun, J. . Goldsby, and J. . DiCarlo, “Tensile Creep and Stress-Rupture Behavior of Polymer Derived SiC Fibers,” in *NASA Technical Memorandum 106692*, 1994.

[5] R. E. Tressler, “Recent developments in fibers and interphases for high temperature ceramic matrix composites,” *Compos. Part A Appl. Sci. Manuf.*, vol. 30, no. 4, pp. 429–437, Apr. 1999.

[6] V. L. Christensen and F. W. Zok, “Insights into internal oxidation of SiC/BN/SiC composites,” *J. Am. Ceram. Soc.*, vol. 106, no. 2, pp. 1561–1575, 2022.

[7] V. E. Collier, W. Xu, R. M. McMeeking, F. W. Zok, and M. R. Begley, “Recession of BN coatings in SiC/SiC composites through reaction with water vapor,” *J. Am. Ceram. Soc.*, no. April, pp. 1–14, 2021.

[8] B. L. Wing and J. W. Halloran, “Subsurface oxidation of boron nitride coatings on silicon carbide fibers in SiC/SiC ceramic matrix composites,” *Ceram. Int.*, vol. 44, no. 14, pp. 17499–17505, 2018.

[9] R. S. Hay and D. Perty, “Coating apparatus for Continuous Tow,” U.S. Patent 5951764, Sep. 14, 1999.

[10] R. S. Hay, “Method for coating continuous tow,” U.S. Patent 5164229, Nov. 17, 1992.

[11] M. A. Kmetz, “Boron Nitride Coated Fibers and Composite Articles containing same,” U.S. Patent 7867554, Jan. 11, 2011.

[12] G. L. Vignoles, *Chemical vapor deposition/ infiltration processes for ceramic composites*, vol. 1964. Elsevier Ltd., 2015.

[13] K. Shima, N. Sato, Y. Funato, Y. Fukushima, T. Momose, and Y. Shimogaki, “Separate evaluation of multiple film-forming species in chemical vapor deposition of SiC using high aspect-ratio microchannels,” *Jpn. J. Appl. Phys.*, vol. 56, no. 6, 2017.

[14] S. K. Griffiths and R. H. Nilson, “Optimum Conditions for Composites Fiber Coating by Chemical Vapor Infiltration,” *J. Electrochem. Soc.*, vol. 145, no. 4, pp. 1263–1272, 1998.

[15] G. L. Vignoles, “Modeling of chemical vapor infiltration processes,” in *Advances in Composites Manufacturing and Process Design*, Elsevier Ltd., 2015, pp. 415–458.

[16] E. O. Einset, N. -B Patibandla, and K. L. Luthra, “Processing Conditions for Boron Nitride Coatings in Fiber Bundles via Chemical Vapor Deposition,” *J. Am. Ceram. Soc.*, vol. 77, no. 12, pp. 3081–3086, 1994.

[17] A. Badran *et al.*, “Automated segmentation of computed tomography images of fiber-reinforced composites by deep learning,” *J. Mater. Res.*, vol. 55, pp. 16273–16289, 2020.

[18] E. Maillet *et al.*, “Combining in-situ synchrotron X-ray microtomography and acoustic emission to characterize damage evolution in ceramic matrix composites,” *J. Eur. Ceram. Soc.*, vol. 39, no. 13, pp. 3546–3556, 2019.

[19] R. S. Hay *et al.*, “Hi-Nicalon-S SiC Fiber Oxidation and Scale Crystallization Kinetics,” *J. Am. Ceram. Soc.*, vol. 94, no. 11, pp. 3983–3991, 2011.

[20] R. S. Hay and R. J. Chater, “Oxidation kinetics strength of Hi-Nicalon ^{TM} -S SiC fiber after oxidation in dry and wet air,” *J. Am. Ceram. Soc.*, vol. 100, no. 9, pp. 4110–4130, Sep. 2017.

[21] R. S. Hay, G. Fair, P. Mogilevsky, and E. Boakye, “Measurement of Fiber Coating Thickness Variation,” in *Fibers , lnterphases and Interfaces*, 2005, pp. 11–18.

[22] G. E. Fair, R. S. Hay, and E. E. Boakye, “Precipitation coating of monazite on woven ceramic fibers: I. feasibility,” *J. Am. Ceram. Soc.*, vol. 90, no. 2, pp. 448–455, 2007.

[23] M. A. Kmetz, “Multilayered Boron Nitride/Silicon Nitride Fiber Coatings,” U.S. Patent 2007/0117484 A1, May 24, 2007.

[24] A. Schneider, G. Hommel, and M. Blettner, “Linear Regression Analysis,” *Dtsch Arztebl Int*, vol. 107, no. 44, pp. 776–782, 2010.

[25] M. R. Begley and J. W. Hutchinson, “Steady-state delamination of bilayers,” in *The mechanics and reliability of films, multilayers and coatings*, Cambridge University Press, 2017, pp. 49–207.

[26] W. Paszkowicz, J. B. Pelka, M. Knapp, T. Szyszko, and S. Podsiadlo, “Lattice parameters and anisotropic thermal expansion of hexagonal boron nitride in the 10-297.5 K temperature range,” *Appl. Phys. A Mater. Sci. Process.*, vol. 75, no. 3, pp. 431–435, 2002.

[27] H. O. Pierson, *HANDBOOK OF CHEMICAL VAPOR DEPOSITION: Principles, Technology and Application*, 2nd ed., no. Cvd. Norwich, New York: William Andrew Publlishing, LLC, 1999.

[28] H. Ichikawa, “Polymer-Derived Ceramic Fibers,” *Annu. Rev. Mater. Res.*, vol. 46, no. 1, pp. 335–356, 2016.

[29] D. J. Denis, *SPSS Data Analysis for Univariate, Bivariate, and Multivariate Statistics*. John Wiley & Sons, Ltd, 2018.

[30] E. W. Thiele, “Relation between Catalytic Activity and Size of Particle,” *Ind. Eng. Chem.*, vol. 31, no. 7, pp. 916–920, 1939.

[31] P. Fenetaud and S. Jacques, “SiC/SiC ceramic matrix composites with BN interphase produced by gas phase routes: An overview,” *Open Ceram.*, vol. 15, no. December 2022, p. 100396, 2023.

[32] M. Wang, L. Jia, H. Xu, A. Li, Y. Peng, and Z. Tang, “Influence of pressure on chemical vapor deposition of boron nitride from BCl3/NH3/H2 gas mixtures,” *Ceram. Int.*, vol. 46, no. 4, pp. 4843–4849, 2020.

[33] V. Cholet and L. Vandenbulcke, “Chemical Vapor Infiltration of Boron Nitride Interphase in Ceramic Fiber Preforms: Discussion of Some Aspects of the Fundamentals of the Isothermal Chemical Vapor Infiltration Process,” *J. Am. Ceram. Soc.*, vol. 76, no. 11, pp. 2846–2858, 1993.

[34] J. M. Zalc, S. C. Reyes, and E. Iglesia, “The effects of diffusion mechanism and void structure on transport rates and tortuosity factors in complex porous structures,” *Chem. Eng. Sci.*, vol. 59, no. 14, pp. 2947–2960, 2004.

[35] J. R. Welty, C. E. Wicks, R. E. Wilson, and G. L. Rorrer, “24.2 The Diffusion Coefficient,” in *Fundamentals of momentum, heat, and mass transfer*, 5th ed., John Wiley & Sons, Inc, 2008, pp. 407–427.

[36] N. Patibandla and K. L. Luthra, “Chemical Vapor Deposition of Boron Nitride,” *J. Electrochem. Soc.*, vol. 139, no. 12, pp. 3558–3565, 1992.

[37] W. Y. Lee, W. J. Lackey, and P. K. Agrawal, “Kinetic Analysis of Chemical Vapor Deposition of Boron Nitride,” *J. Am. Ceram. Soc.*, vol. 74, no. 10, pp. 2642–2648, 1991.

[38] C. F. Berg, “Permeability Description by Characteristic Length, Tortuosity, Constriction and Porosity,” *Transp. Porous Media*, vol. 103, no. 3, pp. 381–400, 2014.

[39] X. Chen and T. D. Papathanasiou, “Micro-scale modeling of axial flow through unidirectional disordered fiber arrays,” *Compos. Sci. Technol.*, vol. 67, no. 7–8, pp. 1286–1293, 2007.

[40] X. Chen and T. D. Papathanasiou, “The transverse permeability of disordered fiber arrays: A statistical correlation in terms of the mean nearest interfiber spacing,” *Transp. Porous Media*, vol. 71, no. 2, pp. 233–251, 2008.

[41] J. Lamon, F. Rebillat, and A. G. Evans, “Microcomposite Test Procedure for Evaluating the Interface Properties of Ceramic Matrix Composites,” *J. Am. Ceram. Soc.*, vol. 78, no. 2, pp. 401–405, 1995.

[42] R. Naslain, “Fibre-matrix interphases and interfaces in ceramic matrix composites processed by CVI,” *Compos. Interfaces*, vol. 1, no. 3, pp. 253–286, 1993.

[43] C. L. Hill, J. W. Reutenauer, K. A. Arpin, S. L. Suib, and A. Michael, “Advanced Ceramic Coatings and Interfaces II,” *Adv. Ceram. Coatings Interfaces II*, pp. 253–264, 2007.

[44] R. J. Kerans, “Life-Limiting behavior and life management of SiC-based composites,” in *Engineered Ceramics: Current Status and Future Prospects, First Edition*, 2016, pp. 160–186.

3.8. Tables and figures

Table I: Reported BN coating thickness ranges in SiC/BN/SiC composites.

Source	Material	Reported coating thickness range
Wing and Halloran (2018) [8]	GE Aviation HiPerComp $[0°/90°]_{2s}$	7000 fiber coating measurements: < 1μm for 63% of fibers, 1–2μm for 16%, 2–3μm for 16%, > 3μm for 5%
Lamon, Rebillat, and Evans (1995) [41]	SiC/BN/SiC microcomposite	0.3 – 0.7 μm
Naslain (1993) [42]	Si-C(O)/BN/SiC composites	0.1 – 2.7 μm
Hill et al (2007) [43]	8H-S CG-Nicalon fabric with CVD BN	0.15 – 0.8 μm
Christensen and Zok (2022) [6]	SiC/BN/SiC minicomposite	0 – 0.6 μm

Table II: Definitions of symbols

$\boldsymbol{A}$	Area of Voronoi cell
$\boldsymbol{C}$	Concentration of reactant
$\boldsymbol{C^0}$	Reference concentration of reactant
$\boldsymbol{D_{eff}}$	Effective diffusion coefficient
$\boldsymbol{D_K}$	Knudsen diffusion coefficient
$\boldsymbol{f}$	Fiber volume fraction
$\boldsymbol{h}$	Coating thickness on individual fiber
$\boldsymbol{\bar{h}}$	Mean coating thickness on individual fiber
$\boldsymbol{h^{max}}$	Maximum coating thickness on individual fiber

$\langle \bar{h} \rangle$	Mean value of $\bar{h}$ for all fibers
$\dot{h}$	Deposition rate
$\dot{h}^o$	Reference deposition rate
$I_{h,r}$	Influence of r on $\bar{h}$
$I_{h,v}$	Influence of v on $\bar{h}$
L	Characteristic preform dimension
M	Molar mass of BCl_3
N_d	Number of fiber-coating debonds
$\bar{N}_d$	Average number of fiber-coating debonds per fiber
N_{ff}	Number of fiber-fiber contacts
$\bar{N}_{ff}$	Average number of fiber-fiber contacts per fiber
N_{fm}	Number of fiber-matrix contacts
$\bar{N}_{fm}$	Average number of fiber-matrix contacts per fiber
r	Minimum distance from fiber centroid to tow boundary
$\bar{r}$	Mean value of r
R^2	Coefficient of determination
R_f	Fiber radius
$\bar{R}_f$	Average fiber radius
R_p	Size of pores
s_h	Standard deviation of coating thickness on individual fiber
$\langle s_h \rangle$	Mean value of s_h for all fibers
$\langle s_{\bar{h}} \rangle$	Standard deviation of $\bar{h}$ for all fibers
s_r	Standard deviation of distance from fiber centroid to tow boundary
s_v	Standard deviation of local fiber volume fraction

$\boldsymbol{S_{h,r}}$	Sensitivity of $\bar{h}$ to r
$\boldsymbol{S_{h,v}}$	Sensitivity of $\bar{h}$ to v
$\boldsymbol{T}$	Temperature
$\boldsymbol{\eta_r}$	Uniformity with respect to distance to tow boundary
$\boldsymbol{\eta_v}$	Uniformity with respect to local fiber volume fraction
$\boldsymbol{\theta}$	Angle
$\boldsymbol{\mu_{h,intra}}$	Intra-fiber thickness variation
$\boldsymbol{\mu_{h,inter}}$	Inter-fiber thickness variation
$\boldsymbol{\mu_r}$	Coefficient of variation of r
$\boldsymbol{\mu_v}$	Coefficient of variation of v
$\boldsymbol{v}$	Local fiber volume fraction
$\boldsymbol{\bar{v}}$	Mean value of v
$\boldsymbol{\rho}$	Molar density of BN
$\boldsymbol{\tau}$	Tortuosity
$\boldsymbol{\phi}$	Porosity
$\boldsymbol{\Gamma}$	Thiele modulus

Table III: Summary of average microstructural characteristics and sensitivity, influence and uniformity parameters.

	Porosity	Mean property & standard deviation			Sensitivity		Influence		Uniformity	
	ϕ	$\langle\bar{h}\rangle$ (μm)	$\bar{r}$ (μm)	$\bar{v}$	$S_{h,r}$	$S_{h,v}$	$I_{h,r}$	$I_{h,v}$	η_r	η_v
A (475 fibers)	0.56	0.91 ± 0.38	54 ± 41	0.44 ± 0.26	-0.04	-0.46	-0.03	-0.27	0.94	0.57
B (430 fibers)	0.92	0.95 ± 0.43	121 ± 94	0.14 ± 0.13	-0.42	-0.17	-0.33	-0.16	0.51	0.73
C (470 fibers)	0.86	0.44 ± 0.17	85 ± 64	0.20 ± 0.17	-0.25	-0.21	-0.19	-0.18	0.69	0.69

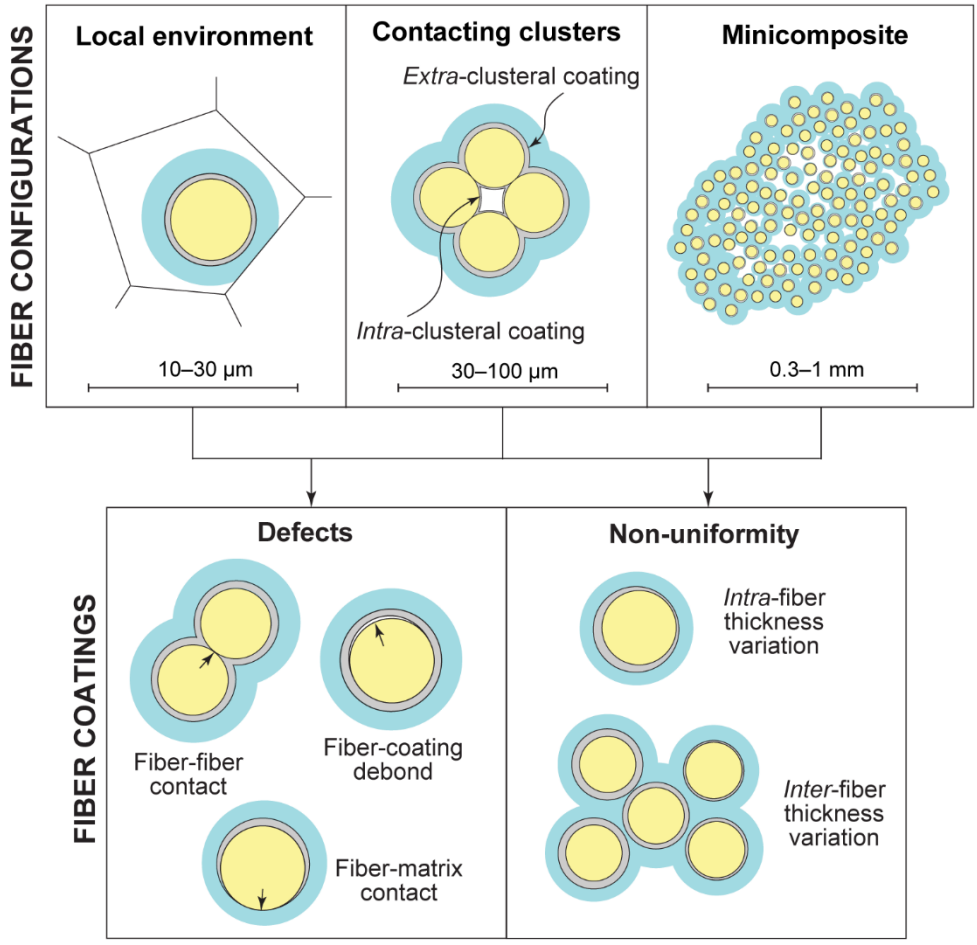

Figure 1: Schematics of typical defects and non-uniformities found in SiC/BN/SiC minicomposites.

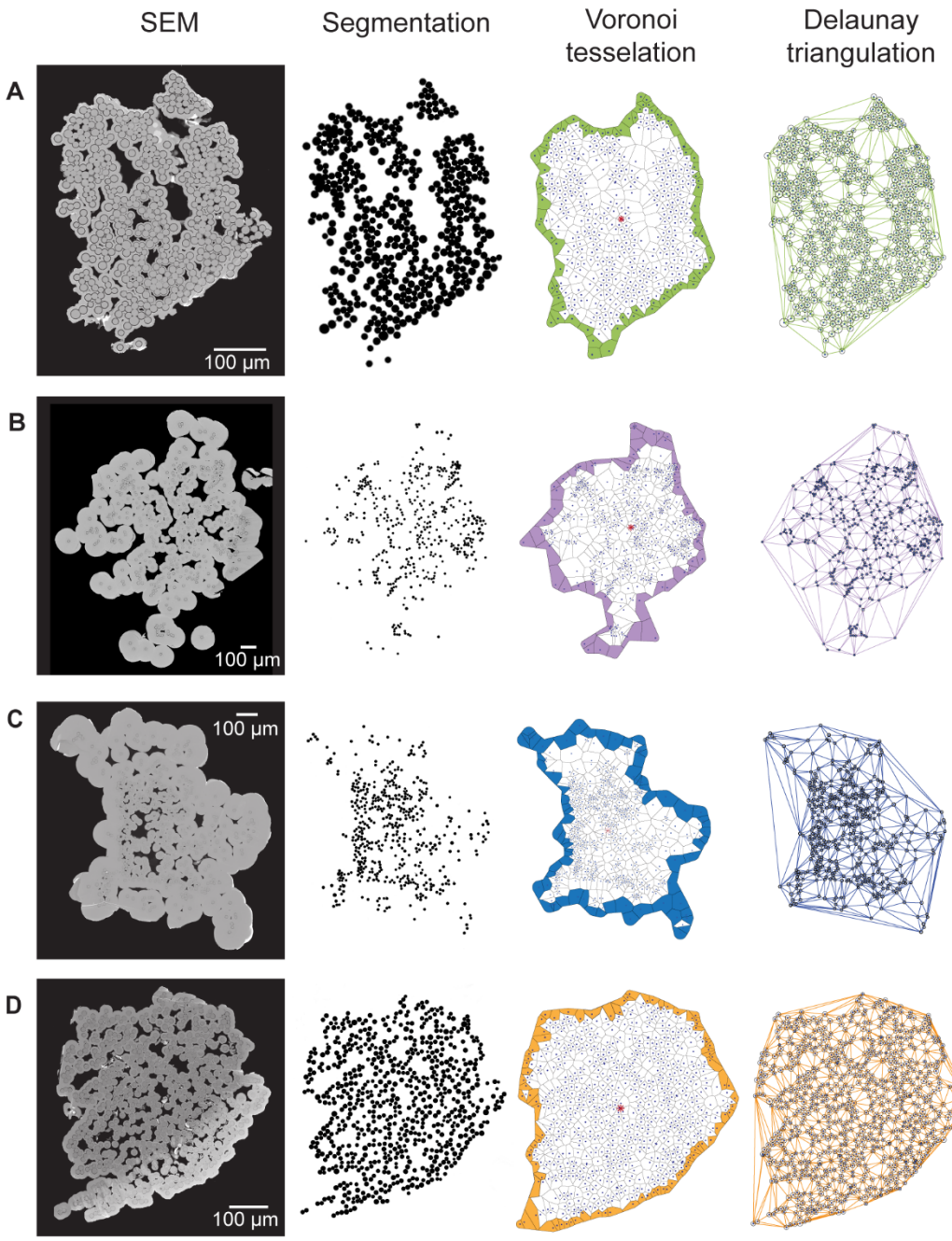

Figure 2: Fiber spatial characteristics are obtained from low magnification SEM and segmented images in combination with Voronoi tessellations and Delaunay triangulations. The shaded Voronoi cells at the tow boundaries are fibers with a local fiber volume fraction and distance to edge equal to 0.

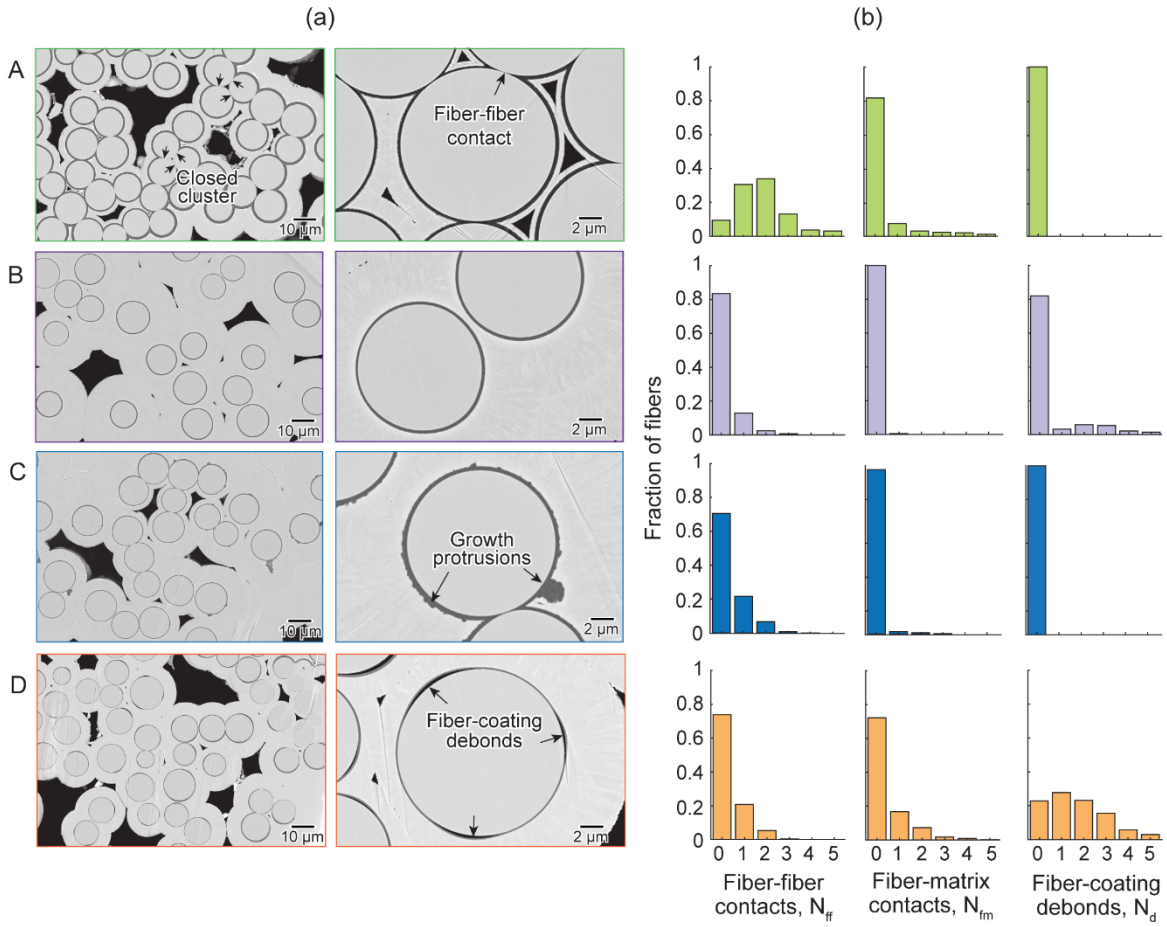

Figure 3: (a) Microstructural features revealed by SEM images at intermediate and high magnifications. (b) Frequencies of defects associated with incomplete coating vary considerably between the four composites. Composite **A** contains the greatest number of fiber-fiber contacts (left column) while **D** contains the greatest number of fiber-coating debonds (right column) and fiber-matrix contacts (center column).

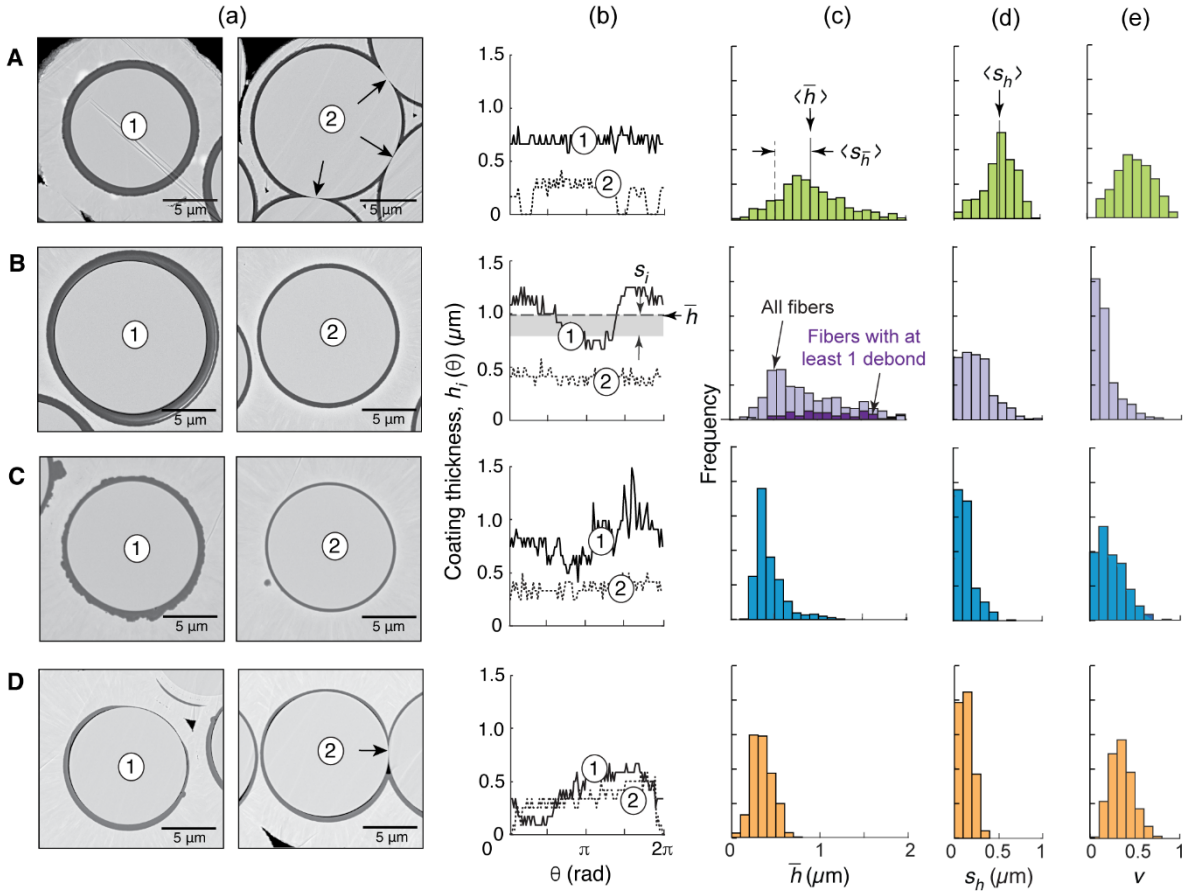

Figure 4: (a) High magnification SEM images showing exemplary coatings. Arrows indicate fiber-fiber contacts. (b) The analysis yields the thickness distribution $h(\theta)$ for each fiber. Distributions of (c) average coating thickness and (d) standard deviation for each fiber are used to calculate intra- and inter-fiber thickness variations. Distribution of debonded coatings in composite **B** is superimposed on the histogram in (c). (e) Distributions of local fiber volume fraction provide measures of the spatial distribution of fibers.

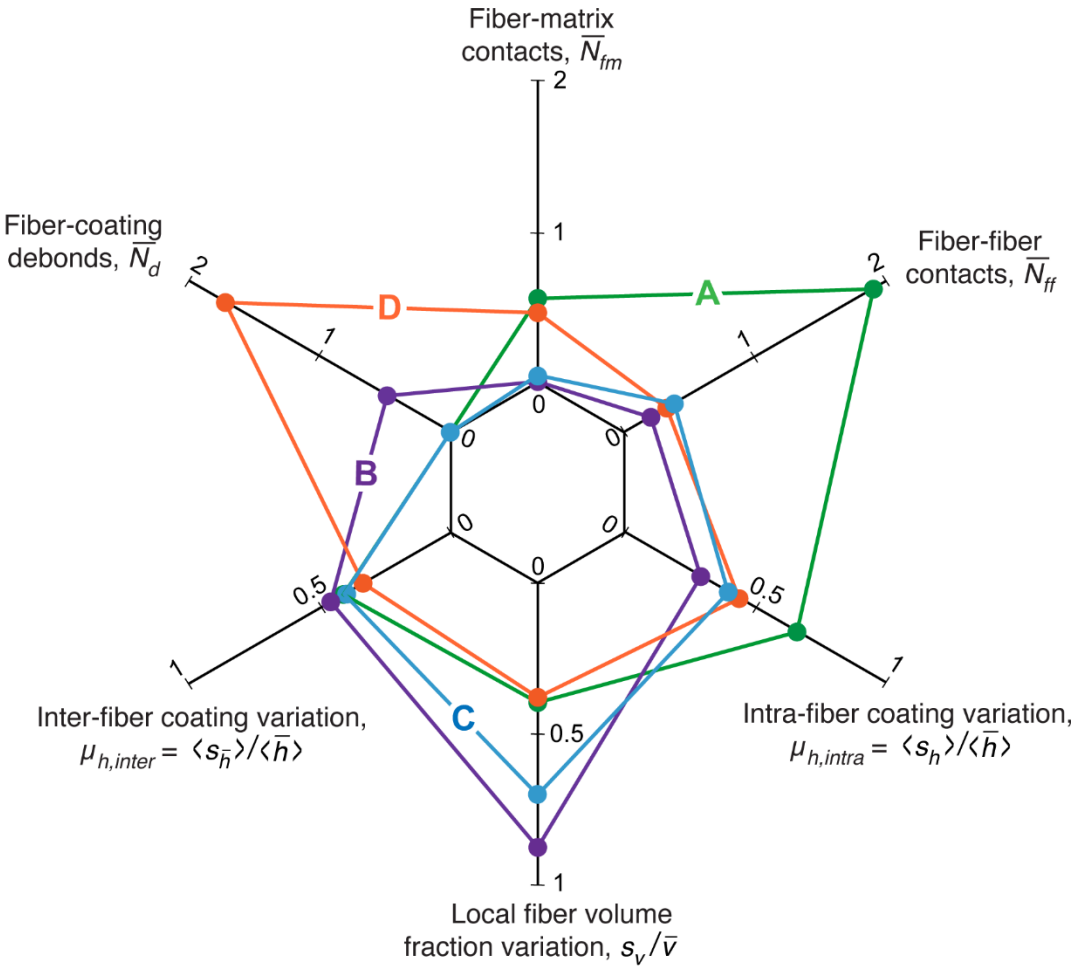

Figure 5: Spider plot summarizing coating defect densities ($\overline{N}_{ff}$, $\overline{N}_{fm}$, $\overline{N}_d$) and microstructure uniformity metrics (μ_v, $\mu_{h,intra}$, $\mu_{h,inter}$) for the four composites. Points for an ideal microstructure would lie on the inner hexagon.

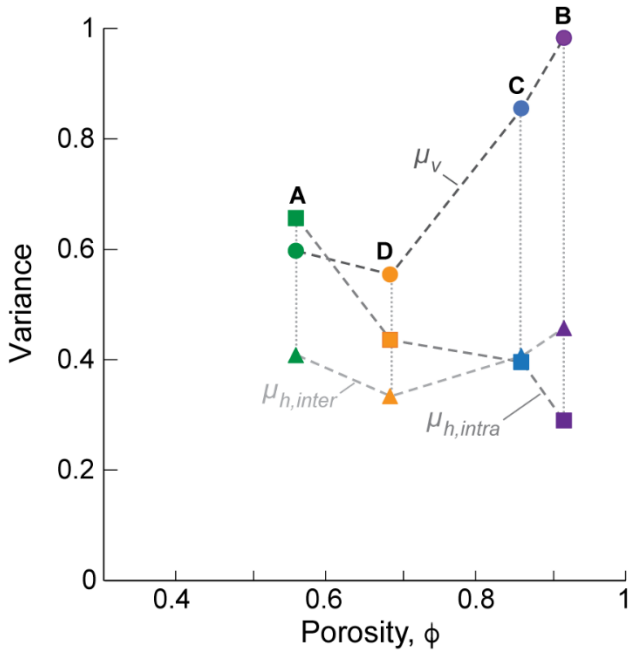

Figure 6: Effects of porosity ϕ on local microstructure variations. The local fiber volume fraction, μ_v, increases with ϕ while the intra-fiber coating thickness variation, $\mu_{h,intra}$ (squares) decreases with ϕ . The inter-fiber coating thickness variation, $\mu_{h,inter}$, is relatively constant.

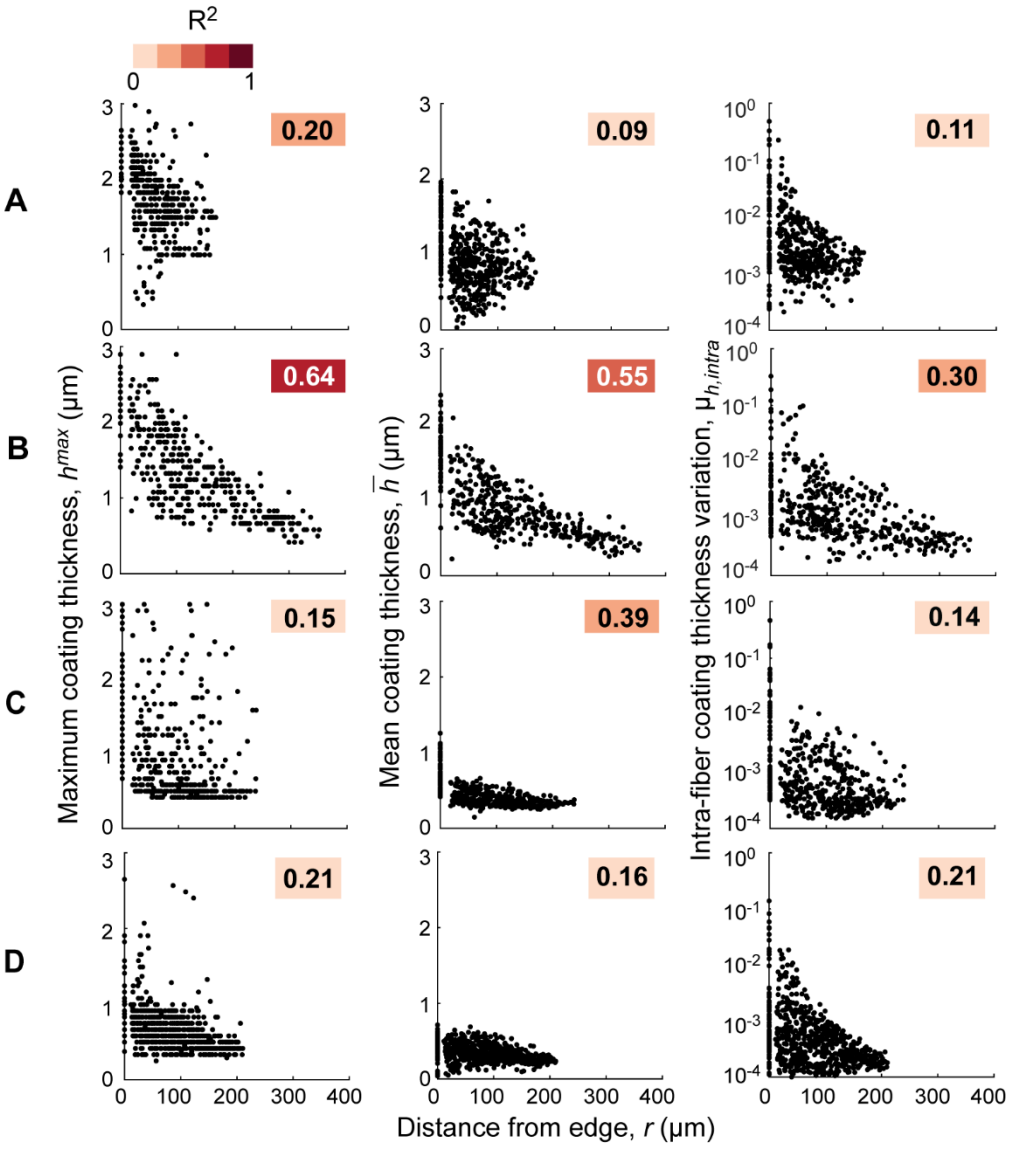

Figure 7: Coating characteristics h^{max}, $\bar{h}$, and $\mu_{h,intra}$ correlate to varying extents with fiber distance from tow boundary. R^2 values from linear regression are displayed in each panel and colored according to strength. Coating thickness and thickness variation in **B** are correlated most strongly with r.

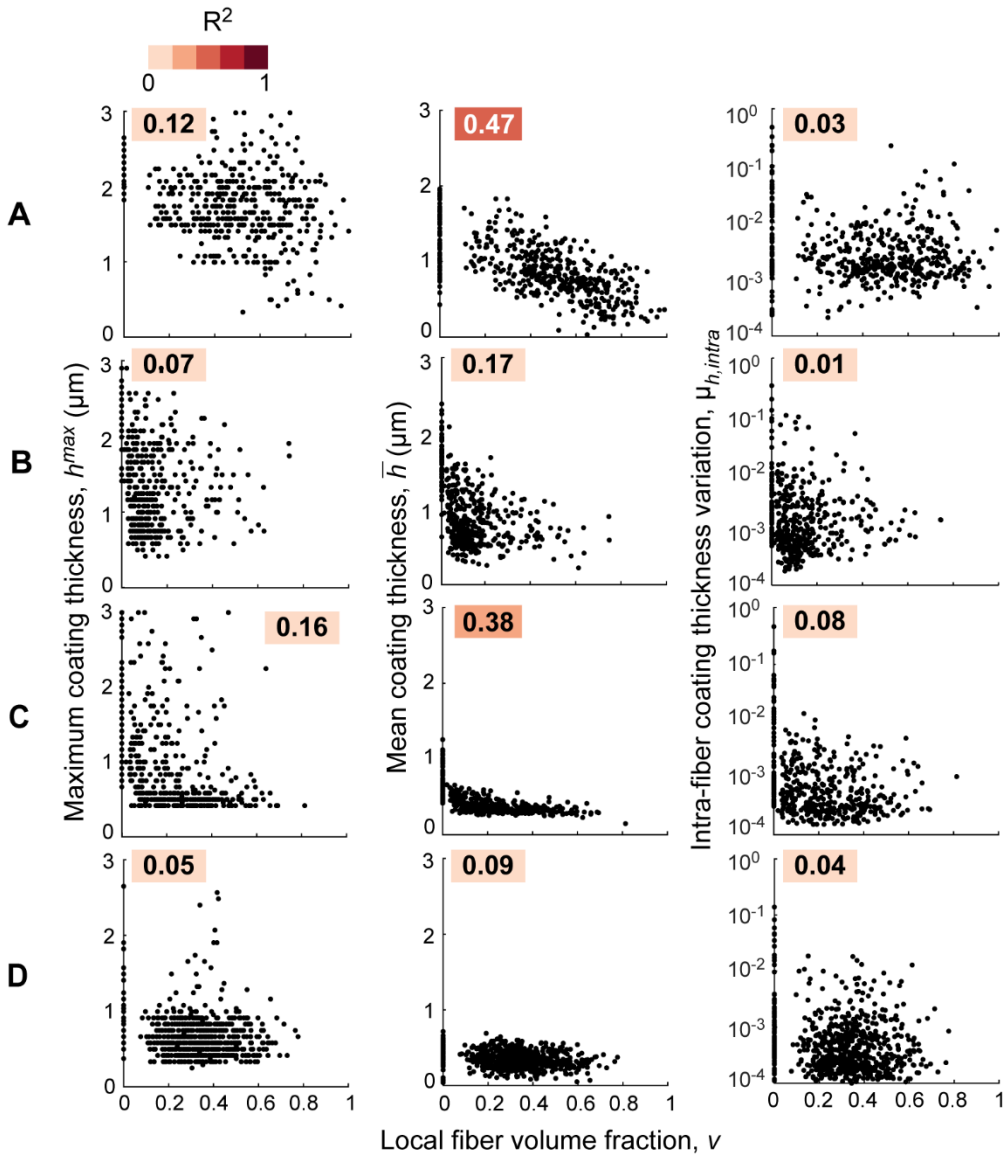

Figure 8: Coating characteristics h^{max}, $\bar{h}$, and $\mu_{h,intra}$ correlate to varying extents with local fiber volume fraction v. R^2 values from linear regression are displayed in each panel and colored according to strength. Mean coating thickness in **A** is most strongly correlated with v.

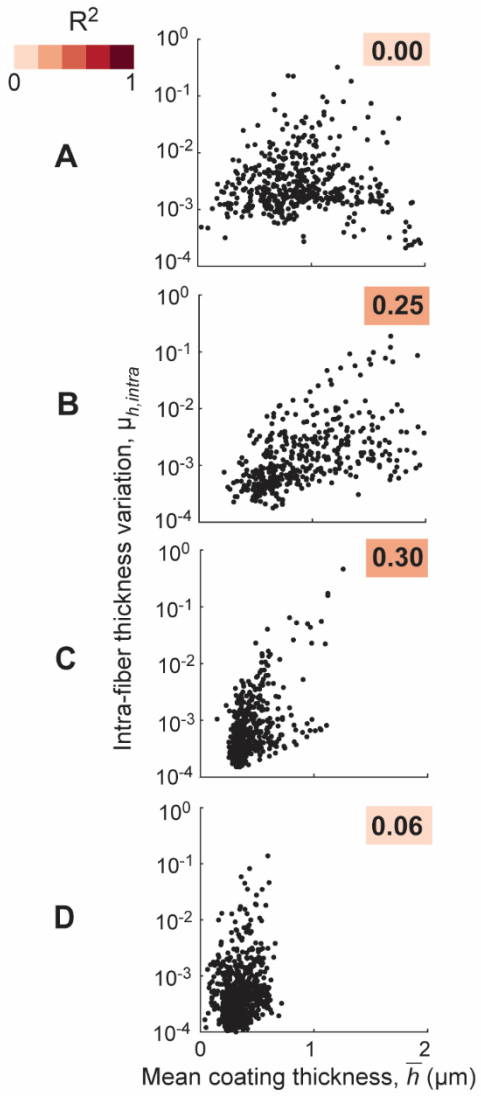

Figure 9: Correlations of $\mu_{h,intra}$ with $\bar{h}$ show that, for composites **B** and **C**, coatings become somewhat more nonuniform as they get thicker.

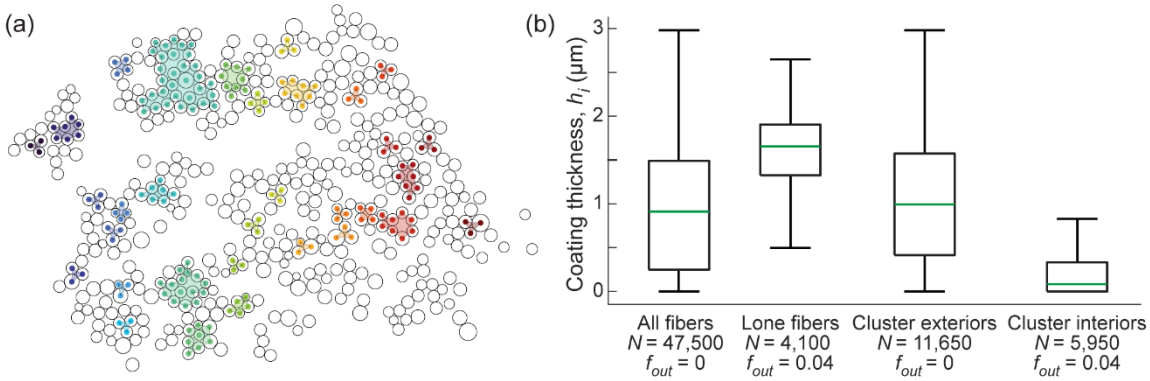

Figure 10: (a) Numerous closed clusters of contacting fibers are evident in composite **A**. Each cluster is indicated by a unique color. (b) Box and whisker plot of coating thickness for all fibers (left) and of thickness sorted by location relative to clusters, showing the detrimental effects of closed clusters on coating deposition. The fraction f_{out} of outliers is less than 5%; thus, for clarity, the outliers are not shown.

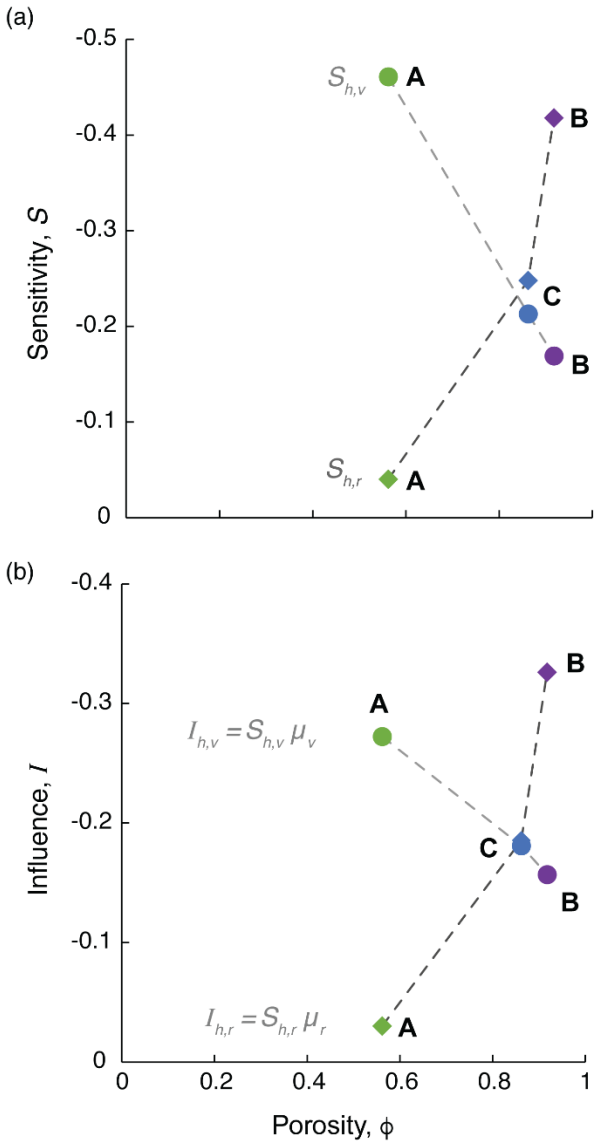

Figure 11: (a) Sensitivities of coating thickness to local fiber volume fraction and to distance from tow boundary trend in opposite directions: the former decreasing and the latter increasing with tow porosity ϕ. (b) Corresponding influence parameters trend similarly to sensitivities.

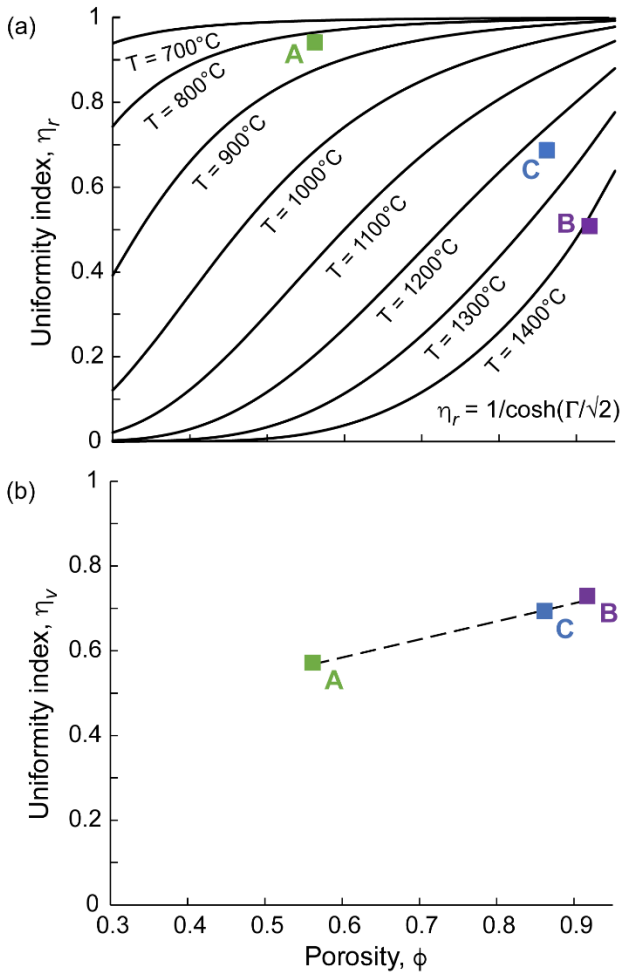

Figure 12: (a) Experimental measurements suggest that the spatial uniformity index η_r decreases with increasing porosity while model predictions from the cylinder model (at constant deposition temperature) follow the opposite trend. The seeming discrepancy is attributable to different deposition temperatures (lowest for **A** and highest for **B**). (b) Uniformity of coating thickness with respect to local fiber volume fraction, η_r, increases with increasing porosity.

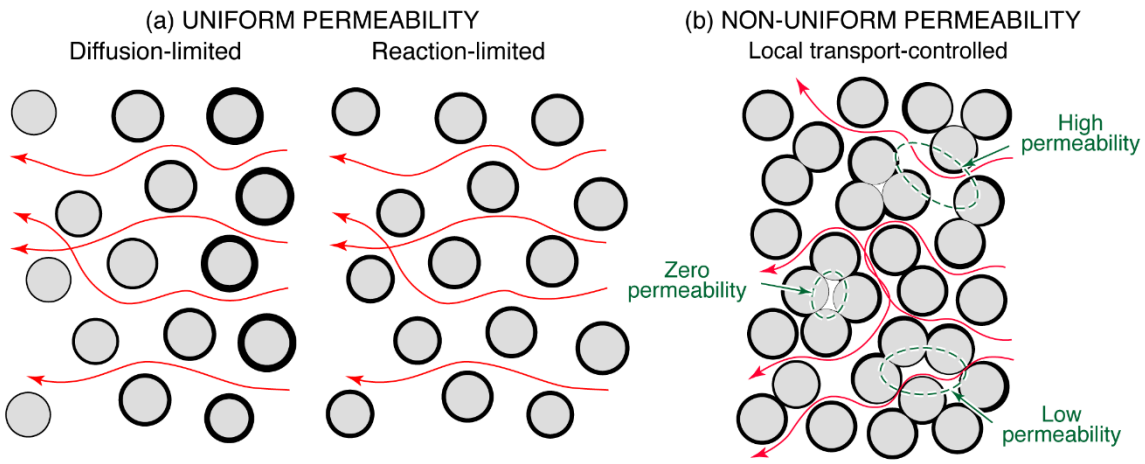

Figure 13: Schematics of behavioral types during CVI into fiber preforms. (a) When permeability is uniform (typically when porosity is high), the Thiele modulus characterizes the balance between reaction rates and diffusion rates. In the diffusion-limited regime, coatings are thickest at the outer boundary and decrease in thickness towards the interior; in the reaction-limited regime, coatings are uniform throughout. (b) In contrast fiber preforms with low porosity generally exhibit non-uniform permeability and thus coating thickness variations are governed to a greater extent by local effects.

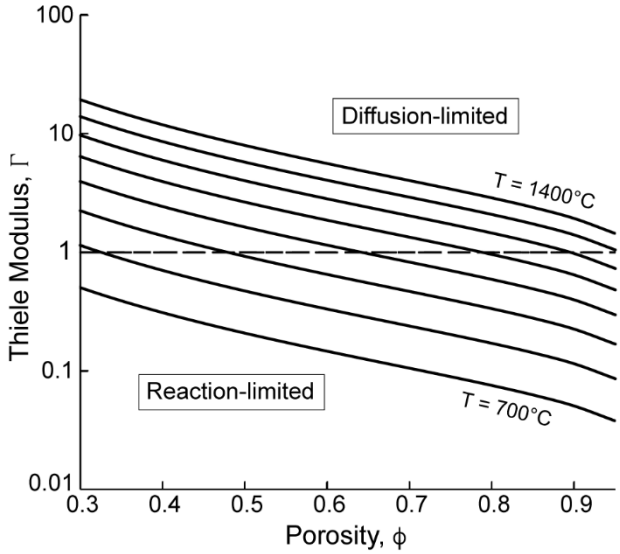

Figure 14: The Thiele modulus decreases with increasing porosity and with decreasing deposition temperature. At low temperatures CVI is reaction-limited and at high temperatures it is diffusion-limited.

Chapter 4[†††]

Insights into Internal Oxidation of SiC/BN/SiC Composites

4.1. Introduction

While a link between oxidation embrittlement of SiC/SiC composites and internal oxidation of BN fiber coatings has been established [1-6], details of the thermochemical processes and the evolution of local constituent compositions and properties within the confined spaces in which these processes occur remain poorly understood. This chapter presents high-fidelity observations of oxidation fronts with the goal of elucidating the event sequence and, in turn, guiding the development of physically-realistic models of composite degradation.

The oxidation process occurs through multiple coupled steps involving mass transport, reaction, and volatilization in the following way:

(i) ***Internal oxidation***: Both BN and SiC oxidize internally in locations where oxidants can gain access, typically through matrix cracks [1, 6]. At moderately high temperatures (500 - 1000°C), the oxidation products, boria and silica, mix to form a low-melting point, low-viscosity borosilicate glass.

(ii) ***Viscous flow***: Each of the two oxidation processes are accompanied by a volume expansion: about 120% in conversion of SiC [7] to amorphous silica and about 60% in conversion of BN to boria (see Appendix for details). The volume expansion combined with the low viscosity [8] and the confined space

[†††] The content of this chapter has previously appeared in the Journal of the American Ceramic Society (Christensen, V.L., Zok, F.W., "Insights into Internal Oxidation of SiC/BN/SiC Composites," *J. Am. Ceram. Soc.*, 106 [2] 1561-1575). It is reproduced here with the permission of John Wiley and Sons.

within which oxidation occurs lead to viscous flow of the evolving oxides into adjacent available space.

(iii) ***Volatilization***: Concurrently, boria volatilizes either directly from the free surface as a boron oxide vapor or after reaction with water as a borohydroxide vapor [9]. The volatilization rate depends on the equilibrium concentrations of the gaseous species, the details of egress pathways, and the flow conditions at the external boundaries [9, 10]. Generally, because of the low partial pressures of borohydroxide gases relative to those of the oxidants, the oxidant concentrations at the reaction site remain essentially constant and uniform throughout; the rate of the process is usually controlled by transport of the product gases *away* from the reaction site [10].

(iv) ***Composition evolution***: Volatilization leads to depletion of boria at the reaction site and subsequent diffusion of boria from distal regions towards the free surfaces. If the volatilization rate exceeds the rate at which boria is replenished, the oxide becomes silica-rich; its viscosity then increases, thereby retarding further flow.

(v) ***Recession cessation***: At sufficiently long times, the silica scales on the fibers and the matrix impinge on one another. If impingement occurs uniformly around the fiber circumference, further transport of oxidants to the reaction zone is significantly retarded, possibly to the point where recession appears to have ceased altogether. While the cessation of further recession is desirable, it comes at the expense of creation of strong bonds between the fibers and the matrix which, in turn, produce high stress elevations in the fibers during

subsequent unloading/reloading or thermal cycling [12]. The composite strength and toughness may then be severely compromised [6, 12].

Together, the physical manifestations of these processes – including formation and mixing of boria and silica, oxide flow associated with constrained expansion, diffusion of various species through the oxides and the narrow channels produced by matrix cracks, and boria volatilization – are exceedingly difficult to predict a priori. Such predictions would require many material and system properties that would not be feasible to measure directly. They would also need to account for large local geometry changes due to movement of phase boundaries caused by oxidation. A more practical approach would be to start with direct observations of the microstructural changes accompanying oxidation and to then infer both the event sequence and the important mechanistic elements needed to develop realistic models.

The standard model that has been used (either explicitly or tacitly) [8–10, 13] in analyzing the internal oxidation processes is illustrated in Figure 1. Here the BN coating is assumed to oxidize at the interface between the BN and the oxidant gases to produce boria as well as N_2 and NO_x gases. The boria in turn reacts with water vapor to produce borohydroxide gases and the gases are then transported away from the reaction site via diffusion through the resulting channels between fibers and matrix and through matrix cracks. Details of the processes at the reaction site are unknown; existing models assume a prescribed (constant) value for the boria activity which, when combined with the gas composition and temperature, sets the equilibrium concentrations of the borohydroxide gases. Adjacent to the reaction site, the exposed SiC matrix and fibers ostensibly oxidize to form a passivating silica scale, as they would if exposed to the same oxidizing environment

on their own. As the BN is progressively consumed at the reaction site and the recession front advances, new (fresh) SiC surfaces are exposed to the oxidants. Since the duration of direct exposure of these surfaces to oxidant gases is shortest at the reaction site, the silica scale thickness at the reaction site is expected to be lowest and increase with distance away from this site (towards the matrix crack location). Impingement of the oxide scales (when it occurs) is expected nearest the matrix crack plane, where the fibers and the matrix have been exposed the longest.

Critically assessing the assumptions underpinning the standard model by direct observation is challenging. Transmission electron microscopy (TEM) yields the highest resolution but is restricted to small specimens and small viewing areas (typically tens of μm). Moreover, preparing TEM foils is hampered by the presence of open gaps between the composite constituents after oxidation, rendering the material in the regions of most interest highly friable. Although the image resolution that can be attained with scanning electron microscopy (SEM) is somewhat lower, SEM has the advantage of enabling observations of larger areas. But even here preparing surfaces suitable for examination is difficult because the layers of interest are very thin, the constituent materials have disparate mechanical polishing characteristics, and gaps between phases are common. To address these issues, a method based on ion mill sectioning/polishing is employed in the current study to produce high-quality surfaces that are amenable to high magnification imaging in an SEM. When combined with oxidation experiments, they yield observations of the oxidation processes with arguably unprecedented fidelity.

The chapter is organized in the following way. The nature of the materials and the methods employed for sample preparation, oxidation and examination are described in

Section 4.2. Microstructural observations from two sample types – one unbroken and another broken in a tensile test – are detailed in Sections 4.3 and 4.4, respectively. A discussion follows, in Section 4.5, with emphasis on an assessment of existing models with respect to experimental observations and the implications of coating oxidation and volatilization on mechanical response.

4.2. Materials and methods

The current work is on unidirectional minicomposites, each consisting of 800 Tyranno ZMI SiC fibers. The fibers had been coated with a thin layer of BN and a thicker jacket of SiC, both by chemical vapor deposition (CVD). The coating thickness, h, typically ranged from 0.1 to 0.5 μm, although regions where fibers had been in contact with one another were devoid of BN. Coatings were also commonly debonded from the fibers along a fraction of the fiber circumference. Examples of such debonds are shown in secondary-electron SEM images in Figure 2. The bright edges on the fiber and the coating signify debonds. Figure 3 shows EDS maps of pristine fibers in both transverse and longitudinal sections. The low B signal reflects the difficulty in detecting light elements by EDS; the stronger N signal serves as a more reliable indicator of the presence of BN. Oxygen was detected in both the ZMI fibers (reported to contain 9 wt% O [15]) and the BN coatings.

Two types of test specimens were employed in the oxidation study. The first was an unbroken composite specimen with a polished transverse cross-section. The fibers on the polished section were examined in an SEM (Thermofisher Apreo C) both before and after oxidation. The phase distributions were obtained from both secondary (SEI) and backscatter electron imaging (BEI) modes as well as EDS maps. The same specimen was then sectioned longitudinally and re-examined in the SEM. In this case, the observations are expected to be

representative of those obtained in minicomposites in which the matrix crack opening displacements are large enough to allow unimpeded transport of the gaseous reaction products to the external environment.

The second test specimen was first broken in a tensile test. One of the broken halves was examined in the SEM and subsequently sectioned longitudinally to examine the matrix cracks and the BN coating debonds near the matrix cracks. The other half was oxidized, sectioned longitudinally, and examined in the SEM. As we infer from subsequent observations, the crack openings in this specimen were sufficiently small to restrict gas flow in and out of the composite and hence retard the rate of volatilization. All sections were created entirely via broad beam ion milling (Leica TIC3x).

All oxidation experiments were performed in a quartz tube furnace at 1000ºC for 12 h in flowing, dry air (Airgas) with a velocity of 4 cm/s in the hot zone. The water content in the furnace exhaust, measured using a humidity sensor (Shaw Meters AcuDew-MP), was about 10 ppm. Specimens of 1 cm length were placed in the furnace so that air flow was parallel to the specimen length.

4.3. Oxidation of unbroken composite

4.3.1 Transverse section

Several distinct features on the transverse section of the unbroken, oxidized composite specimen are illustrated in low and high magnification SEM images in Figs. 4 and 5, respectively:

(i) In locations where the coatings had been thick ($h \approx 0.2–0.5$ μm), the BN was entirely lost, leaving nearly-imperceptibly-thin oxide scales on the fibers and the

matrix and narrow open gaps in the regions previously occupied by BN (Figs. 4B, 5A-D). Thick coatings and hence interface gaps are more prevalent towards the outer edges of the composite.

(ii) In locations where the coatings had been particularly thin ($h < 0.2$ μm), the BN was replaced by an oxide scale that completely filled the resulting gaps (Figs. 4C, 5E-F). Thin coatings are more prevalent in the composite interior where, presumably, the CVD precursor gases had been unable to gain ready access during the coating process.

(iii) In some instances, collections of spherical glass beads were seen in the interface regions. These beads had formed in subsurface regions and had subsequently been extruded out to the free surface, because of the oxidation-induced expansion. The shapes of the beads strongly suggest that the glass viscosity had been very low at the time the glass was extruded out of the gaps.

(iv) Finally, in locations where the coating thickness had been non-uniform around individual fibers – less than 0.2 μm in some regions and greater than 0.2 μm in others – both open gaps and oxide beads were seen at various points around the fiber circumference after oxidation.

Among about 580 fibers examined on the oxidized surface, the vast majority (>95%) had gaps present around most or all of the fiber circumference after oxidation. The remainder did not show evidence of remnant BN or an open gap. While thin glass scales could be identified in some of the latter cases, confirmation of the presence of glass in many cases was challenging because of the low atomic number contrast between SiC and SiO_2 in the BSE images and the thinness of the regions of interest.

4.3.2 Longitudinal section

Backscatter SEM images and accompanying schematic renditions (in Figures 6A,C) along with EDS maps of the same regions (Figures 6B,D) in a longitudinal section through the unbroken, oxidized specimen reveal three distinct regions below the exposed surface:

(i) Over a distance of about 10–20 μm beneath the surface, BN is absent, oxide scale covers the newly-exposed fiber and matrix surfaces, and a gap is present between the oxide scales. The scale thickness near the exposed surface is about 0.1–0.15 μm. It then *increases* with depth, to about 0.4 μm at the end of the BN-depleted region. At this point the two oxide scales have merged over a short distance; presumably recession had locally nearly ceased.

(ii) Further down, over a distance of another 10-20 μm, oxide scales are evident on both the fiber and the matrix surfaces. Between these scales is a wedge-shaped layer of BN with pores and microcracks that thins to a chisel point near the start of the recession zone. Evidently oxygen is transported axially through these regions (over distances of about 10 μm) to the SiC upstream from the reaction front more rapidly than it is laterally through the oxide scales on the fibers (over distances of about 0.1 μm). This difference indicates that the permeability of the former is much higher than that of the latter. The spatial extent of the oxide in these regions is consistently greater along the coating-fiber interface than along the matrix-coating interface. The lengths of remnant BN adjacent to the oxide scales (measured on four fibers) range from 4 to 14 μm along the matrix-coating interface and from 10 μm to over 80 μm along the fiber-coating interface (exceeding the field of view in the latter case). This difference is attributable to

the pre-existing fiber-coating debond cracks which serve as fast pathways for oxidant ingress. Similar features have been observed in other SiC/SiC composites [6, 15, 17].

(iii) Even further down, the BN coatings appear unaffected. One implication is that the SiC fibers and matrix do not getter the oxygen within the BN at the temperature and over the time scale of the current experiment. For reference, the equilibrium activity of oxygen in the presence of SiC and SiO_2 at this temperature is a mere 10^{-27}.

Higher magnification images of two other regions close to the external surface (in Figure 7) reveal greater detail of the phases present as well as some variations in phase topology. In the first (Figs. 7A-C), BN near the start of the recession gap exhibits very small (sub-μm) microcracks as well as a single larger (3–4 μm) microcrack between the BN and the adjacent oxide scale. It also shows a 2–3 μm long continuous segment of oxide scale that, if continuous around the fiber circumference, had presumably sealed the material beneath it. In the second (Figs. 7D-F), sub-μm microcracks and fine pores in the BN extend over a greater length (10–15 μm) in the transition zone between the recession gap and the pristine BN below. Here complete closure appears imminent.

4.4. Oxidation of broken composite

4.4.1 Pre-oxidation observations

The fracture surface of the broken (not oxidized) composite specimen exhibits extensive fiber pull-out, indicative of coating debonding and sliding (Figure 8A). Debonding is also evident in the longitudinal section of this specimen in regions adjacent to matrix cracks

(Figs. 8C, D). Debonding usually occurs at the fiber-coating interface (not at the matrix-coating interface), consistent with the pre-existing partial debonds seen along the same interfaces. Matrix cracks with varying crack opening displacements (from 1 to 7 μm) are evident on the composite exterior (Fig. 8B).

4.4.2 Post-oxidation observations

Although both recession gaps and internal oxide scales are present in the broken, oxidized specimen, the frequency and locations of these features differ from those beneath the surface of the unbroken, oxidized specimen. Among 30 fibers examined across several matrix cracks in the broken, oxidized composite, 90% exhibit an oxide scale that completely seals the region between fiber and matrix (seemingly without recession) while only 10% exhibit recession gaps.

Examples of oxide scale sealing on either side of an individual fiber are shown in Figure 9. On the left side (Figures 9A-C), where the BN coating had been about 0.1 μm thick, the oxide is present in small (sub-μm) beads at the two edges of the matrix crack, reminiscent of the glass beads on the surface of the unbroken, oxidized specimen. Additionally, short wedge-shaped oxide scales are present along the fiber/coating and coating/matrix interfaces to a depth of only about 2 μm. On the right side of the same fiber in the same crack plane (Figures 9D-F), where the BN coating had been thicker (0.2 μm), the oxide bead completely fills the gap between the two matrix cracks (about 4 μm) at the fiber location. Here the oxide scales penetrate deeper along the BN/SiC interfaces (6-8 μm). In both cases remnant BN coating is seen between the oxide scales on the fibers and the matrix almost up to the matrix crack. The relatively large quantity of oxide within the crack and its shape is again attributable to oxidation-induced expansion of both BN and SiC

coupled with a low glass viscosity. Apart from a few fine microcracks and pores within the affected BN, there is no evidence of a recession gap.

The few recession gaps that were seen here were almost exclusively present either near the outer edges of the composite (within about 20 μm, Figures 10A-C) or near a large internal pore that had extended up to the fracture surface and had therefore been connected to the environment (Figure 10D-F). The recession lengths in these cases are 10-20 μm, comparable to those seen in the longitudinal section of the unbroken, oxidized specimen.

4.5. Analysis and discussion

4.5.1 Phenomenological model of coating recession and gap closure

The collection of observations of both the unbroken and the broken specimens after oxidation suggest a common pattern of behaviors, illustrated in Figure 11 and described below. Distinctions in behaviors can be made on the basis of the *boundary conditions* and the *time and length scales* associated with the oxidation processes and with volatilization and removal of B-containing gases.

Locally, the rate of internal oxidation is controlled by the thickness of the intervening oxide and the rate of diffusive transport of oxygen through that oxide. (With an oxygen partial pressure of 0.2 atm and only trace amounts of product gases generated through the chemical reactions, the oxygen concentration remains essentially constant throughout.) In turn, diffusive transport is governed by the permeability of the oxide, which depends sensitively on the boria/silica ratio. Schlichting reported an increase in the oxygen diffusion coefficient of two orders of magnitude when the boria content was increased from 1% to 30% in a B_2O_3/SiO_2 glass [18]. Subsequent volatilization and removal of B-containing gases

is controlled by a combination of (i) the equilibrium partial pressures of the gases at the prevailing temperature, gas composition and boria activity, and (ii) the rate of outward diffusion of gases to the external environment, governed by external boundary conditions and by internal geometry (i.e. the distance from reaction site to environment, the width of channels for gas transport, and diffusivities of gases within those channels). The importance of boundary conditions is evidenced by the differences found between the unbroken, oxidized specimen and the broken, oxidized specimen in the current study. Notably, in the unbroken, oxidized specimen, the diffusion distance involved in the gas transport processes is simply the length of the recession zone: typically <10–20 μm at the end of oxidation in the present experiments. In contrast, in the broken specimen, transport occurs not only through the recession gaps but also through matrix cracks over distances ranging from tens of μm (near the free surface or near large pores that are connected to the environment) to hundreds of μm (for fibers near the composite center).

The schematics in Figure 11 illustrate several possible scenarios of coating recession and gap closure for varying coating thickness and rate of volatilization. When the coatings are thin and volatilization is slow, only a small amount of BN needs to be consumed before the gaps for gas transport are sealed and the process effectively ceases. For somewhat thicker coatings, the amounts of BN removed and oxide produced are greater and the time required to seal the recession gap is greater. These behaviors are representative of most fibers in the broken oxidized specimen in the current experiments. As the coating thickness and volatilization rate increase further, the gaps produced by volatilization require longer times for sealing and hence the recession zones are longer. This behavior is obtained around most fibers in the unbroken, oxidized specimen. In the extreme where the coatings are very

thick and volatilization is rapid, BN is removed without significantly affecting the oxidation rate of newly-exposed matrix and fiber surfaces. This scenario yields the standard model of recession illustrated in Figure 1 and described in the Introduction. Importantly, among a spectrum of behaviors that can be obtained in practice, the standard model only represents one extreme.

4.5.2 Gap closure

Closure of the gaps produced by boria volatilization adjacent to the polished composite surface can be described in terms of: (i) the oxidation kinetics of constituent fibers and matrix, both assumed to follow parabolic growth [19]; and (ii) the molar volume ratios, γ, of oxide products and corresponding consumed materials. Assuming that the time needed to remove the boria *at* the free surface is short relative to the duration of the experiment and that the fibers and the matrix oxidize at the same rate, the evolution of gap width Δ with time t at the free surface is given by

$$\Delta(t) = h - \left[\left(\frac{\gamma_m - 1}{\gamma_m}\right) + \left(\frac{\gamma_f - 1}{\gamma_\mathrm{f}}\right)\right]\sqrt{Bt} \qquad (1)$$

where h is the initial gap width (equivalent to the coating thickness), γ_m is the molar volume ratio of SiO_2 and SiC (2.2), γ_f is the molar volume ratio of SiO_2 and fiber (1.4) (see Appendix), and B is the parabolic rate constant for SiC oxidation (3.5×10^{-3} $\mu m^2/h$ for dry air at 1000°C [20]). In turn, the critical coating thickness h_c below which the gap is expected to be sealed by oxide ($\Delta = 0$) after exposure for a time t is

$$h_c = \left[\left(\frac{\gamma_m - 1}{\gamma_m}\right) + \left(\frac{\gamma_f - 1}{\gamma_\mathrm{f}}\right)\right]\sqrt{Bt} \approx 0.5\sqrt{Bt} \qquad (2)$$

Alternatively, the critical time t_c needed for gap closure is:

$$t_c = \frac{h^2}{B\left[\left(\frac{\gamma_m - 1}{\gamma_m}\right) + \left(\frac{\gamma_f - 1}{\gamma_f}\right)\right]^2} \approx \frac{4h^2}{B} \quad (3)$$

For a 12h exposure at 1000°C in dry air, the predicted critical coating thickness in composites with SiC matrices and Tyranno ZMI fibers is $h_c = 0.17\ \mu m$: comparable to, though slightly lower than, that inferred from the current experiments ($h_c \approx 0.2\ \mu m$). The difference is attributed to accelerated SiC oxidation caused by the presence of boria.

As noted previously, in the standard model (Figure 1), the scale thickness is expected to decrease with depth beneath the surface, a consequence of the shorter times available for oxidation. The experimental results, in contrast, show that oxide scale thickness *increases* with depth and that closure occurs at the base of the recession zone (10-20 μm deep), not at the free surface. The thicker sub-surface oxide scale is likely caused by two effects. First, the time needed to volatilize boria produced in the sub-surface regions is greater than that at the free surface, because of the greater diffusion lengths for the reaction product gases. As a result, boria persists for a longer time and, during that time, accelerates the rate of SiC oxidation. Second, volumetric expansion of the oxide formed at even greater depths – ahead of the recession front, where there is essentially *no* space to accommodate expansion – leads to the outward extrusion of the oxide into the recession zone and thus a thickening of the oxide scale.

The near-absence of recession gaps in the broken oxidized specimen is attributed to a combination of (i) the low rate of dissipation of the reaction product gases away from the reaction site and (ii) essentially fixed oxygen concentration that drives the oxidation process. In contrast to the unbroken, oxidized specimen – where the environment directly above the external surface serves as an infinite sink for the product gases – the gases produced in the

broken specimen must diffuse comparatively long distances through narrow matrix cracks to reach the external environment (typically hundreds of μm). Furthermore, the concentration gradient driving the diffusion process is reduced by the concurrent influx of gases produced at all other fibers intersecting the matrix crack and the collective outward flow of the gases through the same crack. When the influx of these gases into the matrix crack is sufficiently large, gradients in gas concentrations within the matrix crack become vanishingly small and thus the gas concentrations approach their equilibrium values everywhere, effectively arresting both the diffusion process and further volatilization. Despite the cessation of recession, both the SiC and the BN exposed by the matrix crack continue oxidizing, thereby filling the matrix cracks around the fibers and the interface gaps produced earlier by BN volatilization.

4.5.3 Recession length

Beneath a free surface at which an infinite sink for reaction gases is present, the growth of the recession zone is controlled by diffusion of the reaction product gases from the reaction site to the free surface through a gap with progressively-decreasing width. The variation in recession length, L_R, with time, t, is derived from Fick's first law of diffusion [10]:

$$\frac{\partial L_R(t)}{\partial t} = \frac{V_{BN}\bar{m}D_c(t)[C^* - C(t)]}{L_R(t)} \tag{4}$$

where V_{BN} is the molar volume of BN (1.18 x 10^{13} μm^3/mol); $\bar{m}$ is a unitless mass balance term[‡‡‡]; C^* is the equilibrium concentration of gas species at the base of the recession channel; $C(t)$ is the concentration of gas reaction products at the top of the free surface

[‡‡‡] $\bar{m}$ =1 when one mole of BN is consumed in forming one mole of HBO_2(g), $\bar{m}$ =2 when two moles of BN are consumed in forming one mole of B_2O_3(g), and $\bar{m}$ is a weighted average when both HBO_2(g) and B_2O_3(g) are present.

(assumed to be 0); and $D_c(t)$ is the effective diffusivity in the recession gap. In turn $D_c(t)$ is given by a series approximation of the Knudsen, $D_K(t)$, and molecular, D_m, diffusivities, notably [10]:

$$\frac{1}{D_C(t)} = \frac{1}{D_m} + \frac{1}{D_K(t)} \tag{5}$$

D_m is given by the Chapman-Enskog equation:

$$D_m = 1.86x10^{-3} \frac{T^{\frac{3}{2}}}{P\sigma_{air-HBO2}^2 \Omega} \sqrt{\frac{1}{M_{air}} + \frac{1}{M_{HBO2}}} \tag{6}$$

where P is total pressure (1 atm), $\sigma_{air-HBO2}$ is the average collision diameter of air (σ_{air}= 3.7Å) [21] and HBO_2 (σ_{HBO2}= 4.8Å)[10], Ω is the temperature-dependent collision integral (0.4 at 1000°C), M is molecular weight (g/mol), and D_m has units of cm^2/s. $D_k(t)$ depends on the minimum value of $\Delta(t)$ along the recession channel:

$$D_k(t) = \frac{2}{3}\sqrt{\frac{8RT}{\pi M_A}}\Delta(t) \tag{7}$$

where M_A is the weighted average of the molecular weights of the gas products exiting the gap.

For the conditions of interest, D_m = 9.7 x 10^{11} $\mu m^2/h$; for relevant coating thicknesses (from 0.1-0.5 μm), $D_k(t) \ll D_m$, and thus $D_c(t) \approx D_k(t)$. Combining this approximation with Eq. (4) yields the differential equation:

$$\frac{\partial L_R(t)}{\partial t} = \frac{2V_{BN}\overline{m}C^*}{3L_R(t)}\sqrt{\frac{8RT}{\pi M_A}}\left\{h - \left[\left(\frac{\gamma_m - 1}{\gamma_m}\right) + \left(\frac{\gamma_f - 1}{\gamma_f}\right)\right]\sqrt{Bt}\right\} \tag{8}$$

The solution to this equation (obtained using Mathematica) is:

$$L_R(t) = 0.82\sqrt{2tV_{BN}\bar{m}C^*\sqrt{\frac{8RT}{\pi M_A}}\left\{h - \frac{2}{3}\left[\left(\frac{\gamma_m - 1}{\gamma_m}\right) + \left(\frac{\gamma_f - 1}{\gamma_f}\right)\right]\sqrt{Bt}\right\}} \quad (9)$$

With this solution in hand, the remaining parameter to be determined is the equilibrium partial pressure of all gases produced during boria volatilization. In addition to boria gas itself, several borohydroxide species, including HBO_2(g), H_3BO_3(g) and $H_3B_3O_6$, may form. The partial pressures of these gases were calculated using FactSage software (FactSage version 8.0 with FactPS database). The test conditions were: 1000°C, 1 atm total pressure, O_2 activity of 0.2, water vapor partial pressure of 10^{-5} atm, and boria activity, a_{B2O3}, of either 1 or 0.25. The latter values are estimates of the upper and lower bounds: the lower value being the equilibrium mole fraction of boria in borosilicate glass at 1000°C and the higher value being that for pure boria [22]. N_2 was set to balance the remaining atmosphere. The results are plotted in Fig. 12A. In the domain of interest, HBO_2(g) is the dominant species while B_2O_3(g) is second. C^* was calculated using the sum of the two partial pressures, $P = P_{B2O3} + P_{HBO2}$, via $C^* = P/RT$.

The variation in predicted recession length with coating thickness and boria activity for a 12h exposure at 1000°C is shown in Fig. 12B. Experimentally measured values of recession length are also plotted for comparison. Recession lengths were measured from the polished surface to either the base of the open gap or to the start of intact BN. (The two values differ by only a small amount.) Evidently the current model overpredicts recession lengths by a significant margin even for conservative estimates of boria activity (0.25). The overprediction is a consequence of three underlying assumptions: (i) that gap closure occurs at the top of the recession channel, not at its base, (ii) that the SiC oxidation rate is unaffected by the presence of boria, and (iii) that the oxidation-induced volume expansion is

accommodated purely by displacement normal to the oxidizing surfaces, without physical constraint and without flow parallel to the surfaces. The current experimental observations call into question these assumptions and point to the need for more refined models to capture the observed behavior.

4.6. Conclusions and outlook

Microstructural changes accompanying internal oxidation and volatilization in dry air of both unbroken and broken SiC/BN/SiC specimens provide new insights into the event sequence leading to both coating recession and gap closure and highlight deficiencies in existing models of these processes.

(i) When egress of the B-containing reaction product gases is *heavily impeded*, the gas concentrations may approach their respective equilibrium values throughout the available transport space and volatilization may essentially cease. At the same time, local oxidation of the SiC and BN continues, eventually filling the interface gaps and the matrix cracks around the fibers. In this limit, recession gaps are not produced during oxidation and regions of affected BN persist only very short distances (1-2 μm) away from the crack. The processes are therefore manifested as highly-localized lock-up of fibers at the matrix crack locations following relatively short exposures. The deleterious effects of oxide-induced lock-up on composite strength and toughness are well-documented [6, 11].

(ii) When, instead, egress of the B-containing product gases is *unimpeded*, the gases rapidly dissipate into the environment. The gaps produced by volatilization are progressively filled by oxide scales on the newly-exposed matrix and fiber surfaces, but not before a significant recession gap has been produced. This

process eliminates the frictional coupling between fibers and matrix within the recession zones and thus exposes a greater length of fiber to stresses imposed on the composite. Because of the weakest-link scaling character of fiber failure, the reduction in frictional coupling leads to a reduced fiber bundle strength [19, 20]. But these effects are likely to be considerably less detrimental to composite performance than those caused by lock-up.

(iii) In the composites examined in the current study, the closure process involves transport of oxidants along the coating/fiber and coating/matrix interfaces *ahead* of the recession front. The volume expansion associated with oxidation coupled with the low viscosity of the oxides at the temperatures of interest and the confined spaces in which oxidation occurs leads to a thickening of the oxide near the base of the recession zone. Gap closure therefore occurs in sub-surface regions near the recession front rather than at the matrix surface. Pre-existing debond cracks or debond cracks formed during matrix cracking accelerate both the oxidation process ahead of the recession front and the rate of gap closure. These features highlight the importance of *adherent* BN coatings in the oxidative stability of SiC/SiC composites. Additionally, they indicate a need for refined models based on the pertinent thermochemical processes and transport phenomena to better understand and predict the conditions associated with gap closure and the spatial extent of recession and oxidation.

Remarkably, although the water content in the dry air employed in the current study is at *mere ppm levels*, volatilization by reaction of boria with water to form HBO_2 gas is sufficient to cause measurable amounts of recession even following relatively short

exposures at 1000°C. If, instead, water contents were at atm levels, the concentration of B-containing gases would be much higher and hence volatilization would be more rapid. At the same time, since water is a more potent oxidant of SiC than oxygen [25], its presence in large concentrations would also accelerate silica formation. The competition between volatilization of BN and oxidation of SiC would ultimately govern the extent of recession and the time to gap closure.

4.7. Appendix: Calculation of volume expansion for SiO_2 and B_2O_3 formation

The oxidation reactions for stoichiometric SiC, non-stoichiometric Si-O-C fibers, and BN with oxygen are:

$$SiC + \frac{3}{2}O_2(g) \rightarrow SiO_2(s) + CO(g) \qquad (A.1)$$

$$SiC_xO_y + \frac{1}{2}(2 + x - y)O_2(g) \rightarrow SiO_2(s) + xCO(g) \qquad (A.2)$$

$$2BN + \frac{3}{2}O_2(g) \rightarrow B_2O_3(l) + N_2(g) \qquad (A.3)$$

The molar volume change upon conversion of matrix, fiber, or coating to oxide depends on the average atomic masses, M, and mass densities, ρ, of the components involved in the oxidation process (Table A1). The volume ratios are given by:

$$\frac{V_{SiO2}}{V_{SiC}} = \frac{M_{SiO2}\rho_{SiC}}{M_{SiC}\rho_{SiO2}} = 2.2 \qquad (A.4)$$

$$\frac{V_{SiO2}}{V_{SiCxOy}} = \frac{M_{SiO2}\rho_{SiCxOy}}{M_{SiCxOy}\rho_{SiO2}} = 1.4 \qquad (A.5)$$

$$\frac{V_{B2O3}}{V_{BN}} = \frac{M_{B2O3}\rho_{BN}}{2M_{BN}\rho_{B2O3}} = 1.6 \qquad (A.6)$$

The excess O and C in the ZMI fiber are volatilized in the oxidation reaction, leading to a significantly reduced volume expansion relative to that for SiC.

Table A1. Molar masses and mass densities of matrix, fiber and coating materials, and their respective oxides

Component	Average atomic mass, M (g/mol)	Mass density, ρ (g/cm^3)
SiC	40	3.23 [26]
ZMI fiber	49.8	2.48 [15]
h-BN	24.8	2.1 [27]
Amorphous SiO_2	60	2.20 [25, 26]
Amorphous B_2O_3	69.6	1.8 [29]

4.9. References

[1] G. N. Morscher and J. D. Cawley, “Intermediate temperature strength degradation in SiC/SiC composites,” *J. Euro. Ceram. Soc*, vol. 22, pp. 2777–2787, 2002.

[2] K. J. Larochelle and G. N. Morscher, “Tensile stress rupture behavior of a woven ceramic matrix composite in humid environments at intermediate temperature - Part i,” *Appl. Compos. Mater.*, vol. 13, no. 3, pp. 147–172, May 2006.

[3] D. L. Poerschke, M. N. Rossol, and F. W. Zok, “Intermediate temperature oxidative strength degradation of a SiC/SiNC composite with a polymer-derived matrix,” *J. Am. Ceram. Soc.*, vol. 100, no. 4, pp. 1606–1617, Apr. 2017.

[4] G. Morscher, “Tensile Stress Rupture of SiCf/SiCm minicomposites with carbon and boron nitride Interphases at Elevated Temperatures in Air,” *J. Am. Ceram. Soc*, vol. 80, no. 8, pp. 2029–42, 1997.

[5] G. N. Morscher, “Stress-Environmental Effects on Fiber-Refinforced SiC-Based Composites,” in *Ceramic Matrix Composites: Materials, Modeling and Technology*, 2015, pp. 334–352.

[6] F. W. Zok, P. T. Maxwell, K. Kawanishi, and E. B. Callaway, “Degradation of a SiC-SiC composite in water vapor environments,” *J. Am. Ceram. Soc.*, vol. 103, no. 3, pp. 1927–1941, Mar. 2020.

[7] G. Chollon, “Oxidation behaviour of ceramic fibres from the Si±C±N±O system and related sub-systems,” *J. Euro. Ceram. Soc*, vol. 20, pp. 1959–1974, 2000.

[8] B. McFarland and E. J. Opila, “Silicon carbide fiber oxidation behavior in the presence of boron nitride,” *J. Am. Ceram. Soc.*, vol. 101, no. 12, pp. 5534–5551, Dec. 2018.

[9] N. Jacobson, S. Farmer, A. Moore, and H. Sayir, “High-Temperature Oxidation of Boron Nitride: I, Monolithic Boron Nitride,” *J. Am. Ceram. Soc.*, vol. 82, no. 2, pp. 393–398, Dec. 1999.

[10] V. E. Collier, W. Xu, R. M. McMeeking, F. W. Zok, and M. R. Begley, “Recession of BN coatings in SiC/SiC composites through reaction with water vapor,” *J. Am. Ceram. Soc.*, no. April, pp. 1–14, 2021.

[11] T. A. Parthasarathy, B. Cox, O. Sudre, C. Przybyla, and M. K. Cinibulk, “Modeling environmentally induced property degradation of SiC/BN/SiC ceramic matrix composites,” *J. Am. Ceram. Soc.*, vol. 101, no. 3, pp. 973–997, Mar. 2018.

[12] W. Xu, F. W. Zok, and R. M. McMeeking, “Model of Oxidation-Induced Fiber Fracture in SiC/SiC Composites,” *J. Am. Ceram. Soc.*, vol. 97, no. 11, pp. 3676–3683, 2014.

[13] A. Evans, F. Zok, R. McMeeking, and Z. Du, “Models of High-Temperature, Environmentally Assisted Embrittlement in Ceramic-Matrix Composites,” *J. Am. Ceram. Soc*, vol. 79, no. 9, pp. 2345–52, 1996.

[14] N. S. Jacobson, G. N. Morscher, D. R. Bryant, and R. E. Tressler, “High-Temperature Oxidation of Boron Nitride: II, Boron Nitride Layers in Composites,” *J. Am. Ceram. Soc.*, vol. 82, no. 6, pp. 1473–1482, Dec. 2004.

[15] H. Ichikawa, “Polymer-Derived Ceramic Fibers,” *Annu. Rev. Mater. Res.*, vol. 46, no. 1, pp. 335–356, 2016.

[16] D. L. Poerschke, M. N. Rossol, and F. W. Zok, “Intermediate Temperature Internal Oxidation of a SiC/SiCN Composite with a Polymer-Derived Matrix,” *J. Am. Ceram. Soc.*, vol. 99, no. 9, pp. 3120–3128, Sep. 2016.

[17] B. W. Sheldon, E. Y. Sun, S. R. Nutt, and J. J. Brennan, “Oxidation of BN-Coated SiC Fibers in Ceramic Matrix Composites,” *J. Am. Ceram. Soc*, vol. 79, no. 2, pp. 539–543, 1996.

[18] J. Schlichting, “Oxygen transport through glass layers formed by a gel process,” *J. Non. Cryst. Solids*, vol. 63, no. 1–2, pp. 173–181, Feb. 1984.

[19] B. E. Deal and A. S. Grove, “General Relationship for the Thermal Oxidation of Silicon,” *J. Appl. Phys.*, vol. 36, no. 12, pp. 3770–3778, Dec. 1965.

[20] R. S. Hay and R. J. Chater, “Oxidation kinetics strength of Hi-Nicalon ^{TM} -S SiC fiber after oxidation in dry and wet air,” *J. Am. Ceram. Soc.*, vol. 100, no. 9, pp. 4110–4130, Sep. 2017.

[21] D. R. Poirier and G. H. Geiger, *Transport Phenomena in Materials Processing*. 2016.

[22] M. Boike, K. Hilpert, and F. Miiller, “Thermodynamic Activities in B2O3-SiO2 Melts at 1475K,” *J. Am. Ceram. Soc*, vol. 76, no. 11, pp. 2809–2812, 1993.

[23] F. W. Zok, “On weakest link theory and Weibull statistics,” *J. Am. Ceram. Soc.*, 2017.

[24] F. W. Zok, V. E. Collier, and M. R. Begley, “Coating recession effects in ceramic composite strength,” *J. Mech. Phys. Solids*, vol. 156, no. June, p. 104608, 2021.

[25] R. S. Hay and R. Corns, “Passive oxidation kinetics for glass and cristobalite formation on Hi-Nicalon^{TM}-S SiC fibers in steam,” *J. Am. Ceram. Soc.*, vol. 101, no. 11, pp. 5241–5256, Nov. 2018.

[26] S. Budavari, *The Merck Index - Encyclopedia of Chemicals, Drugs and Biologicals*. 1989.

[27] "Boron Nitride Powder," *American Elements: The Advanced Materials Manufacturer*, 2022. .

[28] W. Pabst and E. Gregorová, "Elastic properties of silica polymorphs-a review," *Ceram. - Silikaty*, vol. 57, no. 3, pp. 167–184, 2013.

[29] M. J. O'Neil, *The Merck Index - An Encyclopedia of Chemicals, Drugs, and Biologicals. 13th Edition*. 2001.

4.10 Figures

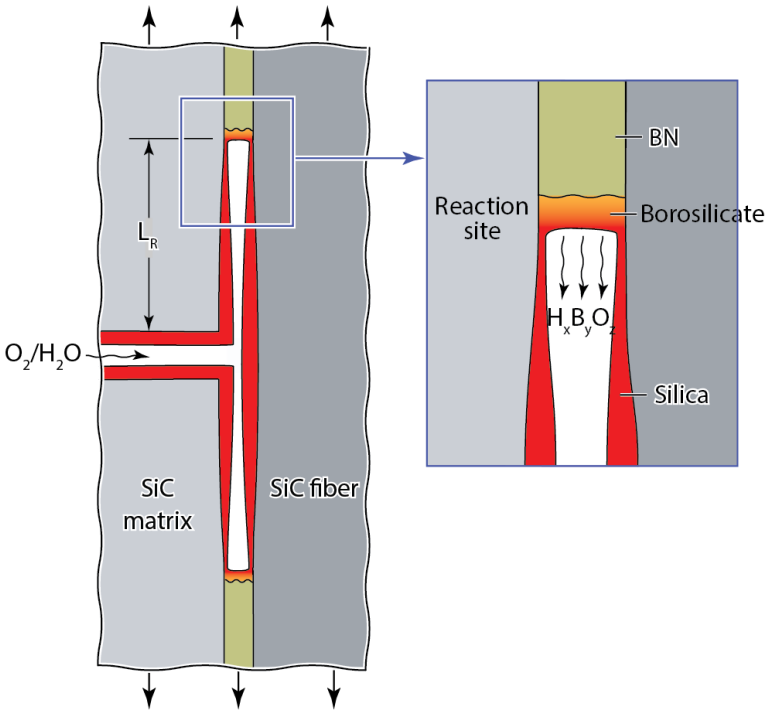

Figure 1. Schematic rendering of the assumed geometry in the standard model used to analyze internal oxidation and volatilization in SiC/SiC composites.

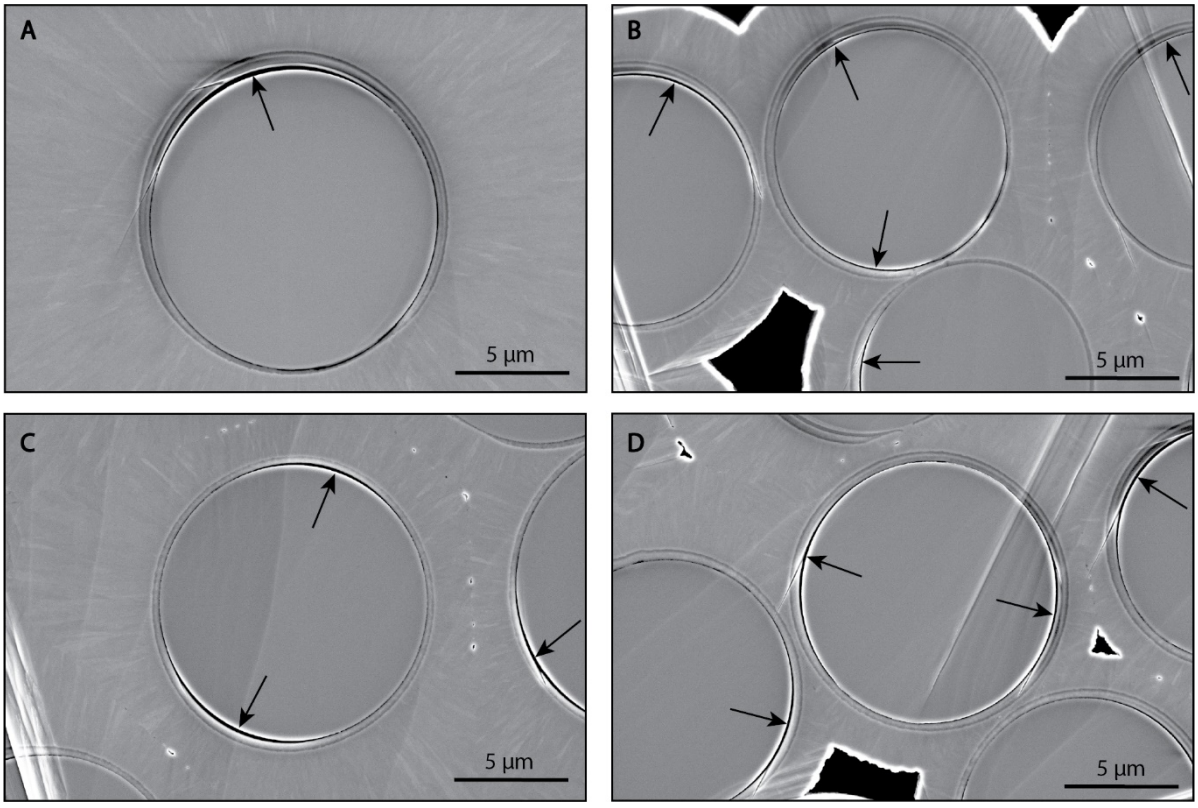

Figure 2. SEM images (in SEI mode) of the unbroken, pristine minicomposite showing debonds between fibers and coating. Debonds are evidenced by the bright edges.

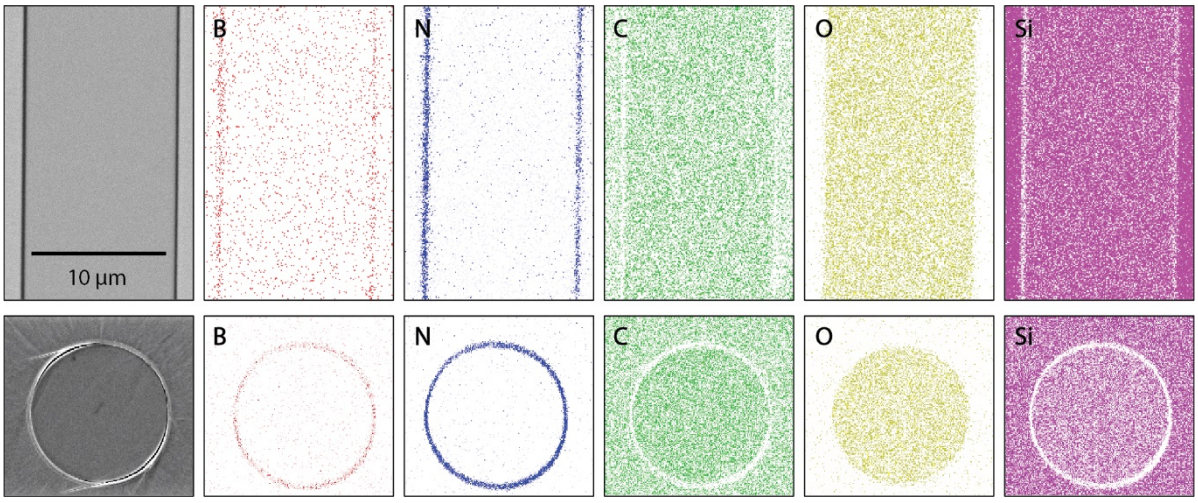

Figure 3. Backscatter electron imaging (BEI) coupled with energy dispersive spectroscopy (EDS) reveals the coatings, evidenced largely by the N signal, in both longitudinal and transverse sections. While a B signal is also evident in the region of pristine coatings, the signal is too weak to reliably identify the presence of BN in oxidized specimens.

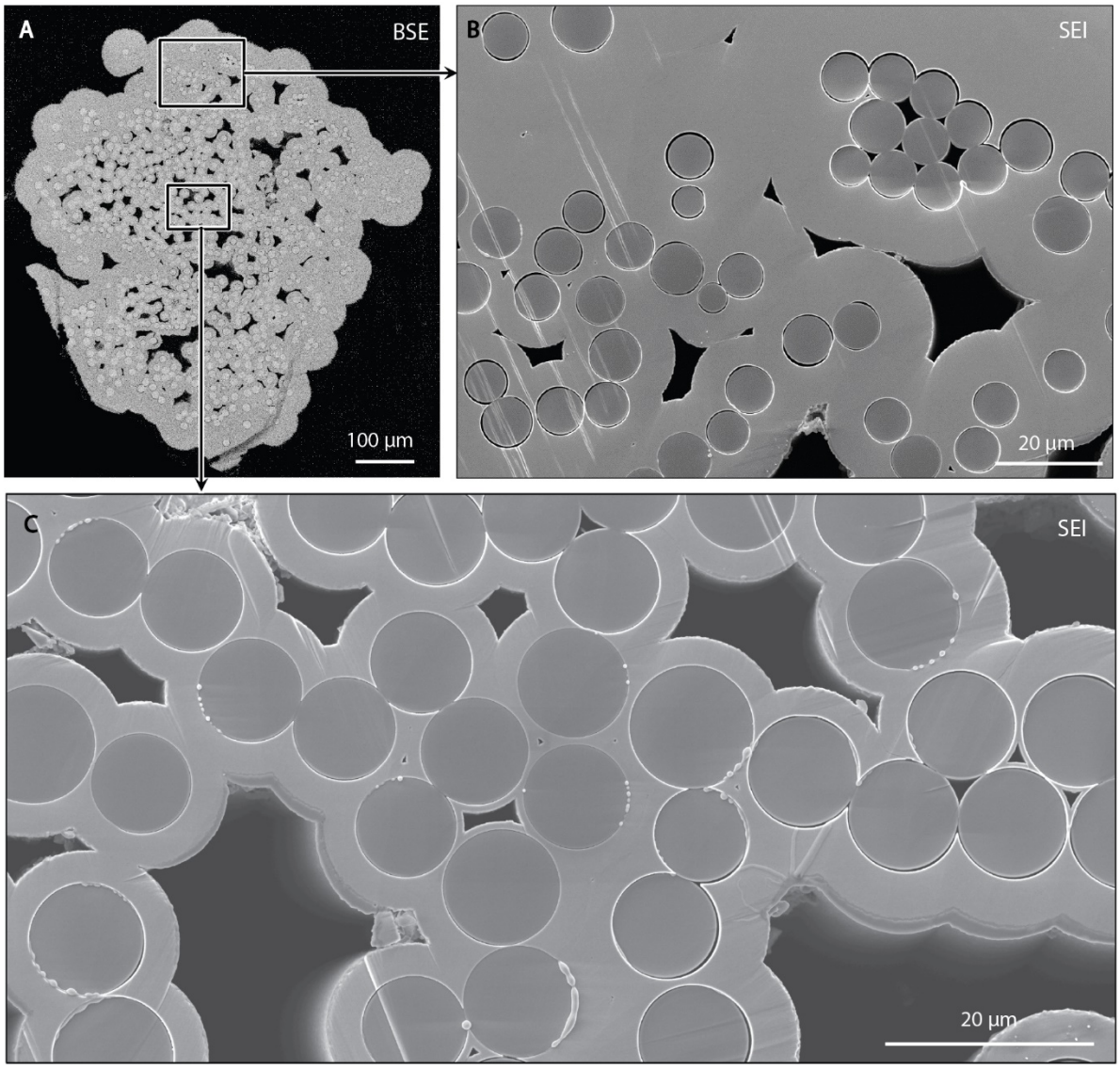

Figure 4. (A) Full unbroken, pristine minicomposite cross-section (in BEI mode) and (B, C) select regions of the unbroken, oxidized composite (in SEI mode). (B) Thick coatings are more prevalent in the outer regions of the tows. These coatings volatilize during oxidation, leaving open gaps between the fibers and the matrix. (C) Thin coatings are more common in the central regions. In these cases, oxidation leads to removal of the BN and the formation of a silica scale that seals the gaps between the fibers and matrix.

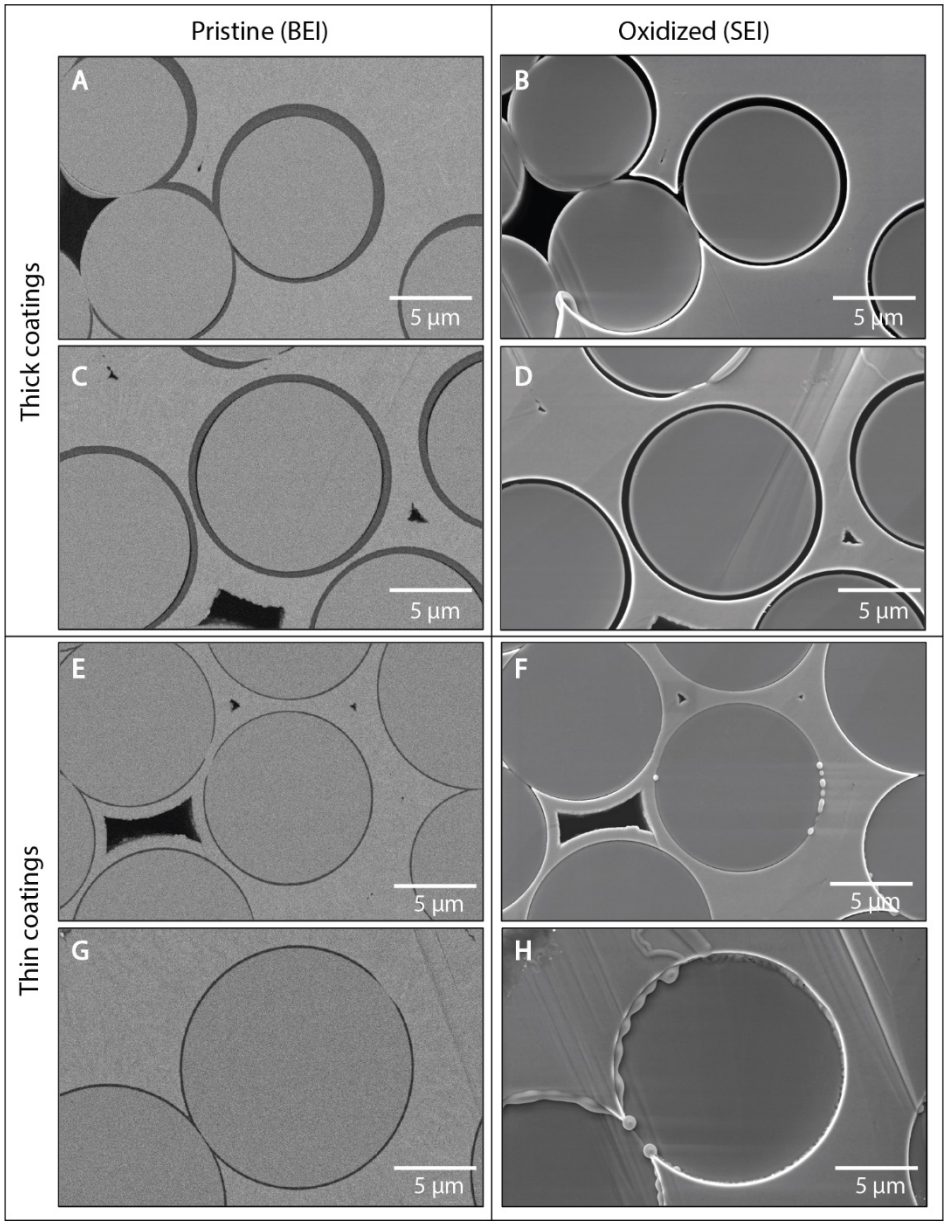

Figure 5. Higher magnification images (relative to those in Figure 4) show representative thick and thin coatings and the changes that transpire during oxidation. (Images in each row are of the identical regions in the unbroken specimen before and after oxidation.)

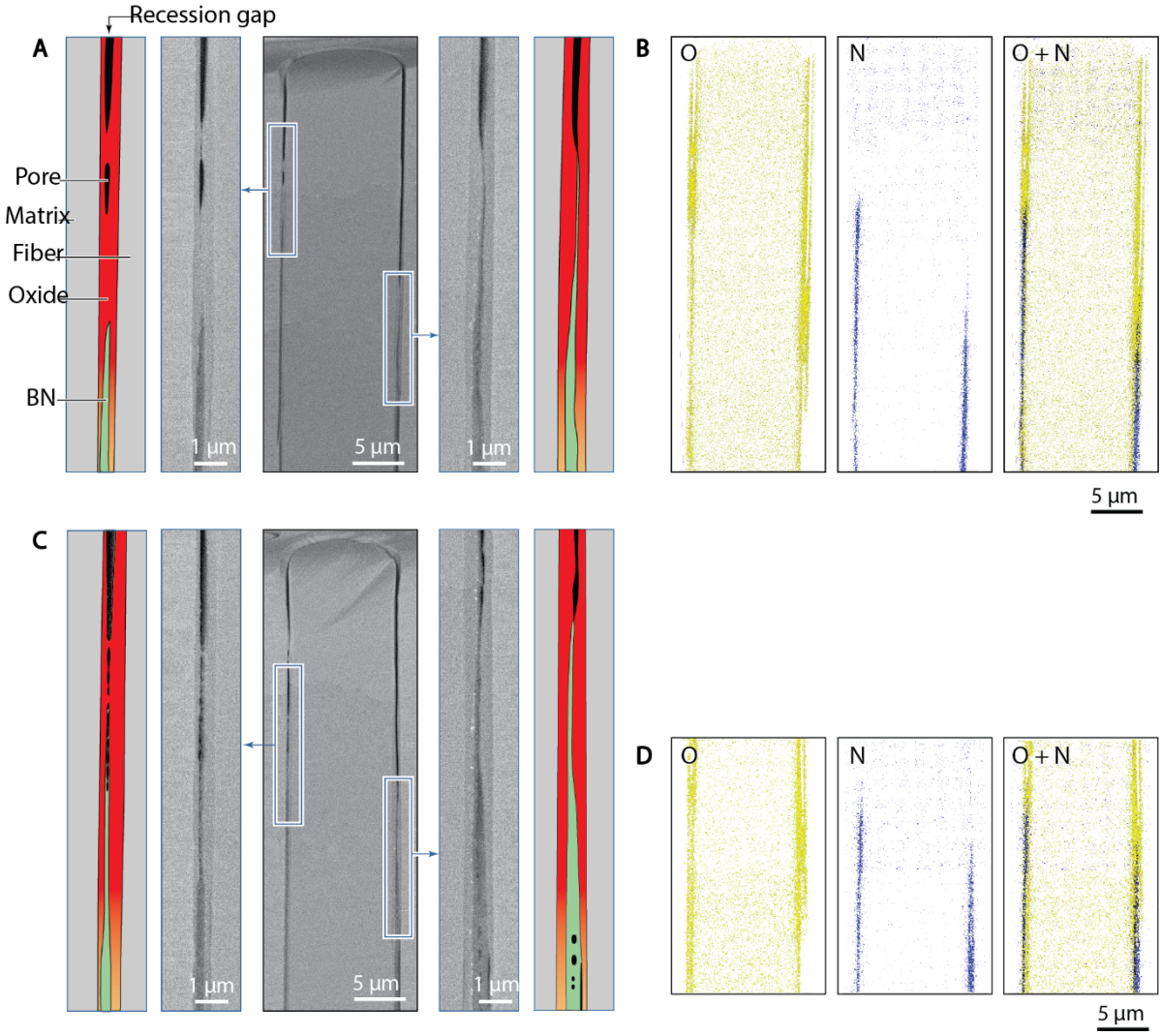

Figure 6. (A,C) Longitudinal section of two representative fibers in the unbroken, oxidized specimen show recession gaps and reaction zones beneath the exposed surface on either side of each fiber. (B,D) EDS maps reveal oxide scales on both the fibers and the matrix in the upper regions where the BN coating has been fully consumed. Deeper into the composite, oxide scales on both the fiber and matrix surfaces and an intervening layer of BN are evident. The schematic renderings were traced from high magnification SEM images of the reaction front.

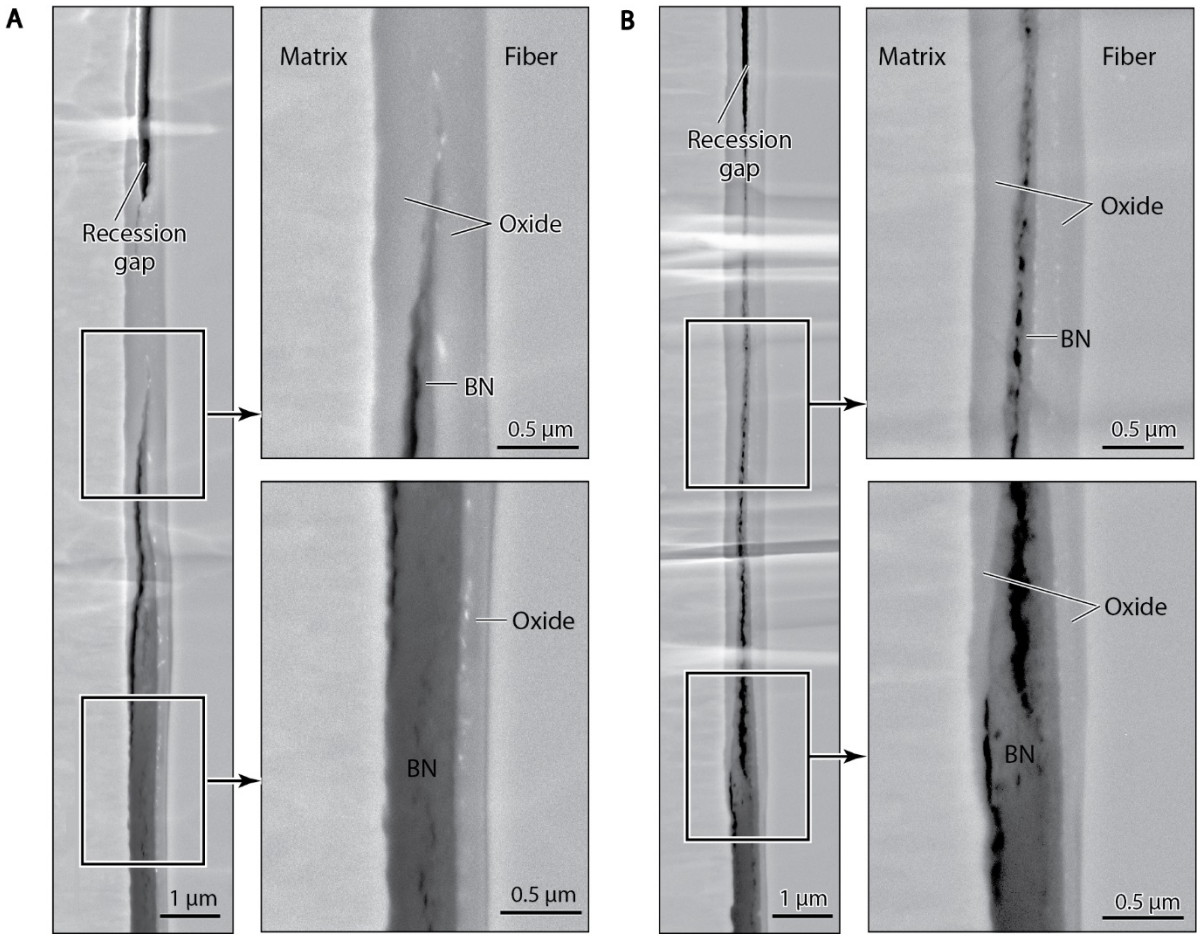

Figure 7: High magnification BEI images of longitudinal section of the unbroken, oxidized specimen showing two additional examples of the transition region between the recession zone (top) and the intact BN (bottom).

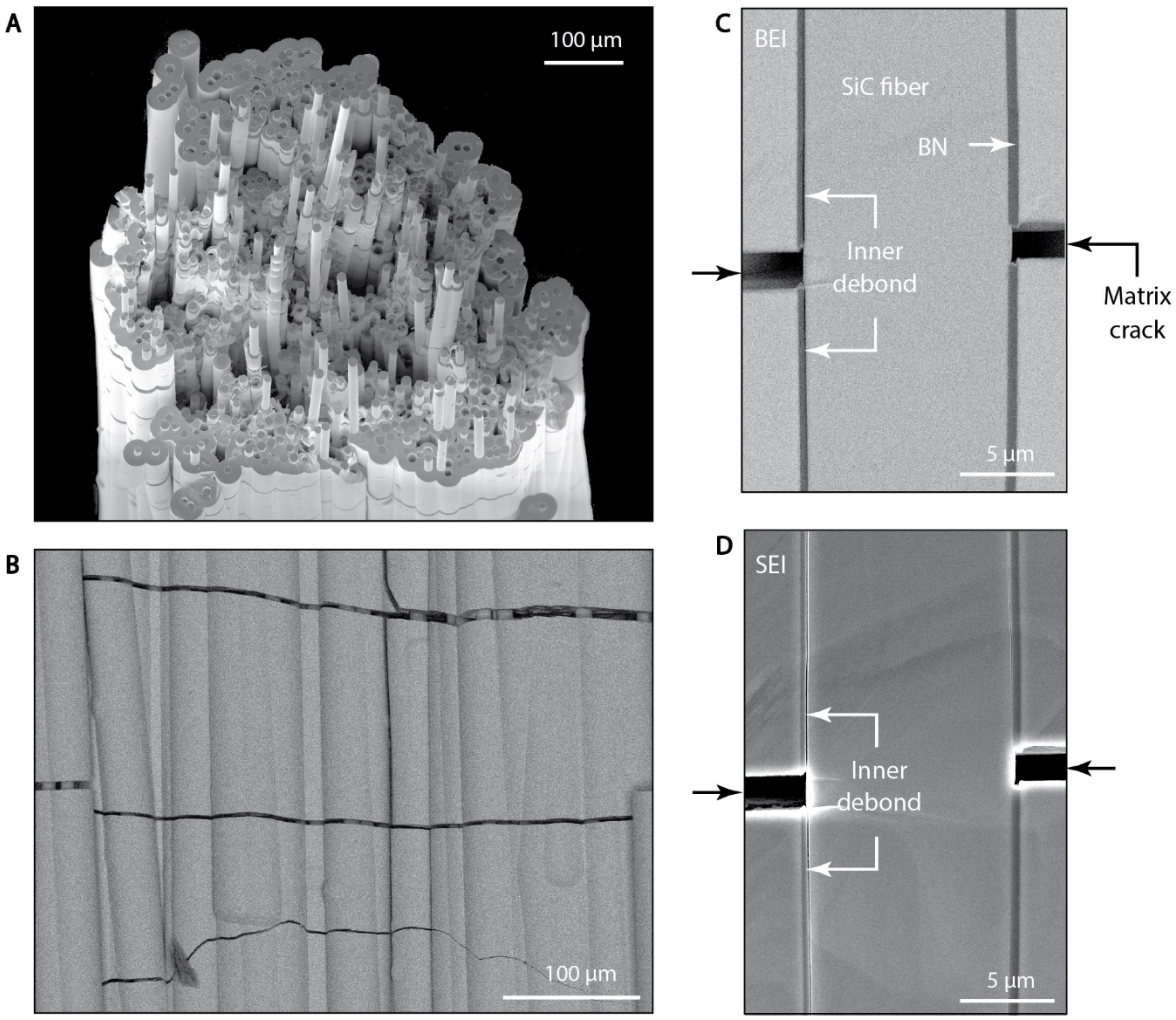

Figure 8. SEM images of the broken (not oxidized) specimen show (A) fiber pullout on the fracture surface and (B) matrix cracks away from the fracture surface. (C, D) Longitudinal section through the broken specimen reveals an inner debond (i.e. between the BN and the fiber).

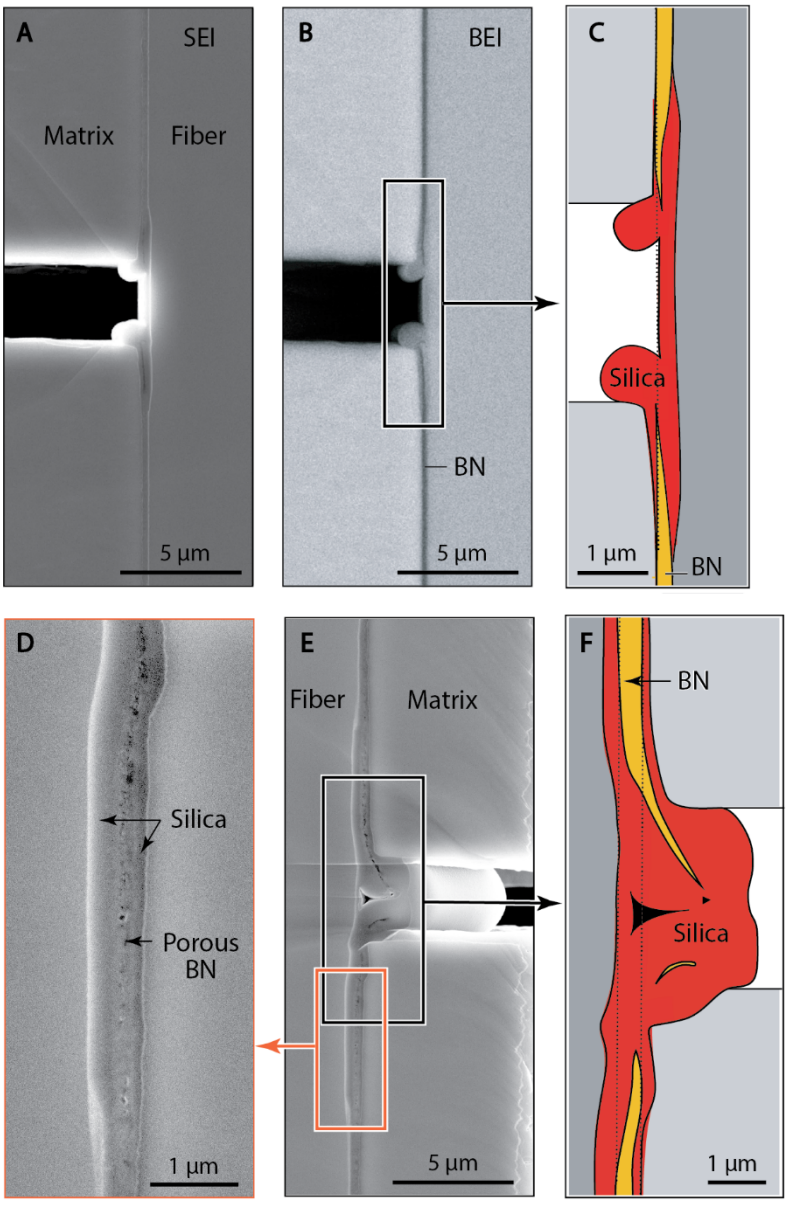

Figure 9. Oxide sealing around a matrix crack on two sides of an individual fiber in the broken, oxidized specimen: (A-C) one with a thin coating (0.1 µm) and (D-F) the other with a thicker coating (0.2 µm). Oxide spills into the matrix crack due to the volume expansion associated with oxidation.

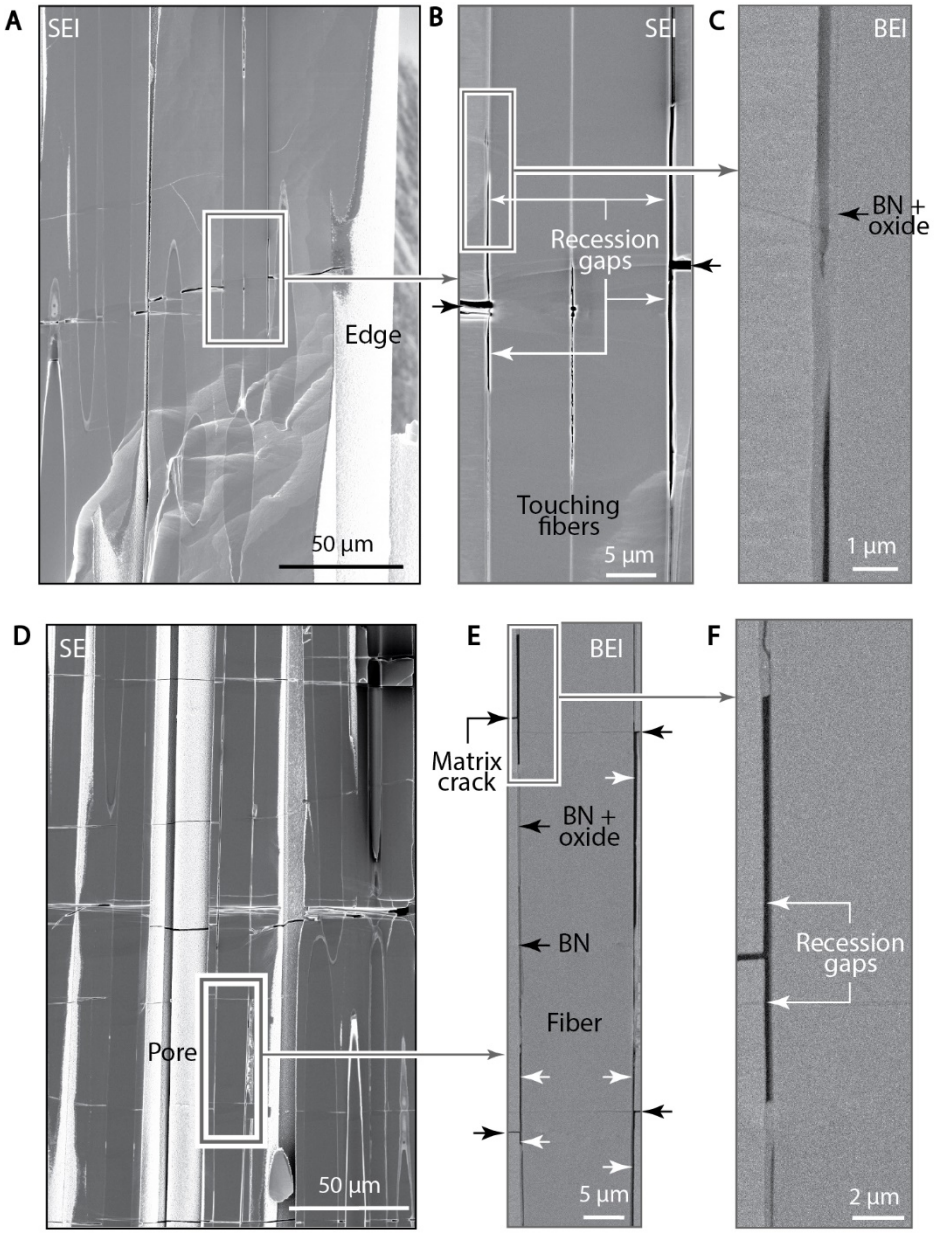

Figure 10. Longitudinal section of the broken, oxidized minicomposite specimen, highlighting recession gaps and matrix crack locations near the edge of the composite (A-C) and in the interior of the composite (D-F) near a pore connected to the fracture surface.

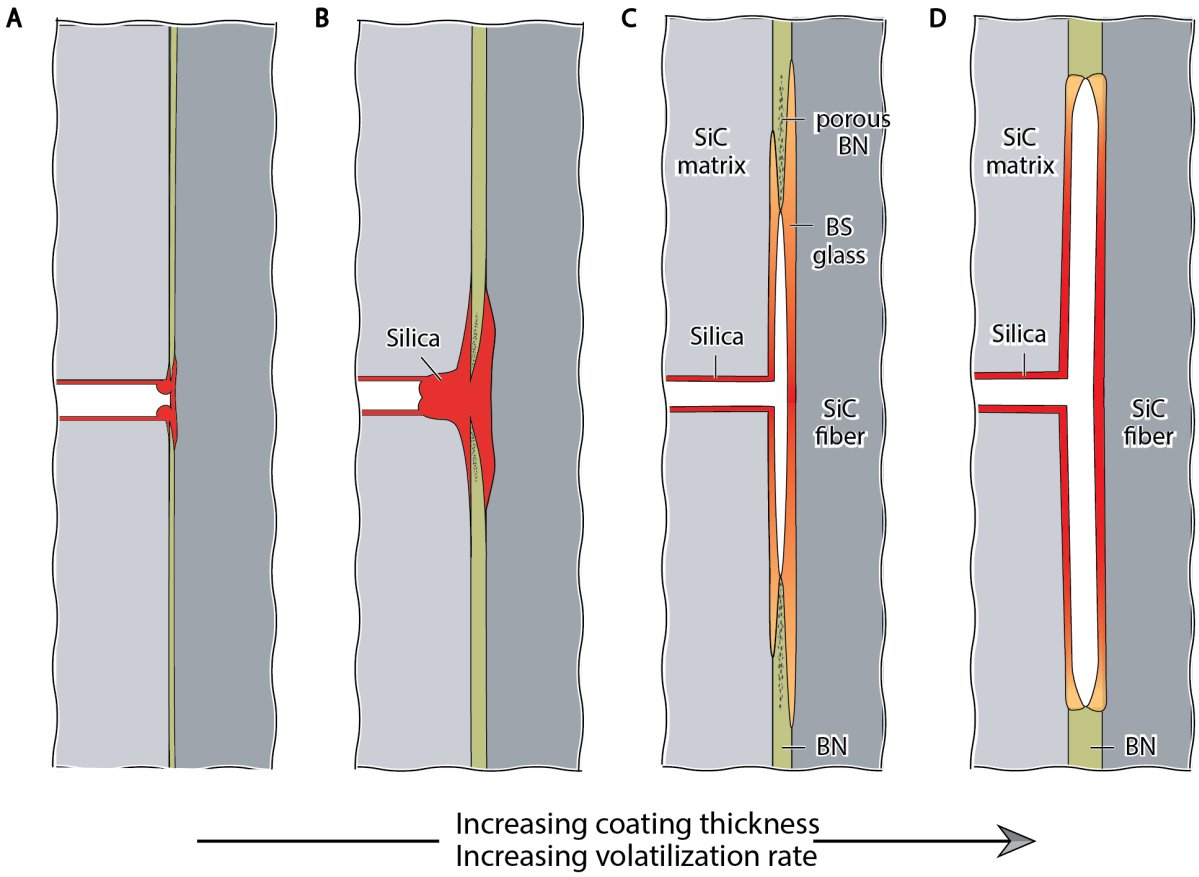

Figure 11. Schematics illustrating transitions in recession and closure behavior as the coating thickness and the volatilization rate increase (from left to right).

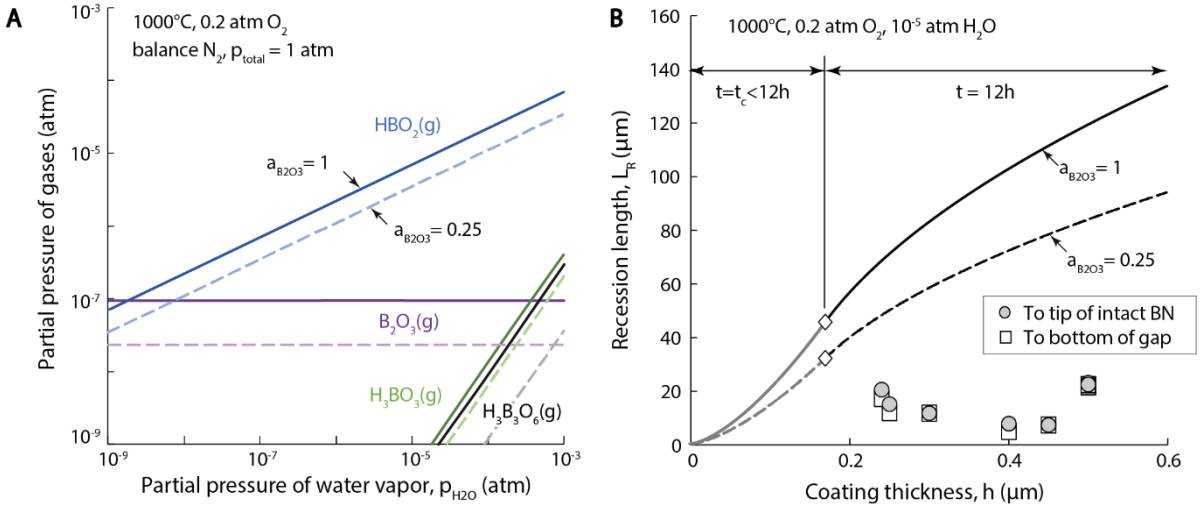

Figure 12. (A) The partial pressures of gases in equilibrium with boria are controlled by water vapor partial pressure and boria activity. Results here are for 1000°C. (B) Variations in recession length with coating thickness and boria activity, for 12h exposure at 1000°C in 0.2 atm of O_2 and 10 ppm H_2O. Gap closure occurs in less than 12h for coating thicknesses less than 0.17 µm, so the critical closure time, t_c, is used to calculate recession length (at closure). The symbols are measured recession lengths from SEM images of longitudinal sections either to the bottom of the open gap or to the start of the intact BN.

Chapter 5

Influence of BN Microstructure on the Oxidation of SiC/BN/SiC Composites

5.1 Introduction

Boron nitride (BN) is the preferred material for fiber coatings in SiC fiber/SiC matrix composites. BN coatings allow cracks initiating in the matrix to deflect, keeping the load-bearing fibers intact and enabling composite failure strains approaching 1%. The single greatest deficiency of BN, however, is its susceptibility to oxidation and volatilization at elevated temperatures, especially in environments containing water vapor. Additionally, the current understanding of the roles of BN microstructure and processing history in BN properties remains poor [1], [2].

BN is typically deposited onto SiC fibers via chemical vapor deposition (CVD). Key process parameters include precursor gas type and concentration, flow rate, and temperature, which together dictate the coating composition and crystallinity [3], [4], [5], [6], [7], [8], [9], [10], [11]. High-temperature (≥1200°C) deposition results in crystalline BN with a hexagonal structure and high texture. Lower temperatures (700-1000°C) yield largely amorphous BN, which may contain domains of turbostratic BN and small (but not insignificant) amounts of oxygen and carbon [12]. The gas flow paths and the spatial arrangement of fibers in the reactor govern the coating thickness uniformity at both micro- and macro-scales [13].

When exposed to oxygen or water vapor at elevated temperature, SiC on its own first forms a passivating (protective) layer of solid silica while BN on its own forms a non-

protective layer of liquid boria. Both silica and boria can volatilize especially in fast-flowing water-containing environments, forming $Si(OH)_4$ and $H_xB_yO_z$ gases [1], [14]. The oxidation behavior of SiC in isolation has been studied extensively and is relatively well understood; less is known about the behavior of BN alone. Even less is known about the behavior of systems in which BN and SiC are in close proximity, especially within the confined spaces in a composite. These deficiencies motivate the current study.

The physical manifestations of BN oxidation and volatilization within SiC/SiC composites are twofold. When the volatilization rate of B-containing species is large relative to the production rate of condensed oxides, gaps form between the fibers and matrix [15], [16], [17], facilitating oxidant transport deeper into the composite and sustaining the recession process. Over time the gaps are filled by oxide scales formed on the exposed fiber and matrix surfaces. Conversely, when the volatilization rate is low, gaps created by consumption of BN are readily filled with oxide, significantly slowing or stopping further recession.

These processes can profoundly affect mechanical properties. Fiber-matrix gaps eliminate the frictional coupling essential for high toughness and strength; if recession continues unabated the composite strength may eventually fall to that of a dry fiber bundle [15]. Conversely, although the oxides filling the recession gaps can effectively impede further recession, they also create strong bonds between fibers and matrix, leading to high stress concentrations during thermal or mechanical cycling [18], [19], [20], [21], [22]. The trade-offs between these phenomena and the preference for recession over gap sealing remain open questions.

The current study examines the effects of BN coating characteristics on subsurface oxidation of SiC/SiC composites in water-rich environments. The chapter is organized in the following way. Three coating types used in this study and the experimental workflow are described in Section 5.2. The chemical compositions of pristine coatings are compared in Section 5.3. Examinations of microstructural changes following oxidation using high resolution imaging techniques are detailed in Section 5.4. Then, in an attempt to infer the event sequences and determine the rate limiting processes, descriptive and analytical models of BN and SiC consumption combined with thermochemistry calculations are elaborated in Section 5.5. Key conclusions follow in Section 5.6.

5.2 Materials and Methods

Unidirectional minicomposites containing individual tows of 500 Hi-Nicalon Type S fibers were produced by CVI (ATL Advanced Coating Solutions, UK). Three types of coatings were deposited: (i) crystalline BN, (ii) amorphous BN, and (iii) Si-doped amorphous BN. In all cases, $BCl_3(g)$ was the principal active precursor gas. Crystalline coatings were produced by deposition at relatively high temperatures (1275-1400°C) while amorphous coatings, both with and without Si-doping, were deposited at lower temperatures (775-875°C). An additional precursor was used for Si-doping.

The experimental workflow is illustrated in Figure 1. Transverse cross-sections through pristine specimens were produced using a broad beam ion mill (Leica TIC 3X). These surfaces were examined via scanning electron microscopy (SEM) in both secondary and backscatter modes (Thermofischer Apreo C). Essentially the entire cross-section of each specimen was imaged at sufficiently high magnification to reliably measure coating thickness on every fiber and the images stitched together in Photoshop. Approximate

(relative) coating compositions were obtained from energy dispersive spectroscopy (EDS) measurements in the SEM. Additionally, thin foils were extracted from pristine specimens with a focused ion beam (FIB) using standard procedures (Thermofischer Helios FIB-SEM) and examined by transmission electron microscopy (TEM, JEOL 2100F). Further chemical analysis was performed using scanning transmission electron microscopy - electron energy loss spectroscopy (STEM-EELS) in the TEM.

The same specimens were oxidized concurrently for either 1h or 12h at 1000°C in flowing, 20 vol% water vapor (balance dry air). Details of the oxidation apparatus are presented elsewhere [23]. Notably, alumina tubes and alumina support hardware were used exclusively for all oxidation experiments. The gas velocity in the hot zone was 4.4 cm/s. The specimens were strategically arranged on notched alumina blocks, ensuring unimpeded gas flow past the polished faces (Figure 2). Following oxidation, the polished surfaces were re-examined in the SEM.

To reveal subsurface features, oxidized specimens were sectioned longitudinally (perpendicular to the polished transverse section) by ion milling. The precise location of the sectioning plane was determined by comparing tilted SEM images of both faces with the montages of the transverse section. The pristine transverse section was used to determine both the coating thickness specific to each sectioned fiber and the location of the sectioning plane relative to the diametral plane through the fiber. In this way the nature and size of oxidation and recession zones could be correlated with the *true* coating thickness (as opposed to projected or apparent thickness on the longitudinal section). Various characteristic features including recession lengths and oxide scale thicknesses on fiber surfaces were measured by SEM. EDS measurements were also made in select locations on

the longitudinal section. A TEM lamella was extracted from the crystalline BN composite after 12h exposure and the BN in the reaction zone was analyzed using EELS.

5.3 Characteristics of pristine coatings

Crystalline BN contains no detectable O or C by SEM EDS (Figure 3) or TEM EELS (Figure 4). The basal planes of hexagonal BN are evident in the TEM and aligned well with the fiber axis (Figure 5b-c). The measured basal plane spacing is 0.338 nm (Figure 5c), almost the same as the theoretical value (0.333 nm). Characteristic π and σ peaks are present in the EELS spectra for both B (200 eV) and N (400 eV), representing in-plane sp2 and out-of-plane van der Waals bonding, respectively (Figure 4) [24], [25]. The average thickness of these coatings is 0.95±0.43 μm [13]. Cracks are present within the BN and at the BN-fiber interface, evidenced in Figure 5a. Debonding between crystalline BN and SiC fibers was also observed in a previous study on the same material via SEM [13]. Partial debond cracks were found in less than 20% of all fibers.

Amorphous BN contains ~10 at% O and 5-10 at% C (EDS, Figure 3). The basal planes of the BN are not as well aligned with the fiber axis as in the crystalline coating and crystallite sizes are on the sub-nm scale, evidenced by the brightfield TEM images and the diffuse diffraction pattern (Figures 5e,f). While π and σ peaks for B and N are present in the EELS spectra, they are broader and lower in intensity than those in crystalline BN (Figure 4) [25]. A carbon edge at 300eV and an oxygen edge at 550eV are also detected. Here the average coating thickness is 0.44±0.18 μm, about half that of the crystalline BN coatings [13].

Si-doped, amorphous BN contains ~5-10 at% each of O, C and Si (EDS, Figure 3). Coatings in these composites are thinner yet, by a factor of 2 relative to the undoped

amorphous BN (0.23±0.10 μm). With such thin coatings, EDS signals from the adjacent fibers and matrix are likely to have greater effect on the measurements within the coatings, yielding anomalously high C and Si levels. The presence of Si within the BN coatings was confirmed by the characteristic Si edge in the 100-150 eV range in the EELS spectrum [12] (not present in the other coatings, Figure 4). Other aspects of the coating structure (Figure 5g,h) and the EELS spectra (Figure 4) are consistent with those of the amorphous BN.

5.4 Post-oxidation observations

5.4.1 General features

The same fibers were examined on transverse sections before and after oxidation (Figure 6). After 1 h exposure, near-surface coatings in all three composites had volatilized, leaving narrow gaps between fibers and matrix independent of coating thickness. A thin, smooth amorphous silica scale was present on the exposed surfaces, as evidenced by strong O signals in EDS maps of exposed surfaces (not shown). Occasionally, small crystalline spherulites were observed on the surface of the Si-doped BN composite, suggesting that constituents in the Si-doped BN may accelerate silica scale crystallization (Figure 6k).

Following 12 h exposure, fiber surfaces were covered with crystalline spherulites of varying size and quantity (Figure 6). Open interface gaps persisted on surfaces of composites with crystalline or undoped amorphous BN. In contrast, regions with thin coatings (<0.3 μm) in the Si-doped BN composite were sealed with oxide protruding slightly above the surface (Figure 6j), while regions with thick coatings (≥0.3 μm) remained open (Figure 6l). The matrix surface adjacent to the gap was covered by a flat oxide scale that was occasionally cracked, suggesting that the scale had crystallized at temperature and had

undergone a phase transformation upon cooling (Figure 6l) [23]. Additionally, fibers originally in contact had fused together with oxide at the contact points (Figure 6i).

5.4.2 Crystalline BN

Crystalline BN volatilizes directly, producing open recession channels without condensed B-containing oxides (Figures 7-8). Silica scales were evident on both fiber and matrix surfaces within the recession channels. The scale thickness was greatest at the exposed surface and decreased with depth into the composite (Figure 9). The recession front was sharply angled with deeper recession along the fiber-BN interface than the BN-matrix interface (Figures 7d and 8e-f). BN within this transition zone appeared porous and flaky, as reported by others [26].

Following 1h exposure, thin silica scales were evident on fiber surfaces adjacent to the porous BN; such scales were not visible on matrix surfaces (Figure 7c). EDS line scans revealed high C levels within the flaky BN, comparable to or exceeding C levels in adjacent fibers and matrix (Figure 7d-e). Slightly beyond the flaky region, the oxygen signal exhibited a narrow peak at the fiber-BN interface, suggesting the presence of a thin oxide scale not discernible in the SEM images (Figure 7d-f). Recession lengths L_R were 55 ± 14μm after 1h exposure, independent of coating thickness (Figure 11).

Similar features were observed after 12 h exposure. C levels within the flaky BN were high, comparable to those in the adjacent fibers and matrix (Figure 8f-g). C was also detected in the flaky BN via TEM EELS (Figure 10). As with the 1-hour exposure, oxygen line scans exhibited narrow peaks at the fiber-BN interface (Figure 8f-h). Ahead of the reaction fronts within the intact BN, C was present at concentrations of ~15 at%. The C persisted within the intact BN ahead of the reaction front even beyond the point where Si

and O were no longer detected (Figure 8f-h). Recession lengths were 280±60μm: about 5 times that after 1h exposure (Figure 11).

Among 13 fibers analyzed across three sequential sections of the 12h exposure specimen, oxide filled the channels at only two locations (Figure 8b-c). In both of these cases the coatings were among the thinnest in the composite (< 0.4 μm). At the reaction front, BN was thin and porous with oxide on both fiber and matrix sides (Figure 8c).

5.4.3 Amorphous BN

Amorphous BN oxidizes along with adjacent fibers and matrix, forming borosilicate glasses that replace the BN coatings. When gaps appear near the exposed surface, the residual oxide scales on fibers and matrix appear to be the same thickness (Figure 8j-k).

Following 1h exposure, the oxides contained many bubbles (Figure 7i-j). In some cases the matrix-BN interface was oxidized preferentially with thin oxide scales evident on the matrix but not the fibers (Figure 7i). Well ahead of the reaction front, bubbles were visible at the fiber-BN interface. Recession lengths (measured from the external surface to the start of intact BN) were 50-100 μm (Figure 11). Effects of coating thickness could not be ascertained as all coatings encountered in this section were relatively thick (>0.25 μm).

Following 12 h exposure the oxidation behavior differed in regions with thin and thick coatings. For coating thickness $h \leq 0.25$ μm, gaps produced by oxidation were filled entirely with short (1.5–20 μm) oxide plugs without bubbles, indicating complete B volatilization. Near the reaction front, the oxide was slightly thicker, forming a bulb-like shape (Figure 8k). In these cases the recession lengths and the open gap lengths were both small (15 μm and 5 μm, respectively) and exhibited consistent features (Figure 12a). In contrast, for $h > 0.25$ μm, oxide plugs were considerably longer (>200 μm) and contained large bubbles (Figure

8m). The BN/oxide interface was straight and the oxide plug composition was uniform (~50 at% O, 30 at% Si, 20 at% C, Figure 8o). Intact BN ahead of the reaction front contained ~10 at% each of Si and O, ~20 at% C, and more B than N (Figure 8p). For thick coatings the recession lengths and the open gap lengths were generally much greater (by about an order of magnitude).

5.4.4 Si-doped amorphous BN

Si-doped BN exhibited oxidation characteristics similar to undoped amorphous BN but with higher oxidation and oxide plug formation rates. After 1 h exposure, gaps were present at the channel tops, with regions below filled with oxide plugs containing bubbles (Figure 7m). Thin BN fragments were occasionally flanked by oxide scales on fibers and matrix (Figure 7p). A vertical EDS line scan through one plug showed increasing B and decreasing Si content with depth (Figure 7q). Beyond the reaction front, pores were visible at the intact BN-fiber interface (Figure 7o).

After 12 h essentially all gaps produced by BN consumption were entirely filled with oxide plugs. Oxide plugs at the reaction front exhibited a bulb-like shape or were uniform in thickness (Figure 8r-s). Thick coatings (>0.4 μm) contained large bubbles within the oxide plugs (Figure 8u). Oxide compositions were similar to those of amorphous BN but with slightly higher O and lower C levels (~55 at% O, 30 at% Si, ~15 at% C, Figure 8w).

Coating thickness on most fibers in the longitudinal section were 0.2 ± 0.05 μm thick. Intact BN was present within about 100 μm of the exposed surface after both 1h and 12h exposures. Oxide plugs for thicker coatings (≥0.4 μm) were significantly longer (about 300 μm) after 12h (Figure 11). The measurements for these coatings exhibited the greatest amount of scatter. Perhaps their most notable feature is their lack of dependence on exposure

time, suggesting that the system had attained a terminal state after no more than 1h exposure.

5.5 Analysis and Discussion

5.5.1 Preliminaries

The discussion focuses on the inferred event sequences and rate-limiting processes governing BN removal and gap closure. In general rates can be limited by transport of oxidants or reaction product gases through open gaps or oxide plugs or by the intrinsic oxidation rates of BN and SiC. These processes lead to local phase changes that can either accelerate or slow further reaction. Event sequences are governed by the intrinsic thermochemical properties of the constituent phases, the initial phase dimensions and configurations, and the transport kinetics.

5.5.2 Conceptual framework of the event sequence

Two schemas represent event sequences leading to coating loss and gap closure (Figure 13). Although labelled with terms specific to the current materials (crystalline and amorphous BN), they broadly depict oxidation behaviors found here and reported elsewhere [2], [14], [17], [27]. While the scenarios elaborated here consider internal oxidation fronts starting from an external surface, conceptually they can be extended to cracked composites in which internal oxidation fronts proceed away from matrix cracks.

In the first schema, recession occurs through direct BN volatilization without an intermediate liquid phase. Provided the supply of water vapor at the external surface is sufficient the recession rate is governed by either gas transport or intrinsic oxidation/volatilization rates. If limited by intrinsic volatilization, a steady-state recession

rate is expected. If limited by gas transport, the recession rate decreases as the gap grows longer [16]. Newly-exposed surfaces form passivating silica scales that grow with linear-parabolic (Deal-Grove) kinetics. Because oxidation only occurs on the exposed surfaces and the surfaces are exposed progressively over time, the scale thickness is greatest at the channel entrance (*i.e.* at the external surface). Oxide scales on fibers and matrix eventually impinge at the top of the channel, essentially arresting recession.

In the second schema, BN oxidizes rapidly to form liquid boria. Since the molar volume of boria is about 1.6 times that of BN, the volume of boria produced exceeds the space made available by BN consumption. Thus the boria spills out onto the external surface and reacts with water vapor to form borohydroxide gases. Molten boria within the channel provides only a weak diffusion barrier and thus BN oxidation proceeds rapidly. SiC adjacent to the boria pool also oxidizes and mixes with the boria to form a borosilicate glass, causing further growth of the liquid pool. Since boria volatilizes much faster than silica[§§§], the borosilicate glass becomes silica-rich. Once the silica content exceeds the saturation limit (about 0.75 at 1000°C [28], [29]) it begins to precipitate out of solution and deposit onto the fiber, matrix and coating surfaces within the channel, significantly slowing further oxidation. Once the BN is isolated from the liquid boria by a sufficiently thick layer of solid silica, BN oxidation essentially ceases while boria volatilization from the remaining liquid continues. Competing boria/silica production and volatilization rates determine gap filling or

[§§§] When L is the diameter of the composite (0.1 cm), the volatilization rate of B_2O_3 ~ 40 μm/h and SiO_2 ~ 0.001 μm/h (calculated using equations detailed in section 1.5.2). This large difference comes from the difference in partial pressures of volatile species predicted for this environment (1000°C, 0.2 atm H_2O). $P_{Si(OH)4}$ is ~4 orders of magnitude lower than P_{HBO}.

opening; low volatilization rates keep gaps filled while higher rates open gaps. Gaps eventually close over longer time scales as silica growth continues.

5.5.3 Thermochemistry of SiC/BN oxidation

To address whether BN oxidation involves an intermediate liquid phase, thermodynamic calculations were performed using FactSage and the FactPS database. In one set of calculations, 1 mole of either SiC or BN was combined with 40 moles of Ar at 1 atm total pressure and 1000°C, the Ar was progressively replaced by H_2O, and the amounts of condensed phases and the partial pressures p of gases were computed. In a second set, 1 mole of SiC and 0.1 moles of BN were combined with 40 moles of Ar and the Ar was again progressively replaced with H_2O. The latter were intended to simulate BN oxidation in an environment controlled by SiC oxidation.

The results are plotted against water activity a_{H_2O} in Figure 14. (Here the gas pressures are not tracked once the requisite constituents have been fully consumed.) The oxidation sequences proceed in the following way:

(i) SiC on its own first forms CO(g) and smaller amounts of SiO(g) (Figure 14a). Silica emerges at $a_{H_2O} \approx 10^{-12}$ while C(s) forms at $a_{H_2O} \approx 3x10^{-9}$. C (s) and SiC (s) are fully consumed at later points (dependent on the initial amounts of SiC and Ar).

(ii) BN on its own initially produces N_2(g), B_2O_3(g), HBO(g) and HBO_2(g) (in decreasing order of concentration) (Figure 14c). Liquid boria emerges at $a_{H_2O} \approx 10^{-11}$: about an order of magnitude greater than that required to produce silica from oxidation of SiC. Beyond this point $p_{B_2O_3}$ plateaus while the partial pressures of the borohydroxide gases rise.

(iii) When SiC is combined with BN (Figure 14b), oxidation of SiC proceeds essentially the same as it does on its own. In contrast, BN remains stable until the point at which both SiC and C have been fully consumed. Only then does liquid boria begin to form. The broader implication is that, if the supply of SiC were sufficiently large, liquid boria may not emerge as an oxidation product of BN and thus BN removal could occur entirely through an active (gas phase) oxidation process.

The preceding calculations are consistent with the absence of liquid boria in the oxidation of crystalline BN. The outstanding question relates to the formation of liquid boria (or borosilicates) in the other two systems. The key difference between them is their O content: essentially nil in the crystalline BN and about 10 at% in both amorphous types. It therefore appears likely that the O in the BN plays a key role in the formation of liquid boria. Previous XPS studies have found O present within a metastable BN_xO_y phase in BN deposited at low temperature [30], [31]. This phase may react faster than pure BN and favor formation of liquid boria (analogous to the behavior of metastable Si-O-C in SiC fibers) [23]. Differences related to the BN microstructure (crystalline vs turbostratic), variations in microstructure through the coating thickness, and the presence of Si dopants may also play a role, as discussed later.

5.5.4 Recession in the absence of borosilicate glass

In the absence of liquid boria the BN recession rate may be controlled by either the intrinsic rate of oxidation/volatilization or the rate of outward transport of product gases through the recession channel. Regardless of the rate-limiting step in the early stages, recession slows as the fiber and matrix surfaces oxidize and the channel narrows. Recession ceases once the

channel has closed by the impingement of oxide scales on the fiber and matrix surfaces. Analysis of this scenarios follows.

5.5.4.1 Reaction control

When reaction controlled, BN volatilizes at a constant rate $\dot{L}_{BN}$ [μm/h] and the recession length is simply[****]:

$$L_R(t) = \dot{L}_{BN}\, t \tag{1}$$

Concomitantly, the exposed fiber and matrix surfaces oxidize, progressively narrowing the channel opening but not necessarily impeding recession. Assuming that fibers and matrix oxidize at the same rate, the channel width at the exposed surface, $\Delta(t)$, is given by:

$$\Delta(t) = h - \frac{YA}{2}\left\{\left[1 + \frac{t}{A^2/4B}\right]^{\frac{1}{2}} - 1\right\} \tag{2a}$$

where

$$Y \equiv \left[\left(\frac{\gamma_m - 1}{\gamma_m}\right) + \left(\frac{\gamma_f - 1}{\gamma_f}\right)\right] \tag{2b}$$

Here *A* and *B* are the linear and parabolic Deal Grove parameters for SiC, and γ_m and γ_f are the molar volume ratios of oxide and oxidizing (SiC) matrix (2.2) and HNS fibers (2.0), respectively [17]. (To a good approximation, *Y*=1.0.) Recession ceases when $\Delta(t) = 0$. The critical coating thickness h_c below which the gap closes before the end of an exposure of duration *t* is therefore:

[****] Table 1 contains a complete list of symbol definitions

$$h_c = \frac{YA}{2}\left\{\left[1 + \frac{t}{A^2/4B}\right]^{\frac{1}{2}} - 1\right\} \tag{3}$$

Alternatively, the closure time t_c for a coating of thickness h is

$$t_c = \frac{1}{4B}\left[\left(\frac{2h}{Y} + A\right)^2 - A^2\right] \tag{4}$$

Thus, for $h > h_c$, the recession length is given by Equation 1; otherwise, for $h < h_c$, it is:

$$L_R(t_c) = \dot{L}_{BN}\, t_c = \frac{\dot{L}_{BN}}{4B}\left[\left(\frac{2h}{Y} + A\right)^2 - A^2\right] \tag{5}$$

These predictions are plotted on Figure 15a. Here the Deal-Grove oxidation parameters are taken from a previous study on HNS fibers under the same environmental conditions (A=0.93μm and B=0.04μm^2/h at 1000°C, 20vol% water [23]). Since data for recession rates of BN under the same conditions are unavailable, the 1 h data from the current study were used to infer an intrinsic recession rate of $\dot{L}_{BN} \approx 50\mu m/h$. Here all of the experimental data lie in the domain $h > h_c$. Despite the absence of data in the low-h domain, the model correctly predicts a recession length that is independent of h. Furthermore, the inferred value of $\dot{L}_{BN}$ is comparable to that previously reported for BN under similar environmental conditions ($\dot{L}_{BN}$=20 μm/h at 800°C, 10% H_2O, balance dry air [2]).

When the same material properties are used with the model to predict the 12h data, the agreement with the measurements in the domain $h < h_c$ appears reasonable, though it breaks down for higher values of h. Specifically, it overestimates recession lengths by roughly a factor of 2. A better fit overall is obtained using a recession rate $\dot{L}_{BN} = 25\mu m/h$.

The preceding analysis assumes that the environment within the recession channel is uniform and the same as the external environment (0.2 atm H_2O). This assumption can be

assessed by analyzing the variations in fiber scale thickness $w(z,t)$ with recession depth, z (Figure 9). Based on the Deal Grove oxidation model, $w(z,t)$ is expected to follow:

$$w(z,t) = \frac{A}{2}\left\{\left[1 + \frac{(t-t_0)}{A^2/4B}\right]^{\frac{1}{2}} - 1\right\} \tag{6}$$

where t is the total exposure time and t_0 is the time at which the SiC at position z was exposed, given by $t_0 = z/\dot{L}_{BN}$. At $z = 0$, $t_0 = 0$ and $h(t)$=h_o, given by the original Deal-Grove model:

$$w_0 = \frac{A}{2}\left\{\left[1 + \frac{t}{A^2/4B}\right]^{\frac{1}{2}} - 1\right\} \tag{7}$$

At the bottom of the channel, $z = L_R$ and $h(z) = 0$. Combining these results yields:

$$w(z,t) = -\frac{A}{2} + \sqrt{\frac{(2w_0 + A)^2}{2} - \frac{z}{2L_R}[(2w_0 + A)^2 - A^2]} \tag{8}$$

Predictions of Equation 8 are compared with experimental measurements after 12h exposure in Figure 9. The predicted curve exhibits the same general trend as the experimental data though it overestimates the data somewhat. We surmise that the discrepancies may be due in part to random measurement errors (as evidenced by the data scatter). These would be particularly large on a relative basis when the scales are very thin (ca 0.1-0.2μm) and the measurements are made via SEM. Systematic errors may also be introduced because of slight rounding of the oxide edges during ion milling, potentially leading to underestimates of scale thickness.

One of the interesting features found in the oxidation of the crystalline BN but not accounted for in the preceding analysis is the steeply-angled reaction front, indicating that recession rates are greatest near the fiber-coating interface. This may be attributed to two

potential sources. First, preferential interface oxidation may be a result of pre-existing fiber-coating debonds, which could serve as preferential pathways for gas ingress. But two other aspects of the oxidation appear at odds with this hypothesis. In addition to the debonds, other cracks are present within the coatings themselves running parallel to the fiber axis; yet there was no evidence of accelerated oxidation along planes internal to the coating. Additionally, a previous detailed study of the coating characteristics of this particular composite found that debonds were seen by SEM in only about 20% of all fibers, yet essentially all of the recession fronts in this composite exhibited the same characteristic angled shape.

The second potential source of the reaction front shape relates to variations in BN microstructure through the coating thickness. Previous studies have found that the BN crystallites that form first on the fiber surface are generally very small and are of a size governed by surface roughness [32]. As BN grows and thickens, the crystallites increase in size and become aligned with the fiber surface [32]. Studies have also shown that small crystallites volatilize faster than large ones because of the greater fraction of disordered BN at the crystallite boundaries and thus a higher overall reactivity. The angled reaction front observed in the current experiments may be a manifestation of such differences in crystallite size at the fiber-coating interface relative to that elsewhere in the coating. We speculate that, if the intrinsic BN volatilization rate is particularly high at the fiber/BN interface, a narrow precursor channel can form at that interface and serve as a fast diffusion path. Further recession would then occur by *lateral (radial) oxidation* of the BN at a rate governed by the reactivity of the basal planes facing the oxidants.

5.5.4.2 Transport control

When recession is controlled by diffusion of gaseous reaction products through the recession channel, the recession rate (obtained from a mole balance of BN) is given by [16]††††:

$$\frac{dL_R}{dt} = \frac{\bar{m}\ \bar{V}_{BN}\ \Delta(t)\ C^*_{vg}\ D}{h\ L_R} \tag{9}$$

where $\bar{m}$ is a unitless mass balance term‡‡‡‡, $\bar{V}_{BN}$ is the molar volume of BN, and C^*_{vg} is the equilibrium concentration of volatilized $H_xB_yO_z$ gases at the reaction front. $C^*_{vg}$is calculated assuming ideal gas behavior: $C^*_{vg} = P_{vg}/RT$ where P_{vg} is the sum of the equilibrium partial pressures of reaction products. These pressures were calculated using FactSage, assuming 1 mole of BN at 1000°C in 0.2 atm H_2O (balance Ar) and suppressing liquid boria formation. D is the gas diffusion coefficient which, for narrow gaps, can be approximated using the Knudsen diffusion coefficient, given by

$$D_k = \frac{2}{3}\sqrt{\frac{8RT}{\pi M_{vg}}}\Delta(t) \tag{10}$$

where M_{vg} is the weighted average molecular weight of the volatile reaction products. Combining Eqs. (2), (9) and (10) yields:

$$\frac{dL_R}{dt} = \frac{2\bar{m}\,\bar{V}_{BN}\,C^*_{vg}}{3h\,L_R}\sqrt{\frac{8RT}{\pi M_{vg}}}\left\{h - Y\left[\frac{-A+\sqrt{A^2+4Bt}}{2}\right]\right\}^2 \tag{11}$$

††††Equation 9 differs from the corresponding equation in reference [16] by a factor $\Delta(t)/h$. The analysis presented in [16] assumes that the width of the BN available for volatilization at the reaction front progressively thins so as to match the gap opening at the channel entrance. In contrast, in the present case, the width of BN available for volatilization is assumed to remain constant, an assumption that is more in line with the experimental observations.

‡‡‡‡ $\bar{m}$ = 1 when 1 mole of BN is consumed in forming 1 mole of HBO_2(g) or H_3BO_3(g), $\bar{m}$ = 3 when 3 moles of BN is consumed in forming 1 mole of $H_3B_3O_6$(g), and $\bar{m}$ is the weighted average when all four gases are present.

(While this differential equation can be solved for $L_R(t)$, the solution is unwieldy and is not shown here.) Here again recession ceases once $\Delta(t) = 0$ and the critical values h_c and t_c are given by (3) and (4), respectively.

The computed recession lengths are plotted on Figure 15a. They over-estimate experimental measurements by an order of magnitude, indicating that the recession rate is not governed by gas transport kinetics and re-affirming the earlier conclusion that the process is reaction-limited. Notwithstanding this conclusion, it seems plausible that the inferred intrinsic volatilization rate may itself be transport-limited at a very *local* scale. That is, extension of the precursor channel, being only tens of nm wide, may be limited by gas transport.

5.5.5 Recession in the presence of borosilicate glass

In the presence of a borosilicate glass, the BN recession rate may be controlled by either the intrinsic oxidation rate (while the glass is boria-rich and non-protective) or the diffusion of oxidants or reaction products through the glass. As one limit, we consider the case where gas diffusivities through the borosilicate glass are large and thus recession is reaction-controlled. In that case the recession length is again described by Equation 1.

Recession is assumed to end once the silica content exceeds the saturation limit and solid silica begins to precipitate out of solution and deposit on the BN surface. Because the volume expansion upon formation of boria and silica are > 1, the volume of oxide produced exceeds the space available from consumption of BN and SiC. An analysis of recession cessation follows (see Figure 13b for corresponding schematics).

Assuming perfect mixing, continuous volatilization of boria at the channel entrance, complete retention of all silica, and equivalent matrix and fiber properties, the fraction X_S of silica within the glass is given by:

$$X_S = \frac{V_S}{V_O} \tag{12}$$

where V_O is the volume of space available in the channel from consumption of both BN and SiC and V_S is the volume of silica formed per unit depth [m^3/m]. V_S is governed by the volumetric SiC consumption rate $\dot{C}_S$ [$m^3/m\ s$] via:

$$V_S = \dot{C}_S\, \gamma_S\, t \tag{13}$$

where γ_S is the volume ratio of silica to SiC. Assuming $\dot{C}_S$ is governed by the linear oxidation rate of SiC and that the growth rate of channel length is governed by the linear oxidation rate of BN, the SiC consumption rate at time *t* becomes:

$$\dot{C}_{SiC} = 2\, \dot{L}_S\, \dot{L}_B\, \gamma_B\, t \tag{14}$$

where $\dot{L}_S$ and $\dot{L}_B$ are the linear consumption rates [m/s] of SiC and BN, respectively, which are related to the linear oxidation rates, B/A, via $\dot{L}_S = (B/A)_S/\gamma_S$ and $\dot{L}_B = (B/A)_B/\gamma_B$. Under the current test conditions $(B/A)_S$ = 0.043 μm/h [23]; that for BN is not known).

From geometry, the volume of space (per unit depth) made available by consumption of SiC and BN is given by:

$$V_O = \dot{L}_B\, \gamma_B\, t\, [\dot{L}_S\, t\, +\, h] \tag{15}$$

Combining Equations 12-15 yields:

$$X_s = \frac{2\, \gamma_S\, \dot{L}_S\, t}{\dot{L}_S\, t + \, h} \tag{16}$$

The critical time t_c at which the silica saturation limit, X_s^c, is reached is:

$$t_c = \frac{h}{\dot{L}_S \left(\frac{2\,\gamma_S}{X_S^c} - 1 \right)} \tag{17}$$

Alternatively, the critical coating thickness below which the glass has reached the silica saturation limit after time *t* is:

$$h_c = \dot{L}_S\, t \left(\frac{2\,\gamma_S}{X_S^c} - 1 \right) \tag{18}$$

Thus, for $h > h_c$, the recession length is given by Equation 1; for $h < h_c$, it is:

$$L_R(t_c) = \dot{L}_B\, t_c = \frac{\dot{L}_B\, h}{\dot{L}_S \left(\frac{2\,\gamma_S}{X_S^c} - 1 \right)} \tag{19}$$

Additionally, if no solid silica is formed after the onset of precipitation, the predicted terminal state of the recession channel at the channel entrance (once all boria has volatilized) would consist of silica scales of equal thickness on the fibers and matrix and an open gap between these scales (Figure 13b). The gap width δ_g normalized by the total channel width δ_c (from fiber surface to matrix surface) is predicted to be $\delta_g/\delta_c = 1 - X_S^c = 0.25$. This result is indeed obtained consistently for thin coatings (h < 0.25 μm), as shown by the observations and measurements in Figure 12.

The model predictions and recession length measurements from the amorphous BN are plotted on Figure 15b. Here the linear oxidation rate of fibers and matrix are taken from a previous study on HNS fibers under the same environmental conditions ($B/A =$ 0.043 μm/h at 1000°C, 20 vol% water [23]) and $X_S^c = 0.75$ at 1000°C [28], [29]. Since data for recession rates of amorphous BN under the same environmental conditions are unavailable, model predictions for $\dot{L}_{BN}$ = 10, 50 and 100 μm/h are presented. The data for $h > 0.25\ \mu m$ for both 1h and 12h exposures fall between predictions for $\dot{L}_{BN}$ = 50 and 100

μm/h, about twice that inferred from the crystalline BN data. This difference is consistent with reported faster oxidation rates of oxygen-containing BN deposited at lower temperatures [1], [2] and comprising smaller crystallites [32]. In contrast, thin coatings ($h < 0.25\ \mu m$) are seemingly consumed more slowly, with $\dot{L}_{BN}$ ~ 10 μm/h. We speculate (without compelling evidence) that the apparent effect of coating thickness on consumption rate may be due to variations in BN composition and structure with coating thickness. But coating thickness itself may not be the cause; rather, differing local chemical environments due to fiber packing during deposition may influence both the terminal coating thickness and the coating characteristics. A deeper investigation of the inter-relationships between coating properties, structure and thickness is needed to address this issue.

Si within amorphous BN coatings has been found to be bonded to oxygen, indicating the presence of metastable pockets of silica or borosilicate between domains of turbostratic BN [30]. This suggests that the consumption of Si-doped BN alone produces a borosilicate. With Si sources both within the coating and along the channel walls, the critical time to reach X_s^c is expected to be shorter than for amorphous BN without Si-doping. As previously noted, overlap in recession length data for 1h and 12h exposures indicate recession for thin coatings ended at times < 1h. The scatter in the data may reflect effects of compositional variations.

5.6 Conclusions and outlook

This study sheds light on some of the intricacies of oxidation of SiC/BN/SiC composites in water-rich environments. The findings relate to the role of BN coating characteristics in oxidation mechanisms and rates as well as the kinetics of oxidation and recession. Additionally, conceptual and analytical models provide a framework for interpreting

experimental measurements and for predicting behaviors over a range of environmental conditions, going beyond those employed here. The key conclusions follow.

First, the BN coating characteristics significantly impact the oxidation behavior. Crystalline BN, deposited at high temperatures, volatilizes directly without an intermediate glass phase and produces open recession channels. These channels are gradually filled with silica scale formed on the fiber and matrix surfaces exposed by BN removal until the channels close and recession effectively ceases. The absence of a boria-containing glass is the direct result of the local chemical environment created by SiC oxidation. It may also be predicated on preferential oxidation of fine BN crystallites at the coating/fiber interface, which brings the reaction products of SiC oxidation in very close proximity to the BN being oxidized. In contrast, amorphous BN and Si-doped amorphous BN, deposited at lower temperatures, contain higher levels of oxygen and carbon and exhibit distinctly different oxidation characteristics. Namely, the latter coatings oxidize to form borosilicate glasses that plug the channels needed for continued recession. While the amorphous BN eventually forms well-defined gaps between silica scales on the fibers and matrix after gap closure at the reaction front, consistent with theoretical predictions, the Si-doped BN oxidizes to produce completely fill gaps.

Second, the study yields insights into the rate-controlling processes in oxidation and recession. For crystalline BN, recession under the current test conditions (1000°C, 20% water vapor) is reaction-controlled rather than transport-controlled, with rates around 25–50 μm/h at. While in principle the oxidation rate would be transport-controlled for very thin coatings, the coatings in the material studied here were relatively thick (≈1 μm) and thus fell largely in the reaction-controlled domain. Amorphous and Si-doped BN show more complex

behavior. The initial recession rates are about twice that of the crystalline BN (50–100 μm/h) and suggest reaction control, despite the presence of a borosilicate glass between the oxidant and the BN. The implications are twofold: (i) the borosilicate glass likely provides minimal barrier to the diffusion of oxidants and (ii) the intrinsic oxidation rates of the amorphous (oxygen-containing) coatings are higher than those of the crystalline coatings, by a factor of about 2.

Finally, the conditions for gap closure and recession cessation differ in these systems. With the crystalline coatings, silica scale formation on the fibers and matrix near the channel mouth controls gas transport and eventually shuts the process down. With the amorphous coatings, in contrast, recession cessation coincides with the point at which the silica content in the borosilicate glass reaches its saturation concentration and solid silica begins to form on the internal fiber, matrix and coating surfaces. This phenomenon is manifested in gap closure near the reaction front rather than at the channel entrance.

5.6 References

[1] N. Jacobson, S. Farmer, A. Moore, and H. Sayir, "High-Temperature Oxidation of Boron Nitride: I, Monolithic Boron Nitride," *J. Am. Ceram. Soc.*, vol. 82, no. 2, pp. 393–98, 1999.

[2] P. Carminati, S. Jacques, and F. Rebillat, "Oxidation/corrosion of BN-based coatings as prospective interphases for SiC/SiC composites," *J Eur Ceram Soc*, vol. 41, no. 5, pp. 3120–3131, 2021, doi: 10.1016/j.jeurceramsoc.2020.07.056.

[3] N. Patibandla and K. L. Luthra, "Chemical Vapor Deposition of Boron Nitride," *J Electrochem Soc*, vol. 139, no. 12, pp. 3558–3565, 1992, doi: 10.1149/1.2069121.

[4] M. Jacquemin, A. Remigy, B. Menacer, V. Mille, C. Barraud, and C. Lazzaroni, "Amorphous and hexagonal boron nitride growth using bromide chemistry," *MRS Commun*, vol. XX, no. xx, pp. 1–6, 2023, doi: 10.1557/s43579-023-00500-9.

[5] M. Yuan, T. Zhou, J. He, and L. Chen, “Formation of boron nitride coatings on silicon carbide fibers using trimethylborate vapor,” *Appl Surf Sci*, vol. 382, pp. 27–33, 2016, doi: 10.1016/j.apsusc.2016.04.080.

[6] E. O. Einset, N. -B Patibandla, and K. L. Luthra, “Processing Conditions for Boron Nitride Coatings in Fiber Bundles via Chemical Vapor Deposition,” *Journal of the American Ceramic Society*, vol. 77, no. 12, pp. 3081–3086, 1994, doi: 10.1111/j.1151-2916.1994.tb04552.x.

[7] M. Wang, L. Jia, H. Xu, A. Li, Y. Peng, and Z. Tang, “Influence of pressure on chemical vapor deposition of boron nitride from BCl3/NH3/H2 gas mixtures,” *Ceram Int*, vol. 46, no. 4, pp. 4843–4849, 2020, doi: 10.1016/j.ceramint.2019.10.218.

[8] M. Chen, L. Pan, X. Xia, W. Zhou, and Y. Li, “Boron nitride (BN) and BN based multiple-layer interphase for SiCf/SiC composites: A review,” *Ceram Int*, vol. 48, no. 23, pp. 34107–34127, 2022, doi: 10.1016/j.ceramint.2022.07.021.

[9] J. Dai, Y. Wang, Z. Xu, R. Mu, and L. He, “Influence of BCl3/NH3 flow ratio on growth and microstructure of CVI-processed boron nitride interfacial coatings,” *Vacuum*, vol. 179, no. May, p. 109484, 2020, doi: 10.1016/j.vacuum.2020.109484.

[10] M. Leparoux, L. Vandenbulcke, and C. Clinard, “Influence of isothermal chemical vapor deposition and chemical vapor infiltration conditions on the deposition kinetics and structure of boron nitride,” *Journal of the American Ceramic Society*, vol. 82, no. 5, pp. 1187–1195, 1999, doi: 10.1111/j.1151-2916.1999.tb01894.x.

[11] V. Cholet and L. Vandenbulcke, “Chemical Vapor Infiltration of Boron Nitride Interphase in Ceramic Fiber Preforms: Discussion of Some Aspects of the Fundamentals of the Isothermal Chemical Vapor Infiltration Process,” *Journal of the American Ceramic Society*, vol. 76, no. 11, pp. 2846–2858, 1993, doi: 10.1111/j.1151-2916.1993.tb04026.x.

[12] O. Dugne *et al.*, “Interface characterization by TEM, AES and SIMS in tough SiC (ex-PCS) fibre-SiC (CVI) matrix composites with a BN interphase,” *J Mater Sci*, vol. 28, no. 13, pp. 3409–3422, 1993, doi: 10.1007/BF01159815.

[13] V. L. Christensen, A. F. Samuel, N. Han, and F. W. Zok, “Microstructure characterization and process-structure correlations in SiC/BN/SiC minicomposites,” *Acta Mater*, vol. 264, no. December 2023, p. 119589, 2024, doi: 10.1016/j.actamat.2023.119589.

[14] N. S. Jacobson, G. N. Morscher, D. R. Bryant, and R. E. Tressler, “High-Temperature Oxidation of Boron Nitride: II, Boron Nitride Layers in Composites,” *Journal of the American Ceramic Society*, vol. 82, no. 6, pp. 1473–1482, Dec. 2004, doi: 10.1111/j.1151-2916.1999.tb01944.x.

[15] F. W. Zok, V. E. Collier, and M. R. Begley, “Coating recession effects in ceramic composite strength,” *J Mech Phys Solids*, vol. 156, no. June, p. 104608, 2021, doi: 10.1016/j.jmps.2021.104608.

[16] V. E. Collier, W. Xu, R. M. McMeeking, F. W. Zok, and M. R. Begley, “Recession of BN coatings in SiC/SiC composites through reaction with water vapor,” *Journal of the American Ceramic Society*, no. April, pp. 1–14, 2021, doi: 10.1111/jace.18052.

[17] V. L. Christensen and F. W. Zok, “Insights into internal oxidation of SiC/BN/SiC composites,” *Journal of the American Ceramic Society*, vol. 106, no. 2, pp. 1561–1575, 2022, doi: 10.1111/jace.18834.

[18] G. Morscher, “Tensile Stress Rupture of SiCf/SiCm minicomposites with carbon and boron nitride Interphases at Elevated Temperatures in Air,” *J. Am. Ceram. Soc*, vol. 80, no. 8, pp. 2029–42, 1997.

[19] K. J. Larochelle and G. N. Morscher, “Tensile stress rupture behavior of a woven ceramic matrix composite in humid environments at intermediate temperature - Part i,” *Applied Composite Materials*, vol. 13, no. 3, pp. 147–172, May 2006, doi: 10.1007/s10443-006-9009-8.

[20] G. N. Morscher and J. D. Cawley, “Intermediate temperature strength degradation in SiC/SiC composites,” *J. Euro. Ceram. Soc*, vol. 22, pp. 2777–2787, 2002, [Online]. Available: www.elsevier.com/locate/jeurceramsoc

[21] G. N. Morscher, J. Hurst, and D. Brewer, “Intermediate-Temperature Stress Rupture of a Woven Hi-Nicalon, BN-Interphase, SiC-Matrix Composite in Air,” *Journal of the American Ceramic Society*, vol. 83, no. 6, pp. 1441–1449, Jun. 2000, doi: 10.1111/j.1151-2916.2000.tb01408.x.

[22] F. W. Zok, P. T. Maxwell, K. Kawanishi, and E. B. Callaway, “Degradation of a SiC-SiC composite in water vapor environments,” *Journal of the American Ceramic Society*, vol. 103, no. 3, pp. 1927–1941, Mar. 2020, doi: 10.1111/jace.16838.

[23] V. L. Christensen, A. R. Ericks, I. N. Duan, and F. W. Zok, “Oxidation of SiC fibers in water vapor,” no. March, pp. 1–19, 2024, doi: 10.1111/jace.19903.

[24] M. Leparoux, L. Vandenbulcke, V. Serin, and J. Sevely, “The interphase and interface microstructure and chemistry of isothermal/isobaric chemical vapour infiltration SiC/BN/SiC composites : TEM and electron energy loss studies,” *J Mater Sci*, vol. 32, no. 17, pp. 4595–4602, 1997, doi: 10.1023/A:1018633603920.

[25] J. Y. Huang, H. Yasuda, and H. Mori, “HRTEM and EELS studies on the amorphization of hexagonal boron nitride induced by ball milling,” *Journal of the American Ceramic Society*, vol. 83, no. 2, pp. 403–409, 2000, doi: 10.1111/j.1151-2916.2000.tb01204.x.

[26] D. L. Poerschke, M. N. Rossol, and F. W. Zok, “Intermediate Temperature Internal Oxidation of a SiC/SiCN Composite with a Polymer-Derived Matrix,” *Journal of the American Ceramic Society*, vol. 99, no. 9, pp. 3120–3128, Sep. 2016, doi: 10.1111/jace.14275.

[27] K. N. Detwiler and E. J. Opila, “Oxidation of SiC/BN/SiC ceramic matrix composites in dry and wet oxygen at intermediate temperatures,” *J Eur Ceram Soc*, vol. 42, no. 10, pp. 4110–4120, 2022, doi: 10.1016/j.jeurceramsoc.2022.04.003.

[28] M. A. Azim, B. Gorr, H. J. Christ, M. Heilmaier, U. Koch, and M. Engelhard, “Characterization of Oxidation Kinetics of Mo–Si–B-Based Materials,” *Oxidation of Metals*, vol. 87, no. 1–2, pp. 89–108, 2017, doi: 10.1007/s11085-016-9659-3.

[29] M. Boike, K. Hilpert, and F. Miiller, “Thermodynamic Activities in B2O3-SiO2 Melts at 1475K,” *J. Am. Ceram. Soc*, vol. 76, no. 11, pp. 2809–2812, 1993.

[30] K. L. More, K. S. Ailey, R. A. Lowden, and H. T. Lin, “Evaluating the effect of oxygen content in BN interfacial coatings on the stability of SiC/BN/SiC composites,” *Compos Part A Appl Sci Manuf*, vol. 30, no. 4, pp. 463–470, 1999, doi: 10.1016/S1359-835X(98)00135-3.

[31] C. Guimon *et al.*, “XPS Study of BN Thin Films Deposited by CVD on SiC Plane Substrates,” 1990.

[32] H. Plaisantin, S. Jacques, J. Danet, G. Camus, and H. Delpouve, “TEM characterization of turbostratic and rhombohedral BN interphases synthesized by chemical vapour infiltration in SiC/SiC-Si composites,” *Mater Charact*, vol. 172, 2021, doi: 10.1016/j.matchar.2020.110857.

[33] D. R. Gaskell, *An Introduction to Transport Phenomena in Materials Engineering*, Second. Momentum press, LLC, 2012. [Online]. Available: https://ocw.mit.edu/courses/materials-science-and-engineering/3-185-transport-phenomena-in-materials-engineering-fall-2003/#

5.7 Tables and Figures

Table 1: Definitions of symbols

a	Activity
A	Linear Deal Grove parameter
B	Parabolic Deal Grove parameter
B/A	Linear growth rate
C^*	Equilibrium concentration
D	Diffusion coefficient
D_k	Knudsen diffusion coefficient
D_m	Molecular diffusion coefficient
h	Coating thickness
k	Mass transfer coefficient
L_R	Recession length
$\dot{L}$	Linear consumption/recession rate
$\bar{m}$	Moles of gas per mole of material consumed
M	Weighted average molecular weight
P	Pressure
R	Universal gas constant
Re	Reynolds number
Sc	Schmidt number
t	Time
t_0	Time to surface exposure

T	Temperature
$\bar{V}$	Molar volume
V	Volume
V_0	Volume of available space
w	Scale thickness
w_0	Scale thickness at channel entrance
X	Mole fraction
X^c	Saturation concentration
z	Depth beneath exposed surface
δ_c	Recession channel width
δ_g	Recession channel gap width
Δ	Channel width at exposed surface
γ	Volume ratio (oxide:oxidizing material)
λ	Characteristic distance
Ω	Collision integral
ρ	Density
σ	Collision diameter
μ	Viscosity
ν	Velocity

Common subscripts

B	Boria

c	Critical value
eg	Environment gas
f	Fiber
m	Matrix
S	Silica
vg	Volatilizing gas

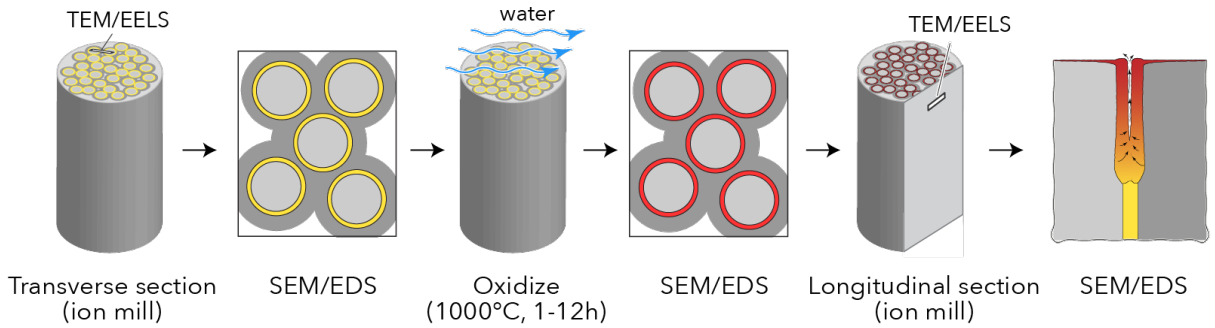

Figure 1: Experimental workflow in current study.

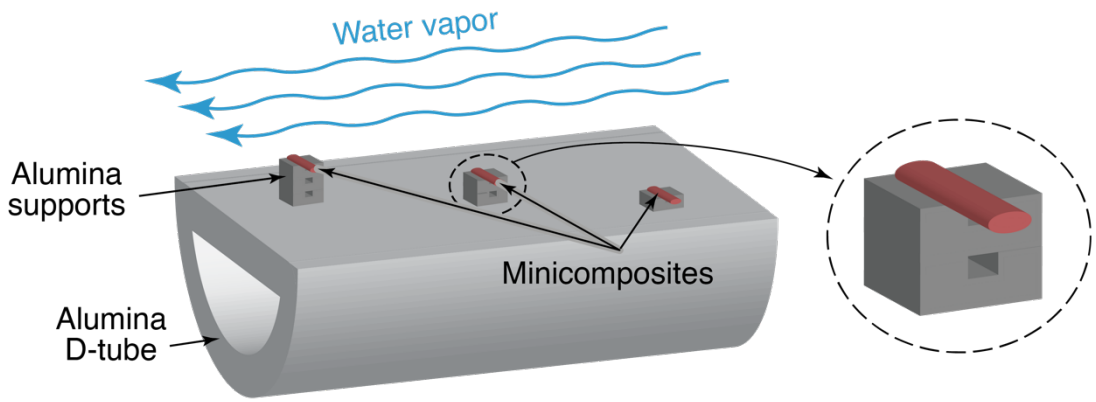

Figure 2: Arrangement of 3 minicomposite specimens in the oxidation furnace.

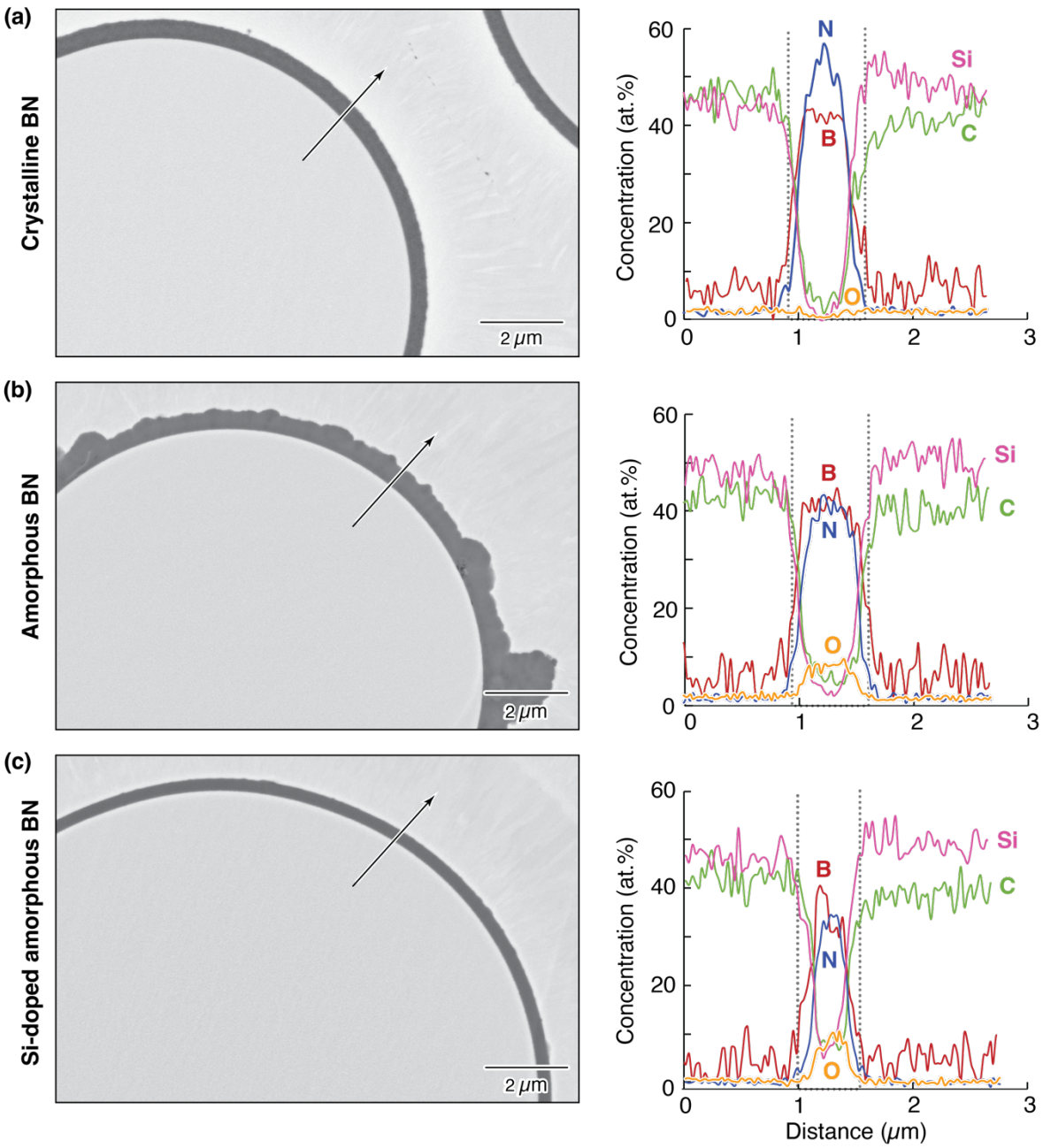

Figure 3: SEM images and EDS line scans of pristine coatings showing (a) the near absence of C or O in the crystalline BN and (b, c) the presence of O (about 10 at%) in both the amorphous and the Si-doped BN. While a Si signal within the doped BN is evident, the Si content cannot be reliably determined, because of the coating thickness in combination with the finite interaction volume of the electron beam with the sample, which can yield contributions to Si from the adjoining SiC fibers and matrix. Determining C-contents in the amorphous and the Si-doped BN is similarly problematic.

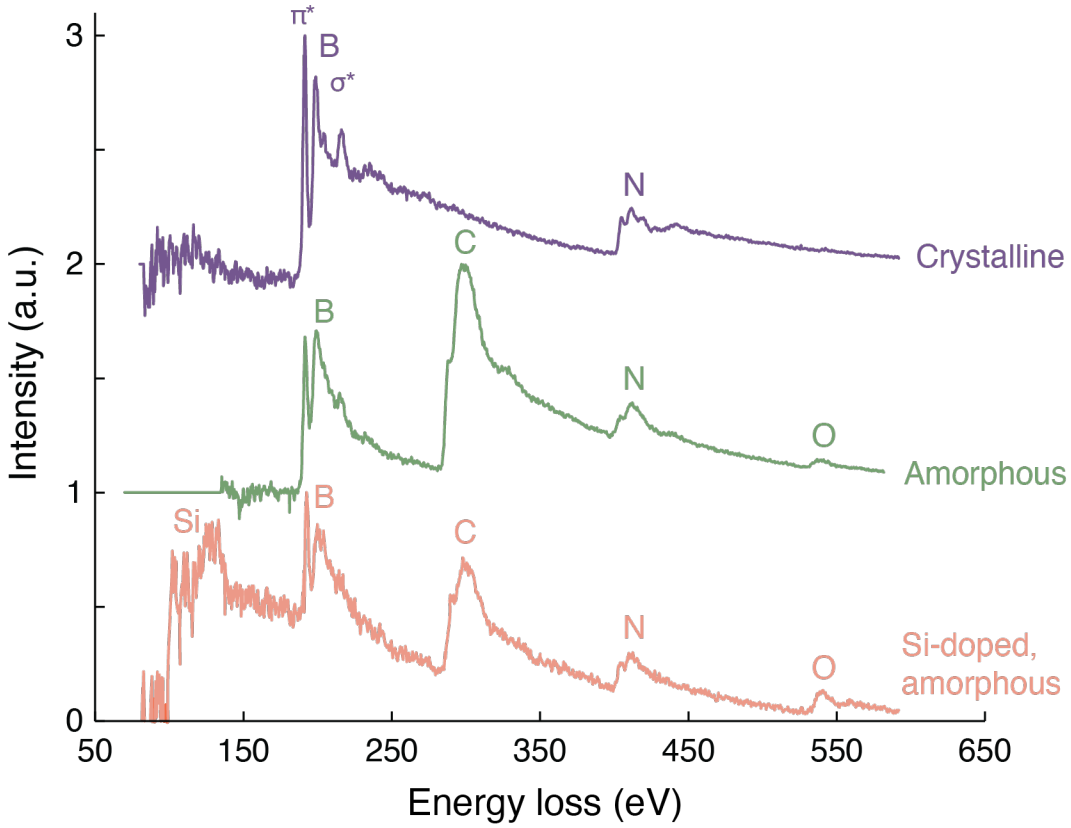

Figure 4: EELS spectra of crystalline BN, amorphous BN, and Si-doped BN. The amorphous and Si-doped coatings contain C and O in addition to B and N. The spectrum for the doped coating also confirms the presence of Si.

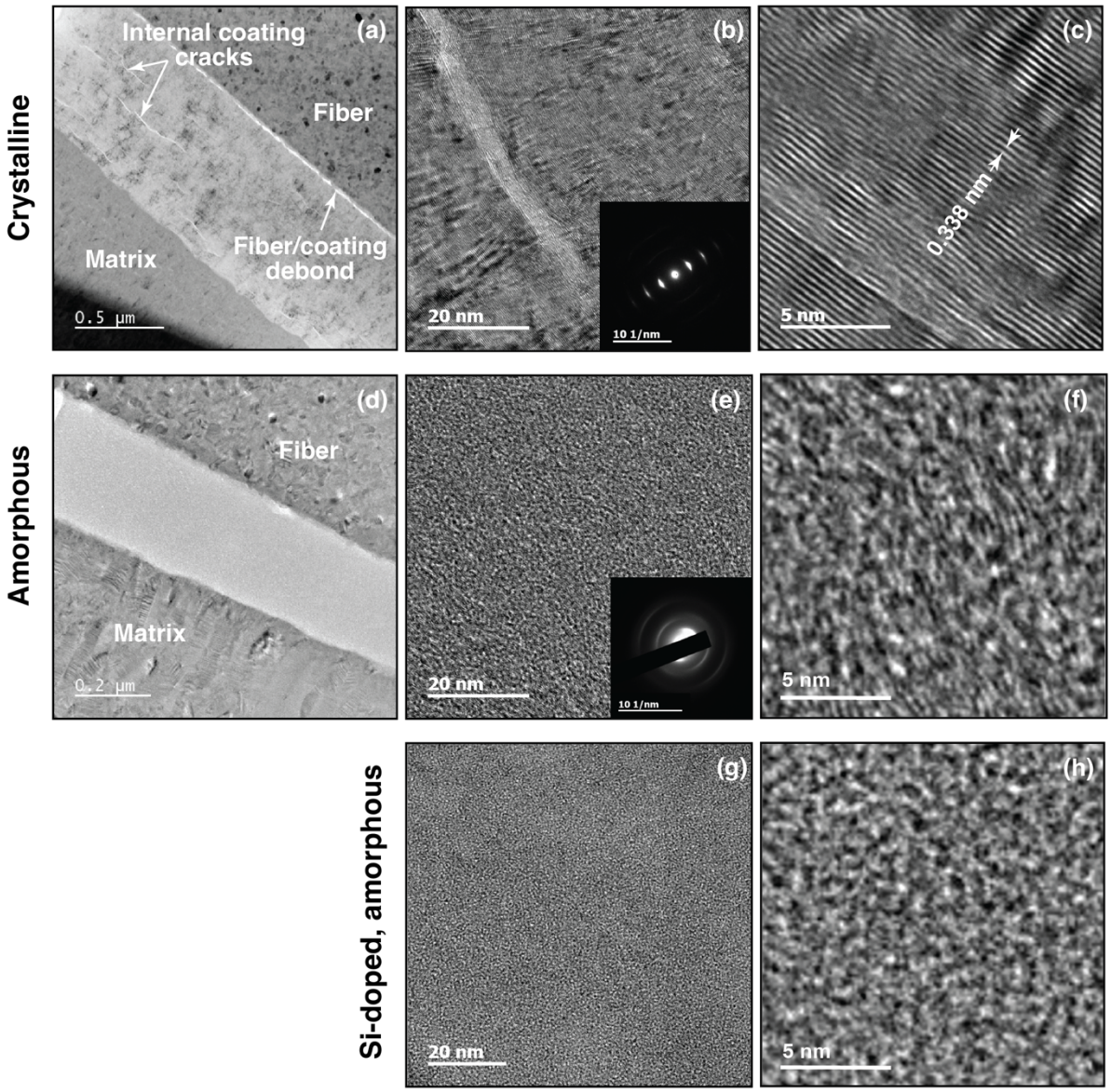

Figure 5: TEM images of the three BN types at various magnifications. (a-c) Crystalline BN is highly textured with basal planes aligned with the fiber axis. Cracks are visible within the BN and at the BN-fiber interface. (d-h) Amorphous coatings exhibit smaller crystallites that are only weakly aligned with the fiber axis while (g, h) the Si-doped coating exhibits even weaker ordering.

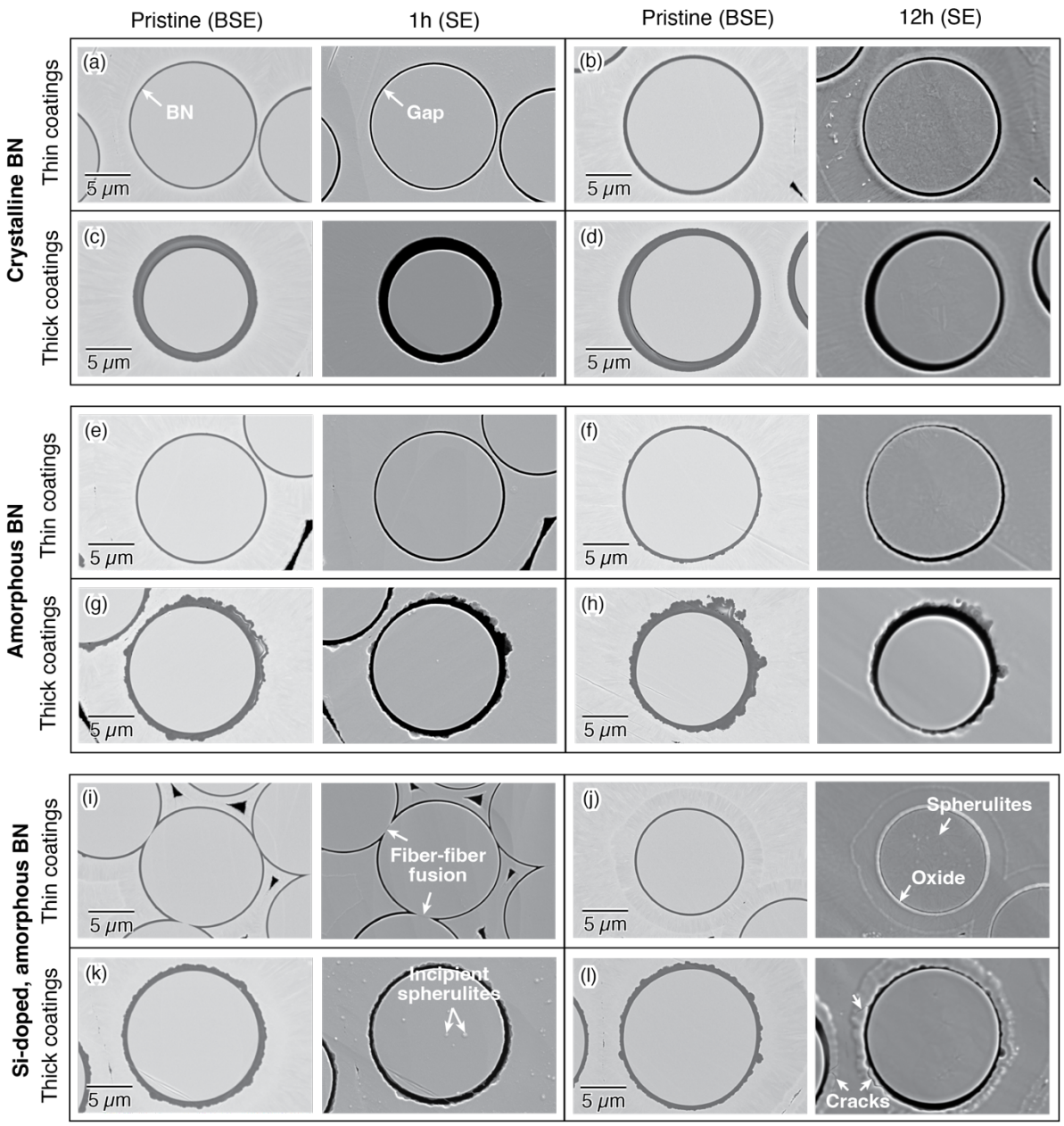

Figure 6: Representative fibers with thin and thick coatings on the exposed surface of composites before and after either 1h or 12h oxidation exposures for crystalline, amorphous and Si-doped BN.

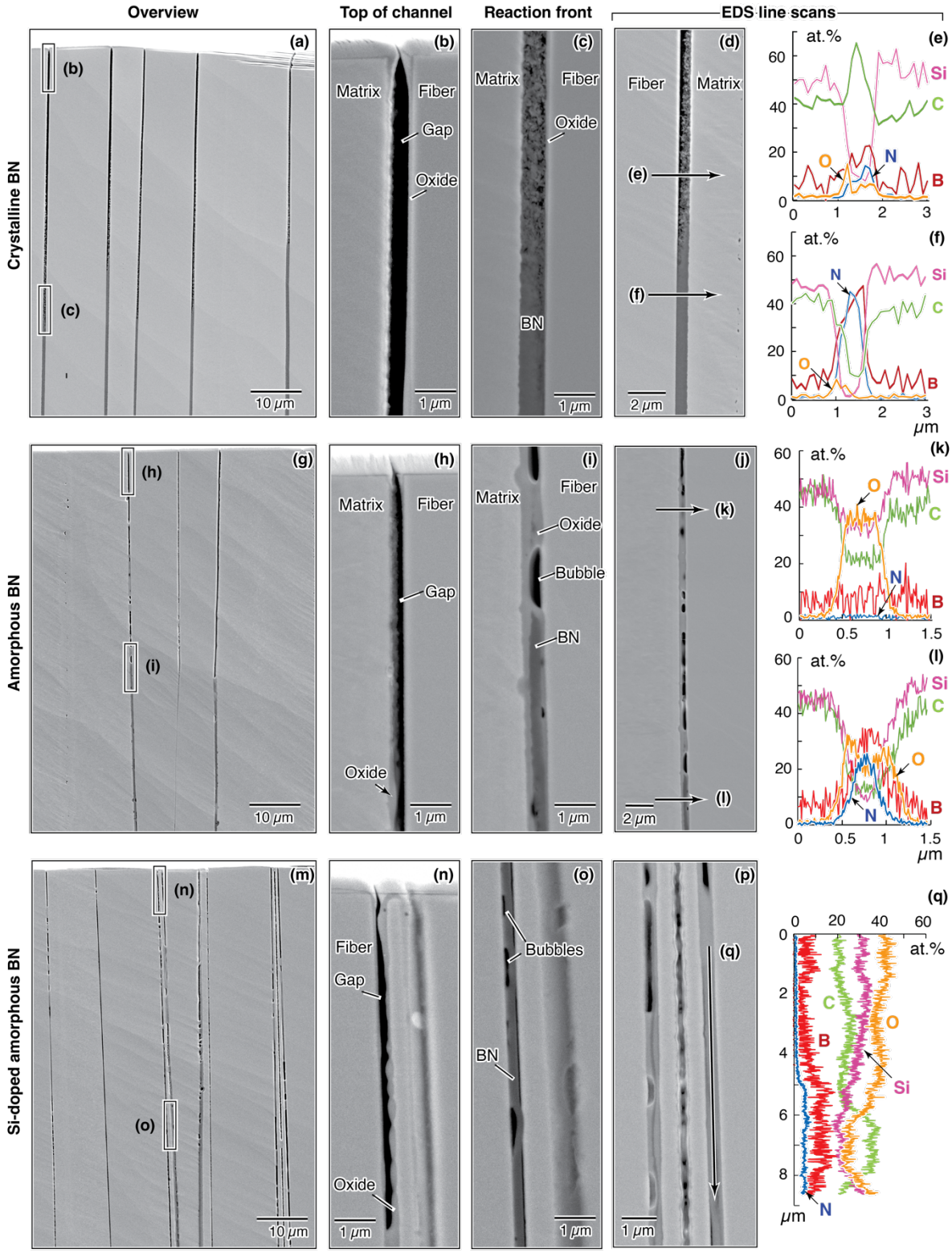

Figure 7: SEM images and EDS line scans of longitudinal sections after 1h exposure.

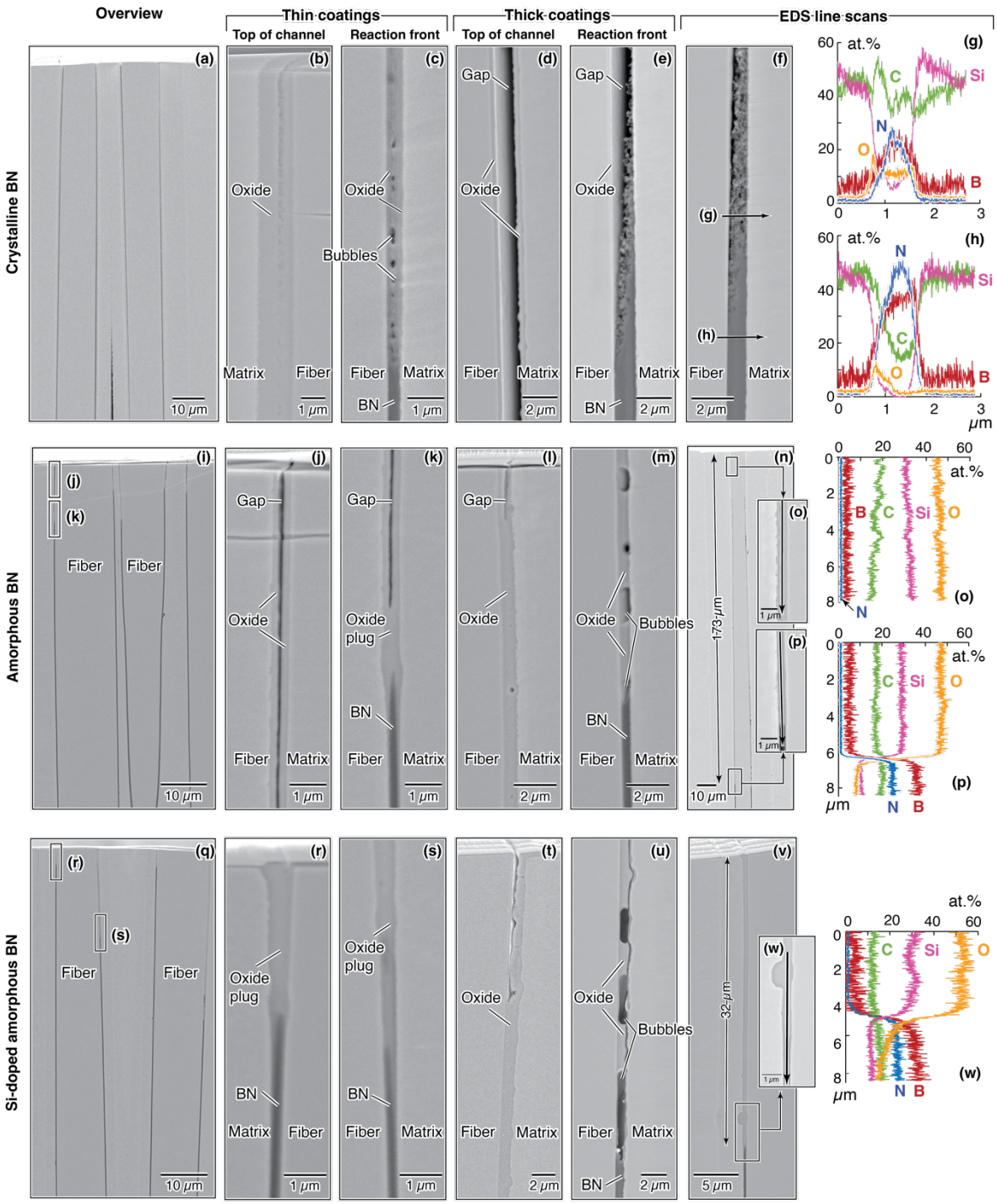

Figure 8: SEM images and EDS line scans of longitudinal sections after 12h exposure.

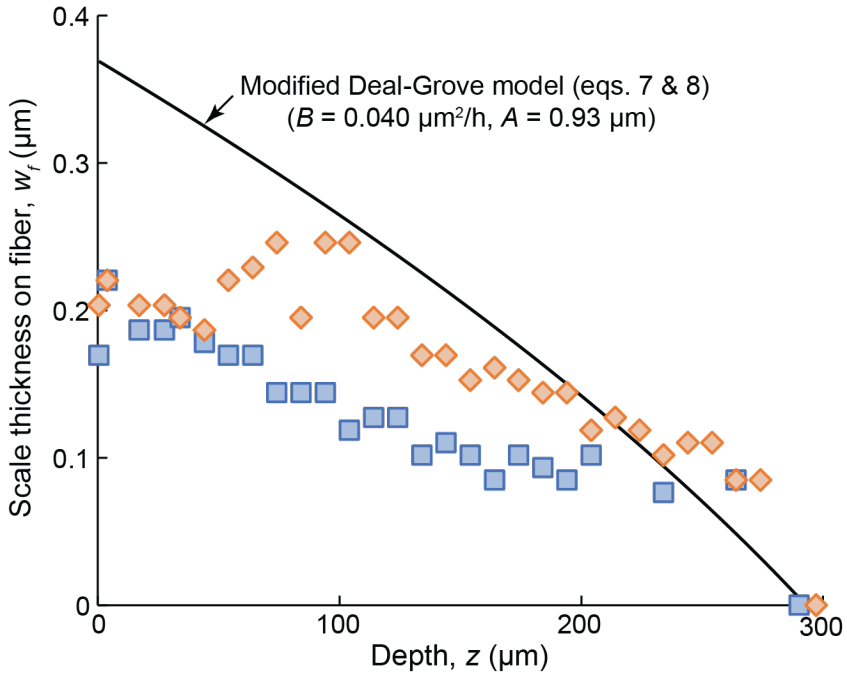

Figure 9: Variation in silica scale thickness on HNS fiber with depth into a channel after 12h exposure. The data sets correspond to measurements made on either side of the same fiber, corrected for the geometric effects caused by sectioning the fiber along a non-diametral plane.

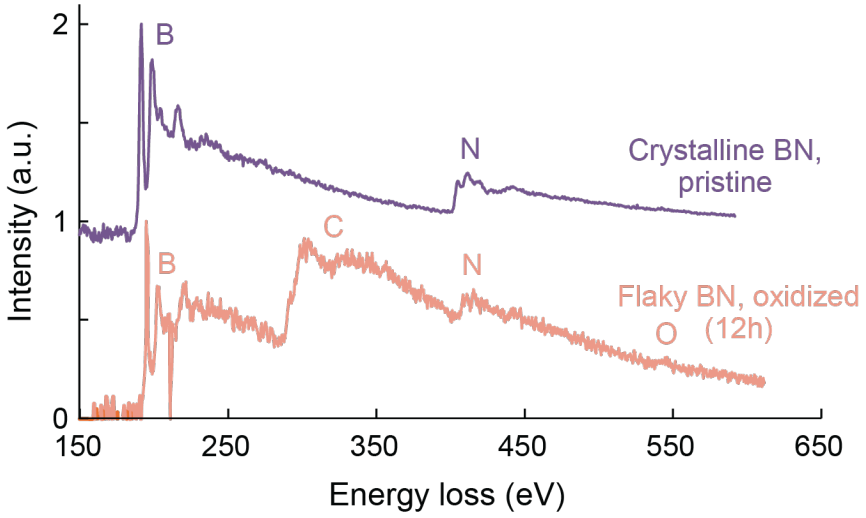

Figure 10: EELS spectrum of flaky crystalline BN post 12h exposure, showing a strong carbon edge that is not present in the pristine material.

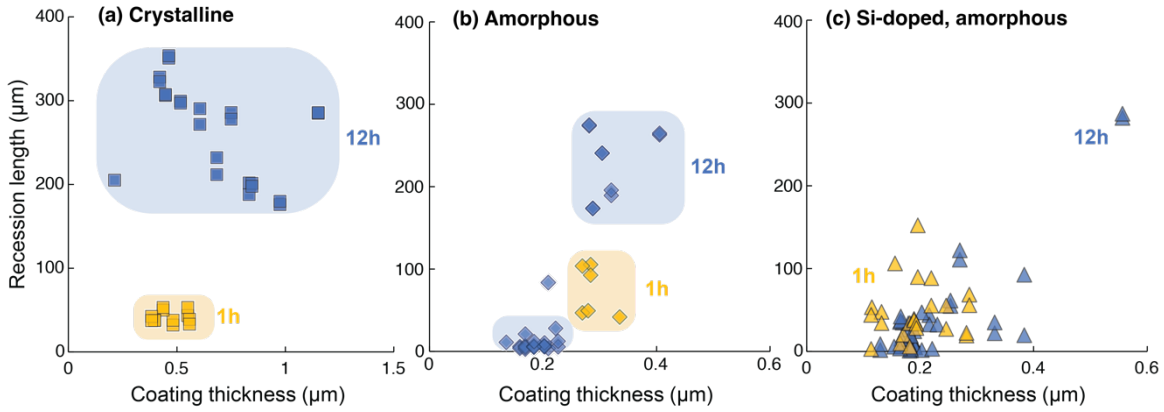

Figure 11: Effects of coating thickness on recession length after 1h and 12h exposures of (a) crystalline, (b) amorphous, and (c) Si-doped, amorphous coatings. (Note differences in x-axis scales).

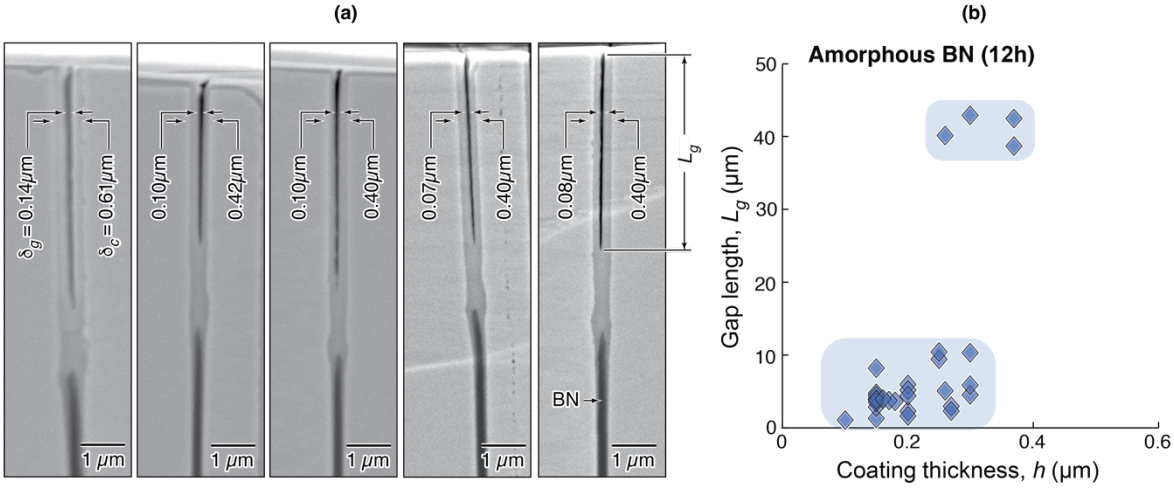

Figure 12: (a) Recession channels and oxide plugs obtained in thin amorphous BN coatings after 12h exposure. The features are remarkably qualitatively and quantitatively consistent between regions. The ratio of gap width δ_g to total channel width δ_c is ~ 0.25. (b) The measured gap lengths appear to be divided into two pools, distinguished roughly by coating thickness.

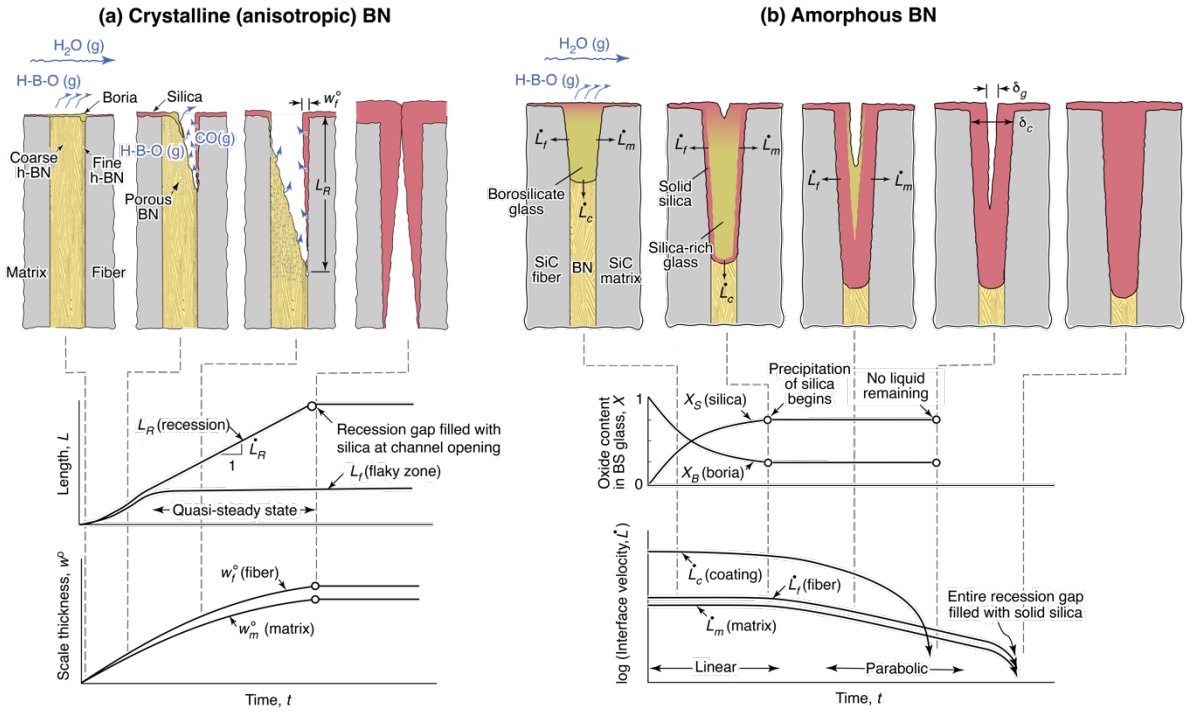

Figure 13: Two schemas for BN oxidation.

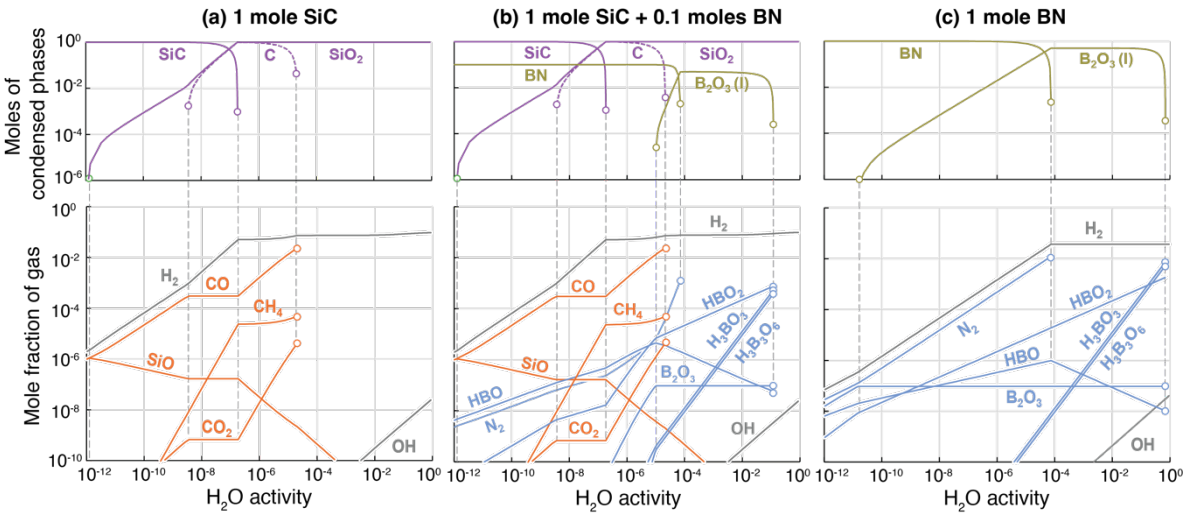

Figure 14: FactSage calculations for (a) 1 mole of SiC, (b) 0.1 moles BN with 1 mole SiC, and (c) 1 mole of BN in Ar environment with increasing H_2O. Circles denote points at which the constituents needed to produce the gas have been fully consumed, e.g. CO, CO_2 and CH_4 are not tracked once both SiC and C are consumed.

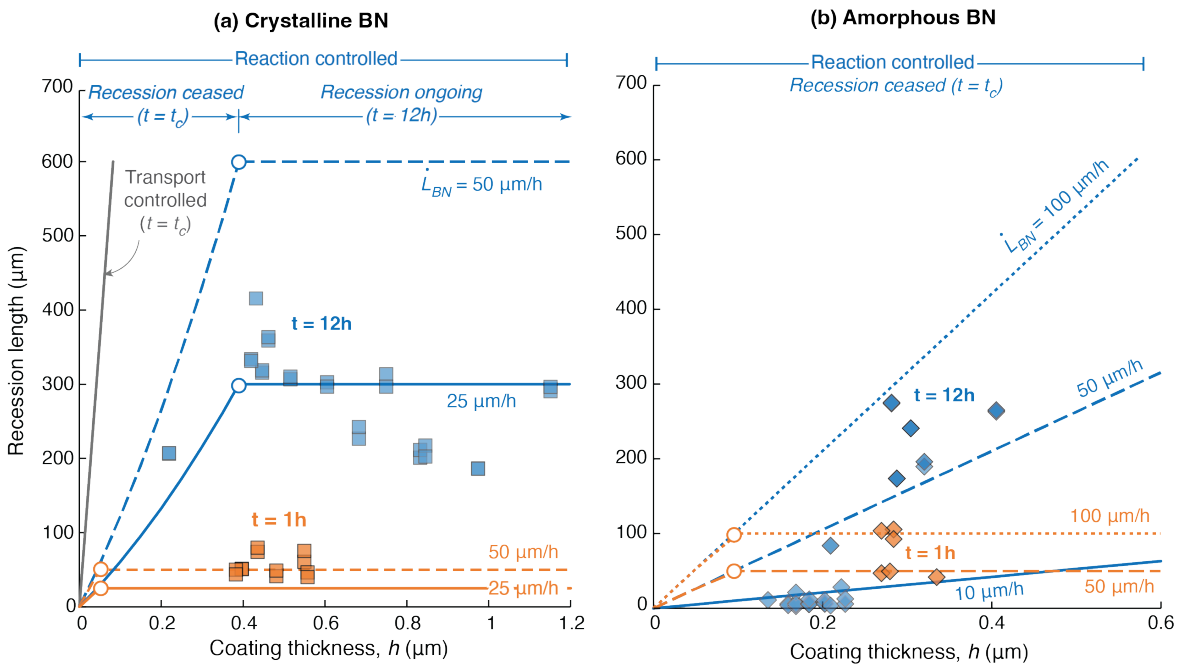

Figure 15: Diffusion-controlled and reaction-controlled models for (a) recession in the absence of liquid boria and (b) recession in the presence of borosilicate glass. Designations of behavioral domains in blue across the top of the figures pertain to the 12h exposure; similar designations are implied for the 1h exposure, using the orange (rather than blue) open circles as the transition points. The predicted transition point for amorphous BN at 12h (in b) occurs at 1.15µm.

Chapter 6

Conclusions and Future Recommendations

6.1 General conclusions and impact

This body of work elucidated mechanisms for internal oxidation of SiC/BN/SiC composites and established critical connections between oxidation behavior and structural and chemical characteristics of the constituent phases. The study employed specimens of increasing complexity, starting with bare fibers, then focusing on pristine minicomposite surfaces, and finally examining broken minicomposites with matrix cracks. The methodologies developed herein to characterize fiber bundles and composite microstructures provide a foundation for assessing: (i) the quality of as-processed composite microstructures using quantitative metrics, (ii) the phase evolution of BN coatings, SiC fibers, and SiC matrices in subsurface regions and near matrix cracks after oxidation treatment, and (iii) the effect of fiber and coating compositions and coating thickness on oxidation behavior.

Chapter 2 demonstrated that subtle differences between commercially available SiC fiber compositions result in significant variations in scale growth, crystallization, and cracking behavior. Analysis of scale thicknesses after exposures revealed that: (i) the interface reaction rates at early times depend on the amorphous Si-O-C and graphite contents in the fibers, (ii) when scale crystallization occurs, permeability decreases by a factor of 2 compared to amorphous scales, and (iii) following scale crystallization, further exposure leads to scale cracking due to the generation of tensile hoop stresses at temperature and additional bi-axial stresses upon cooling from the cristobalite phase transformation. This improved understanding of the underlying physical, chemical, and mechanical phenomena

serves as a baseline for interpreting measurements on more complex composite materials. Additionally, the properties obtained from the study of bare fibers can be directly incorporated into models of internal oxidation (as demonstrated in Chapter 5).

In Chapter 3, pristine minicomposite microstructures were analyzed using high-fidelity SEM images and custom MATLAB codes. Closed fiber clusters formed by tow twisting were identified as sources of coating non-uniformity, with coating thicknesses on cluster interiors being much smaller than those on cluster exteriors. Outside of these features, mean coating thickness correlated most strongly with distance from the tow exterior. Variations in coating thickness with position were rationalized in terms of a model of coupled gas diffusion and chemical reaction. This work should allow manufacturers and others to evaluate their composites quantitatively and make informed process improvements to increase coating uniformity and reduce defects across the composite. Furthermore, it was demonstrated that improving coating non-uniformity caused by one source may exacerbate non-uniformity caused by other sources, making it particularly challenging to attain full coating uniformity. In one example, the influence of local fiber volume fraction and distance from the tow edge on coating variance were found to trend in opposite directions with tow porosity.

Chapter 4 presented the first high-fidelity images of reaction zones, revealing differences in phase evolution in subsurface regions and adjacent to matrix cracks. Notably, in a dry air environment with ppm-levels of water vapor, BN coatings exposed at external surfaces were oxidized and volatilized, leaving behind relatively long recession gaps and oxide plugs. Comparing coatings on identical fibers before and after oxidation also revealed that thin coatings are more likely to be sealed with oxide plugs while thick coatings are

replaced with open recession channels. Coatings adjacent to matrix cracks exhibited differences in the extent of oxidation and recession because of transport limitations on removal of gaseous reaction products through matrix cracks. In these cases, the greatest recession distances were found near the composite edges or near large internal pores connected to the fracture surface. On the composite interior, BN coating channels were sealed with oxide plugs. Fiber-coating debonds were found to serve as additional pathways for oxidant transport, causing deeper oxidation at fiber-coating interfaces than matrix-coating interfaces, and were a major source of spatial variations in oxidation behavior within the composite. An existing recession model, based on gas transport-limited reaction rates, was found to over-predict the measured recession lengths. This deficiency, along with differences in the physical manifestations of the recession process, inspired the development of alternative analytical models that account for different rate-limiting mechanisms in Chapter 5.

Chapter 5 focused on the influence of BN coating composition on oxidation behavior in a water vapor-laden environment. Three types of BN were studied, each resulting in distinct behaviors. Crystalline BN oxidized without forming borosilicate glass, instead producing open channels that were eventually sealed at the channel opening due to oxidation of the fiber and matrix surfaces. Thermochemistry calculations showed that BN can volatilize directly without an intermediate liquid in gaseous environments set by neighboring SiC oxidation. In these cases, coating recession is reaction-controlled, with rates depending on the average BN crystallite size. Gradients in BN crystallites from fiber to matrix as deposition proceeds could create the angled recession fronts that were observed. Oxidation of the amorphous BN samples produced borosilicate glasses. Once boria volatilized, silica

glasses sealed fiber to matrix. The differences in behavior were used to devise two schema by which the oxidation/volatilization processes occur. In turn, these schema were used as a basis to develop new analytical models that describe some aspects of the process.

6.2 Future work

The procedures, tools, and analysis techniques developed in this work position the field well to investigate the connections between microstructure evolution during oxidation and changes in composite properties. Some of the opportunities for future work have a greater application focus, where fiber architectures and specimen geometries are more complex and test environments reflect service-relevant conditions. Other opportunities exist for fundamental research that would aid in elucidating details of mechanisms, material properties, process sequences, and reaction rates. Both types are discussed below.

6.2.1 Role of oxidation in mechanical behavior: Coating recession vs plugging

One of the key questions raised by this work is how coating recession and oxide plugging affect mechanical response. While oxide plugs can effectively arrest recession, they create strong fiber-matrix bonds that compromise local damage tolerance. On the other hand, while coating recession alone (without formation of condensed phases) eliminates shear coupling between fibers and matrix and may continue unabated, it does not lead to local stress elevations of the type produced by oxide plugs. What are the performance tradeoffs between having longer, open recession channels or shorter channels filled with oxide? Addressing this question is key to identifying strategies to tailor coatings to produce desired behaviors.

These questions could be addressed using two types of mechanical tests with two types of material. In the first, minicomposites would be pre-cracked to various levels above

the matrix cracking limit but below the ultimate strength. The test specimens would be examined to determine the crack locations and crack opening displacements. They would then be exposed to an oxidizing treatment of the kind employed in this study, potentially over a broad range of temperatures, environments and durations. The retained tensile properties would be measured and compared with those of the pristine material. Broken test specimens would be examined to determine the nature of the fracture surface, specifically the degree to which fiber breaks are correlated, the role of fiber-fiber or fiber-matrix fusion, and the spatial distribution of reaction products (e.g. oxides) that could be implicated in property degradation. Such examinations would be conducted using a combination of SEM and confocal microscopy. Subsurface features could be obtained from transverse and longitudinal sections through the broken specimens. Tests of this type would be performed on two groups of materials: one with crystalline BN coatings (to study the role of recession) and another with amorphous (borosilicate producing) BN. Comparative studies of this kind would be extremely informative in addressing the outstanding questions.

Recognizing that the oxides generated from amorphous BN would be solid at the temperature of these mechanical tests, complementary stress-rupture experiments would be conducted at various stresses at the temperatures of interest in the oxidative environment. In this case, the mechanical/rheological properties of the borosilicate glasses would differ significantly from those at room temperature, initially with a low viscosity and unable to support or generate substantial stress, but later with higher viscosity as the glass becomes silica-rich. For composites with crystalline BN, the progressive reduction in load transfer between phases caused by recession would be expected to lead to time-dependent fracture if the applied stress is sufficiently high, i.e. above the dry fiber bundle strength.

Experimental studies of this kind would inform the development or implementation of new models and simulations of fiber fragmentation that incorporate the pertinent phase evolution and fracture mechanisms. Monte-Carlo simulations in particular would be well-positioned to incorporate statistical variations in microstructural features like fused fibers and/or fiber clusters. The proposed experiments will help validate assumptions used in the simulations. Parametric studies would also provide insights into domains in which behaviors are severely affected by oxidation.

6.2.2 Cyclic oxidation

Volume expansion associated with the formation of oxides, coupled with the geometric constraints on volume expansion within composites, can lead to large internal stresses, especially at lower temperatures where oxides are unable to relax stress. Moreover these stresses can change dramatically with temperature, because of changes in constituent properties, thermal expansion mismatch between phases, and strains generated by phase transformations. In light of the brittle nature of the constituents and the potential for GPa-level stresses, thermal cycling may lead to microcracking that accumulates and degrades composite properties.

Some key questions that arise from these considerations include: (i) What are the critical conditions (e.g., oxidant concentration, temperature, time, oxide composition and thickness) that lead to crack formation in oxide scales? (ii) How does the morphology and location of oxides (e.g., within the matrix crack or in the interphase region) influence their susceptibility to cracking during thermal cycling? (iii) To what extent can oxidation-induced stresses cause fiber fracture in the absence of external loads, and how does this depend on the composite geometry, fiber composition and coating properties?

To address these questions, a systematic investigation of the effects of thermal cycling on oxide scale integrity and composite properties is recommended. This investigation should include:

(i) Finite element analysis (FEA) to model the stress distribution within oxide scales and adjacent composite constituents during thermal cycling. These simulations would incorporate temperature-dependent material properties, oxide growth kinetics, and viscoelastic behavior of the oxide scales. Parametric studies couldbe conducted to investigate the influence of oxide composition, thickness, and morphology on stress development and potential for cracking. FEA would provide valuable insights into the critical conditions that lead to cracking of oxide scales and could guide the design of experiments to validate these predictions. Models built for oxide growth beneath an EBC could be adapted for oxide spilling into a matrix crack [1].

(ii) Cyclic oxidation experiments on fiber bundles, uncracked minicomposites, and pre-cracked minicomposites with varying interphase coatings (e.g., different BN crystallinities and thicknesses). Samples would be exposed to oxidizing environments at different temperatures and durations, followed by cooling to room temperature. Multiple cycles with varying dwell times would be employed to assess the cumulative effects of thermal cycling. The experimental conditions could be informed by the FEA results to focus on the most critical parameters.

(iii) Detailed characterization of oxide scale microstructure and damage using techniques such as longitudinal sectioning/SEM and micro x-ray computed tomography (XCT) scanning [2]. These techniques could provide insights into the spatial distribution and morphology of oxides, as well as the presence of cracks or other damage within

the oxide scales, fibers, and matrix. The experimental observations would be compared with the FEA predictions to validate and refine the models.

(iv) Tensile testing of cycled samples to evaluate the impact of oxidation-induced damage on fiber bundle and composite properties. Comparison of mechanical properties before and after thermal cycling would help quantify the extent of degradation and identify critical damage mechanisms. The results could be correlated with the microstructural observations and FEA predictions to develop a comprehensive understanding of the relationships between oxidation-induced damage and mechanical performance.

By starting with FEA and focusing on tensile tests for mechanical characterization, this investigation provides a rational approach to understanding the factors governing oxidation-induced damage in SiC/BN/SiC composites during thermal cycling. The combination of computational modeling, targeted experiments, and advanced characterization techniques would enable the development of predictive models and design guidelines for enhanced composite durability in high-temperature, cyclic environments.

6.2.3 Role of other combustion products on oxidation behavior

In gas turbine engines, combustion of jet fuel produces a complex mixture of gases, including carbon dioxide (CO_2), water vapor (H_2O), nitrogen (N_2), and smaller amounts of nitrogen oxides (NO_x), carbon monoxide (CO), unburned hydrocarbons (UHC), sulfur oxides (SO_x), and particulate matter (PM). The primary products of complete combustion are CO_2 and H_2O, and their relative amounts can be determined from the general combustion reaction of a hydrocarbon fuel (C_xH_y) with air:

$$C_xH_y + \left(\frac{x+y}{4}\right)(O_2 + 3.76N_2) \rightarrow xCO_2 + \left(\frac{y}{2}\right)H_2O + \frac{3.76(x+y)}{4}N_2$$

The stoichiometric ratio of CO_2 to H_2O produced depends on the hydrogen-to-carbon ratio (y/x) of the fuel. For most jet fuels, this ratio is approximately 2, meaning that for every mole of CO_2 produced, about 1 mole of H_2O is generated. In other words, the combustion of jet fuel produces roughly equal amounts of CO_2 and H_2O on a mole basis. However, the actual molar ratio of CO_2 to H_2O in the exhaust gas may vary with fuel composition, engine operating conditions, and combustion efficiency .

To better understand the oxidation behavior of SiC/BN/SiC composites in engine-relevant environments, it is important to investigate how the presence of CO_2 and N_2 in the gas stream affects the thermodynamic driving forces for the oxidation of SiC and BN. CO_2 and N_2 are not typically considered active oxidants like H_2O, but their presence in the gas mixture could potentially alter the critical activities at which SiO_2 and B_2O_3 form and/or the equilibrium partial pressures of volatile species, which could change the overall oxidation kinetics.

To explore this question, a two-pronged approach is recommended. First, thermodynamic predictions using FactSage software would be performed to calculate the equilibrium partial pressures of key volatile species (such as $Si(OH)_4$, SiO, CO, $H_xB_yO_z$, etc.) in gas mixtures containing various ratios of H_2O, CO_2, and N_2 at relevant temperatures and pressures. These calculations would provide insights into how the presence of CO_2 and N_2 affect the thermodynamic driving forces for SiC and BN oxidation. If the calculations reveal significant differences compared to cases of pure H_2O, comparative oxidation experiments could be conducted using SiC fibers and SiC/BN/SiC composites in gas mixtures containing H_2O, CO_2 and N_2.

By systematically varying the concentrations of H_2O, CO_2, and N_2 in the oxidizing environment, the relative contributions of each gas species to the overall oxidation behavior could be assessed. In-situ and post-exposure characterization using techniques like TGA and mass spectrometry, SEM, EDS, and XRD would reveal changes in oxidation and volatilization rates, and oxide scale composition and morphology, compared to the baseline experiments in dry and wet air.

6.2.4 Properties of borosilicate glasses: viscosity, permeability, and volatilization rates

The viscoelastic properties of the borosilicate glass formed during the oxidation of SiC/BN/SiC composites play a crucial role in determining the evolution of the recession front with time and the stress state within the oxidized regions. Both viscosity and permeability are expected to evolve with time as the composition of the borosilicate glass changes due to the volatilization of B_2O_3 and the continued oxidation of the composite constituents. However, the time-dependent viscosity and gas diffusivities of these borosilicate glasses are currently unknown, presenting a significant challenge for modeling coating recession and stress evolution.

The viscosity of borosilicate glasses with different compositions should be measured as a function of time and temperature. This could be done with mixtures of pure B_2O_3 and SiO_2 powders using high-temperature viscometry [3] or differential thermal analysis (DTA) [4]. Introducing an oxidizing environment into the viscometer paired with a mass spectrometer at the outlet would provide complementary information about the composition of volatile species, enabling the correlation of volatilization rates with changes in viscosity over time.

In addition to viscosity, the permeability of the borosilicate glass to oxidants and reaction products is critical for modeling oxidation kinetics. The oxide composition influences its structure, which in turn affects its permeability. While diffusivities of H_2O, O_2, and various reaction products through borosilicate glasses are currently unknown, effective diffusivities could be determined by conducting experiments on model systems. For example, if amorphous, CVD BN or B_2O_3 sol gels were deposited on flat CVD SiC substrates in a uniform layer, diffusion couple experiments could be conducted to track borosilicate composition at the interface and loss of BN from the surface. A combination of SEM imaging and XPS depth profiling (or SIMS) would be utilized to study the composition evolution of the stack and oxide formation at the interface prior to complete loss of BN or B_2O_3.

By measuring the time-dependent viscosity and permeability of borosilicate glasses formed during the oxidation of SiC/BN/SiC composites and correlating these properties with the composition and structure of the oxide, it may be possible to develop more accurate models of the stress evolution and oxidation kinetics within these materials. This, in turn, will enable the prediction of oxidation-induced damage and the development of strategies for mitigating such damage through the tailoring of the composite constituents and interphase coatings. Ultimately, a fundamental understanding of the properties of borosilicate glasses would be instrumental in designing SiC/BN/SiC composites with enhanced durability in high-temperature, oxidizing environments.

6.3 References

[1] S. Sehr, V. Collier, F. Zok, and M. R. Begley, "Oxide growth and stress evolution underneath cracked environmental barrier coatings," *J Mech Phys Solids*, vol. 175, no. March, p. 105275, 2023, doi: 10.1016/j.jmps.2023.105275.

[2] A. M. Hilmas, K. M. Sevener, and J. W. Halloran, "Damage evolution in SiC/SiC unidirectional composites by X-ray tomography," *Journal of the American Ceramic Society*, vol. 103, no. 5, pp. 3436–3447, 2020, doi: 10.1111/jace.17017.

[3] "VIS 413 High Temperature Viscometer," Waters TA instruments. [Online]. Available: https://www.tainstruments.com/vis-413-high-temperature-viscometer/

[4] S. Sukenaga *et al.*, "Effect of calcium and potassium oxide addition on the viscosity and fragility of a calcium aluminosilicate melt," *Journal of the American Ceramic Society*, vol. 107, no. 6, pp. 3822–3836, 2024, doi: 10.1111/jace.19722.